Modelling and control of photobioreactors under dynamic light regimes

Joel Ignacio Fierro Ulloa

UNIVERSITÉ CÔTE D'AZUR | ÉCOLE DOCTORALE SCIENCES ET TECHNOLOGIES DE L'INFORMATION ET DE LA COMMUNICATION

THÈSE DE DOCTORAT

Modélisation et contrôle de photobioréacteurs en régime de lumière dynamique

Joel Ignacio Fierro Ulloa

Centre Inria d'Université Côte d'Azur, Biocore Team

Présentée en vue de l'obtention du grade de docteur en:
Contrôle, optimisation, prospective d'Université Côte d'Azur

Dirigée par:
Olivier Bernard, Directeur de Recherche, Centre Inria d'Université Côte d'Azur

Co-encadrée par:
Benoît Chachuat, Professeur, Imperial College London
Liudi Lu, Chercheur, University of Geneva

Soutenue le:
29 Octobre, 2024

Devant le jury, composé de:

Eugenio Cinquemani, Directeur de Recherche, Centre Inria de l'Université Grenoble Alpes

Francis Mairet, Chercheur, Ifremer

Jean-Baptiste Caillau, Professeur, Centre Inria d'Université Côte d'Azur

Pedro Gajardo, Professeur, Universidad Técnica Federico Santa María

digitalgae THE DIGITALGAESATION PROJECT

Inria

Modélisation et contrôle de photobioréacteurs en régime de lumière dynamique

Modelling and Control of photobioreactors under dynamic light regimes

Jury

Président du jury

Jean-Baptiste Caillau, Professeur, Université Côte d'Azur, CNRS, Inria, LJAD

Rapporteurs

Eugenio Cinquemani, Directeur de Recherche, Centre Inria de l'Université Grenoble Alpes
Francis Mairet, Chercheur, Ifremer

Examinateurs

Pedro Gajardo, Professeur, Departamento de Matemática, Universidad Técnica Federico Santa María

Directeur de thèse

Olivier Bernard, Directeur de Recherche, Centre Inria d'Université Côte d'Azur

Co-encadrants

Benoît Chachuat, Professeur, Department of Chemical Engineering, Imperial College London, UK
Liudi Lu, Chercheur, section of Mathematics, University of Geneva

Modélisation et contrôle de photobioréacteurs en régime de lumière dynamique

Résumé

Les microalgues peuvent produire de la biomasse en utilisant la lumière comme source d'énergie grâce à la photosynthèse. La biomasse algale permet de produire efficacement des aliments pour animaux, des produits pharmaceutiques etc. A plus long terme, les microalgues pourront être utilisées pour la production d'énergie ou le traitement des eaux usées. La culture de ces micro-organismes est réalisée dans des photobioréacteurs dont la forme, la taille et le mode d'utilisation varient. En outre, les microalgues sont connues pour leur taux de croissance rapide et leur capacité à se développer dans divers environnements, ce qui en fait une source très polyvalente. Elles absorbent le CO2, ce qui contribue à atténuer les émissions de gaz à effet de serre, et peuvent pousser sur des terres non arables. La source de lumière peut être naturelle ou artificielle et constitue l'un des facteurs les plus importants dont l'utilisation doit être optimisée.

Cette thèse se concentre sur les modèles mathématiques qui décrivent les effets de la lumière sur la croissance des microalgues et explore les problèmes de contrôle liés à leur culture, en considérant les différents phénomènes qui se produisent dans les centres de réaction de la photosynthèse. L'analyse de la dynamique rapide de la photosynthèse permet de comprendre comment la lumière perçue par les cellules, y compris du fait du mélange dans un photobioréacteur, peut affecter la croissance.

Lorsqu'un photobioréacteur utilise de la lumière artificielle, l'intensité de la lumière peut être définie comme une variable de contrôle. En explorant les différentes échelles de temps des phénomènes de photoinhibition et de photoacclimatation, les problèmes de contrôle optimal sont étudiés dans le but de maximiser la biomasse récoltée d'un photobioréacteur continu. Le principe du maximum de Pontryagin et les méthodes directes d'optimisation sont utilisées pour traiter ce type de problèmes.

D'autre part, comme chaque photobioréacteur et chaque espèce de microalgues a des caractéristiques spécifiques, le développement de modèles adaptables à différentes conditions est un défi important abordé dans cette thèse. Pour y parvenir, des modèles hybrides qui intègrent des équations différentielles ordinaires et des réseaux neuronaux artificiels sont proposés pour modéliser les procédés à base de microalgues. Cette thèse se propose de fournir un cadre complet pour l'optimisation de la culture des microalgues, en s'appuyant à la fois sur la modélisation mathématique et sur des techniques d'apprentissage automatique de pointe pour améliorer la productivité et l'efficacité dans divers scénarios de culture. En outre, elle cherche également à approfondir des sujets théoriques fondamentaux dans la théorie du contrôle optimal, afin de proposer et d'analyser de nouveaux algorithmes qui peuvent être utilisés pour d'autres types de problèmes.

Mots clés: Microalgues, Systèmes dynamiques non linéaires, Contrôle Optimal, Réseaux de Neuroneaux artificiels

Modelling and Control of photobioreactors under dynamic light regimes

Abstract

Microalgae can produce biomass using light as an energy source through photosynthesis. Algal biomass has great potential for the production of food, feed, pharmaceuticals and, at longer time scale for wastewater treatment or bioenergy production. The cultivation of these microorganisms is carried out in photobioreactors which vary in shape, size, and mode of operation. Additionally, microalgae are known for their rapid growth rates and ability to thrive in a variety of environments, making them a highly versatile source. They absorb CO2, helping to mitigate greenhouse gas emissions, and can grow on non-arable land. The light source can be natural or artificial, and it is one of the most important factors in the process. The objective of this PhD is to propose strategy for optimally using light.

This thesis focused on mathematical models that describes the effects of light on the growth of microalgae and explores control problems related to their cultivation, considering different phenomena that occurs in the reaction centers of photosynthesis. The analysis of the fast dynamics of the photosynthesis is investigated through modelling to understand how different patterns of light, including the mixing within a photobioreactor, affect the growth of the microalgae.

When a photobioreactor uses artificial light, the intensity of the light can be set as a control variable. Models for exploring the timescales of different phenomena as photoinhibition and photoacclimation are presented. Optimal control strategies are setup using Pontryagin's maximum principle and direct methods, with the objective to maximize the harvested biomass of a continuous photobioreactor.

On the other hand, as each photobioreactor and microalgae species have specific parameters, developing adaptable models for different conditions is a significant challenge addressed in this thesis. To achieve this, hybrid models that combine ordinary differential equations and artificial neural networks are developed for modelling and controlling microalgae-based processes. This thesis aims to provide a comprehensive framework for optimizing microalgae cultivation, leveraging both mathematical modelling and cutting-edge machine learning techniques to enhance productivity and efficiency in various cultivation scenarios. Additionally, it also seeks to go into fundamental theoretical topics in optimal control theory, to propose and analyze new algorithms that can address other types of problems.

Keywords: Microalgae, Non-linear Dynamical Systems, Optimal Control, Neural networks

Acknowledgments

To begin with, I start by thanking my supervisor, Olivier Bernard, for the pleasant work we did together and for the freedom and trust he gave me to do this research.

I am very grateful with all the members of the jury, in particular with Liudi Lu for participate and collaborate with me in developing this thesis, specially because the first part if this thesis is a continuation of his work, and to Benoit Chachuat for receiving me twice in London, and for the challenges that for the challenges he imposed on me in the last part of this thesis. Thanks to Eugenio Cinquemani, Francis Mairet, Pedro Gajardo, and Jean-Baptiste Caillau for reading this manuscript.

I would like to thanks to the team *McCore et al.* I am referring to all the people in INRIA with whom I have shared, those who are here today and also those have already left. I want to thank those with whom I started at the same time and who are still around today: Odile Burckard, David Loiseaux and Ali Gharib. I would also like to thank Walid Djema for helping me a lot at the beginning of my stay in France and for the work we did together.

Not only do I have to thank to the European Union's Horizon 2020 research and innovation programme under the Marie Skłodowska-Curie grant agreement No. 955520, but also the whole team of Digitalgaesation project. I had the opportunity to share with all the members of the team in different activities that enriched this thesis and helped me to understand many things that seemed foreign to me about microalgae.

Agradezco con mucho amor a mi familia. A mis padres, que pese a la distancia, siempre siento que están conmigo preocupándose por mi y quienes me dieron el empuje inicial en mi vida para llegar hasta donde estoy ahora.

Contents

Introduction **19**

1 Introduction **19**

2 State of the art **25**
2.1 Modelling nutrient and light effects on the growth of microalgae 25
2.1.1 Light gradient 27
2.1.2 Timescales 28
2.1.3 The Han model of photosystem II 28
2.1.4 Photoacclimation 29
2.2 Optimal control problems in microalgae-based processes 30
2.3 Neural Differential Equations 31

I Average growth rate under fluctuating light **33**

3 Theoretical growth rate of microalgae under high/low-flashing light **35**
3.1 Introduction 35
3.2 Description of the model 36
3.2.1 Han model 36
3.2.2 Light regimes and the two simplified models 38
3.2.3 Accounting for the light gradient 40
3.2.4 Model limitations 40
3.2.5 Exact asymptotic solution of the Han model 40
3.3 Study of Case I: Slowly varying irradiance 42
3.3.1 Average growth rate and analysis 43
3.3.2 Enhancement of the growth rate 43
3.4 Study of Case II: fast varying light 46
3.4.1 Average growth rate 46
3.4.2 Small-T flashing light 47
3.5 Study of Case III: the intermediate case 48
3.6 Illustration with simulation studies 50
3.6.1 Parameter settings 50
3.6.2 Quality of the approximated solution 50
3.6.3 Connection between Case I and Case II 50

3.6.4 Improvement of the growth rate . . . 51
3.7 Conclusion and perspectives . . . 53

4 Should hydrodynamics be taken into account when calculating the growth rate of microalgae in a photobioreactor? 57
4.1 Introduction . . . 57
4.2 Biological and hydrodynamic model . . . 58
4.2.1 Biological model . . . 58
4.2.2 Computational fluid dynamic model . . . 61
4.2.3 Hydrodynamics and cell tracking . . . 61
4.2.4 Light distribution within the raceway pond . . . 63
4.2.5 Growth rate in the raceway pond . . . 64
4.3 Formal analysis of the average growth rate . . . 65
4.3.1 A bound for the dynamic growth rate in the photobioreactor . . . 66
4.3.2 Periodic light signals . . . 68
4.4 Numerical simulations . . . 72
4.4.1 Two periodic examples . . . 72
4.4.2 The raceway case . . . 73
4.4.3 Correction of the cell distribution . . . 74
4.5 Conclusions . . . 77

II Optimal control problems in photobioreactors 79

5 Optimal control of microalgae culture accounting for photoinhibition and light attenuation 81
5.1 Introduction . . . 81
5.2 Mathematical model . . . 82
5.2.1 The reduced Han model for photobioreactors . . . 82
5.2.2 Light attenuation due to biomass . . . 82
5.3 Statement of the optimal control problem . . . 83
5.4 Necessary conditions on optimal controls . . . 83
5.4.1 The PMP maximization condition . . . 84
5.5 Properties of the adjoint variables and the optimal controls . . . 86
5.5.1 An assumption over the growth rate . . . 87
5.6 Estimating biomass in the singular arc . . . 89
5.7 Direct optimization . . . 89
5.8 Conclusion . . . 92

6 Optimal control of photobioreactor accounting for photoinhibition and photoacclimation 93
6.1 Introduction . . . 93
6.2 Dynamic Model Formulation . . . 94
6.3 Optimal Control Problem Statement . . . 95
6.4 Formal Analysis . . . 96
6.5 The non-perturbed problem . . . 99
6.6 Numerical Investigations . . . 102

6.6.1 Structure of the Optimal Dilution Rate . . . 103
6.6.2 Approximate Feedback Control on Light Irradiance . . . 105
6.6.3 Approximate Optimal Biomass Concentration . . . 105
6.7 Discussion . . . 106
6.7.1 The effect of Timescales . . . 106
6.7.2 Exploiting Self-Shading . . . 106
6.8 Conclusions . . . 107

III Neural differential equations for microalgae modelling and control 109

7 NeuralODEs for microalgae growth modelling 111
7.1 Introduction . . . 111
7.2 Methods . . . 112
7.2.1 The general neural ODE model . . . 112
7.2.2 The integrator cell . . . 112
7.2.3 Training the model . . . 113
7.2.4 Sensitivity equations . . . 114
7.2.5 Direct method . . . 114
7.2.6 Adjoint method . . . 114
7.2.7 Description of the dataset . . . 115
7.2.8 Data augmentation and mini-batch training . . . 117
7.2.9 First model: NN as growth function . . . 118
7.2.10 Second model: Using NNs to correct bias of kinetic model . . . 119
7.2.11 Implementation in other libraries . . . 120
7.2.12 Comparison with a Support Vector Regression approach . . . 121
7.3 Results and Discussions . . . 122
7.4 Conclusions . . . 123

8 Solving optimal control problems using neural differential equations 125
8.1 Introduction . . . 125
8.2 Materials and methods . . . 126
8.2.1 Bounded neural controls . . . 126
8.2.2 Gradient properties . . . 128
8.2.3 Numerical computation of the gradient . . . 129
8.3 Numerical Examples . . . 130
8.3.1 A solver for Mayer problems . . . 130
8.3.2 A two hidden layers neural control . . . 130
8.3.3 Example 1: Simple Bang-Bang optimal control . . . 130
8.3.4 Example 2: the double integrator . . . 134
8.3.5 Example 3: periodic harvesting of a photobioeactor . . . 136
8.4 Conclusions . . . 138

9 A method to solve non-linear optimal problems via squashing parameterization 141
9.1 Introduction . . . 141
9.2 Problem formulation and methods . . . 142

9.2.1 Approximated solution via squashing functions . . . 142
9.2.2 Convergence analysis . . . 144
9.2.3 How Gradient descent activate restrictions . . . 145
9.3 Numerical example: The double integrator problem . . . 148
9.4 Discussion: neural controls . . . 150
9.5 Conclusions . . . 150

10 Conclusion **155**

Appendix 161

A Complement of Chapter 3 **161**
A.1 Analytical Computations . . . 161
A.1.1 Case I: Large period T . . . 161
A.1.2 Case II: Small period T . . . 162
A.1.3 Proof of Lemma 3.1 . . . 165
A.1.4 Exact growth rate . . . 166
A.1.5 Eigenvalues of matrix M . . . 168
A.2 Proof of Lemma 3.3 . . . 168

B Complement of Chapter 7 **171**
B.1 Sensitivity equations and the Runge-Kutta methods . . . 171
B.2 Proof of Propostion 7.1 . . . 172
B.3 Monod Model . . . 173

C Optimal control problem with box constraints **175**
C.1 Control parameterization methods . . . 177

D Complement of Chapter 8 **179**
D.1 Proof of Proposition 8.2 . . . 179
D.2 Proof of Proposition 8.3 . . . 180
D.3 Implementation of a neural solver in Python . . . 181

List of Figures

1.1 **A**: Large production plan of *Dunaliella* at Hutt Lagoon, Western Australia. **B**: Large-scale plant of 18 ha for *Arthrospira* production in California, the USA. Image from [92]. 20

1.2 Schematic representation of different types of photobioreactors: **A** and **E** Helical tubular type photobioreactor, **B** and **D** Flat panel photobioreactor, **C** Column type photobioreactor. From [133]. 21

2.1 Schematic representation of a flat panel photobioreactor. The photobioreactor is illuminated only in one side. There is a gradient of light within the photobioreactor due to the self-shading of the microalgae. The microalgae that are closer to the illuminated surface perceive more photons than the microalgae on the opposite side. 26

2.2 From [13]. Schematic representation of the type of models of algal productivity, where P is the rate of photosynthesis, I the light intensity, T temperature, R_D rate of day-time respiration, R_N the rate of night-time maintenance, λ the maintenance coefficient, μ the specific rate of photosynthesis, X cell concentration and ξ being a constant. 27

2.3 After absorbing photons, reaction centers move from state A to B at a rate proportional to σI, where σ is the *effective cross section* of the reaction center and I is the irradiance. The minimal time required for an electron to transfer from water on the donor side of PSII to terminal electron acceptors is called *turnover time* and denoted by τ, so that τ^{-1} corresponds to the rate of the state B passing to state A. Excessive light absorption leads to photoinhibition of the PSII (C state) at a rate $k_d\sigma I$ and has a recovery rate k_r. 29

3.2 Illustration of the two light regimes. The high/low regime (blue) in which the function I_s has a period T and switches from $I_{\max}$ to $I_{\min}$ for a time ηT and $(1-\eta)T$ respectively. The constant light regime (red) which is considered as the weighted average between $I_{\max}$ and $I_{\min}$. 39

3.3 Comparison of the two modelling approximations with the exact solution of the states of the Han model. The state A and C of the exact solutions (3.7) (continuous yellow line), of the small-T model (3.12) (segmented blue line) and of the large-T model (3.10) (segmented red line) are provided for $I_{\max} = 2000\,\mu\mathrm{mol\,m^{-2}\,s^{-1}}$, $I_{\min} = 300\,\mu\mathrm{mol\,m^{-2}\,s^{-1}}$, $\eta = 0.4$, $y = 0$ and four different values of T. 51

3.4 The exact average growth rate (3.16) (continuous yellow line), the average growth rate of the large-T model (3.19) (segmented red line) and the average growth rate of the small-T model (3.27) (segmented blue line). The period T is plotted in log scale. In this case $\eta = 0.5$ 52

3.5 Illustration of Theorem 3.2, where approximation $\bar{\mu}_S^T \approx \mu_S^\eta$ holds for different combinations of $I_{\max}, I_{\min}$ and η. 54

3.6 Average growth rate as a function of period T and optical depth y. Case II for small-T model (blue curve) and in the Case I for large-T model (red curve). The continuous line correspond to the approximation that fits the values of T. In this case, $I_{\max} = 2000\,\mu\text{mol}\,\text{m}^{-2}\,\text{s}^{-1}$, $I_{\min} = 500\,\mu\text{mol}\,\text{m}^{-2}\,\text{s}^{-1}$, $\eta = 0.5$. 55

4.1 2D Mesh of the simulated raceway pond. 61

4.2 Representation of the raceway and the velocity field with some particles obtained from the CFD simulations. The height correspond to $0.3(m)$ and it is scaled with a factor of 5 to have a better visualization. The paddle wheel simulated in this image works at 20 RPM (rounds per minute). 63

4.3 Actual growth rate μ_A and static approximation μ_S for a simulated trajectory in the raceway operated at 20 RPM with an initial height of water equal to $0.3(m)$. The maximum value of the function μ_S is denoted by $\mu_{\max}$ and the depth at which this value is reached by z_{opt}. 64

4.4 Dynamic and static growth rate of the light signal taking from (4.32). 74

4.5 Dynamic and static growth rate of the trajectory given by (4.33). 75

4.6 For 8 different velocities of the paddle wheel, the estimated actual average growth rate $\overline{\overline{\mu}}_A^w$ (segmented red line), and the weighted space-time static growth rate $\overline{\overline{\mu}}_S^w$ (segmented blue line). The hydrodynamics is simulated for 1 hour. The values of N_{par} are different for each simulation, and they are shown in Table 4.2. The average height of the water is $H_0 = 0.3(m)$. 76

5.1 The optimal controls (in red), and the states (in blue). In the dilution plot, we also represent $\mu - R$ (black dotted line) to illustrate the Proposition 5.5. In the light plot, we also represent I_{opt} defined in (5.36), and the value of the perceived light I_x (the black dotted line). The magenta dashed line in the biomass concentration plot corresponds to x_s defined in Section 5.6. 90

6.1 **Left:** Numerical solution with initial conditions $x(0) = 1$ and $I_{\text{g}}(0) = 200$. Red lines: optimal dilution rate and irradiance controls. Blue lines: optimal biomass concentration and growth irradiance states. Black dotted lines: value of $\mu - R$ (D plot) and approximate feedback control in Equation (6.45) (I plot). Vertical gray dotted lines: final harvest time T_{harv}. Blue dotted line: solution of Equation (6.46). **Right:** Model parameter values [105]. 103

6.2 Optimal trajectories for the initial concentration $x(0) = 1\ \text{g}\,\text{L}^{-1}$ and different initial growth irradiance $I_{\text{g}}(0) = 1000, 600, 400, 200\ \mu\text{mol}\,\text{m}^{-2}\text{s}^{-1}$. The dotted lines represent the solution of the Equation (6.46), which correspond to the approximation of the optimal biomass. 104

6.3 Phase diagram of the net biomass productivity $(\mu(x, I_g) - R)x$ and turnpike-like behavior. Dotted black lines: dynamic trajectories of biomass concentration x and growth irradiance I_g under the feedback control I_{cl}. Solid black line: maximal biomass concentration in terms of the growth irradiance I_g. Solid blue lines: selected trajectories from the initial biomass concentration $x(0) = 1\ \mathrm{g\,L^{-1}}$ and different initial growth irradiance $I_g(0) = 1000, 600, 400, 200\ \mu\mathrm{mol\,m^{-2}s^{-1}}$. 106

7.1 The integrator cell corresponds to an explicit Runge-Kutta method implemented as a recurrent neural network. The collection of all the hidden states corresponds to the numerical solution of the equation (7.2). 113

7.2 Illustration of the cropping process for data augmentation. The first batch is obtained from the first C data points; the second batch selects the C data points after a stride S starting from the initial point; the third one corresponds to the C data points after twice S from the initial point, and so on the following ones. The last C data points are also added. Then the sequence is split into batches of the same length C, covering all the original time vectors. Then the small batches are used to train the model solving equation (7.1) with the respective initial condition. 116

7.3 Measured biomass, irradiance, and temperature for batch cultivation of *Phaeodactylum tricornutum* in a flat-panel airlift photobioreactor. 117

7.4 Flat panel photobioreactor where the microalgae were cultivated. 118

7.5 Schematic representation of the model (7.7) using a neural network composed of two hidden layers. 119

7.6 Predictions of the Model 7.7 in black. Training set in blue, test set in green. 119

7.7 Schematic representation of the model (7.8), where the neural network is turned off, and the model (7.9), where the neural network is trained after fixing the physical parameters $\boldsymbol{\omega}$. 120

7.8 The continuous black line and the continuous red line correspond to the predictions of the model (7.8) and model (7.9) respectively. Train set is coloured in blue and the test set in green. The details of the error of each batch is shown in Table 7.3. 121

8.1 Scheme of the neural control with a squashing activation function. The output layer, that we call *Squashing Layer* is key to introduce the constraints of the optimal control problem. 127

8.2 Scheme of the forward pass of the model and the two types of backward pass: the variational, solving the adjoint equation backward in time, and the direct one, where the backpropagation algorithm acts in the internal operations of the numerical solver. 128

8.3 **Example 1**. Dashed line: theoretical solution. Continuous line: the solution given by $D_{w,b}$ after 10000 iterations. 131

8.4 **Example 1**. Loss function $J_{[0,T]}(D_{w,b})$ as a function of the parameters (w, b) together with the evolution of the parameters in the training process. The training process was carried out using the Adam optimization algorithm in 10000 epochs using a constant learning rate of 0.1 132

8.5 **Example 2**. Solutions of the neural controls compared with the solution proposed in [26] shown as a segmented line. The neural solutions are shown as solid lines. The same neural network is bounded in three different ways. **Left:** the neural network bounded with a squashing function (8.20). **Center:** the neural network clipped to the bounds of the control (8.21). **Right:** the neural network is bounded with a sin function (8.22). 134
8.6 **Example 2**. Cost function over the iterations of the ADAM algorithm. Continuous line: the neural control (8.20). Dash-dotted line: the neural control (8.21) Gray dashed line: the neural control (8.22). Dotted line: the loss function reported in [26]. 135
8.7 **Example 3**. $I_0(t)$ given by (8.24). The black continuous lines correspond to the solution given by a neural control composed of two hidden layers with 20 neurons for two different light regimes I_0. The dashed line correspond to the numerical solution given by BOCOP. The yellow continuous line correspond to the light regime. 137
8.8 **Example 3**. $I_0(t)$ given by (8.26). The black continuous lines correspond to the solution given by a neural control composed of two hidden layers with 20 neurons for two different light regimes I_0. The dashed line correspond to the numerical solution given by BOCOP. The yellow continuous line correspond to the light regime. 138

9.1 **Left:** Comparison between the solution of the method proposed, and the solution presented in [26]. **Right:** The cost function for each step as a continuous line and the optimal value founded in [26] plotted with a dotted line. 149
9.2 Solutions of four NLP solvers using the parameterization (9.2) using a direct shooting method. 151
9.3 Solutions of four NLP solvers using the parameterization (9.12) using a direct shooting method. 152
9.4 Solutions considering $N = 1000$ time steps using the BONMIN algorithm from CasADi. 153

List of Tables

3.1 Parameter values for Han Model. 50

4.1 Parameter values of the Han model. 72
4.2 Number of simulated particles and total CPU time simulation for each experience. . 77

5.1 Parameters values for the biological model. 91

7.1 Details of the dataset. 118
7.2 The comparison of SVR and the hybrid model in terms of various factors 122
7.3 RSME and the percentage error of the models in every batch of the dataset. 123

8.1 **Example 1**. Computation times to solve problem (8.10). Time required to compute 1000 iterations of the Adam algorithm at constant learning rate of 0.1 for different ODE solvers with different number of time steps considering. To compute the total time (a solution with 10000 epochs), the time should multiply by 10. The numerical tests were run on a computer with an Intel Core i7-12700H using, 16GB RAM. . . . 133
8.2 **Example 3**. Comparison of the performance index P_h between the BOCOP's solution and the neural control. 137

9.1 Computation time for solving problem (8.18) using different NLP solvers implemented in CasADi considering $N = 100$ time steps. 150

Introduction

Chapter 1

Introduction

Microalgae and photobioreactors

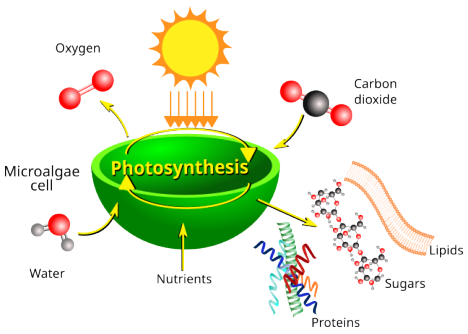

Microalgae are a diverse group of photosynthetic microorganisms found in various aquatic environments. These unicellular microscopic organisms, invisible to the naked eye, can perform photosynthesis, a process by which they convert light energy (natural or artificial), carbon dioxide, and water into biomass, releasing oxygen as a byproduct. Microalgae, together with cyanobacteria (also known as blue-green algae), form the well-known phytoplankton group which not only produce more half of the planet's oxygen, but are also the basis of the ocean's food chain.

Microalgae and cyanobacteria have attracted considerable interest for their potential applications in various industries due to their rich biochemical composition, as they can produce a wide range of valuable compounds, including lipids, proteins, and pigments [134]. For example, Spirulina is the most cultivated microalga worldwide due to the high content of proteins and many companies offer a variety of products derived from Spirulina, such as tablets, flakes, powder, pasta, or drinks [36, 81].

Photobioreactor are specialized vessels designed to cultivate photosynthetic organisms under controlled environmental conditions. Some of them use sunlight like the open ponds, or artificial light in a very controlled environment. Open ponds offer a simple and cost-effective approach, but they present a high level of contamination and other problems such as low gas-liquid mass transfer rate [65]. Much work has focused on the improvement of open ponds [10, 122]. On the other hand, closed systems are designed to overcome the problems associated to open ponds.

There is a large market for today's commercially available photobioreactors. Tubular photobioreactors, for example, are made of glass or plastic tubes, and their cultures are re-circulated with a pump. The diameter of the tubes is relatively small (around 0.1 m) to provide light to all the

Figure 1.1: **A**: Large production plan of *Dunaliella* at Hutt Lagoon, Western Australia. **B**: Large-scale plant of 18 ha for *Arthrospira* production in California, the USA. Image from [92].

microalgae cells. The length of the tubes is, in principle, not limited in any way, but it determines the residence time and the mixing within the photobioreactor [95].

Modelling and optimization of biomass evolution are the motivations for this work. On the one hand, the great diversity of microalgae species and the different cultivation methods make the modelling task a case-by-case one, meaning that each photobioreactor needs its own model. The same is true for the optimization bioprocesses associated with microalgae.

Modelling microalgae growth

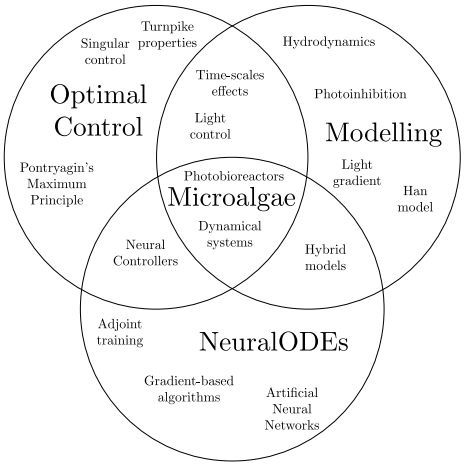

Microalgae growth is highly affected by the light intensity that they receive. Lack of light reduces growth, whereas over-exposition to strong light can damage certain proteins and slow down the photon harvesting process. Typically, both conditions are present in photobioreactors: one single cell can perceive low light in the deepest part of the culture and suddenly, due to mixing, go to the most illuminated part experimenting photoinhibition. We do not fully understand how the exposition of a strong light gradient in the culture affects the growth of each individual cell, yet some mathematical models are able to predict the production of microalgae in some conditions.

In addition to the fact that microalgae face a strong light gradient in bioreactors, they have evolved adaptive mechanisms to overcome photoinhibition, the so-called photoacclimation, in which each cell can modify the amount of pigments in order to avoid damage to the photosynthetic machinery. Both phenomena have different timescales: while the photodamage and recovery processes have timescales of minutes, photoacclimation has a timescale of days. Both phenomena affect the growth rate of the

microalgae. Coupling two different models for different phenomena is challenging, especially if they have different timescales.

Mathematical models are calibrated on the basis of available experiments. But the conditions under these experiments are especial in microalgae-based processed. For example, not all bioreactors have the same geometry and operating conditions and some of them have more than one species of microalgae, and the resulting interactions cannot be neglected. Moreover, some mathematical models can be very accurate in some conditions and useless in other situations. Then the list of microalgae models is very large, and still increasing. Most of them are non-linear, then model calibration becomes difficult. In addition, calibration must often be done with data that do not come from dynamic regimes. Usually, one model is developed to explain a single phenomenon that affects microalgae, and then coupled with other models. A common practice is to calibrate the new coupled model, keeping some parameter values from the literature.

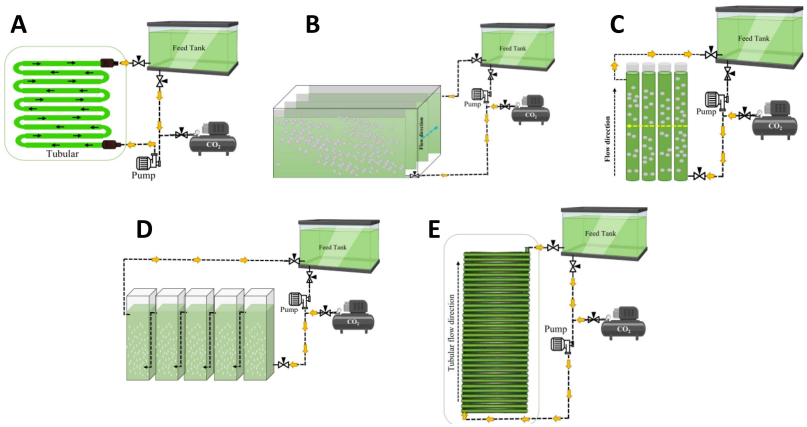

Figure 1.2: Schematic representation of different types of photobioreactors: **A** and **E** Helical tubular type photobioreactor, **B** and **D** Flat panel photobioreactor, **C** Column type photobioreactor. From [133].

Optimal control problems in microalgae cultivation

In recent years, there has been a notable increase in the industrial cultivation of microalgae, accompanied by the development of new technologies such as photobioreactors, sensors, and controllers. These new technologies are capable of estimating biomass inside the photobioreactor. When the data is recorded, mathematical models can be fitted in order to forecast the biomass taking into account different factors, as light intensity, dilution rate, pH, nutrient concentrations, etc. In industrial production levels, several questions are of interest in order to make the most of our resources and constraints. For example: What is the optimal performance of the process and how to reach it ? How should the photobioreactor be operated to maximize the production of biomass or any compound of interest? Which operational parameters should be manipulated? Do some biological phenomena specific to microalgae influence production?

Given a certain objective, for example, to maximize biomass production, the question is: how

do we set our controls? The Pontryagin's maximum principle (PMP) is a mathematical tool that can be used to answer these questions. When a mathematical model of our system, written as a set of ordinary differential equations, has well-defined the influence of these controls, PMP can be applied to find the optimal control. The principle provides the necessary conditions for a control to be optimal in the presence of constraints. However, these necessary conditions are not easy to decipher and most of the time one must resort to a software that is able to solve an approximation of the problem. By combining the theoretical results delivered by PMP and the numerical simulations of some software, we can gradually discover the structure of our optimal control. Why gradually? Discovering the secrets of an optimal control strategy is like piecing together a puzzle. At the beginning, a few conditions can be derived from the PMP, for example, the optimal operation of the dilution rate can take three values, zero, at its maximum value and a third value that's unknown. Numerical simulations can help us determine this unknown value.

Thesis organization

This manuscript focuses on modelling the growth of microalgae. Although there are several factors that affect the growth of these microorganisms, in this work, we focused on the light factor. A significant part of this thesis is based on the optimization of microalgae-based processes. Describing these bioprocess using ordinary differential equations, we study the problem of maximizing the harvested biomass using the theory of optimal control.

This thesis can be divided in three major topics:

1. The modelling of the microalgae growth under fluctuating lights.
2. The optimal control problems related to microalgae in a light field.
3. The use of artificial networks for modelling and controlling microalgae based-processes.

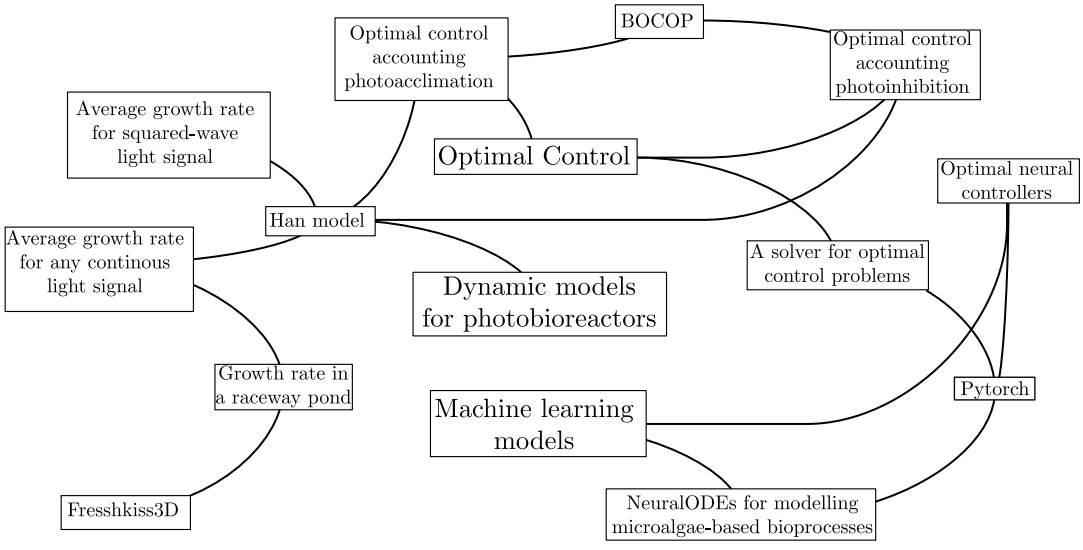

This thesis begins with the study of the Han model, which relates photoinhibition to microalgae

growth. It is interesting to compute the average growth when the algae are subjected to a light that follows a squared-wave function, as explored in Chapter 3. Generalizing this sketchy work for more realistic light signals is natural. In Chapter 4, we study of the average growth rate for any continuous light signal, especially for light signals extracted from Lagrangian trajectories from a simulated raceway pond hydrodynamics using the software `Freshkiss3D` developed by INRIA.

Considering Han's model, two optimal control problems were considered, whose objective is to maximize the biomass production in a photobioreactor. In Chapter 5, we present the first problem, which considers the fast dynamics of the photosynthesis. The second problem investigates the effect of photoacclimation, and the results are presented in Chapter 6.

In Chapter 7 we explore the use of neuralODEs (or hybrid models) to model the growth of the microalgae in a photobioreactor. The growth rate is estimated using neural networks, we give a complete theory on how a neural network is trained within a dynamic system, we illustrate different techniques to train the neural network. Then, in Chapter 8, we study how artificial neural networks can be used to solve optimal control problems.

Motivated by the preceding chapter, in Chapter 9 we derive a shooting method to solve optimal control problems with fixed time horizon and box constraints on the control. This chapter has no relation with microalgae, but is a complement of the previous.

Thesis-related publications

Published publications

Fierro Ulloa, J. I., Lu, L. D., & Bernard, O. (2023). Theoretical growth rate of microalgae under high/low-flashing light. Journal of Mathematical Biology, 86(4), 48.

Fierro Ulloa, J. I., Djema, W., & Bernard, O. (2023, July). Optimal control of microalgae culture accounting for photoinhibition and light attenuation. In IFAC World Congress 2023, Yokohama, JAPAN.

Gao, Y., Fierro Ulloa, J. I., Perré, P., Lopes, F., & Bernard, O. (2023). Microalgal biofilm behavior under light/dark cycles. IFAC-PapersOnLine, 56(2), 9739-9744.

Fierro Ulloa, J. I., Chachuat B., Bernard O. Optimal control of photobioreactor accounting for photoinhibition and photoacclimation. ADCHEM 2024, Jul 2024, Toronto, Canada.

Non-published publications

Fierro Ulloa, J. I., Syed T., Bernard O., Yeh Y., Brinitzer G., Mädler J. Differential neural networks for microalgae growth modelling. (To submit to Engineering Applications of Artificial Intelligence).

Fierro Ulloa, J. I., Lu, L. D., & Bernard, O. Should hydrodynamics be taken into account when calculating the growth rate of microalgae in a photobioreactor?. (To submit to SIAM Journal on Applied Mathematics).

Fierro Ulloa, J. I., Chachuat B., Bernard O. Solving optimal control problems using neural differential equations. (Work in progress).

Chapter 2

State of the art

2.1 Modelling nutrient and light effects on the growth of microalgae

The growth of microalgae (and microorganism in general) is often described using mathematical models. Probably the most famous one is the exponential growth equation, proposed by Thomas Robert Malthus, in his Essay on the Principle of Population (1798), where the evolution of biomass is given by the ordinary differential equation:

$$\frac{d}{dt}x = \mu x.$$

On the contrary to this primitive model assuming a constant growth rate μ, many factors affect μ, among others, light, nutrients, pH, dissolved oxygen, temperature. Also, there are some specificities among the large range of microalgal and cyanobacteria species, and often models consider a very limited number of limiting elements (typically light and temperature). This is why there is a huge literature for modelling the function μ [83, 37], there are different types of models, which are often bricks that can be combined for considering: external nutrient concentration, internal nutrient storage, light-limitation, light attenuation, photoinhibition, the effect of temperature, pH level, carbon concentration, dissolved oxygen and many other factors.

The Monod kinetics [97] has been used for more than 70 years to model the effect of a nutrient on the growth of microorganisms. In this model, the growth rate μ is a bounded function of the concentration of a limiting nutrient s, defined as

$$\mu(s) = \mu_{\max}\frac{s}{s + k_s}, \tag{2.1}$$

where $\mu_{\max}$ is the maximal growth rate, and k_s the half saturation constant. In early models of microalgae growth, light is treated as a limiting nutrient [141], *i.e.*, the light intensity I is replaced in equation (2.1).

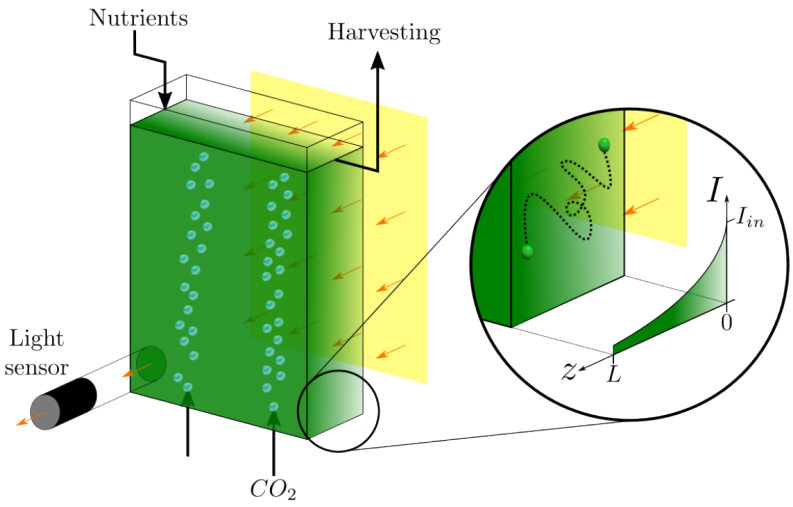

Figure 2.1: Schematic representation of a flat panel photobioreactor. The photobioreactor is illuminated only in one side. There is a gradient of light within the photobioreactor due to the self-shading of the microalgae. The microalgae that are closer to the illuminated surface perceive more photons than the microalgae on the opposite side.

Nutrients can also have a negative effect if the concentration is too high [7]. To model this inhibitory effect, the Haldane description has been used, where the growth rate depends on a nutrient s that can inhibit the growth at high concentration as follows:

$$\mu(s) = \mu_{\max} \frac{s}{s + k_s + \frac{s^2}{k_i}}, \tag{2.2}$$

where k_i, $\mu_{\max}$ and k_s are the constants of the model. In the same way, light can have an inhibitor effect over the growth of microalgae, which is the so-called photoinhibition. In terms of modelling, the same Haldane description has been used to model the inhibitory effect of light, again, changing s by the light intensity I in the function (2.2).

Actually, it has been demonstrated by Droop [46] that representing growth rate of microalgae and cyanobacteria by a function depending on the external nutrient concentration was inaccurate. A more realistic representation relates growth to the total amount of the limiting element available in the biomass. This so-called internal quota represents the intracellular concentration of the limiting element. For example, if nitrogen is limiting, and is provided to the culture through nitrate (NO_3^-), the growth rate will depend on the quota $q = \frac{N}{C}$ which represent the ratio of nitrogen to carbon in the cells. The standard Droop model therefore represents growth rate by the following function:

$$\mu(q) = \bar{\mu}\left(1 - \frac{Q_0}{q}\right),$$

where the parameter $\bar{\mu}$ represents the theoretical growth rate at infinite quota, and Q_0 is the minimum quota.

2.1.1 Light gradient

Microalgae growth models are inspired by bacterial growth models. The key difference between these two microorganisms is the light necessary for the microalgae to grow. This makes a big difference, especially since it cannot be assumed that the amount of photons is evenly distributed within the photobioreactor. Perfect mixing assumes that there are no spatial gradients of matter within the reactor. Most of the models assume perfect mixing, but light distribution is not homogeneous.

In a flat panel photobioreactor (Figure 2.1), light illuminates one face of the reactor. If the light intensity is I_{in}, then the light at position z from the illuminated face, is given by the law of Beer-Lambert:

$$I(z) = I_{\text{in}} e^{-\xi z}. \tag{2.3}$$

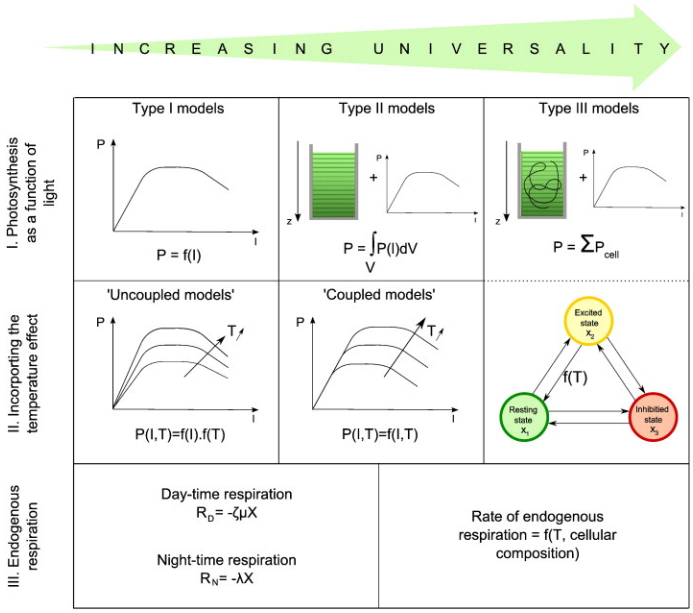

Figure 2.2: From [13]. Schematic representation of the type of models of algal productivity, where P is the rate of photosynthesis, I the light intensity, T temperature, R_D rate of day-time respiration, R_N the rate of night-time maintenance, λ the maintenance coefficient, μ the specific rate of photosynthesis, X cell concentration and ξ being a constant.

There are mainly three ways to deal with the light gradient within a photobioreactor [13]. According to Bechet et al. [13] growth function has been classified into three categories: Type I, Type II or Type III:

- **Type I**: if the model predicts the growth rate as a function of the incident light reaching the photobioreactor, or as a function of the average light within the photobioreactor.
- **Type II**: if the growth is computed as the average of local growth rates within the cultivation without considering short light cycles.

- **Type III**: if the model accounts for both light gradient and short light cycles.

Assuming that mixing is much faster than the photosynthetic processes, it means that the cells respond to the average light intensity (Type I). Assuming that mixing is slower than the photosynthetic processes, the growth rate corresponds to the average growth rate over the culture depth (Type II) [19, 75]. If both timescales are intricate, the type III model is required.

2.1.2 Timescales

Biological processes in microalgae operate on a wide range of timescales, from milliseconds to weeks, many processes are necessary to grow and divide. Damaging processes can reduce the growth rate, and even be lethal for the cell. Microalgae have different mechanisms to re-synthesize molecules for replacing the damaged ones. These mechanisms have different timescales, for example, there are different photoacclimation processes operating from milliseconds to days [111]. In the next section, we introduce the Han model, which can be used to model the fast dynamics of photosynthesis and can be also upgraded to represent the acclimation of the microalgae to fluctuating light.

2.1.3 The Han model of photosystem II

When the light energy is absorbed by the light harvesting complex, it generates enough energy to break up a water molecule and recover an electron, initiating a series of electron transport reactions. These photosynthetic reactions lead to the production of ATP and NADPH. The photosynthetic unit (PSU) is a complex of pigments and proteins coupled to a reaction center, where these reactions take place [94]. The PSUs are both in photosystem-I (PSI) and photosystem-II (PSII).

The Han model [66] describes the effect of light intensity in the PSII and it provides a framework for understanding the complex interactions between light intensity, photodamage, and repair processes in microalgae. Specifically, photoinhibition is the reduction in the photosynthetic capacity due to damages in key proteins within the PSU-II. In this model, the reaction centers of PSU-II can take three states:

- Open state A: the reaction center is ready to harvest photons.
- Closed state B: the reaction center is processing the energy absorbed from photons.
- Inhibited state C: the center is damaged and can not harvest photons.

Photoinhibition is a dynamic balance between the rate of photodamage to PSII and the rate of its repair. The probability of being on each state is described by the following differential equations:

$$\begin{aligned}
\dot{A} &= -\sigma I A + \frac{B}{\tau}, \\
\dot{B} &= \sigma I A - \frac{B}{\tau} + k_r \sigma I B, \\
\dot{C} &= -k_r C + k_d \sigma I B,
\end{aligned}$$

with the condition

$$A + B + C = 1.$$

In this model, the growth rate is proportional to the state A, and at steady state, the growth rate follows a Haldane description, given by

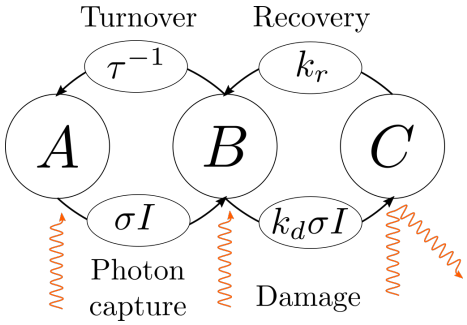

Figure 2.3: After absorbing photons, reaction centers move from state A to B at a rate proportional to σI, where σ is the *effective cross section* of the reaction center and I is the irradiance. The minimal time required for an electron to transfer from water on the donor side of PSII to terminal electron acceptors is called *turnover time* and denoted by τ, so that τ^{-1} corresponds to the rate of the state B passing to state A. Excessive light absorption leads to photoinhibition of the PSII (C state) at a rate $k_d \sigma I$ and has a recovery rate k_r.

$$\mu_{\text{Steady State}} = \frac{K\sigma I}{1 + \tau\sigma I + \frac{k_d}{k_r}\tau(\sigma I)^2}.$$

The photodamage increases with increasing light intensity. At low light intensities, the rate of photodamage is low, and the repair processes can keep up, preventing significant photoinhibition. However, at high light intensities, the rate of photodamage exceeds the repair capacity, leading to a net decrease in PSII functionality and overall photosynthetic efficiency.

2.1.4 Photoacclimation

Microalgae are able to modify the amount and the composition of certain pigments to both adapt the flux of harvested energy to the cell need and to protect themselves against damages resulting from an excess of energy. This is the so-called photoacclimation. An extension of the Han model [105] can model the effect of photoacclimation based on the change of chlorophyll content. The carbon-specific chlorophyll quota θ [$g_{\text{Chl}}\, g_{\text{C}}^{-1}$], corresponding to the amount of chlorophyll per unit of biomass, is described as

$$\theta = \psi \frac{k_l}{I_{\text{g}} + k_l} q,$$

where I_{g} [$\mu\text{mol}\, \text{m}^{-2}\text{s}^{-1}$] is the so-called growth irradiance, and it represents the light irradiance at which the cells are acclimated, q [$g_{\text{N}}\, \text{m}^{-3}$] represents the carbon-specific nitrogen quota, ψ [$g_{\text{Chl}} g_{\text{N}}^{-1}$] and k_I [$\mu\text{mol}\, \text{m}^{-2}\text{s}^{-1}$] are fixed parameters. The dynamic evolution of I_{g} is related to the light irradiance I following the equation:

$$\dot{I}_{\text{g}} = \delta\mu(I - I_{\text{g}}).$$

Other models [49, 55] propose a first-order dynamics for the amount of chlorophyll quota as

$$\dot{\theta} = \delta'(\theta^* - \theta),$$

where θ^* is proposed as a function of the light I as

$$\theta^* = \theta_{\max} - (\theta_{\max} - \theta_{\min})\frac{I}{I + I_c},$$

where $\theta_{\max}, \theta_{\min}, I_c$ are constants of the model. In all the cases, photoacclimation is represented as a graded reduction of photosynthetic pigment content in response to increased irradiance, although it can also involve changes in pigment complement and in the electron transfer chain components [86].

2.2 Optimal control problems in microalgae-based processes

Optimal control in microalgae-based bioprocesses is an interesting intersection of biotechnology, engineering and applied mathematics. One of the challenges in these processes lies in optimizing the various parameters and conditions to maximize productivity and efficiency. This includes controlling factors such as light intensity, nutrient supply, temperature, pH, and carbon dioxide concentration (which is closely related to the pH). The goal is to determine the optimal operational strategies that will yield the highest biomass or desired product concentration (such as lipids, carotenoids, or proteins). Optimal control theory provides a powerful framework to address these challenges. By formulating the process as a dynamic system, optimal control aims to identify time-dependent (open loop) control variables that drive the system towards a desired outcome.

Different optimal problems related with microalgae have been analyzed in the literature. One of the most common problems is the optimization of productivity in a perfectly mixed continuous reactor. In such a reactor, called chemostat, the change of population density x can be expressed as:

$$\dot{x} = \text{Population growth} - \text{population loss}. \tag{2.4}$$

The dilution rate D, of a continuous culture corresponds to the ratio between the flow rate F, and the volume V (often assumed to be constant). Equation (2.4) is generally written:

$$\dot{x} = \mu x - Dx. \tag{2.5}$$

Where the net growth rate μ depends on various factors affecting the photobioreactor environment. Light is the most studied factor for optimal control of high density photobioreactors, especially since its availability is affected by the biomass density (self shading phenomenon).

The problem of maximizing the biomass production using natural periodic light was addressed by Grognard et al. [63], accounting for light attenuation. The evolution of the biomass x is governed by the following equation:

$$\dot{x} = \frac{\nu(t)x}{\kappa + x} - Rx - Dx,$$

where ν is a function that takes into account light/dark cycles and light attenuation within the photobioreactor using the Beer-Lambert law. The constant R represents the respiration rate of the microalgae. The dilution rate D, of a continuous culture corresponds to the ratio between the flow rate F, and the reactor volume V. The objective function is the harvested biomass in the period T given by

$$\int_0^T D(t)Vx(t)dt,$$

In this work, periodic conditions for the process operation are assumed, *i.e.*, $x(0) = x(T)$.

There are other applications of optimal control theory in microalgae-based processes, for example, in [43, 42], two distinct microalgae species are described by the following dynamic system

$$\begin{cases} \dot{s} = (s_{\text{in}} - s)D - \sum_{i=1}^{2} \rho_i(s)x_i, \\ \dot{q}_i = \rho_i(s) - \mu_i(q_i)q_i, \\ \dot{x}_i = (\mu_i(q_i) - D)x_i \end{cases}$$

where $i = 1, 2$ represent each species, s is the total substrate concentration, s_{in} is the input concentration of the substrate, x_i is the i-th species-biomass concentration, and q_i is the internal quota for the i-th species. The functions ρ_i quantify the rate of substrate absorption and μ_i are the growth rates. The control is the dilution rate D which is assumed to be bounded and non-negative. The objective is to minimize the time to go from the initial conditions to the target set

$$\mathcal{T} = \{(q_1, q_2, x_1, x_2) \in (0, \infty)^4 : x_2 < \varepsilon x_1\},$$

where $\varepsilon > 0$ is a fixed tolerance value. This problem aims to minimize the time to select two distinct microalgae populations. This problem present some turnpike properties [44] that are analyzed using the theory developed in [146].

Another interesting application of optimal control was developed in [87], where photoacclimation behavior is related to an optimal control problem of resource allocation.

2.3 Neural Differential Equations

The function (2.5) in a photobioreactor depends on many factors which can be process dependent. Then, for each photobioreactor, each species and each growth conditions a parametric function μ must be proposed. There is a long list of functions μ that have been used in the last years associated to a broad set of photobioreactor-related parameters [13, 37, 84].

As a matter of example, light has a strong effect on the growth rate. Accurately representing the light extinction is challenging. The Beer-Lambert equation (2.3), which accounts for the resulting effect of absorbance and scattering, is no more valid for very turbid medium with multiple scattering. More recent models take into account more complex distribution of light within the photobioreactor [77, 35, 140], but are often assuming simple reactor geometries. Accounting for photon multi-diffusion in complex geometries is still an unsolved problem. Light induces photoacclimation, a biased estimation of the light field will also bias the estimate of the pigment content, and further of the growth rate. Among all the factors affecting growth, some are rarely included, such as oxygen or the availability of micro-nutrients. This illustrates the difficulty in accurately computing the growth function μ based on mechanistic and validated models. It results that the maximum productivity will depend on several factors which are difficult to represent in a PBR.

To address the problem of growth function modelling, a possible solution is to replace the function μ by a *Universal Approximator* that takes as inputs all the different variables of the system and calibrate it using the available data. In this thesis, we study the implementation of artificial neural networks (ANNs). Integrating ANNs in ordinary differential equations is a method known

as *Hybrid Modelling* in chemical engineering [107, 119, 124, 99] and neural differential equations (neuralODEs) in the machine learning community [30, 79, 102, 128]. We will use both terminology in this thesis.

This approach has been used to model an anaerobic digester, for example, in [16], two bacteria x_1 and x_2 growth consuming two different substrates s_1 and s_2, following the dynamic system:

$$\begin{aligned}
\dot{x}_1 &= \mu_1(s_1)x - 1 - \alpha D x_1, \\
\dot{x}_2 &= \mu_2(s_2)x_2 - \alpha D x_2, \\
\dot{s}_1 &= -k_1\mu_1(s_1)x_1 + D(s_{1,\text{in}} - s_1), \\
\dot{s}_2 &= -k_2\mu_2(s_2)x_2 + k_3\mu_1(s_1)x_1 + D(s_{2,\text{in}} - s_2), \\
q_{\text{CH4}} &= k_4\mu_2(s_2)x_2,
\end{aligned}$$

where D is the dilution rate, $s_{1,\text{in}}, s_{2,\text{in}}$ are the influent concentration of the substrates s_1 and s_2. The k_1, k_2, k_3, k_4 are the yield coefficients associated with the bacterial growth. q_{CH4} denotes the methane flow rate, α is a parameter reflecting if the biomass is affected or not by the dilution effect. The specific growth rates of x_1 and x_2 are denoted by μ_1 and μ_2. The growth of x_1 only depends on the substrate s_1 and, similarly, the growth of x_2 only depends on the substrate s_2. Each growth rate μ_i is replaced by an artificial network fulfilling the next hypothesis

- μ_1 is a non-negative increasing function of s_1, and $\mu_1(0) = 0$.
- μ_2 is a non-negative function of s_2 that tends toward zero for high values of s_2 and $\mu_2(0) = 0$.

After training the neural networks, the growth rates μ_i show a behavior similar to the Monod and Haldane functions.

In [28, 107] a general hybrid model for a stirred tank bioreactor is proposed as

$$\dot{c} = KH(c)\rho - Dc + u,$$

where $c \in \mathbb{R}^n$ is the vector of n concentrations, the matrix $K \in \mathbb{R}^{n\times r}$ contains the information of the yield of the reactions, $H(c) \in \mathbb{R}^{r\times r}$ is the matrix of known kinetic expressions, u is a vector of input volumetric rates (this includes volumetric feed rates and gas-liquid volumetric mass transfer rates), and ρ is a vector of r unknown kinetic functions. The vector ρ is then replaced by a neural network whose input is c.

The list of hybrid models in chemical and biochemical engineering is increasing [56, 29, 74], but just few hybrid models have been proposed for modelling the dynamics of microalgae cultivation processes [157, 38, 139]. The list of machine learning models applied to microalgae-based processes is large [143] but for most of them, machine learning models are used for other purposes, such as the classification of dead and living microalgae [123], classification of different microalgae species [108], or prediction of microalgae growth rate in steady regime of the culture [106].

Part I

Average growth rate under fluctuating light

Chapter 3

Theoretical growth rate of microalgae under high/low-flashing light

This chapter reproduces [53] Published in the *Journal of Mathematical Biology*. The introduction presented here differs from the published version.

Abstract

Dynamic light regimes strongly impact microalgal photosynthesis efficiency. Finding the optimal way to supply light is then a tricky problem, especially when the growth rate is inhibited by overexposition to light and, at the same time, there is a lack of light in the deepest part of the culture. In this chapter, we use the Han model to study the theoretical microalgal growth rate by applying periodically two different light intensities. Two approaches are considered depending on the period of the light pattern. For a large light period, we demonstrate that the average photosynthetic rate can be improved under some conditions. Moreover, we can also enhance the growth rate at steady state as given by the PI-curve. Although, these conditions change through the depth of a bioreactor. This theoretical improvement in the range of 10 to 15% is due to a recovery of photoinhibited cells during the high irradiance phase. We give a minimal value of the duty cycle for which the optimal irradiance is perceived by the algae culture under flashing light regime.

3.1 Introduction

In this chapter, we explore the consequences of the Han model [66] for cultures where light is the limiting factor. Han's model describes the photosynthesis process by representing the reaction center dynamics through three states, one of them corresponding to photoinhibition. This model has been used by several authors who demonstrated that it can properly predict the growth rate of cultures submitted to a periodic light/dark alternation [13, 9, 116]. Moreover, it has been coupled with acclimation [105], and chlorophyll fluorescence models [103].

Flashing light is often considered as a method to reduce photoinhibition and to increase the productivity in photobioreactors. This consists of a periodic succession of light and dark phases. There is a lot of research on the benefit of providing light through flashes [2, 50, 1, 132]. The flashing light, however, rarely produces an enhancement on the algal production in comparison with the constant light of the same average irradiance [3]. In this chapter, we consider a different light regime, namely the high/low flashing light regime. The microalgae culture is considered to be exposed to a periodic succession of high irradiance followed by lower irradiance. This light regime is more representative of real conditions in dense cultures of microalgae, where light is absorbed and scattered by the algae culture and cannot penetrate deeply into the liquid medium [137]. As a consequence, cells oscillate randomly between the surface layer at high irradiance and the deeper layers at lower irradiance [40].

The aim of this chapter is to go beyond the flashing light pattern to understand how a high/low flashing light affects the growth rate of microalgae. To address this question, we reduce the Han model into only one differential equation. This simplification depends on the timescale of the period of the high/low flashing light configuration. We differentiate two cases regarding large and small timescales. Meanwhile, we provide an approximation of the average growth rate for each case, and compare the solutions of the simplified models with the exact solution of the system. With these simplified models, we prove that the solution of this system, considering the high/low flashing light configuration, converge to a periodical solution, and we study their properties.

We show that the average growth rate under a high/low flashing light regime can be greater than the growth under constant light regime with the same average irradiance. We also prove theoretically that for high frequencies (or short period of the light pattern) the growth rate under the high/low flashing light regime is equal to the growth rate under the constant light regime. We consider the local optical depth concept defined in [17] for our analysis to condense the effect of the depth and biomass in the light attenuation.

This chapter is organized as follows. In Section 3.2, we present the growth model and the light setting. In Section 3.3, we analyze what happen in the large period approach which will be called *Large-T model* and how this case can improve the growth rate comparing to the continuous light regime. In Section 3.4, we study the small period approach called *Small-T model*, and we give an interval in which the algae culture perceives the optimal light if we consider the flashing light configuration. Section 3.5 justifies the approximations made in the previous sections. Finally, in Section 3.6, we test numerically the results.

3.2 Description of the model

3.2.1 Han model

In the Han model [66], reaction centers of PSII can take three states: open or reactive (state A), closed or activated (state B) and inhibited (state C). After absorbing photons, reaction centers move from state A to B at a rate proportional to σI, where σ is the *effective cross section* of the reaction center and I is the irradiance. The minimal time required for an electron to transfer from water on the donor side of PSII to terminal electron acceptors is called *turnover time* and denoted by τ, so that τ^{-1} corresponds to the rate of state B passing to state A. Excessive light absorption leads to photoinhibition of the PSII (C state) at a rate $k_d\sigma I$ and has a recovery rate k_r. Figure 3.1a

presents the relation between these three states. The dynamics of PSIIs at the three states can be

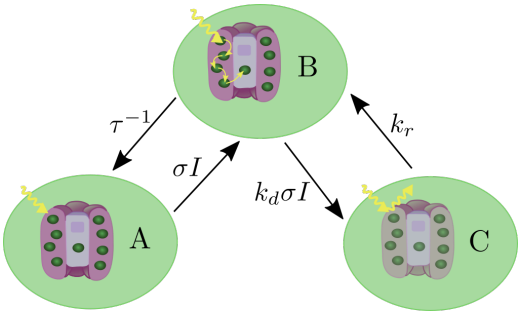

(a) Illustration of the Han Model.

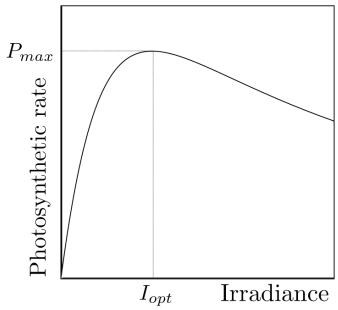

(b) PI-curve when A is at steady state following the Haldane description given by (3.4)

described by the following differential equations, which describe the proportion of each state:

$$\begin{aligned}\frac{\mathrm{d}A}{\mathrm{d}t} &= -I\sigma A + \frac{B}{\tau},\\ \frac{\mathrm{d}B}{\mathrm{d}t} &= I\sigma A - \frac{B}{\tau} + k_r C - k_d\sigma I B,\\ \frac{\mathrm{d}C}{\mathrm{d}t} &= -k_r C + k_d\sigma I B,\end{aligned} \tag{3.1}$$

and these three states satisfy:

$$A + B + C = 1. \tag{3.2}$$

Then system (3.1) is defined in the domain $\{(A,B,C) \in [0,1]^3 : A+B+C = 1\}$, which is well defined due to the fact that $\frac{\mathrm{d}}{\mathrm{d}t}(A+B+C) = 0$. On the other hand, growth rate μ depends entirely on the irradiance that the algae perceived, and it is proportional to $I\sigma A$:

$$\mu := K\sigma I A, \tag{3.3}$$

where K corresponds to the growth rate coefficient.

At steady state of system (3.1), the growth rate given by the Han model, for a constant irradiance I can be computed explicitly by

$$\mu_S(I) := \frac{K\sigma I}{1 + \tau\sigma I + \frac{k_d}{k_r}\tau(\sigma I)^2}. \tag{3.4}$$

This formulation corresponds to a Haldane description of the PI-curve accounting for photoinhibition. In Figure 3.1b, we present a generic form of the PI-curve with this description. The maximum of this function is given by

$$\mu_{\max} := \frac{K}{\tau + 2\sqrt{\frac{k_d}{k_r}\tau}}, \tag{3.5}$$

which is achieved with the irradiance I_{opt} given by

$$I_{\text{opt}} := \frac{1}{\sigma\sqrt{\frac{k_d}{k_r}\tau}}. \tag{3.6}$$

The details of the above computation and the link between (3.4) and the Haldane description can be found for instance in [85, Proposition 1.2.1].

Using Equation (3.2), we can eliminate B to reduce the system (3.1) into two equations:

$$\frac{\mathrm{d}}{\mathrm{d}t}\begin{pmatrix}A\\C\end{pmatrix} = \begin{pmatrix}1 & 0\\0 & k_d\end{pmatrix}\left[-\begin{pmatrix}\sigma I + \frac{1}{\tau} & \frac{1}{\tau}\\ \sigma I & \sigma I + \frac{k_r}{k_d}\end{pmatrix}\begin{pmatrix}A\\C\end{pmatrix} + \begin{pmatrix}\frac{1}{\tau}\\ \sigma I\end{pmatrix}\right], \tag{3.7}$$

which can be also rewritten as

$$\frac{\mathrm{d}}{\mathrm{d}t}\begin{pmatrix}A\\C\end{pmatrix} = -M(I)\begin{pmatrix}A\\C\end{pmatrix} + N(I),$$

where

$$M(I) := \begin{pmatrix}\sigma I + \frac{1}{\tau} & \frac{1}{\tau}\\ k_d\sigma I & k_d\sigma I + k_r\end{pmatrix}, \quad N(I) := \begin{pmatrix}\frac{1}{\tau}\\ k_d\sigma I\end{pmatrix}. \tag{3.8}$$

For every value of $I \in \mathbb{R}^+$, the matrix $-M(I)$ is Hurwitz (see Appendix A.1.5) and invertible. Then $M^{-1}(I)N$ is the only asymptotically stable equilibrium, which can be computed explicitly by

$$\begin{pmatrix}A^*\\C^*\end{pmatrix} := M^{-1}(I)N(I) = \frac{1}{1 + \tau\sigma I + \frac{k_d}{k_r}\tau(\sigma I)^2}\begin{pmatrix}1\\ \tau\frac{k_d}{k_r}(\sigma I)^2\end{pmatrix},$$

with A^*, C^* the steady state of A, C. Using the definition of the growth rate (3.3), one re-finds (3.4) by multiplying A^* with $K\sigma I$.

3.2.2 Light regimes and the two simplified models

Definitions

Let us consider two light regimes, namely the constant regime and the high/low-flashing light regime. For the constant light regime, the reactor receives a constant irradiance at the surface. For high/low-flashing light regime, a periodic piece-wise constant irradiance (c.f. Figure 3.2) is applied at the reactor surface. Let us denote by $I_{\max}$ (resp. $I_{\min}$) the maximum (resp. minimum) irradiance and by $\eta \in (0, 1)$ the duty cycle. We can then define the average irradiance by

$$I_\eta := \eta I_{\max} + (1 - \eta)I_{\min}. \tag{3.9}$$

The reactor is assumed to be illuminated continuously with irradiance I_η for the constant light regime, whereas in the high/low light regime, we assume that the reactor is exposed regularly between a high irradiance $I_{\max}$ for ηT and a low irradiance $I_{\min}$ for $(1 - \eta)T$. See Figure 3.2.

Depending on the scale of T, we study two cases: when T is small compared with the Han model parameters τ, meaning that $T < \tau$ (the order of magnitude is milliseconds), we call this case *Small-T model* or high frequency model, and when T is large, *i.e.* when $T > 1/k_r$ (the order of magnitude is hours), we refer this case as *Large-T model* or low frequency model. The reduction methodology, depending on the light signal frequency, is now detailed.

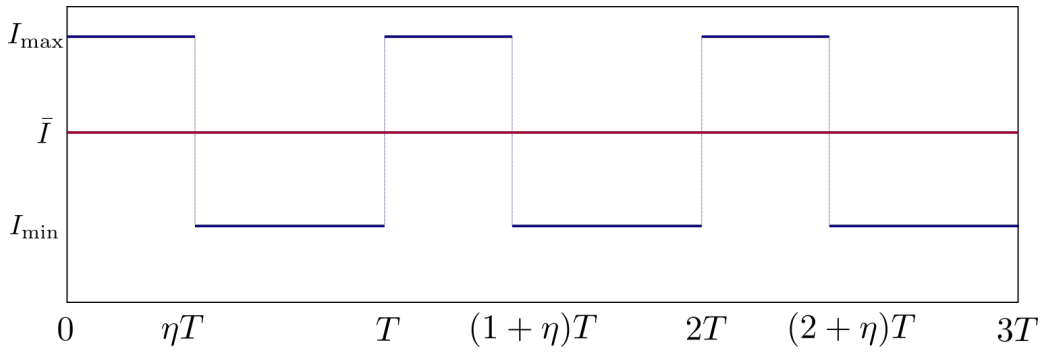

Figure 3.2: Illustration of the two light regimes. The high/low regime (blue) in which the function I_s has a period T and switches from $I_{\max}$ to $I_{\min}$ for a time ηT and $(1-\eta)T$ respectively. The constant light regime (red) which is considered as the weighted average between $I_{\max}$ and $I_{\min}$.

Case I: Large-T model (low frequency model)

When light stays constant for a large enough time (we will justify later that large enough relies on the value of $1/k_r$), the dynamics of A reaches the steady state much faster than C [68]. Then, it is possible to apply a fast-slow approximation by using the perturbation theory [78]. More precisely, we consider the slow manifold $A = \frac{1-C}{1+\tau\sigma I}$ (*i.e.* the pseudo steady state of A) to reduce the dynamics into one single equation on the photoinhibition state C:

$$\frac{\mathrm{d}C}{\mathrm{d}t} = -(\alpha(I) + k_r)C + \alpha(I), \tag{3.10}$$

with

$$\alpha(I) = \frac{k_d \tau(\sigma I)^2}{1+\tau\sigma I}. \tag{3.11}$$

System (3.7) has slow-fast timescales due to the factor k_d. For example, Table 3.1 presents some parameter values in the literature [61, 82], k_d is on the order of 10^{-4}. Then, the entries of the following matrices:

$$\begin{pmatrix} \sigma I + \frac{1}{\tau} & \frac{1}{\tau} \\ \sigma I & \frac{k_r}{k_d} + \sigma I \end{pmatrix} \quad \text{and} \quad \begin{pmatrix} \frac{1}{\tau} \\ \sigma I \end{pmatrix}$$

have values greater than 0.1 when considering an irradiance I in the order of $1000\,\mu\mathrm{mol\,m^{-2}s^{-1}}$. The theory of slow/fast manifolds [78] holds for autonomous systems. Although our system is nonautonomous, we can apply this principle to the system (3.7) in the interval $(0, \eta T)$ considering constant light equal to $I_{\max}$ and then considering the system with constant light $I_{\min}$ in the interval $(\eta T, T)$ since light do not affect the timescales of the system. The periodic solution of this system is computed in Appendix A.1.1.

Case II: Small-T model (high frequency model)

When light varies very rapidly compared to the system dynamics, the dynamics of the photoinhibition state C stays approximately constant [68]. Under the assumption that C is constant, we

can then apply averaging methods [127] to simplify the system (3.7) into one equation on the open state A:

$$\frac{\mathrm{d}A}{\mathrm{d}t} = -\left(\sigma I + \frac{1}{\tau}\right) A + \frac{k_r - k_d\sigma\overline{IA}}{\tau(k_d\sigma\bar{I} + k_r)}, \tag{3.12}$$

with $\bar{I} = \frac{1}{T}\int_0^T I(t)\mathrm{d}t$ and $\overline{IA} = \frac{1}{T}\int_0^T I(t)A(t)\mathrm{d}t$. The details of this deduction and the solution of the system are described in Appendix A.1.2.

3.2.3 Accounting for the light gradient

Photobioreactors are illuminated at the surface and the light is attenuated along the depth z due to the light absorption and scattering. The generalized Beer-Lambert law is chosen for modelling this phenomenon:

$$I(y) \coloneqq I_s e^{-y}. \tag{3.13}$$

where $y := \varepsilon(X)z$, is the so-called local optical depth [17]. The vertical position is denoted by z. The light extinction coefficient $\varepsilon(X) > 0$ depends on the concentration of the microalgae X. Local optical depth (dimensionless) is a concept that integrates the attenuation of light due to pigment absorption and scattering. At local optical depth y, the light perceived is the fraction e^{-y} of the irradiance at the bioreactor surface. The advantage of this formulation is that it can integrate nonlinear effects of the extinction coefficient due to multiscattering [98]. The darkest reactor part is characterized by a low remaining light, typically $\frac{I_{\text{out}}}{I_{\text{in}}} < 0.1$ which corresponds to the case $y > 2.3$ [19]. Some of our results hold for small values of local optical depth (meaning $y < 1$, where light extinction is lower than 36%).

Here, we assume that the algal biomass does not change at the considered timescale. From the definition of light attenuation (3.13), we denote by $I_H(y) = I_{\max}e^{-y}$ (resp. $I_L(y) = I_{\min}e^{-y}$) the high irradiance (resp. the low irradiance) at local optical depth y.

When illuminated by a constant irradiance I_η, the irradiance perceived at local optical depth y is given by $I_M(y) = I_\eta e^{-y}$. By choosing I_η as (3.9), we guarantee that the continuous light regime and the high/low flashing light regime provide the same amount of energy. Our objective is to compare the average growth rate for these two systems.

3.2.4 Model limitations

This model does not represent all the mechanisms involved in the photosynthesis, and how other factors such as temperature, pH or nutrients affect growth rate. It assumes that growth rate is driven by the PSII dynamics. For the considered timescales (from mseconds to hours), the dynamics of Calvin's cycle, and especially through RubisCo is not considered as a limiting factor. The pigment change as an acclimation mechanism to a varying light is also not represented. However, it has been shown that for fast varying light signal, cells acclimate to average irradiance [34], which is kept constant along our study.

3.2.5 Exact asymptotic solution of the Han model

For any initial condition of the Han model states (A and C), we prove in Lemma 3.2 that, for a periodic signal of light I, the solution of (3.7) converges to the unique periodic solution. This

property is used to focus on the asymptotic periodic solution for the two models. We define the asymptotic exact T-averaged growth rate $\bar{\mu}^{\mathrm{T}}$ by

$$\bar{\mu}^{\mathrm{T}}(y) = \frac{1}{T}\int_0^T \mu(y,t)\mathrm{d}t, \tag{3.14}$$

where μ is defined in (3.3) and A is considered as the periodic solution of (3.1). Using the definition of M in (3.8), let us denote $M_H(y) = M(I_H(y))$, $N_H(y) = N_H(I_H(y))$, $M_L(y) = M(I_L(y))$, $N_L(y) = N(I_L(y))$.

Lemma 3.1

The system (3.7) under the periodic high/low light regime admits a unique periodic solution (A_p, C_p).

The computations of this periodic solution are given in Appendix A.1.3.

Lemma 3.2

All solutions of (3.7) under the periodic high/low light regime converge to the periodic solution.

Proof. Let $(A,C)^T$ a solution of (3.7) under high/low light regime and $(A_p, C_p)^T$ the periodic solution of (3.7). Then $\xi \coloneqq (A,C)^T - (A_p, C_p)^T$ is a solution of the impulsive differential equation

$$\begin{cases} \dot{\xi}(t) &= -M(t)\xi(t), \quad \text{for } t \neq t_k, \\ \xi(t_k^+) &= \xi(t_k), \end{cases}$$

where

$$t_0 = 0,$$
$$t_k = \begin{cases} t_{k-1} + \eta T, & \text{if } k \text{ is odd}, \\ t_{k-1} + (1-\eta)T, & \text{if } k \text{ is even}, \end{cases}$$

is the sequence of discontinuities of the light function in the high/low regime and M is defined in (3.8). Let us denote by Λ_H, Λ_L the largest eigenvalues of the matrices M_H and M_L respectively. Note that $t_{2k} = kT$. Our goal is to prove that for every $k \in \mathbb{N}$ we have

$$\|\xi(t)\| \leq e^{-k\Lambda_\eta T}\|\xi(0)\|\ , \quad \forall t \in [t_{2k}, t_{2(k+1)}], \tag{3.15}$$

where $\Lambda_\eta = \eta\Lambda_H + (1-\eta)\Lambda_L$. Since the matrix is constant in the intervals (t_k, t_{k+1}) for every k, we have that

$$\xi(t) = \begin{cases} e^{-tM_H}\xi(0), & \text{if } t \in [t_0, t_1), \\ e^{-tM_L}e^{-\eta T M_H}\xi(0), & \text{if } t \in [t_1, t_2]. \end{cases}$$

This implies that

$$\|\xi(t)\| = \begin{cases} \|e^{-tM_H}\|\|\xi(0)\|, & \text{if } t \in [t_0, t_1), \\ \|e^{-tM_L}e^{-\eta T M_H}\|\|\xi(0)\|, & \text{if } t \in [t_1, t_2], \end{cases}$$

and $\|\xi(t)\| \leq \|\xi(0)\|$ for $t \in [t_0, t_2]$. Now, suppose that (3.15) holds for k, let us prove that this also holds for $k+1$. Let $t \in [t_{2(k+1)}, t_{2(k+2)}]$, then

$$\xi(t) = \begin{cases} e^{-tM_H}\xi(t_{2(k+1)}) & \text{if } t \in [t_{2(k+1)}, t_{2(k+1)+1}), \\ e^{-tM_L}e^{-\eta TM_H}\xi(t_{2(k+1)}) & \text{if } t \in [t_{2(k+1)+1}, t_{2(k+2)}]. \end{cases}$$

As $\xi(t_{2(k+1)}) = e^{-(1-\eta)TM_L}e^{-\eta TM_H}\xi(t_{2k})$, and $\|\xi(t_{2k})\| \leq e^{-k\Lambda_\eta T}\|\xi(0)\|$, then

$$\begin{aligned} \|\xi(t_{2(k+1)})\| &= \|e^{-(1-\eta)TM_L}e^{-\eta TM_H}\xi(t_{2k})\| \\ &\leq e^{-T\Lambda_\eta}\|\xi(t_{2k})\| \\ &\leq e^{-(k+1)T\Lambda_\eta}\|\xi(0)\|, \end{aligned}$$

and we can conclude that

$$\begin{aligned} \|\xi(t)\| &= \begin{cases} \|e^{-tM_H}\|e^{-(k+1)T\Lambda_\eta}\|\xi(0)\| & \text{if } t \in [t_{2(k+1)}, t_{2(k+1)+1}), \\ \|e^{-tM_L}e^{-\eta TM_H}e^{-(k+1)T\Lambda_\eta}\|\xi(0)\| & \text{if } t \in [t_{2(k+1)+1}, t_{2(k+2)}). \end{cases} \\ &\leq e^{-(k+1)T\Lambda_\eta}\|\xi(0)\|. \end{aligned}$$

Finally, as (3.15) holds, taking $k \to \infty$ we conclude that $\|\xi(t)\| \to 0$ as $t \to \infty$. □

Solving (3.7) in periodic case and using the definition of the growth rate (3.3), it is possible to analytically compute the exact T-average growth rate in the high/low-flashing light as

$$\bar{\mu}^{\mathrm{T}}(y) = \eta\mu_S(I_H(y)) + (1-\eta)\mu_S(I_L(y)) - \frac{K\sigma}{T}\delta(y,T), \tag{3.16}$$

where the function μ_S is defined in (3.4), δ is the first component of the vector

$$\begin{aligned} \Delta = \Big[& I_H(y)M_H^{-1}(y)\left(\mathrm{Id} - e^{-\eta TM_H(y)}\right)\left(\mathrm{Id} - e^{-(1-\eta)TM_L(y)}e^{-\eta TM_H(y)}\right)^{-1}\left(\mathrm{Id} - e^{-(1-\eta)TM_L(y}\right) \\ & - I_L(y)M_L^{-1}(y)\left(\mathrm{Id} - e^{-(1-\eta)TM_L(y)}\right)\left(\mathrm{Id} - e^{-\eta TM_H(y)}e^{-(1-\eta)TM_L(y)}\right)^{-1}\left(\mathrm{Id} - e^{-\eta TM_H(y)}\right)\Big] \\ & \cdot \left(M_H^{-1}(y)N_H(y) - M_L^{-1}(y)N_L(y)\right), \end{aligned} \tag{3.17}$$

with Id the identity matrix in $\mathbb{R}^{2\times 2}$. The details of the computations are given in A.1.4.

3.3 Study of Case I: Slowly varying irradiance

In this section, we present an analysis based on the growth rate calculated using the large-T model. We show in particular that the average growth rate can be greater than the values of the PI-curve derived from the Han model. We give the conditions to get an enhanced average growth rate based on the local convexity of the function μ_S.

3.3.1 Average growth rate and analysis

In large-T model, the growth rate can be derived from (3.3) as

$$\mu = K\sigma I A = (1-C)\gamma(I), \tag{3.18}$$

with $\gamma(I) = \frac{K\sigma I}{1+\tau\sigma I}$ and C the periodic solution of (3.10). For a given local optical depth y, the T-average growth rate for the high/low light regime can be computed explicitly by

$$\bar{\mu}^{\mathrm{T}}(y) = \frac{1}{T}\int_0^T \mu(y,t)\mathrm{d}t = \eta\mu_S(I_H(y)) + (1-\eta)\mu_S(I_L(y)) + \frac{\zeta_1(y,\eta,T)\zeta_2(y)}{Tk_r}, \tag{3.19}$$

with

$$\zeta_1(y,\eta,T) = \frac{\left(1-e^{-(\alpha_L(y)+k_r)T(1-\eta)}\right)\left(1-e^{-(\alpha_H(y)+k_r)T\eta}\right)}{1-e^{-(\alpha_L(y)+k_r)T(1-\eta)-(\alpha_H(y)+k_r)T\eta)}},$$
$$\zeta_2(y) = \Big(\frac{\alpha_H(y)}{\alpha_H(y)+k_r} - \frac{\alpha_L(y)}{\alpha_L(y)+k_r}\Big)\big(\mu_S(I_H(y)) - \mu_S(I_L(y))\big),$$

where α is defined in (3.11) and we extend the notation as $\alpha_H(y) := \alpha(I_H(y))$ and $\alpha_L(y) := \alpha(I_L(y))$. The details of the computations are presented in A.1.1. Let us denote by $\mu_S^\eta(y)$ the convex combination in (3.19):

$$\mu_S^\eta(y) := \eta\mu_S(I_H(y)) + (1-\eta)\mu_S(I_L(y)). \tag{3.20}$$

When T is large enough, we can approximate the T-average growth rate by (3.20). Indeed, it is straightforward to see that $0 \le \zeta_1(y,\eta,T) \le 1$ and $0 \le \frac{\alpha(I)}{\alpha(I)+k_r} \le 1$, therefore, one has

$$\left|\bar{\mu}^{\mathrm{T}}(y) - \mu_S^\eta(y)\right| = \left|\frac{\zeta_1(y,\eta,T)\zeta_2(y)}{Tk_r}\right| \le \frac{|\mu_S(I_H(y)) - \mu_S(I_L(y))|}{Tk_r} \le \frac{\mu_{\max}}{Tk_r},$$

where the last inequality is obtained by taking the maximum growth rate of the Han model given by (3.5). This leads to the following result.

Theorem 3.1

For a large enough period T, for every local optical depth $y \ge 0$ we have

$$\lim_{T\to+\infty} \bar{\mu}^{\mathrm{T}}(y) = \mu_S^\eta(y).$$

Furthermore, the convergence is uniformly in y and $\left|\bar{\mu}^{\mathrm{T}}(y) - \mu_S^\eta(y)\right| = \mathcal{O}(1/T)$.

3.3.2 Enhancement of the growth rate

Growth rate in high/low light regime can be enhanced or reduced compared to that of the constant light regime. More precisely, this relies on the local convexity of the function μ_S with respect to the irradiance I. Depending on the value of I, this can be either convex or concave. The next lemma clarifies the critical value of the irradiance.

Lemma 3.3

There exists an irradiance I_c, for which μ_S is a strictly convex function in $(I_c, +\infty)$ and strictly concave in $(0, I_c)$. This value only depends on the parameters (k_d, k_r, τ, σ), *i.e.*,

$$I_c = \begin{cases} \frac{2}{\sigma\sqrt{\frac{k_d}{k_r}\tau}} \cos\left(\frac{1}{3}\arccos\left(\frac{\sqrt{\tau}}{2\sqrt{\frac{k_d}{k_r}}}\right)\right) & \text{if } \tau \leq 4\frac{k_d}{k_r}, \\ \frac{2}{\sigma\sqrt{\frac{k_d}{k_r}\tau}} \cosh\left(\frac{1}{3}\operatorname{arccosh}\left(\frac{\sqrt{\tau}}{2\sqrt{\frac{k_d}{k_r}}}\right)\right) & \text{if } \tau > 4\frac{k_d}{k_r}. \end{cases} \tag{3.21}$$

The proof is given in A.2. This lemma enables us to state the next theorem, which is our main result. In this theorem, we provide conditions to enhance the growth rate, meaning that the average growth rate calculated in (3.19) is greater than the growth rate obtained for the continuous light regime I_η. Also, Figure 3.5a illustrates in the curve μ_S the value of I_c positioned on the right of I_{opt}.

Theorem 3.2

Let I_c defined by (3.21). For every couple $(I_{\max},\ I_{\min})$, such that $I_{\max} > I_{\min} > I_c$, there exists $T > 0$ and $\eta \in (0, 1)$ such that

$$\bar{\mu}^{\mathrm{T}}(0) \geq \mu_S(I_\eta), \tag{3.22}$$

where $I_\eta = \eta I_{\max} + (1-\eta) I_{\min}$.

Proof. Setting $y = 0$ in (3.19) gives

$$\bar{\mu}^{\mathrm{T}}(0) = \eta\mu_S(I_{\max}) + (1-\eta)\mu_S(I_{\min}) + \frac{\zeta_1(0,\eta,T)\zeta_2(0)}{Tk_r}.$$

Recall that

$$\begin{aligned} \zeta_2(0) &= \Big(\frac{\alpha_H(0)}{\alpha_H(0)+k_r} - \frac{\alpha_L(0)}{\alpha_L(0)+k_r}\Big)\big(\mu_S(I_H(0)) - \mu_S(I_L(0))\big), \\ &= \Big(\frac{\alpha(I_{\max})}{\alpha(I_{\max})+k_r} - \frac{\alpha(I_{\min})}{\alpha(I_{\min})+k_r}\Big)\big(\mu_S(I_{\max}) - \mu_S(I_{\min})\big). \end{aligned}$$

In $(I_c, +\infty)$ the function μ_S is decreasing, then $\mu_S(I_{\max}) - \mu_S(I_{\min}) < 0$. Moreover, the function $I \mapsto \frac{\alpha(I)}{\alpha(I)+k_r}$ is increasing, hence $\zeta_2(0) < 0$. On the other hand, one has $0 \leq \zeta_1(0,\eta,T) \leq 1$ and $0 \leq \frac{\alpha(I)}{\alpha(I)+k_r} \leq 1$ for $I \geq 0$. All together implies that

$$\bar{\mu}^{\mathrm{T}}(0) \geq \eta\mu_S(I_{\max}) + (1-\eta)\mu_S(I_{\min}) + \frac{1}{Tk_r}\left(\mu_S(I_{\max}) - \mu_S(I_{\min})\right). \tag{3.23}$$

To conclude, we have to find T such that the right-hand side of (3.23) is greater than $\mu_S(I_\eta)$ which is equivalent to the condition

$$\frac{1}{Tk_r} \leq \frac{\mu_S(I_\eta) - \eta\mu_S(I_{\max}) - (1-\eta)\mu_S(I_{\min})}{\mu_S(I_{\max}) - \mu_S(I_{\min})}. \tag{3.24}$$

Since $\mu_S(I)$ is convex and decreasing on interval $(I_c, +\infty)$, the right-hand side of (3.24) is always positive. Therefore, a couple (T, η) verifying condition (3.24) will ensure the inequality (3.22). This concludes the proof. □

For $I_{\max}, I_{\min} \in (I_c, +\infty)$ and $y = 0$ (*i.e.*, at the surface), one can find a period T and a duty cycle η such that the T-average growth rate under the high/low light regime is greater than the constant average light regime. Based on the condition (3.24), if η is near to 0 or 1 we need larger T, since the right-hand side of the inequality approaches to zero in this case. This improvement can also be valid for other choices of light (see Figure 3.5).

On the other hand, one can see that a condition between T and η is needed to give an interpretation of this improvement in the growth rate. Assume that the condition (3.24) holds for some T and η. Since $\mu_S(I_\eta) \geq \mu_S(I_{\max})$, then one has

$$\begin{aligned}
\frac{1}{Tk_r} &\leq \frac{\mu_S(I_\eta) - \eta\mu_S(I_{\max}) - (1-\eta)\mu_S(I_{\min})}{\mu_S(I_{\max}) - \mu_S(I_{\min})} \\
&\leq \frac{\mu_S(I_{\max}) - \eta\mu_S(I_{\max}) - (1-\eta)\mu_S(I_{\min})}{\mu_S(I_{\max}) - \mu_S(I_{\min})} \\
&= 1 - \eta,
\end{aligned}$$

or, in other words, $(1-\eta)T \geq \frac{1}{k_r}$. The time needed for recovering a damaged reaction center is $\frac{1}{k_r}$ and, $(1-\eta)T$ represents the time that the system is exposed under the low light. Therefore, by considering the exposed time under the low light which is larger than recovering time $\frac{1}{k_r}$, the average growth rate at the surface can be enhanced in the high/low light regime. Assuming T large enough, we have the approximation

$$\bar{\mu}^{\mathrm{T}}(y) \approx \mu_S^\eta(y). \tag{3.25}$$

Then we can state the next theorem which will provide the optimal duty cycle η for enhancing the growth rate.

Theorem 3.3

For large T, choosing $I_{\max} > I_{\min} > I_c$, at the top of the bioreactor, there exists $\eta \in (0, 1)$ which maximize the difference between the average growth rate in the high/low-flashing light regime, leading to a T-average growth rate larger than the one in continuous light regime.

Proof. Setting $y = 0$. In the limit case of the large-T model, we approximate the average growth rate with (3.25). The optimum η_{opt} is defined as

$$\eta_{\mathrm{opt}} := \underset{\eta\in(0,1)}{\operatorname{argmax}}\, \eta\mu_S(I_{\max}) + (1-\eta)\mu_S(I_{\min}) - \mu_S(I_\eta),$$

which solution is such that

$$\frac{\mathrm{d}}{\mathrm{d}I}\mu_S(I_{\eta_{\mathrm{opt}}}) = \frac{\mu_S(I_{\max}) - \mu_S(I_{\min})}{I_{\max} - I_{\min}}, \tag{3.26}$$

and the existence is ensured by the mean value theorem. □

This optimal η is actually the one which is capable of achieving the maximal difference between $\bar{\mu}^{\mathrm{T}}(0)$ and $\mu_S(I_\eta)$. Moreover, (3.26) can be rewritten as

$$0 = \left[1 + \tau\sigma I_{\eta_{\mathrm{opt}}} + \frac{k_d}{k_r}\tau(\sigma I_{\eta_{\mathrm{opt}}})^2\right]^2 \frac{\mu_S(I_{\max}) - \mu_S(I_{\min})}{K\sigma(I_{\max} - I_{\min})} + \frac{k_d}{k_r}\tau(\sigma I_{\eta_{\mathrm{opt}}})^2 - 1.$$

3.4 Study of Case II: fast varying light

In this section, we present the value of the T-average growth rate using the Small-T model, meaning that $T < \tau$. Recall that τ is the time during which one photon is processed in the PSU, thus T is in the order of milliseconds. We prove that the average growth rate, in the limit, corresponds to $\mu_S(I_\eta)$, then we provide an analysis in the flashing light regime, and we define the optimal local optical depth in this case.

3.4.1 Average growth rate

Recall that, by definition (3.14), the T-average growth rate can be computed by

$$\bar{\mu}^{\mathrm{T}} = \frac{1}{T}\int_0^T K\sigma I A \mathrm{d}t = K\sigma\overline{IA}.$$

Then $\bar{\mu}^{\mathrm{T}}$ is computed by

$$\bar{\mu}^{\mathrm{T}}(y) = \frac{K\sigma k_r I_M(y)\big(1 + \xi_1(y)\xi_2(y,T)\big)}{k_r + k_r\tau\sigma I_M(y) + k_d\tau\big(\sigma I_M(y)\big)^2 + k_d\sigma I_M(y)\xi_1(y)\xi_2(y,T)}, \tag{3.27}$$

where

$$\xi_1(y) = \frac{\sigma\big(I_H(y) - I_L(y)\big)^2\eta(1-\eta)}{\tau\beta_H(y)\beta_L(y)},$$
$$\xi_2(y,T) = \frac{(1 - e^{-\beta_H(y)\eta T})(1 - e^{-\beta_L(y)(1-\eta)T})}{T(1 - e^{-\beta_H(y)\eta T - \beta_L(y)(1-\eta)T})}\frac{\eta\beta_H(y) + (1-\eta)\beta_L(y)}{\eta(1-\eta)\beta_H(y)\beta_L(y)} - 1,$$

$\beta_H(y) := \beta(I_H(y))$ and $\beta_L(y) := \beta(I_L(y))$. The details of the computation are given in A.1.2. Since

$$\lim_{T\to 0}\frac{(1 - e^{-\beta_H(y)\eta T})(1 - e^{-\beta_L(y)(1-\eta)T})}{T(1 - e^{-\beta_H(y)\eta T - \beta_L(y)(1-\eta)T})} = \frac{\eta(1-\eta)\beta_H(y)\beta_L(y)}{\beta_H(y) + \beta_L(y)},$$

one has $\lim_{T\to 0}\xi_2(y,T) = 0$. This leads to the following result.

Theorem 3.4

For rapid light alternation, one has for every local optical depth $y > 0$ $\lim_{T\to 0} \bar{\mu}^{\mathrm{T}}(y) = \mu_S(I_M(y))$.

In the limit, when $T \to 0$, the growth rate of the high/low-flashing light is the same as the growth rate at steady state of A (full light integration) by considering the irradiance I_η. In this case, the algae perceives the average irradiance for growing and there is no possible gain in growth rate compared to continuous light.

3.4.2 Small-T flashing light

Flashing light corresponds to the particular case of the high/low-flashing light when $I_{\min} = 0$. Based on our previous analysis, we present the local optical depth at which the algae culture perceives the optimal irradiance for growing.

Assume that the approximation $\bar{\mu}^{\mathrm{T}}(y) \approx \mu_S(I_\eta(y))$ holds. By Theorem 3.4, the light perceived by the algae at local optical depth y is $I_\eta(y) = \eta I_{\max} e^{-y}$. In this case, we can give an explicit expression for the local optical depth at which the algae culture perceives the optimal light, and consequently, the depth where the optimal light is perceived. This expression depends on the duty cycle η which, in practice, can be settled and then, we can select the local optical depth in a certain range of values. We define the *optimal local optical depth* as the local optical depth in which the average growth rate achieves the maximum of the growth rate.

Lemma 3.4

Considering flashing light, let $I_{\max}$ the maximum irradiance provided at the top of the bioreactor, η the duty cycle and σ, k_d, k_r, τ the parameters of the Han model. The optimal local optical depth is given by

$$y_{\mathrm{opt}} = \ln\left(I_{\max}\sigma\sqrt{\frac{k_d}{k_r}}\tau\eta\right) \tag{3.28}$$

Proof. The growth rate, considering flashing light and the limit case of the small-T model correspond to

$$\bar{\mu}^{\mathrm{T}}(y) = \mu_S(\eta I_{\max} e^{-y}) = \mu_S(I_{\max} e^{-(y-\ln(\eta))}).$$

Matching the value of the optimal light of the function μ_S given by (3.6) and the growth rate calculated above, we obtain the equality

$$I_{\max} e^{-(y_{\mathrm{opt}} - \ln\eta)} = \frac{1}{\sigma\sqrt{\frac{k_d}{k_r}}\tau},$$

and isolating y_{opt} we get the value (3.28). □

As η tends to zero, y_{opt} can take negative values. Negative values are meaningless, the algae culture does not perceive the optimal light in this case and all the culture is under the photo-limited condition. Hence, the choice of the duty cycle η impacts productivity. For including the optimal light into the culture, we have to consider the inequality

$$\eta \geq \frac{1}{I_{\max}\sigma\sqrt{\frac{k_d}{k_r}\tau}}.$$

Using the definition of I_{opt}, this is equivalent to the condition:

$$\eta \geq \frac{I_{\text{opt}}}{I_{\max}}.$$

In conclusion, for every value of η in the range of $[I_{\text{opt}}/I_{\max}, 1)$ the optimal light is perceived in the culture. By setting $\eta = I_{\text{opt}}/I_{\max}$, the optimal light is then perceived at the top of the culture.

Considering $y = aXz$ where, X is the concentration of the culture, z is the depth and a is the light attenuation constant. Then, the depth at which the culture perceives the optimal light intensity is given by

$$z_{\text{opt}} = \frac{1}{aX}\ln\left(I_{\max}\sigma\sqrt{\frac{k_d}{k_r}\tau\eta}\right).$$

So, as the concentration increase through time, z_{opt} decrease. One way to counteract this effect is to increase the value of the duty cycle η.

3.5 Study of Case III: the intermediate case

We analyzed the large and the small-T model, then gave the limit of the T-averaged growth rate in Theorem 3.1 and Theorem 3.4 when $T \to +\infty$ and $T \to 0$ respectively. Meanwhile, we evaluated the T-average growth rate without considering the simplified models given in (3.16) named as the asymptotic exact growth rate. In this section, we show that the limits of (3.16) are the same as the results in Theorem 3.1 and Theorem 3.4.

Proposition 3.1

The exact average growth rate (3.16) converges to μ_S^η as $T \to +\infty$ and it also converges to $\mu_S(I_M)$ when $T \to 0$.

Proof. Let us first prove that if $T \to +\infty$, then $\bar{\mu}^{\text{T}}$ given by (3.16) converges to μ_S^η. The eigenvalues of the matrices M_H and M_L are positive (see Appendix A.1.5) and then, the exponential matrices

$$e^{-\eta T M_H(y)} \quad \text{and} \quad e^{-(1-\eta)TM_L(y)}$$

converge to the zero matrix as $T \to +\infty$ for every local optical depth y. Thus,

$$\lim_{T\to+\infty}\Delta = \left[I_H(y)M_H^{-1}(y) - I_L(y)M_L^{-1}(y)\right]\left(M_H^{-1}(y)N_H(y) - M_L^{-1}(y)N_L(y)\right),$$

where Δ is defined in (3.17). From the exact growth rate given by (3.16), we can also conclude that

$$\lim_{T\to+\infty} \bar{\mu}^{\mathrm{T}}(y) = \eta\mu_s(I_H(y)) + (1-\eta)\mu_S(I_L(y)) = \mu_S^{\eta}(y),$$

which is the result of Theorem 3.1. Now, for the other case, we have that

$$\lim_{T\to 0} \frac{\Delta}{T} = \eta(1-\eta)M_{\eta}^{-1}(y)(I_H(y)M_L(y) - I_L M_H(y))[(M_H^{-1}(y)N_H(y) - M_L^{-1}(y)N_L(y)],$$

where $M_\eta(y) = \eta M_H(y) + (1-\eta)M_L(y)$. We can manipulate this term and get that

$$\begin{aligned}\lim_{T\to 0} \frac{\Delta}{T} &= M_{\eta}^{-1}\left[-I_\eta N_\eta + \eta I_H M_\eta M_H^{-1} N_H + (1-\eta) I_L M_\eta M_L^{-1} N_L\right](y) \\ &= -I_\eta(y) M_\eta^{-1}(y) N_\eta(y) + \eta I_H(y) M_H^{-1}(y) N_H(y) + (1-\eta) I_L(y) M_L^{-1}(y) N_L(y).\end{aligned}$$

Replacing this limit in (3.16), we conclude that

$$\lim_{T\to 0} \bar{\mu}^{\mathrm{T}}(y) = \mu_S(I_\eta(y)).$$

This corroborates the behavior of the mean of the growth rate in the large-T and small-T models. $\square$

3.6 Illustration with simulation studies

3.6.1 Parameter settings

The Han model parameters in literature are different depending on the authors and the studied species. Here we consider the values taken from three studies [61, 82] and present in Table 3.1.

Parameter	Symbol	[61]	[82]	Unit
Recovery rate	k_r	$6.8 \cdot 10^{-3}$	$4.8 \cdot 10^{-4}$	s^{-1}
Damage rate	k_d	$2.99 \cdot 10^{-4}$	$2.99 \cdot 10^{-4}$	-
Turnover time	τ	0.25	6.8493	s
Effective cross-section	σ	0.047	0.0029	$\mathrm{m}^2\,\mu\mathrm{mol}^{-1}$
Growth rate coefficient	K	$8.7 \cdot 10^{-6}$	$3.6467 \cdot 10^{-4}$	-
Optimal light	I_{opt}	202.93	166.94	$\mu\mathrm{mol}\,\mathrm{m}^{-2}\mathrm{s}^{-1}$
Critical light	I_c	414.29	356.24	$\mu\mathrm{mol}\,\mathrm{m}^{-2}\mathrm{s}^{-1}$

Table 3.1: Parameter values for Han Model.

In this section, we provide some numerical tests to illustrate the two approximations and the exact solution of the Han system.

3.6.2 Quality of the approximated solution

First, we illustrate the difference between the two approximations and the exact solution. In Figure 3.3 the solution of A and C is plotted for $T = 0.5\,\mathrm{s}$ and $T = 3600\,\mathrm{s}$. For the small-T model, $0.5\,\mathrm{s}$ is considered. The large-T model is then a non-accurate approximation. As for $T = 3600\,\mathrm{s}$ we need to drop the assumption of C constant. In this case, the small-T model is far from the real solution. We observe that A and C change between two values, these values correspond to the steady states considering $I_{\max}$ and $I_{\min}$.

As expected, one can see that (3.12) provides a good approximation for small period (in this case for $T = 0.5\,\mathrm{s}$) and (3.10) provides a good approximation for large period ($T = 3600\,\mathrm{s}$). On the other hand, the quality of the approximation depends on the time period T.

3.6.3 Connection between Case I and Case II

Here we study the connection of the average growth rate between the one obtained from the large-T model (3.10), the small-T model (3.12) and the exact model (3.7). More precisely, we compute the T-average growth rate at the surface $\bar{\mu}^{\mathrm{T}}(0)$ by varying the period T from $T = 0.01\,\mathrm{s}$ to $T = 36\,000\,\mathrm{s}$, and the results are shown in Figure 3.4a. As $T \to 0$ the average growth rate converges

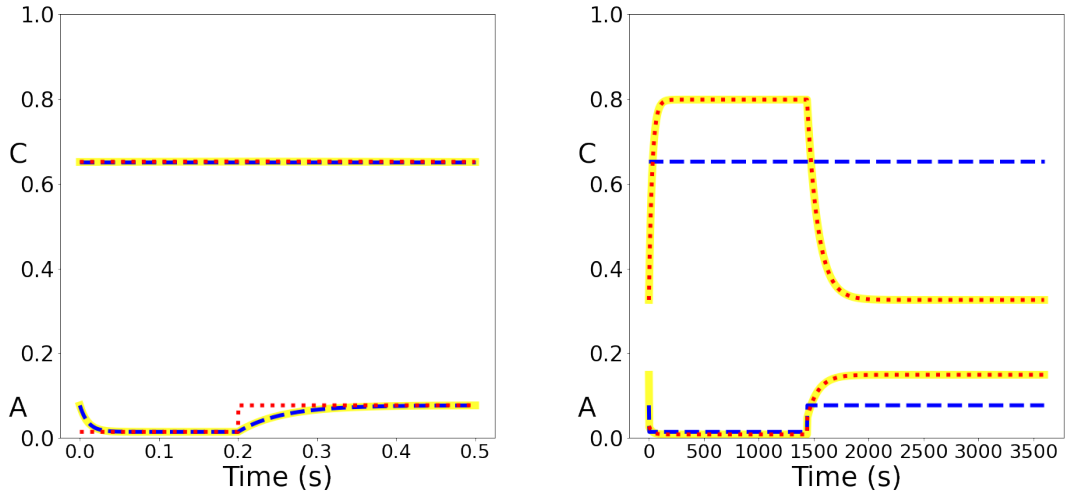

(a) $T = 0.5$s

(b) $T = 3600$s

Figure 3.3: Comparison of the two modelling approximations with the exact solution of the states of the Han model. The state A and C of the exact solutions (3.7) (continuous yellow line), of the small-T model (3.12) (segmented blue line) and of the large-T model (3.10) (segmented red line) are provided for $I_{\max} = 2000\,\mu\text{mol}\,\text{m}^{-2}\,\text{s}^{-1}$, $I_{\min} = 300\,\mu\text{mol}\,\text{m}^{-2}\,\text{s}^{-1}$, $\eta = 0.4$, $y = 0$ and four different values of T.

to the value $\mu_S(I_\eta(0)$, whereas $\bar{\mu}^{\text{T}} \to \mu_\eta(0)$ when $T \to +\infty$. Moreover, the inequality (3.22) holds for $T >= 174\,\text{s}$ as shown in Figure 3.4a, which is not the case in Figure 3.4b. Note that the time needed to process a photon (τ) and the time needed to recover a reaction center ($1/k_r$) are also given in Figure 3.4.

Small Period For $T \in (0, \tau]$ Small-T model gives a good approximation. As the light change in a timescale lower than the time of processing photons, in this case, the algae perceives the average of the light (i.e, I_η at the top).

Transition Period For $T \in (\tau, \frac{1}{k_r})$ the small period started to fail, and consider the large-T model is more accurate.

Large Period For $T \in [\frac{1}{k_r}, \infty)$ Large-T model fits. If a high light is combined with a low light, then some damaged reaction centers can be recovered, and we can get an improvement of the T-average growth rate compared to the continuous light regime.

3.6.4 Improvement of the growth rate

As shown in Theorem 3.2, there exists an improvement in the growth rate when the irradiance I_H and I_L are greater than the value of I_c as the case presented in Figure 3.5a. Unfortunately, the irradiance decreases when the local optical depth increases breaking the condition $I_H, I_L \geq I_c$, and

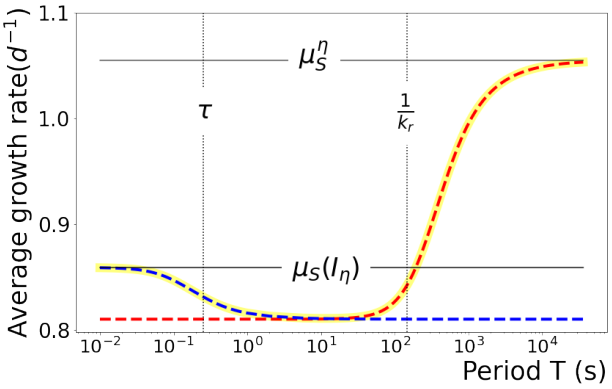

(a) $I_{\max} = 2000\,\mu\text{mol}\,\text{m}^{-2}\text{s}^{-1}$ and $I_{\min} = 10\,\mu\text{mol}\,\text{m}^{-2}\text{s}^{-1}$.

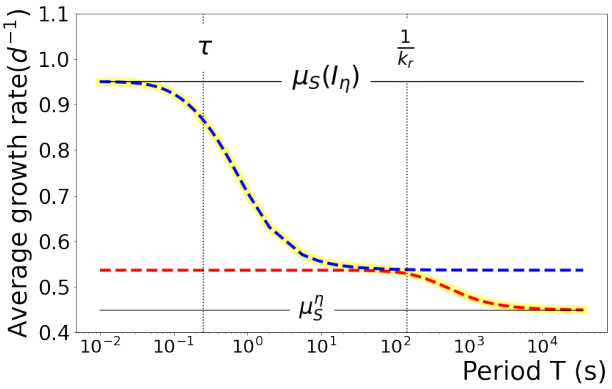

(b) $I_{\max} = 2000\,\mu\text{mol}\,\text{m}^{-2}\text{s}^{-1}$ and $I_{\min} = 10\,\mu\text{mol}\,\text{m}^{-2}\text{s}^{-1}$.

Figure 3.4: The exact average growth rate (3.16) (continuous yellow line), the average growth rate of the large-T model (3.19) (segmented red line) and the average growth rate of the small-T model (3.27) (segmented blue line). The period T is plotted in log scale. In this case $\eta = 0.5$

then, the improvement is no longer perceived. In Figure 3.5d, the T-average growth rate (black curve) is plotted as a function of the local optical depth, and it has greater values than the PI-curve of the Han model (blue curve). This means that the improvement perceived at the surface are still true when going deeper in the culture, but for larger values of y the T-average growth rate is smaller than the blue curve. Roughly speaking, this improvement is perceived in the section of the bioreactor receiving strong irradiance that inhibits photosynthesis.

It is possible to relax the condition $I_{\max} > I_{\min} > I_c$ in Theorem 3.2. For example, let us fix $I_{\max} > I_c$ and $I_{\min} < I_c$ as is shown in Figure 3.5b, for the two different values of the duty cycle η_1 and η_2, the average growth rate is denoted $\mu_S^{\eta_1}$ and $\mu_S^{\eta_2}$ respectively. In this case, the average growth rate considering the duty cycle η_2 is greater than the growth rate in continuous light with the same average light $\mu_S(I_{\eta_2})$, but for the duty cycle η_1 the growth rate is lower than with the continuous

light. If we consider, for example, the parameters of [61] where $I_c = 202.93$ (μmol m^{-2}s^{-1}) (see Table 3.1), $I_{\max} = 2000$ (μmol m^{-2}s^{-1}), $I_{\min} = 100$ (μmol m^{-2}s^{-1}). For η_1 the growth rate in continuous light regime is 13.7% larger than the average growth rate, and, for η_2 it is 12.5% smaller.

On the other hand, some selections for $I_{\min}$ can only give lower values of the T-average growth rate comparing with the PI-curve as we can see in Figure 3.5c. In this case, every selection of η provides a T-average growth rate lower than the PI-curve.

Figure 3.6 summarizes the behavior of the two models representing the simplifications of Case I and Case II. The exact growth rate is plotted in the form of a polygon. We can see that, for greater values of T, the exact growth rate coincides with the T-averaged growth rate of the large-T model. In this case, the hypotheses of Theorem 3.2 are satisfied. The red polygon corresponds to the surface of the bioreactor ($y = 0$) where the curve of the T-average growth rate of the large-T model is greater to the T-average growth rate of the small-T model due to Theorem 3.2. Note that in the small-T model, the average growth rate matches $\mu_S(I_\eta)$, which corresponds to the continuous light regime with the same average irradiance. As y becomes larger, the growth rate for Case I is lower than for the constant light regime, as shown in the green and blue polygon.

3.7 Conclusion and perspectives

We analyze the T-averaged growth rate in the high/low flashing light configuration in two simplified cases: for large period T and small period T. In the small-T model, we can simply approximate the T-average growth rate by considering $\mu_S(\eta I_H + (1-\eta)I_L)$, and for the large period T, we can approximate the T-average growth rate by considering $\eta\mu_S(I_H) + (1-\eta)\mu_S(I_L)$. In terms of growth rate, there is no distinction between the constant regime with light I_η and switching the light quickly between I_H and I_L in the time ηT and $(1-\eta)T$ respectively. In contrast, in the large-T model, we can improve the growth rate if we consider a low local optical depth. In this case, combining a high inhibiting irradiance and a lower irradiance with a period greater than $1/k_r$ (in the range of hours) in average, the growth rate will be higher than the one considering continuous light regime with the same average irradiance. Although, for higher local optical depth, the growth rate is lower than the constant light regime.

Most of our computations are still valid if the acclimation is modelled as a variation of the cross-section σ as a fixed parameter, for example, in the model of [105], σ is a function of the chlorophyll content, consequently, the value of A varies depending on the light at which the microalgae is acclimated. Then, in order to adapt our calculations, the parameter σ must change and be fixed in advance. Finally, two different light regimes can be compared changing the value of σ. On the other hand, microalgae are subjected to stochastic changes in the light regime that they perceive due to the mixing of the bioreactor. Although, we do not consider mixing in the computations, our calculations could be extended if a simplification of the hydrodynamic is considered. For example, a continuously illuminated bioreactor could be divided in two sections: a thin layer close to the illuminated surface and another layer photolimited. Both layers would be associated with a characteristic light intensity, then, assuming we know the fraction of time that the algae spend in each layer, the computations of the average growth rate can be used. This approach was already considered with a similar model in [154], but considering that the irradiance in the photolimited layer is zero.

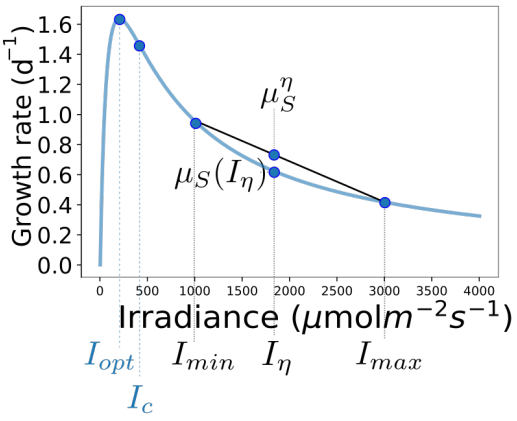

(a) $I_{\max}$ and $I_{\min}$ are greater than I_c. In this configuration, for each $\eta \in (0.1)$ we can find T for which $\mu_S(I_\eta) > \mu_S(I_\eta)$.

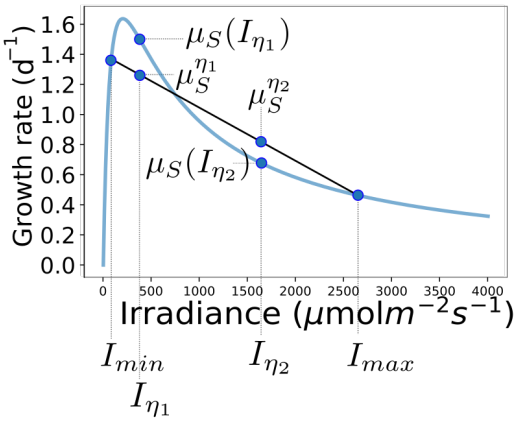

(b) When $I_{\min} < I_c$, we can still improve the average growth rate for some values of η. In this case, $\mu_S^{\eta_1} > \mu_S(I_{\eta_2})$ and $\mu_S^{\eta_2} < \mu_S(I_{\eta_1})$ for η_1.

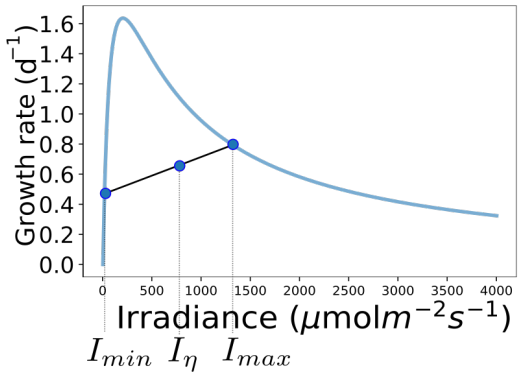

(c) For some configurations, it is impossible to find a fraction η and a period T for which $\mu_S^\eta > \mu_S(I_\eta)$.

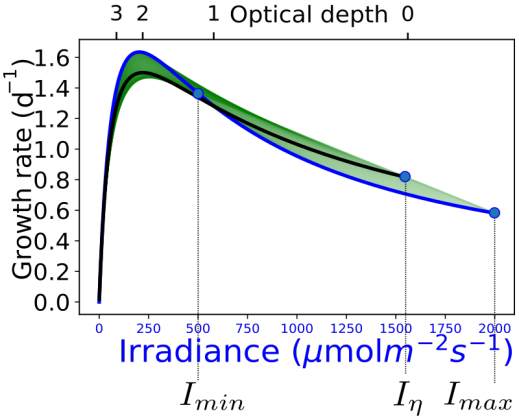

(d) The green area represents all the possible values for μ_S^η if we vary the local optical depth and η for a given $I_{\max}$ and $I_{\min}$. The black line correspond to the values of μ_S^η for a fixed value of η.

Figure 3.5: Illustration of Theorem 3.2, where approximation $\bar{\mu}_S^T \approx \mu_S^\eta$ holds for different combinations of $I_{\max}, I_{\min}$ and η.

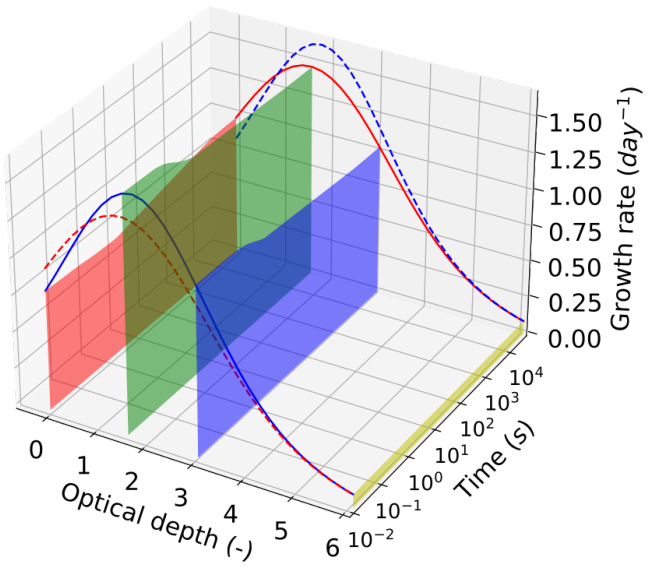

Figure 3.6: Average growth rate as a function of period T and optical depth y. Case II for small-T model (blue curve) and in the Case I for large-T model (red curve). The continuous line correspond to the approximation that fits the values of T. In this case, $I_{\max} = 2000\,\mu\text{mol}\,\text{m}^{-2}\,\text{s}^{-1}$, $I_{\min} = 500\,\mu\text{mol}\,\text{m}^{-2}\,\text{s}^{-1}$, $\eta = 0.5$.

Chapter 4

Should hydrodynamics be taken into account when calculating the growth rate of microalgae in a photobioreactor?

4.1 Introduction

In a photobioreactor, the zones near the light source, experience intense illumination, while the area in the deepest layers are in the dark. In addition, the photobioreactor is intensively mixed to avoid biomass sedimentation or spatial heterogeneity of the nutrients. It results that cells are advected through a light gradient, so that they perceive a succession of high and low light intensities. Photon harvesting is a dynamical process in microalgae, and the average growth rate within a photobioreactor results from this complex interplay between photosystem dynamics and hydrodynamics [19]. Accounting for such a complex interaction is a challenging problem, which needs to represent accurately both the hydrodynamics within the reactor and the dynamics of photon harvesting in response to light variations.

When a cell is advected in a photobioreactor, it perceives a continuous light signal over time. Using the Han model [67, 66], we will study the influence of this fluctuating signal on the growth rate. Taking into account the typical timescale of light variations, we will simplify the Han model considering a slow-fast approximation. Then, we will compare the outcome of this simplified Han model, with the predictions of the model at steady state. Our calculations will first be applied to simple periodic light signals and then to realistic light patterns derived from computational fluid dynamics simulations in a specific photobioreactors (raceway system) where mixing is carried out by a paddle wheel.

This chapter is organized as follows: in Section 4.2 we present the basis of the Han model. We define two strategies for computing the growth rate. Accounting for the dynamics of the

photosystem, we use μ_A and assuming a static response, we use μ_S. We write an explicit relation between the two functions, and we present one of the main results of this chapter in Theorem 4.1, which establishes the relationship between the time average of the dynamic growth rate (μ_A) and the static growth rate (μ_S). In Section 4.3.2, we study continuous periodic light signals, and show that every solution of the Han model converges to the unique periodic solution. In Proposition 4.3 and in Theorem 4.2 we give the exact average growth rate for any continuous periodic light signal, and we present two cases, to simulate the mixing in a photobioreactor. Finally, in Section 4.2.2 we analyze the case of the raceway pond, where we use a CFD model to simulate particles in the photobioreactor, tracking the light perceived by each individual microalgae. We compare the two growth rate functions, and we refine the average growth rate computation to take into account the spatial component. We demonstrate a close relation between the hydrodynamics and the average growth rate in Proposition 4.2.

4.2 Biological and hydrodynamic model

4.2.1 Biological model

We consider the mechanistic model of Han [66] which characterizes the photoinhibition induced by the photodamage of the photosystem II (PSII). There are three possible states for the PSII: open or reactive state A, closed or activated state B, and inhibited or damaged state C. The dynamics of PSII can be described by the differential equations:

$$\begin{aligned}
\frac{\mathrm{d}A}{\mathrm{d}t} &= -I\sigma_P A + \frac{B}{\tau},\\
\frac{\mathrm{d}B}{\mathrm{d}t} &= I\sigma_P A - \frac{B}{\tau} + k_r C - k_d \sigma_P I B,\\
\frac{\mathrm{d}C}{\mathrm{d}t} &= -k_r C + k_d \sigma_P I B,
\end{aligned} \tag{4.1}$$

where σ_P ($\mathrm{m}^2\mu\mathrm{mol}^{-1}$) is the effective cross-section of the PSII, I ($\mu\mathrm{molm}^{-2}\mathrm{s}^{-1}$) is the light intensity perceived by the microalgae starting from 0, τ (s) is the minimal time required for an electron to transfer from water on the donor side of the photosynthetic unit to the terminal electron acceptors, which is also called the turnover time, k_d ($-$) is the damage rate and k_r (s^{-1}) is the recovery rate of the PSII. A, B and C represents a probability distribution of each state such that we have

$$A + B + C = 1. \tag{4.2}$$

The algal growth rate is assumed to be proportional to the open state A and the light intensity I. More precisely, the growth rate given by the kinetic model corresponds to

$$\mu_A(I, A) \coloneqq \alpha\sigma_P I A, \tag{4.3}$$

where α ($-$) is a constant of proportionality. At steady state, the state A of the system (4.1) tends towards A_S[19]. It corresponds exactly to a Haldane model where growth rate is a function of light, that is

$$\mu_S(I) = \alpha\sigma_P I A_S = \alpha\sigma_P I \frac{1}{1 + \tau\sigma_P I + \frac{k_d}{k_r}\tau(\sigma_P I)^2}. \tag{4.4}$$

The maximum of μ_S is given by

$$\mu_{\max} = \frac{\alpha}{\tau + 2\sqrt{\frac{k_d}{k_r}\tau}},$$

and it is reached when the light value is

$$I_{\text{opt}} = \frac{1}{\sigma_P \sqrt{\frac{k_d}{k_r}\tau}}. \tag{4.5}$$

The growth rate results from the dynamics of (4.1). As shown in [53], taking into account relationship (4.2) and substituting it into system (4.1), we end up with two equations

$$\begin{aligned} \frac{\mathrm{d}A}{\mathrm{d}t} &= -\left(\sigma_P I + \frac{1}{\tau}\right) A - \frac{1}{\tau} C + \frac{1}{\tau}, \\ \frac{\mathrm{d}C}{\mathrm{d}t} &= \varepsilon \left[-\sigma_P I A - \left(\sigma_P I + \frac{k_r}{k_d}\right) C + \sigma_P I \right], \end{aligned} \tag{4.6}$$

which has slow/fast timescales due to the presence of the factor $\varepsilon = k_d$. In this case, we can consider the slow manifold proposed in [78]

$$A = \frac{1 - C}{1 + \tau \sigma_P I}, \tag{4.7}$$

and reduce the system (4.6) to a single equation for C given by

$$\frac{\mathrm{d}C}{\mathrm{d}t} = -(\gamma(I) + k_r)C + \gamma(I), \tag{4.8}$$

with $\gamma(I) \coloneqq \frac{k_d \tau (\sigma_P I)^2}{1 + \tau \sigma_P I}$. In particular, the steady state of C is given by

$$C_S \coloneqq \frac{\gamma(I)}{\gamma(I) + k_r} = \frac{\frac{k_d}{k_r}\tau(\sigma_P I)^2}{1 + \tau\sigma_P I + \frac{k_d}{k_r}\tau(\sigma_P I)^2}.$$

Consequently, the steady state of A can be obtained by substituting C_S into (4.7). Let us consider $0 \leq I_{\min} \leq I_{\max}$. We present an estimation of the actual growth rate μ_A for a continuous bounded light signal $I : [0, +\infty) \to [I_{\min}, I_{\max}]$ as a function of the static growth rate μ_S. For simplicity of notation, we write in the following $\mu_A(t)$ instead of $\mu_A(I(t), A(C(t), I(t)))$ and $\mu_S(t)$ instead of $\mu_S(I(t))$. We show next that the initial condition $A(0)$ can be ignored, and also we present an estimation of μ_S.

Proposition 4.1

Let $I : [0, +\infty) \to [I_{\min}, I_{\max}]$ be a continuous bounded light signal. Assuming that $A(0) = 0$, the actual growth rate μ_A can be written as

$$\mu_A(t) = \mu_S(t)(\gamma(I(t)) + k_r) \int_0^t e^{-\int_s^t \gamma(I(w)) + k_r \mathrm{d}w} \mathrm{d}s. \tag{4.9}$$

And for any initial condition $A(0) = A_0$ the associated growth rate converge to (4.9). Fur-

thermore, the following estimations hold

$$\mu_S(t)\frac{\gamma(I(t))+k_r}{\gamma(I_{\max})+k_r}\left(1-e^{-(\gamma(I_{\max})+k_r)t}\right)\leq \mu_A(t)\leq \ \mu_S(t)\frac{\gamma(I(t))+k_r}{\gamma(I_{\min})+k_r}. \tag{4.10}$$

Proof. The general solution of (4.8) is given by

$$C(t)=C(0)e^{-\int_0^t\gamma(I(w))+k_r\mathrm{d}w}+\int_0^t\gamma(I(s))e^{-\int_s^t\gamma(I(w))+k_r\mathrm{d}w}\mathrm{d}s. \tag{4.11}$$

Using then (4.7), A can be written as

$$\begin{aligned}A(A(0),t)=&A(0)\frac{1+\tau\sigma_P I(0)}{1+\tau\sigma_P I(t)}e^{-\int_0^t\gamma(I(w))+k_r\mathrm{d}w}\\&+A_S(t)(\gamma(I(t))+k_r)\int_0^t e^{-\int_s^t\gamma(I(w))+k_r\mathrm{d}w}\mathrm{d}s.\end{aligned} \tag{4.12}$$

If $A(0)=0$, then

$$A(0;t)=A_S(t)(\gamma(I(t))+k_r)\int_0^t e^{-\int_s^t\gamma(I(w))+k_r dw}\mathrm{d}s, \tag{4.13}$$

Note that if $A(0)\neq 0$, for t large enough, the first term of the right-hand side of (4.12) goes to zero as $\gamma(I)+k_r>0$. Equation (4.9) is deduced from the definition (4.3) and (4.4). The upper bound in (4.10) follows from the fact that γ is an increasing function of I and

$$\begin{aligned}\int_0^t e^{-\int_s^t\gamma(I(w))+k_r\mathrm{d}w}\mathrm{d}s&\leq\int_0^t e^{-\int_s^t\gamma(I_{\min})+k_r\mathrm{d}w}\mathrm{d}s\\&=\frac{1-e^{-(\gamma(I_{\min})+k_r)t}}{\gamma(I_{\min})+k_r}\\&\leq\frac{1}{\gamma(I_{\min})+k_r}.\end{aligned}$$

For a similar reason, the lower bound is given by

$$\int_0^t e^{-\int_s^t\gamma(I(w))+k_r\mathrm{d}w}\mathrm{d}s\geq\int_0^t e^{-\int_s^t\gamma(I_{\max})+k_r\mathrm{d}w}\mathrm{d}s=\frac{1-e^{-(\gamma(I_{\max})+k_r)t}}{\gamma(I_{\max})+k_r}.$$

Substituing these two bounds into (4.13) and using again the definition (4.3) and (4.4), we obtain the estimation (4.10). Finally, if $A(0)=A_0\neq 0$, the associated solution is given by (4.12), and then

$$\begin{aligned}|A(A(0);t)-A(0;t)|&=|A(0)|\frac{1+\tau\sigma_P I(0)}{1+\tau\sigma_P I(t)}e^{-\int_0^t\gamma(I(w))+k_r\mathrm{d}w},\\&\leq|A(0)|\frac{1+\tau\sigma_P I_{\max}}{1+\tau\sigma_P I_{\min}}e^{-\int_0^t\gamma(I(w))+k_r\mathrm{d}w},\\&\leq|A(0)|\frac{1+\tau\sigma_P I_{\max}}{1+\tau\sigma_P I_{\min}}e^{-k_r t}.\end{aligned} \tag{4.14}$$

The right hand part of the inequality converge to zero, then $A(A(0);t)$ converges to $A(0;t)$. □

As proposition 4.1 holds, in the following, we will assume that the initial condition of the state A is zero. We define the temporal average dynamic growth rate by

$$\overline{\mu}_A := \frac{1}{T}\int_0^T \mu_A(t)\mathrm{d}t.$$

In the same way, the temporal average static growth rate is defined by

$$\overline{\mu}_S := \frac{1}{T}\int_0^T \mu_S(t)\mathrm{d}t.$$

4.2.2 Computational fluid dynamic model

The water flow in a raceway pond can be simulated with Computational fluid dynamics (CFD) which integrate the Navier-Stokes equations. Several studies have simulated the velocity field in open ponds with CFD [109, 118]. A Lagrangian approaches were also used for assessing the mixing efficiency in the algae culture. For example, in [4], mixing length is computed as a result of different paddle wheel velocities.

Here, we use a 2D triangular mesh representing a real raceway of the Environmental Biotechnology Laboratory of INRAE Narbonne, France [73] (See Figure 4.1). The third dimension is given by the discretization of the free surface following the model in [5]

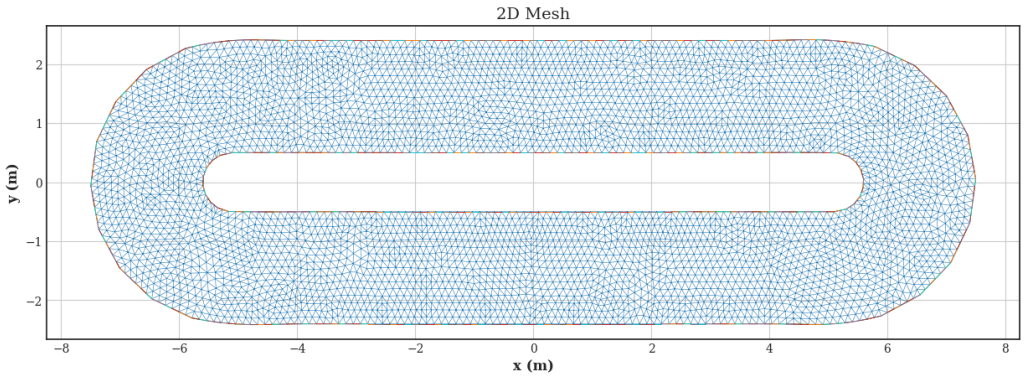

Figure 4.1: 2D Mesh of the simulated raceway pond.

4.2.3 Hydrodynamics and cell tracking

A layer-averaged Euler and Navier Stokes model for the numerical simulation of incompressible free surface is presented in [5]. The multi-layered model correspond to a Galerkin type approximation. The system is solved using a fixed 2D mesh of the bottom of the raceway and the layers are defined by the water depth, giving the third dimension of the system. The incompressible and

hydrostatic Navier-Stokes system with free surface used corresponds to

$$\begin{aligned} \nabla \mathbf{U} &= 0, \\ \frac{\partial \mathbf{u}}{\partial t} + \nabla_{x,y}(\mathbf{u} \otimes \mathbf{u}) + \frac{\partial \mathbf{u} w}{\partial z} &= \frac{1}{\rho_0} \nabla_{x,y} \sigma_P + \frac{\mu}{\rho_0} \frac{\partial^2 \mathbf{u}}{\partial z^2} + \mathbf{F}_{x,z}, \\ \frac{\partial p}{\partial z} &= -\rho_0 g + \mathbf{F}_z, \end{aligned} \tag{4.15}$$

where $\mathbf{U} = (u, v, w)^T$ is the velocity of the liquid, $\mathbf{u} = (u, v)^T$ is the horizontal velocity, σ is $-pI_d + \Sigma$, where $\Sigma = \mu \nabla_{x,y} \mathbf{u}$ is the total stress tensor, p is the pressure, g is the gravity acceleration constant, ρ_0 is the fluid density and μ is the viscosity coefficient. The fluid is assumed to be Newtonian. The paddle wheel is modelled by the force $\mathbf{F}$ [15] given by

$$\mathbf{F} = F \left(\sqrt{(x - x_{wheel})^2 + (z - z_{wheel})^2} \omega \right)^2 \begin{pmatrix} \cos(\theta) \\ 0 \\ \sin(\theta) \end{pmatrix}, \tag{4.16}$$

where F is a constant, θ is the angle between the vertical axis and the blade and $\omega = \dot{\theta}$, and x_{wheel}, z_{wheel} are the coordinates of the paddle wheel in the x and z axis respectively. Note that the force does not affect the y-axis which is parallel to the central axis of the paddle wheel. This technique demonstrated its efficiency for minimizing the computational time [15].

Lagrangian's trajectories of several particles are reconstructed from the Eulerian description given by Equation (4.15) denoted by $(\mathbf{X}_n)_{i=1}^{N_{par}}$, where N_{par} is the number of simulated particles. The position of each particle $\mathbf{X}_n(t) = (x_n, y_n, z_n)^T$ is computed by solving the equation

$$\begin{aligned} \frac{d\mathbf{X}_n(t)}{dt} &= \mathbf{U}(t), \\ \mathbf{X}_n(0) &= (x_{n0}, y_{n0}, z_{n0})^T, \end{aligned} \tag{4.17}$$

where (x_{n0}, y_{n0}, z_{n0}) is the initial position of the particle. We denote by Ω the domain of the raceway. We initiate the position of the particles randomly, following a uniform distribution in the domain Ω.

The CFD model was already validated using a Pulsed Ultrasonic Doppler Velocimetry [73]. Other similar works based in the same pond [69, 104] have considered a growth model tracking the position of Lagrangian trajectories base in the same model eqs. (4.15) to (4.17). Figure 4.2 show the distribution of the velocity magnitude in the raceway pond simulated and the streamlines after 10 minutes of simulations. The paddle wheel is positioned just above the red surface. Some cells (in white) are represented together with their respective streamlines. The trajectories of the cells are mainly horizontal in the straight sections of the raceway pond. The fluid domain along the z-axis is delimited by the free surface denoted by $\eta(t, x, y)$, then the system (4.15) is completed with the following boundary condition:

$$\frac{\partial \eta}{\partial t} \mathbf{u} \cdot \nabla_{x,y} \eta = 0.$$

For more details of the hydrodynamic model, see [5].

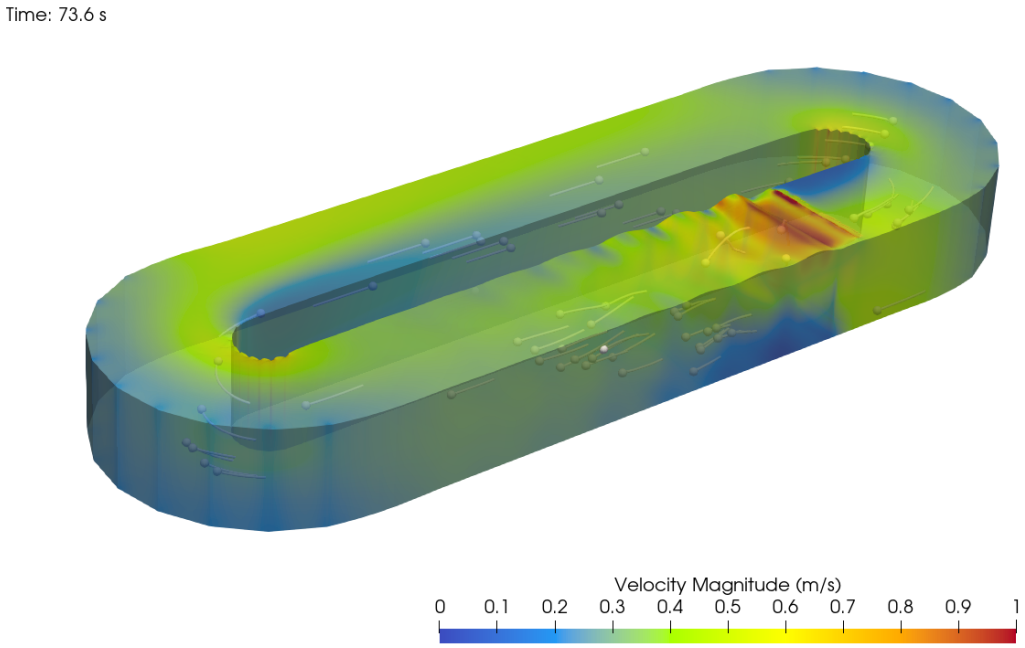

Figure 4.2: Representation of the raceway and the velocity field with some particles obtained from the CFD simulations. The height correspond to $0.3(m)$ and it is scaled with a factor of 5 to have a better visualization. The paddle wheel simulated in this image works at 20 RPM (rounds per minute).

4.2.4 Light distribution within the raceway pond

We assume that the light arrives perpendicular to the ground surface. The light reaching a cell $\mathbf{X}_n$ travels a distance equal to:

$$\eta(t, x_n, y_n) - z_n,$$

from the surface to the position of the cell, then the light signal I_n that perceives this particle is computed with the Beer-Lambert law as

$$I_n(t) = I_0 e^{-\xi(\eta(t,x_n,y_n)-z_n)}, \tag{4.18}$$

where $\xi > 0$ is a positive constant. Figure 4.3 shows the tracking of a single cell within the raceway pond. We distinguish two areas within the photobioreactor: the photoinhibited section in light green, where the light perceived is greater than the optimal light I_{opt} defined in Equation (4.5), and the photolimited section in dark green, where the light is lower than I_{opt}. Also, we show the optimal depth z_{opt} which correspond to the depth at which the algae perceive the light I_{opt} given by

$$z_{\text{opt}} = \frac{1}{\xi} \ln\left(\frac{I_0}{I_{opt}}\right).$$

When the particle goes from the photolimited area to the photoinhibited area, crossing z_{opt}, the difference between μ_S and μ_A is more observable. This occurs when the particle moves faster in

the z-axis than the photoinhibition mechanism. Here, the actual growth rate μ_A could reach larger values than predicted with the approximation μ_S. Otherwise, if the cell does not go through this section fast enough, then μ_S can accurately approximate μ_A as explained in Section 4.31.

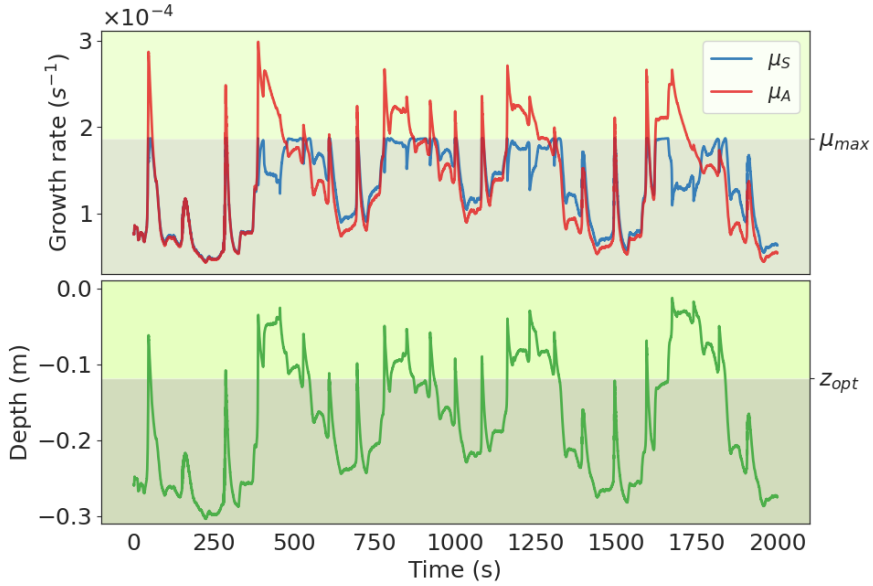

Figure 4.3: Actual growth rate μ_A and static approximation μ_S for a simulated trajectory in the raceway operated at 20 RPM with an initial height of water equal to $0.3(m)$. The maximum value of the function μ_S is denoted by $\mu_{\max}$ and the depth at which this value is reached by z_{opt}.

4.2.5 Growth rate in the raceway pond

To estimate the actual growth rate in the raceway pond, we average the growth rate of all simulated particles moving within the photobioreactor, then the space-time average dynamic growth rate is defined as

$$\overline{\overline{\mu}}_A = \frac{1}{N_{par}} \sum_{n=1}^{N_{par}} \overline{\mu}_A(I_n), \tag{4.19}$$

in the same way, we define the space-time average static growth rate as

$$\overline{\overline{\mu}}_S = \frac{1}{N_{par}} \sum_{n=1}^{N_{par}} \overline{\mu}_S(I_n). \tag{4.20}$$

In the Eulerian description, the static growth rate μ_S can be computed for every point in the domain of the raceway Ω. At each point $(x, y, z) \in \Omega$, the light is computed in the same way as in

Equation (4.18), then it is possible to define the volume average growth rate:

$$\overline{\mu}_\Omega = \frac{1}{V(\Omega)} \int_\Omega \mu_S(I(x,y,z))dxdydz,$$

where $V(\Omega)$ is the volume of the raceway and the light I is now given by:

$$I(x,y,z) = I_0 e^{-\xi(\eta(t,x,y)-z)}.$$

4.3 Formal analysis of the average growth rate

We next show the relation between $\overline{\mu}_A$ and $\overline{\mu}_S$.

Theorem 4.1

Let I be a bounded continuous light signal perceived by a single cell. Assuming that $A(0) = 0$, then the temporal average dynamics growth rate $\overline{\mu}_A$ can be written as a function of the temporal average static growth rate $\overline{\mu}_S$ via

$$\overline{\mu}_A = \overline{\mu}_S + \overline{\mu}_H + \mathcal{O}(1/T), \tag{4.21}$$

where

$$\overline{\mu}_H \coloneqq \frac{1}{T} \int_0^T \frac{\mathrm{d}\mu_S(t)}{\mathrm{d}t} \phi(t) \mathrm{d}t, \tag{4.22}$$

with

$$\phi(t) \coloneqq \int_0^t e^{-\int_s^t \gamma(I(w))+k_r \mathrm{d}w} \mathrm{d}s, \tag{4.23}$$

and

$$\mathcal{O}(1/T) = -\frac{\mu_S(T)}{T} \int_0^T e^{-\int_s^T \gamma(I(w))+k_r \mathrm{d}w} \mathrm{d}s,$$

which goes to zero when $T \to +\infty$.

Interpretation of Theorem 4.1: In a system mainly laminar, where cells stay at a constant depth (or are slowly advected vertically), for which the dynamical component of the growth rate $\overline{\mu}_H$ is negligible, the average growth rate over a sufficiently long time period can be accurately computed using the static approximation $\overline{\mu}_S$ based on the Haldane model. In a system with high velocities in the direction of the light gradient, this approximation must be refined.

Proof. Using (4.9) and integration by parts, we find

$$\begin{aligned}
\int_0^T \mu_A(t)\mathrm{d}t &= \int_0^T \mu_S(t)(\gamma(I(t))+k_r)\int_0^t e^{-\int_s^t \gamma(I(w))+k_r\mathrm{d}w}\mathrm{d}s\mathrm{d}t \\
&= \int_0^T \int_s^T \mu_S(t)(\gamma(I(t))+k_r)e^{-\int_s^t \gamma(I(w))+k_r\mathrm{d}w}\mathrm{d}t\mathrm{d}s \\
&= -\int_0^T \int_s^T \mu_S(t)\frac{\mathrm{d}}{\mathrm{d}t}\left(e^{-\int_s^t \gamma(I(w))+k_r\mathrm{d}w}\right)\mathrm{d}t\mathrm{d}s \\
&= \int_0^T \mu_S(s) - \mu_S(T)e^{-\int_s^T \gamma(I(w))+k_r\mathrm{d}w}\mathrm{d}s \\
&\quad + \int_0^T \int_s^T \frac{\mathrm{d}}{\mathrm{d}t}(\mu_S(t))e^{-\int_s^t \gamma(I(w))+k_r\mathrm{d}w}\mathrm{d}t\mathrm{d}s.
\end{aligned}$$

Dividing by T we get (4.21). The integral

$$\phi(T) = \int_0^T e^{-\int_s^T \gamma(I(w))+k_r\mathrm{d}w}\mathrm{d}s,$$

can be upper bounded by

$$\phi(T) \leq \int_0^T e^{-(\gamma(I_{\min})+k_r)(T-s)}\mathrm{d}s = \frac{1-e^{-(\gamma(I_{\min})+k_r)T}}{\gamma(I_{\min})+k_r}, \tag{4.24}$$

and can be lower bounded by

$$\phi(T) \geq \int_0^T e^{-(\gamma(I_{\max})+k_r)(T-s)}\mathrm{d}s = \frac{1-e^{-(\gamma(I_{\max})+k_r)T}}{\gamma(I_{\max})+k_r}. \tag{4.25}$$

This reveals the fact that $\mathcal{O}(1/T) \to 0$ as $T \to \infty$. □

Note that

$$|\mathcal{O}(1/T)| \leq \frac{\mu_{\max}}{T}\frac{1}{\gamma(I_{\min})+k_r} \leq \frac{\mu_{\max}}{T}\frac{1}{k_r}.$$

Then, for $T \gg 1/k_r$, we can approximate $\overline{\mu}_A$ with

$$\overline{\mu}_A \approx \overline{\mu}_S + \overline{\mu}_H,$$

where $\overline{\mu}_H$ is defined in (4.22). The quantity $1/k_r$ corresponds to the time needed to go from the state C to B in the Han model, and $T \gg 1/k_r$ means that the period T must be large enough to incorporate the effect of the recovery.

4.3.1 A bound for the dynamic growth rate in the photobioreactor

To complete the numerical simulation, we discuss how the hydrodynamics of the raceway pond affects the actual growth rate $\overline{\overline{\mu}}_A$ in the following proposition.

Proposition 4.2

The space-time average dynamic growth rate can be bounded by the average velocity in the z-axis v_z as

$$\overline{\overline{\mu}}_A \leq \overline{\overline{\mu}}_S + \frac{\alpha\xi\sigma_P I_0}{k_r}\frac{1}{N_{par}}\sum_{n=1}^{N_{par}}\frac{1}{T}\int_0^T |v_z(t,\mathbf{X}_n)|dt + \frac{\mu_{\max}}{Tk_r}. \tag{4.26}$$

Proof. For each particle $\mathbf{X}_n$, with its respective light signal I_n, we have

$$\begin{aligned}
|\overline{\mu}_A(I_n)| &\leq \frac{1}{T}\int_0^T \left|\frac{d\mu_S(I_n(t))}{dt}\right| \phi(I_n(t))dt, \\
&= \frac{1}{T}\int_0^T \left|\frac{d\mu_S(I_n(t))}{dI_n}\frac{dI_n(t)}{dt}\right| \phi(I_n(t))dt.
\end{aligned}$$

The inequality in Equation (4.24) still holds here, then

$$\begin{aligned}
|\overline{\mu}_A(I_n)| &\leq \frac{1}{T}\int_0^T \left|\frac{d\mu_S(I_n(t))}{dI_n}\frac{dI_n(t)}{dt}\right| \frac{(1-e^{-(\gamma(I_{n,\min}+k_r)t})}{\gamma(I_{n,\min})+k_r}dt, \\
&\leq \frac{1}{T(\gamma(I_{n,\min})+k_r)}\int_0^T \left|\frac{d\mu_S(I_n(t))}{dI_n}\frac{dI_n(t)}{dt}\right| dt, \\
&\leq \frac{1}{Tk_r}\int_0^T \left|\frac{d\mu_S(I_n(t))}{dI_n}\frac{dI_n(t)}{dt}\right| dt,
\end{aligned}$$

where $I_{n,\min}$ is the minimum value of I_n in the interval $[0,T]$. Note that from the Beer-Lambert law, we have $\frac{d}{dt}I_n(t) = -\xi I_n v_z(t,\mathbf{X}_n)$, with v_z the velocity in the z-axis of the raceway pond. It follows that

$$|\overline{\mu}_A(I_n)| \leq \frac{\xi}{Tk_r}\int_0^T \left|\frac{d\mu_S(I_n(t))}{dI_n} I_n(t) v_z(t,\mathbf{X}_n)\right| dt.$$

Note that $\max_{I\geq 0}\frac{d}{dI}\mu_S(I) = \alpha\sigma_P$, and $I_n(t) \leq I_0$, then

$$|\overline{\mu}_A(I_n)| \leq \frac{\alpha\xi\sigma_P I_0}{Tk_r}\int_0^T |v_z(t,\mathbf{X}_n)|\, dt.$$

Using Equation (4.21):

$$\begin{aligned}
\overline{\overline{\mu}}_A &= \overline{\overline{\mu}}_S + \frac{1}{N_{par}}\sum_{n=1}^{N_{par}} \overline{\mu}_H(I_n) - \frac{\mu_S(I_n(t))}{T}\phi(I_n(t)), \\
&\leq \overline{\overline{\mu}}_S + \frac{1}{N_{par}}\sum_{n=1}^{N_{par}} |\overline{\mu}_H(I_n)| + \frac{\mu_S(I_n(t))}{T}\phi(I_n(t)), \\
&\leq \overline{\overline{\mu}}_S + \frac{1}{N_{par}}\sum_{n=1}^{N_{par}} \frac{\alpha\xi\sigma_P I_0}{Tk_r}\int_0^T |v_z(t,\mathbf{X}_n)|dt + \frac{\mu_{\max}}{Tk_r},
\end{aligned}$$

which proves the inequality (4.26). □

Interpretation of Proposition 4.2: We can ignore the term $\mu_{\max}/T$ in (4.26) as T is large enough. Then, the difference between the average growth rate $\overline{\overline{\mu}}_A$ and $\overline{\overline{\mu}}_S$ cannot be bigger than

$$\frac{\alpha\xi\sigma_P I_0}{k_r}\overline{|v_z|},$$

where

$$\overline{|v_z|} = \frac{1}{N_{par}}\sum_{n=1}^{N_{par}}\int_0^T |v_z(t,\mathbf{X}_n)|dt.$$

Here, $\overline{|v_z|}$ is an indicator of how mixed is the photobioreactor in the z-axis. Where a non-mixed photobioreactor will have $\overline{|v_z|} = 0$, showing no difference between $\overline{\overline{\mu}}_S$ and $\overline{\overline{\mu}}_A$. Also, the value of ξ plays an important role, where lower values of this parameter present less variations of the light gradient inside the reactor.

4.3.2 Periodic light signals

When the light signal is periodic, we can be more accurate in the results. Let T now be the period of the continuous light signal I perceived by the cell, we have the following result.

Proposition 4.3

Let I a continuous periodic function, i.e., $I(t+T) = I(t)\ \forall t \in [0,+\infty)$. Then, every solution of (4.8) converges to a unique periodic solution.

Proof. The periodic solution C_p is obtained by imposing $C_p(T) = C_p(0)$ in (4.11), and we find

$$C_p(0) = \frac{\int_0^T \gamma(I(s))e^{-\int_s^T \gamma(I(w))+k_r \mathrm{d}w}ds}{1-e^{-\int_0^T \gamma(I(w))+k_r \mathrm{d}w}}.$$

Let C be a solution of (4.8) and $\varepsilon = C - C_p$, we have

$$\dot{\varepsilon} = -(\gamma(I)+k_r)\varepsilon.$$

The solution is given by

$$\varepsilon(t) = \varepsilon(0)e^{-\int_0^t \gamma(I(s))\mathrm{d}s}e^{-k_r t},$$

which can be bounded by

$$|\varepsilon(t)| \leq |\varepsilon(0)|e^{-(\gamma(I_{\min})+k_r)t}.$$

Then ε goes to zero as $t \to \infty$. □

Proposition 4.4: Dynamic growth rate for periodic signal

Let us consider a continuous periodic light signal I of period T, i.e., $I(T) = I(0)$. Then the actual growth rate μ_A associated with the only periodic solution of C_p is given by:

$$\mu_A(t) = \mu_S(t)(\gamma(I(t))+k_r)\left[\phi(t) + \frac{\phi(T)O(T)}{1-O(T)}\right], \tag{4.27}$$

where ϕ is given by (4.23) and

$$O(T) = e^{-\int_0^T \gamma(I(w))+k_r \mathrm{d}w}.$$

Proof. From (4.12), we have

$$\mu_A(T) = \mu_S(T)(\gamma(I(t)) + k_r)\phi(T) + \mu_A(0)\frac{I(T)}{I(0)}\frac{1+\tau\sigma_P I(0)}{1+\tau\sigma_P I(T)}e^{-\int_0^T \gamma(I(w))+k_r \mathrm{d}w}.$$

As the function I is periodic, then $I(T) = I(0)$, and as $C_p(0) = C_p(T)$, the growth rate is also periodic, then imposing $\mu_A(T) = \mu_A(0)$, we can obtain its value as:

$$\mu_A(T) = \mu_S(T)(\gamma(I(t)) + k_r)\phi(T) + \mu_A(T)e^{-\int_0^T \gamma(I(w))+k_r \mathrm{d}w},$$

and finally

$$\mu_A(T) = \mu_S(T)\frac{(\gamma(I(t)) + k_r)\phi(T)}{1 - e^{-\int_0^T \gamma(I(w))+k_r \mathrm{d}w}}.$$

□

In the same way we can compute the temporal average dynamic growth rate in the periodic case.

Theorem 4.2: Average growth rate in the periodic case

Considering a periodic light signal I of period T. The temporal average dynamic growth rate $\overline{\mu}_A$ is given by:

$$\overline{\mu}_A = \overline{\mu}_S + \frac{1}{1-O(T)}\left[\overline{\mu}_H + \frac{O(T)}{T}\int_0^T \phi(T) - \phi(t)\mathrm{d}t\right]. \tag{4.28}$$

Interpretation of Theorem 4.2: this theorem clarifies the results of 4.1, and better characterizes the dynamical component of the growth rate $\overline{\mu}_H$ which must be added to the static approximation $\overline{\mu}_S$ when the velocities along the light gradient are marked.

Proof. The proof follows the same steps as in theorem 4.1 using the dynamic growth rate computed in the periodic case (4.27). □

Note that, when T is large enough, meaning that $T \gg 1/k_r$, $O(T) \to 0$, leading again to the same approximation in the non-periodic case, i.e., $\overline{\mu}_A \approx \overline{\mu}_S + \overline{\mu}_H$.

Characterization of the dynamical component $\overline{\mu}_H$ as a function of the light regime

We have already seen that the average dynamic growth rate can be approximated by $\overline{\mu}_S \approx \overline{\mu}_S + \overline{\mu}_H$, and we present two numerical examples where $\overline{\mu}_H + \mathcal{O}(1/T)$ goes to zero as the period of these periodical signals goes to $+\infty$, which means that $\overline{\mu}_S$ becomes an accurate approximation for longer periods. In this section, we will estimate a lower and upper bound of $\overline{\mu}_H$ to understand its relation with the speed of the light signal I.

Proposition 4.5

Let $I : [0, T] \to [0, +\infty)$ be a light signal of class $\mathcal{C}^1$, such that $I_{\min} \leq I(t) \leq I_{\max}\ \forall t \in [0, T]$. Let assume that all the stationary points of the function $t \mapsto \mu_S(I(t))$ are isolated. If $\{t_i\}_{i=0}^m$ denotes the partition of $[0, T]$ where, $t_0 = 0$, $t_m = T$, and $\frac{d\mu_S(I(t_i))}{dt} = 0$, then

$$-\frac{\mu_{\max}}{T}\frac{|\mathcal{I}_-|}{\gamma(I_{\max}) + k_r} \leq \overline{\mu}_H \leq \frac{\mu_{\max}}{T}\frac{|\mathcal{I}_+|}{\gamma(I_{\min}) + k_r},$$

where $|\mathcal{I}_+|$ and $|\mathcal{I}_-|$ are the cardinality of the sets:

$$\mathcal{I}_+ := \left\{ i : \frac{\mathrm{d}\mu_S(I(t))}{\mathrm{d}t} > 0\ \forall t \in (t_i, t_{i+i}) \right\},$$
$$\mathcal{I}_- := \left\{ i : \frac{\mathrm{d}\mu_S(I(t))}{\mathrm{d}t} < 0\ \forall t \in (t_i, t_{i+i}) \right\}.$$

Proof. According to this definition, $\overline{\mu}_H$ can be decomposed into a positive part and a negative part as

$$\overline{\mu}_H = \overline{\mu}_H^+ + \overline{\mu}_H^-,$$

where

$$\overline{\mu}_H^+ := \frac{1}{T}\sum_{i \in \mathcal{I}_+} \int_{t_i}^{t_{i+1}} \frac{\mathrm{d}\mu_S(t)}{\mathrm{d}t}\phi(t)\mathrm{d}t, \tag{4.29}$$

$$\overline{\mu}_H^- := \frac{1}{T}\sum_{i \in \mathcal{I}_-} \int_{t_i}^{t_{i+1}} \frac{\mathrm{d}\mu_S(t)}{\mathrm{d}t}\phi(t)\mathrm{d}t. \tag{4.30}$$

Now, we can give an upper bound for the positive part $\overline{\mu}_H^+$ using (4.24)

$$\begin{aligned}\overline{\mu}_H^+ &= \frac{1}{T}\sum_{i\in\mathcal{I}_+}\int_{t_i}^{t_{i+1}}\frac{\mathrm{d}\mu_S(t)}{\mathrm{d}t}\phi(t)\mathrm{d}t,\\ &\leq \frac{1}{T}\frac{1}{\gamma(I_{\min})+k_r}\sum_{i\in\mathcal{I}_+}\int_{t_i}^{t_{i+1}}\frac{\mathrm{d}\mu_S(t)}{\mathrm{d}t}\mathrm{d}t,\\ &= \frac{1}{T}\frac{1}{\gamma(I_{\min})+k_r}\sum_{i\in\mathcal{I}_+}\mu_S(t_{i+1})-\mu_S(t_i).\end{aligned}$$

In the same way, we can give a lower bound for the negative part using (4.25):

$$\begin{aligned}\overline{\mu}_H^- &= \frac{1}{T}\sum_{i\in\mathcal{I}_-}\int_{t_i}^{t_{i+1}}\frac{\mathrm{d}\mu_S(t)}{\mathrm{d}t}\phi(t)\mathrm{d}t,\\ &\geq \frac{1}{T}\frac{1}{\gamma(I_{\max})+k_r}\sum_{i\in\mathcal{I}_-}\int_{t_i}^{t_{i+1}}\frac{\mathrm{d}\mu_S(t)}{\mathrm{d}t}\mathrm{d}t,\\ &= \frac{1}{T}\frac{1}{\gamma(I_{\max})+k_r}\sum_{i\in\mathcal{I}_-}\mu_S(t_{i+1})-\mu_S(t_i).\end{aligned}$$

Note that $\overline{\mu}_H^- \leq \overline{\mu}_H \leq \overline{\mu}_H^+$, due to the sign of each term. Then, using the lower bound of $\overline{\mu}_H^-$ and the upper bound of $\overline{\mu}_H^+$, we find:

$$\frac{1}{T}\frac{\sum_{i\in\mathcal{I}_-}\mu_S(t_{i+1})-\mu_S(t_i)}{\gamma(I_{\max})+k_r} \leq \overline{\mu}_H \leq \frac{1}{T}\frac{\sum_{i\in\mathcal{I}_+}\mu_S(t_{i+1})-\mu_S(t_i)}{\gamma(I_{\min})+k_r}.$$

Then, as $\mu_S(t_{i+1})-\mu_S(t_i)\leq\mu_{\max}$, we have

$$-\frac{1}{T}\frac{\sum_{i\in\mathcal{I}_-}\mu_{\max}}{\gamma(I_{\max})+k_r} \leq \overline{\mu}_H \leq \frac{1}{T}\frac{\sum_{i\in\mathcal{I}_+}\mu_{\max}}{\gamma(I_{\min})+k_r}.$$

□

Interpretation of Proposition 4.5. When a particle moves inside a photobioreactor that is constantly mixed, it will not stay in the same position and, therefore, the amount of light it perceives cannot be constant in any interval, so the function I cannot be constant in any interval, so the function $t \to\mapsto \mu_S(I(t))$ will only have isolated stationary points. The value of $\overline{\mu}_H$ is bounded by the number of times that the derivative of $\mu_S(I(t))$ changes sign. If I is a periodical function as the ones analyzed in the Section 4.3.2, the two sums

$$\sum_{i\in\mathcal{I}_+}\mu(t_{i+1})-\mu(t_i), \text{ and } \sum_{i\in\mathcal{I}_-}\mu(t_{i+1})-\mu(t_i),$$

are independent of T. If $T\to+\infty$, then $\overline{\mu}_H$ converges to 0.

A lower bound of $\overline{\mu}_H$

If we could choose the trajectory of a microalgae, we would like to choose the one that can maximize the value of $\overline{\mu}_H$. So, the question is which type of signals provide a higher value of $\overline{\mu}_H$. To give and insight of this, we give a lower bound for $\overline{\mu}_H^+$:

$$\begin{aligned}
\overline{\mu}_H^+ &= \frac{1}{T}\sum_{i\in\mathcal{I}_+}\int_{t_i}^{t_{i+1}}\frac{d\mu_S(I(t))}{dt}\int_0^t e^{-\int_s^t \gamma(I(w))+k_r dw}dsdt \\
\overline{\mu}_H^+ &\geq \frac{1}{T}\sum_{i\in\mathcal{I}_+}\int_{t_i}^{t_{i+1}}\frac{d\mu_S(I(t))}{dt}\int_0^{t_i} e^{-\int_s^{t_{i+1}} \gamma(I(w))+k_r dw}dsdt, \\
\overline{\mu}_H^+ &\geq \frac{1}{T}\sum_{i\in\mathcal{I}_+}\int_{t_i}^{t_{i+1}}\frac{d\mu_S(I(t))}{dt}\int_0^{t_i} e^{-(\gamma(I_{\max}))+k_r)(t_{i+1}-s)}dsdt, \\
\overline{\mu}_H^+ &\geq \frac{1}{T}\sum_{i\in\mathcal{I}_+}\frac{\delta_i}{\gamma(I_{\max})+k_r}(\mu_S(I(t_{i+1}))-\mu_S(I(t_i))),
\end{aligned} \tag{4.31}$$

where

$$\delta_i = e^{-(\gamma(I_{\max})+k_r)(t_{i+1}-t_i)}(1-e^{-(\gamma(I_{\max})+k_r)t_i}).$$

Increasing the value of $\overline{\mu}_H^+$, increases the value of $\overline{\mu}_A$. To increase the value of $\overline{\mu}_H^+$, we can look at the value of $\delta_i(\mu_S(I(t_{i+1}))-\mu_S(I(t_i)))$. The value of δ_i is larger when the time interval (t_{i+1}, t_i) is small. Then, each short interval where the value $\mu_S(I(t_i))$ moves to a higher value $\mu_S(I(t_{i+1}))$ helps to increase the value of $\overline{\mu}_H^+$, and consequently, $\overline{\mu}_A$.

4.4 Numerical simulations

4.4.1 Two periodic examples

For the numerical test, we chose the parameter values of the Han model from [61] as shown in Table 4.1. To illustrate the behavior of the dynamic growth rate, and specifically to compare it

Parameter	Value	Unit
k_r	$6.8\cdot10^{-3}$	s^{-1}
k_d	$2.99\cdot10^{-4}$	-
τ	0.25	s
σ_P	0.047	$m^2\mu mol^{-1}$
α	$8.7\cdot10^{-6}$	-

Table 4.1: Parameter values of the Han model.

with the static one, we consider two examples of periodic light signals. First, we consider the simple periodic function for the depth of a cell

$$z(t) = \frac{H_0}{2}\left(1+\sin\left(\frac{2\pi}{T}t\right)\right). \tag{4.32}$$

The light signal, using the Beer-Lambert law, corresponds to $I(t) = I_0 e^{-\xi z(t)}$ and the static growth rate is $\mu_S(t) = \mu_S(I(t))$. In this case, the value of $\overline{\mu}_S$ is independent of T, by doing the change of variable $s = t/T$, we have

$$\overline{\mu}_S = \frac{1}{T}\int_0^T \mu_S(I(t))\mathrm{d}t = \int_0^1 \frac{\alpha\sigma_P I_0 e^{-\xi z(s)}}{1+\tau\sigma_P I_0 e^{-\xi z(s)} + \frac{k_d}{k_r}\tau\left(\sigma_P I_0 e^{-\xi z(s)}\right)^2}\mathrm{d}s.$$

In Figure 4.4a, μ_A is illustrated the periodic solution given by (4.27)As expected, for T large enough, the difference $\overline{\mu}_A - \overline{\mu}_S$ can be approximated by $\overline{\mu}_H$. Numerically, the term $\overline{\mu}_H$, is close to zero. In fact, the difference in percentage, computed as

$$\text{Difference in } \% = 100 \cdot \frac{\overline{\mu}_A - \overline{\mu}_S}{\overline{\mu}_S},$$

is lower than 2% as illustrated in Figure 4.4b. As shown in the same figure, $\overline{\mu}_A$ is always greater than $\overline{\mu}_S$ and the difference between them becomes small as T increases. When the light dynamics becomes slower, the approximation $\overline{\mu}_A \approx \overline{\mu}_S$ becomes more and more excellent. This gain is not always true, as shown in the second example.

For the second example, let us consider the function

$$z(t) = H_0 - 4H_0 \frac{e^{-\left(\sin\left(\frac{2\pi t}{T}\right)-\frac{1}{2}\right)}}{\left(1+e^{-\left(\sin\left(\frac{2\pi t}{T}\right)-\frac{1}{2}\right)}\right)^2}, \tag{4.33}$$

which has a period T. By doing the same change of variable as before, the temporal average static growth rate is independent of T. This function describes a movement closer to the surface and does not travel to the deepest part of the culture as in the previous example. Figure 4.5b shows the convergence of $\overline{\mu}_A$ to $\overline{\mu}_S$ as T goes to ∞. The difference between $\overline{\mu}_S$ and $\overline{\mu}_A$ in percentage is higger than the previous case. Also, the value of $\overline{\mu}_A$ is always lower than the value of $\overline{\mu}_S$.

In both examples, μ_A converges to μ_S (see Figure 4.4a and Figure 4.5a). We can see a difference when the value of T is lower than 1500. In this range, we can say that, a strong mixing in the first example promotes growth, where, the second example can represent a poor mixing.

4.4.2 The raceway case

We simulate 8 different conditions by changing the velocity of the paddle wheel for a simulated time of one hour. The initial positions of the particles (x_{n0}, y_{n0}, z_{n0}) are randomly generated following an independent uniform distribution $x_{n0} \sim \mathcal{U}_{[x_{\min}, x_{\max}]}$, $y_{n0} \sim \mathcal{U}_{[y_{\min}, y_{\max}]}$, $z_{n0} \sim \mathcal{U}_{[z_{\min}, z_{\max}]}$, where the volume

$$B = [x_{\min}, x_{\max}] \times [y_{\min}, y_{\max}] \times [z_{\min}, z_{\max}],$$

is such that $\Omega \subset B$, then we ignore the particles outside the domain Ω of the raceway pond. Due to this process, the simulations made have a different number of simulated particles N_{par}. Table 4.2 shows the number of simulated particles for each simulation and also the total time of CPU used. The software Freshkiss3D solve the Equation (4.15) at the same time it tracks the particles solving Equation (4.17). Experiments were run on a computer with an Intel Xeon w-2223 processor running at 1200 MHz with a total of 15677 MB of RAM, using Fedora version 39.

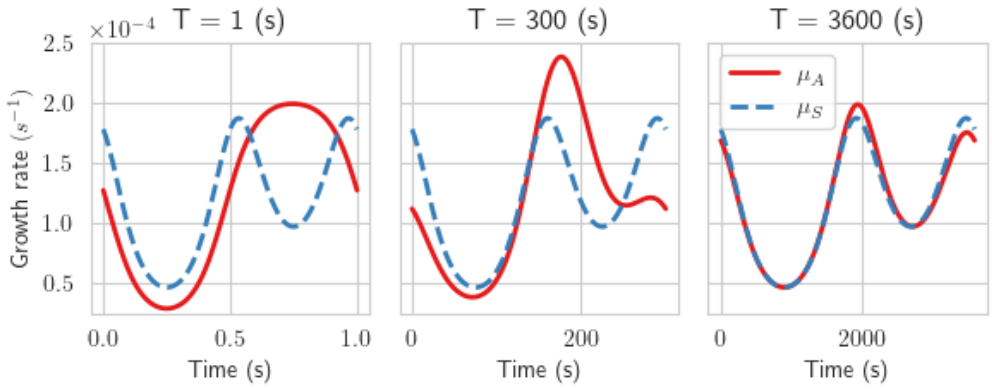

(a) Periodic solution of the actual growth rate μ_A (continuous red line) when the light signal is given by the depth following the function (4.32) and the approximation with the static growth rate (blue dashed line) for three different values of T.

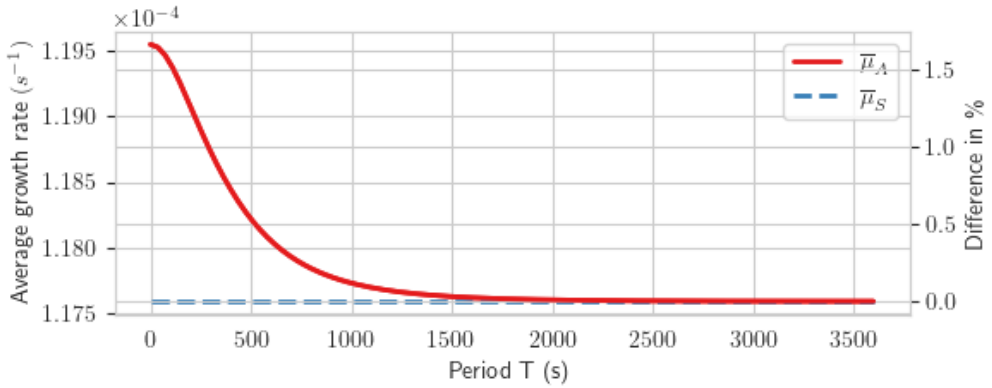

(b) Actual growth rate (continuous red line) and the approximation with the average static growth rate (dashed blue line) for different values of T. The right axis shows the percentage difference.

Figure 4.4: Dynamic and static growth rate of the light signal taking from (4.32).

4.4.3 Correction of the cell distribution

The particles needed to compute $\overline{\overline{\mu}}_A$ and $\overline{\overline{\mu}}_S$ should be representative of the entire raceway pond, this means that the distribution should be uniform, at least on the z-axis. At the beginning, the uniform distribution is imposed, but after some time of simulation, due to error accumulation in a periodic domain, the distribution of the particles change. It follows that the space-time average dynamic growth rate is not representative anymore. To tackle this problem, more particles could be simulated, but this solution is very CPU demanding and time-consuming. Another approach consists in correcting the particle's distribution at each time, to have a set of particles that perma-

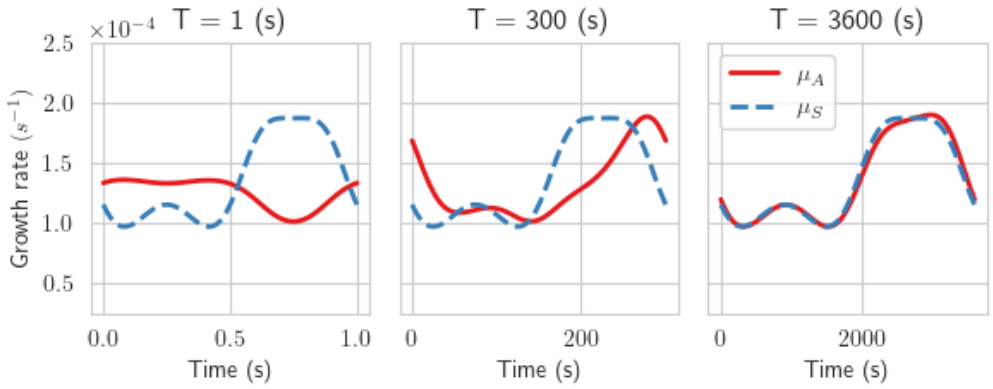

(a) The periodic solution of the dynamic growth rate μ_A (continuous red line) when the light signal is given by the depth described by (4.33) and the static growth rate (blue dashed line) for three different values of T.

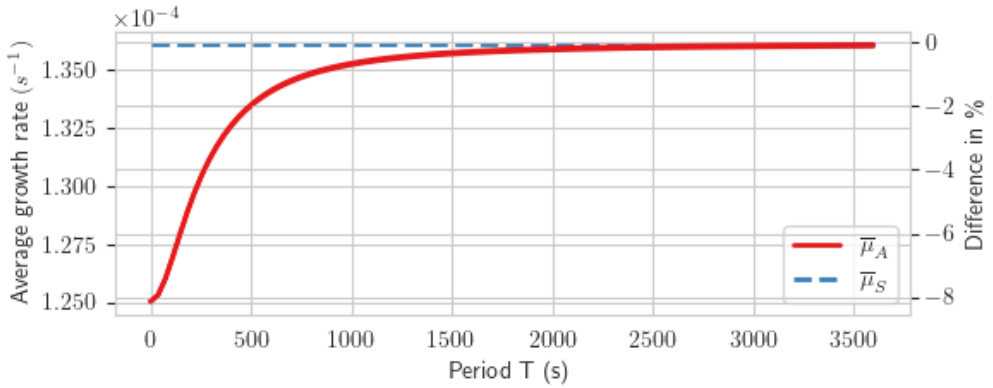

(b) Average dynamic growth rate (continuous red line) and the average static growth rate (dashed blue line) for different values of T. The right axis shows the percentage difference.

Figure 4.5: Dynamic and static growth rate of the trajectory given by (4.33).

nently represent an actual distribution. The weighted averages can then be defined as:

$$\overline{\overline{\mu}}_A^w = \frac{1}{T}\int_0^T \frac{\sum_{n=1}^{N_{par}} \frac{\mu_A(I_n(t))}{h(t)}}{\sum_{n=1}^{N_{par}} \frac{1}{h(t)}} dt,$$

and

$$\overline{\overline{\mu}}_S^w = \frac{1}{T}\int_0^T \frac{\sum_{n=1}^{N_{par}} \frac{\mu_S(I_n(t))}{h(t)}}{\sum_{n=1}^{N_{par}} \frac{1}{h(t)}} dt,$$

for $\overline{\overline{\mu}}_A$ and $\overline{\overline{\mu}}_S$ respectively. Here $h(t)$ is the probability density function of the depth of the particles at the instant t. If the free surface is perfectly flat with depth H_0, we have that $h_n(0) = 1/H_0$ by

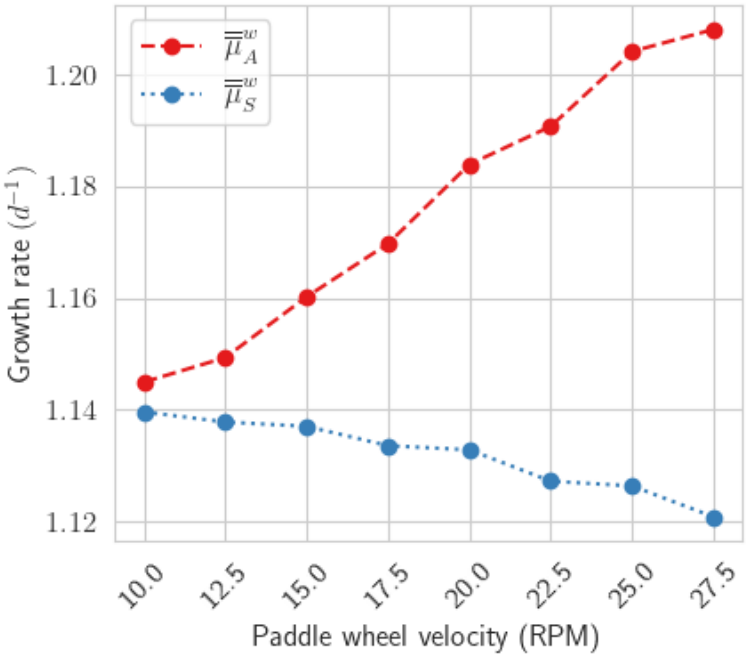

Figure 4.6: For 8 different velocities of the paddle wheel, the estimated actual average growth rate $\overline{\overline{\mu}}^w_A$ (segmented red line), and the weighted space-time static growth rate $\overline{\overline{\mu}}^w_S$ (segmented blue line). The hydrodynamics is simulated for 1 hour. The values of N_{par} are different for each simulation, and they are shown in Table 4.2. The average height of the water is $H_0 = 0.3(m)$.

construction, and we recover the expression (4.19) and (4.20).

Figure 4.6 shows the computation of $\overline{\mu}_\Omega$, $\overline{\overline{\mu}}^w_A$, and $\overline{\overline{\mu}}^w_A$. When the particle number N_{par} is large enough, the space-time average static growth rate defined in Equation (4.20) converges to the volume average growth rate in the sense that

$$\lim_{N_{par}\to\infty} \frac{1}{N_{par}} \sum_{n=1}^{N_{par}} \overline{\mu}_S(I_n) = \overline{\mu}_\Omega, \tag{4.34}$$

when the fluid is incompressible [144]. Numerical simulations do not show a noticeable difference in the height of the waves formed on the free surface. As, the volume average growth rate depends only on the shape of the photobioreactor, or in the case of the raceway pond, the shape of the free surface and the volume that it defines. Then two raceway ponds with equivalent shape lead to the same average growth rate, which is completely determined by the incident light intensity and the optical depth [90, Theorem 3]. In this sense, the average static growth rate $\overline{\overline{\mu}}_S$ does not take into account the effect of the hydrodynamics. This effect can be seen in Figure 4.6, where the corrected average have a small variation (1.1395 d^{-1} for 10 RPM and 1.12080 d^{-1} for 27.5 PRM).

RPM	N_{par}	Total simulation time (hrs)
10	3094	714.8
12.5	3057	620.4
15	3064	742.2
17.5	3073	663.1
20	3064	779.3
22.5	3034	695.1
25	3034	810.5
27.5	3048	730.4

Table 4.2: Number of simulated particles and total CPU time simulation for each experience.

4.5 Conclusions

We present a numerical method to calculate the average growth rate in a photobioreactor, accounting for hydrodynamics. The starting point is the Han model, which takes into account the light history of the microalgae. This model coupled with the hydrodynamics can capture the influence of the mixing device. To better understand the effect that mixing can have on growth, we illustrate with two simple periodic functions; the first one increases the actual growth rate compared to the static value, and the second one shows the opposite trend.

We implement the light harvesting model in the light field generated by the hydrodynamics of the raceway pond. Since the computational cost is very high for simulating reactor hydrodynamics and tracking the particles to compute the average growth rate, we present an alternative way to compute this growth rate, correcting the distribution in the depth of the particles to have a better representation of the raceway pond.

The computations made in the case of the raceway can be adjusted to other types of reactors. For example, the relationship between the actual growth rate and the velocity in the z-axis of the raceway can be transposed to other photobioreactors, depending on the distribution of light inside the reactor. It can even be used to optimise the reactor geometry, to better benefit from this dynamical effect.

Not all models are able to capture the effect of hydrodynamics, and extending a model to do so it is not straightforward. In this study, we propose a way to take into account the hydrodynamics where we conclude that a better mixing of the photobioreactor, in the raceway pond case, increases the productivity of the photobioreactor. The answer to whether or not hydrodynamics should be considered among the factors affecting microalgae growth has no single answer, since it will depend on the geometry of the photobioreactor and the light distribution inside it. However, in this chapter, we present upper and lower bounds on the growth function that may be useful in determining when hydrodynamics should be considered.

Part II

Optimal control problems in photobioreactors

Chapter 5

Optimal control of microalgae culture accounting for photoinhibition and light attenuation

This chapter reproduces [52] presented at the 22nd IFAC World Congress, Yokohama, Japan. The introduction presented here differs from the published article.

Abstract

In a photobioreactor, due to the gradient of light, microalgae are successively exposed to conditions of low and high (inhibiting) light. This phenomenon can be captured by the Han model, which is a common mechanistic model of photoinhibition. Based on Han's description, we introduce a dynamic system of microalgae growth involving two control variables: the light intensity and the dilution rate of the reactor. This model is derived from slow/fast dynamic considerations in a chemostat system accounting for the light gradient due to absorption and scattering following the Lambert-Beer's law. Then, we formulate and study an optimal control problem in order to fully-characterize the optimal light supply and dilution strategies that maximize the harvested biomass. Our study, mainly based on Pontryagin's maximum principle (PMP), shows that singular arcs and *turnpike*-like behaviors appear in the optimal solution. In particular, we prove that the optimal strategy maintains the biomass at a constant level along singular arcs, and we determine its static value. The theoretical results are illustrated throughout this paper using a direct optimization method.

5.1 Introduction

Pontryagin's maximum principle (PMP, [114]) provides powerful tools to address the optimal control problems encountered in biotechnology, and turns out to be highly effective in solving optimization and control problems in photobioreactors [11, 41, 87]. In several cases, it has been

reported that the optimal solutions associated to these OCPs often exhibit a *turnpike*-like behaviour when the operation time is large enough (see, *e.g.*, [27, 44]). Generally speaking, the *turnpike* feature states that the optimal solutions approach a static behaviour or stay close to a steady-state most of the time [146, 115]. We formulate and analyse an optimal control problem with two states: the concentration of the microalgae culture inside a photobioreactor and the fraction of photoinhibited photosystems of the cells. Two controls are considered: the light intensity and the dilution rate of the bioreactor. The dynamic system is based on the reduction of the Han model presented in the Chapters 3 and 4.

This chapter is organized as follows. In Section 5.2 we introduce the biological model describing the evolution of the biomass in the photobioreactor. In Section 5.3, we state the optimal control problem (OCP) of interest. In Sections 5.4-5.5, we derive some properties of the optimal solution of the studied OCP, then we state our main result: the bioreactor must be operated at constant biomass describing turnpike properties. Next, in Section 5.6, we determine the value of the optimal biomass. Finally, in Section 5.7, we illustrate our results using direct optimization methods (implemented in `BOCOP`: optimal control solver).

5.2 Mathematical model

5.2.1 The reduced Han model for photobioreactors

We consider a photobioreactor in continuous mode operation. The biomass concentration of microalgae x (mgL^{-1}) evolves following the equation:

$$\dot{x} = \mu x - Rx - Dx, \tag{5.1}$$

where R (s^{-1}) is the specific maintenance rate [21], D (s^{-1}) is the dilution rate of the reactor (ratio of the influent flow rate over the volume of the reactor). The growth rate $\mu(s^{-1})$ is derived from the reduced Han model [53, 66, 68] as follows. Let us denote c (dimensionless) the fraction of photosynthetic units that are damaged due to excess of light on the photobioreactor and I_x ($\mu\text{mol}^{-1} \cdot m^{-1} \cdot s^{-1}$) the irradiance perceived by the culture, the dynamics of c can be derived from the Han model as,

$$\dot{c} = \frac{k_d \tau (\sigma I_x)^2}{1 + \tau \sigma I_x}(1 - c) - k_r c. \tag{5.2}$$

Here σ corresponds to the effective cross-section, τ is called turnover time (time needed to harvest one photon), k_d and k_r are the damage and repair rate respectively. The growth rate is then computed as [53],

$$\mu = \frac{K \sigma I_x (1 - c)}{1 + \tau \sigma I_x}. \tag{5.3}$$

5.2.2 Light attenuation due to biomass

Light availability decreases in the photobioreactor due to the self-shading and the light absorption of the chlorophyll content of the microalgae. We differentiate the irradiance that is applied to the culture, denoted by I ($\mu\text{mol}^{-1} \cdot m^{-1} \cdot s^{-1}$), which can be controlled, and the irradiance perceived by the culture I_x which affects the evolution of the state c. The perceived irradiance

I_x (μmol$^{-1} \cdot m^{-1} \cdot s^{-1}$) follows the Beer-Lambert law,

$$I_x = Ie^{-\xi x}, \tag{5.4}$$

where ξ (mg$^{-1}\cdot$L) is a coefficient derived from the light extinction rate and from the photobioreactor depth.

5.3 Statement of the optimal control problem

We define the *total biomass harvested* over the time window $[0, T_f]$ by,

$$J_{[0,T_f]}(D, I) = \int_0^{T_f} x(t)D(t)dt, \tag{5.5}$$

where x is the solution of the equation (5.1), here the controls are the irradiance I and the dilution rate D. The sets of admissible controls $\mathcal{D}$ and $\mathcal{I}$ are defined as,

$$\begin{aligned} \mathcal{D} &:= \{D : [0, +\infty) \to [0, D_{\max}] \ \ ; \ \ D(\cdot) \in \mathcal{L}^\infty_{loc}(\mathbb{R}_+)\}, \\ \mathcal{I} &:= \{I : [0, +\infty) \to [0, I_{\max}] \ \ ; \ \ I(\cdot) \in \mathcal{L}^\infty_{loc}(\mathbb{R}_+)\}, \end{aligned} \tag{5.6}$$

where $\mathcal{L}^\infty_{loc}(\mathbb{R}_+)$ is the space of locally integrable functions on every compact on $\mathbb{R}_+$, $D_{\max} > 0$ is the maximum dilution rate given by the pump feeding capacity and $I_{\max}$ is the maximum light intensity that can be applied.

For admissible non-negative initial conditions, we seek admissible controls, $D \in \mathcal{D}$ and $I \in \mathcal{I}$, over a fixed time window $[0, T_f]$, that maximize the harvested biomass. Thus, the optimal control problem of interest reads as follows,

$$\begin{aligned} \max_{\substack{D\in\mathcal{D},\\ I\in\mathcal{I}.}} \quad & J_{[0,T_f]}(D, I) = \int_0^{T_f} x(t)D(t)dt, \\ \text{s.t.} \quad & \dot{x} = \frac{K\sigma I_x(1-c)}{1+\tau\sigma I_x}x - Dx - Rx, \\ & \dot{c} = \frac{k_d\tau(\sigma I_x)^2}{1+\tau\sigma I_x}(1-c) - k_r c, \end{aligned} \tag{OCP}$$

5.4 Necessary conditions on optimal controls

We apply the Pontryagin's Maximum Principle (PMP), [149, 33, 71, 145]) to derive necessary conditions satisfied by the optimal controls in (OCP). Let us denote by $X = (x, c)$ and $\lambda = (\lambda_x, \lambda_c)$ respectively the state and adjoint variables. Then, the Hamiltonian, $H(X, \lambda, D, I)$, associated with (OCP) is defined by,

$$H(X, \lambda, \lambda_0, D, I) = \lambda^T \dot{X} + \lambda_0 xD.$$

We note that the Hamiltonian is linear w.r.t. the control D, then we rewrite,

$$H(X, \lambda, \lambda_0, D, I) = \Psi(X, \lambda, I) + \varphi(X, \lambda)D + \tilde{\varphi}(X, \lambda), \tag{5.7}$$

where,

$$\Psi(X,\lambda,I) = \frac{K\sigma I_x(1-c)}{1+\tau\sigma I_x}\lambda_x x + \frac{k_d\tau(\sigma I_x)^2(1-c)}{1+\tau\sigma I_x}\lambda_c, \tag{5.8}$$

$$\varphi(X,\lambda) = [-\lambda_x + \lambda_0]x, \tag{5.9}$$

$$\tilde{\varphi}(X,\lambda) = -R\lambda_x x - k_r\lambda_c c. \tag{5.10}$$

The function φ is the so-called switching function w.r.t. the control D. Since (OCP) is stated as a maximization problem, we fix $\lambda_0 = 1$, assuming that the extremals are normal. Pontryagin's Maximum Principle states that if (X, D, I) is optimal, then the absolutely-continuous adjoint state $\lambda = (\lambda_x, \lambda_c)$, satisfies,

$$\dot{\lambda}_x = -\partial H/\partial x, \quad \dot{\lambda}_c = -\partial H/\partial c.$$

Therefore, it follows that,

$$\begin{cases} \dot{\lambda}_x = \lambda_x\left[\mu\left(\dfrac{\xi x}{1+\tau\sigma I_x} - 1\right) + (D+R)\right] - D + \lambda_c\dfrac{k_d\xi\mu\tau\sigma I_x(2+\tau\sigma I_x)}{K(1+\tau\sigma I_x)}, \\ \dot{\lambda}_c = \lambda_x\dfrac{K\sigma I_x}{1+\tau\sigma I_x}x + \lambda_c\left[\dfrac{k_d\tau(\sigma I_x)^2}{1+\tau\sigma I_x} + k_r\right]. \end{cases} \tag{5.11}$$

In (OCP), the final conditions $x(T_f)$ and $c(T_f)$ are free. Therefore, the transversality conditions are given by,

$$\lambda_x(T_f) = 0, \quad \lambda_c(T_f) = 0. \tag{5.12}$$

5.4.1 The PMP maximization condition

The Pontryagin's principle states that the controls D and I satisfy, for almost all $t \in [0, T_f]$, the maximization condition,

$$(D(t), I(t)) \in \underset{\substack{u\in[0,D_{\max}],\\ v\in[0,I_{\max}].}}{\operatorname{argmax}} H(X(t), \lambda(t), \lambda_0, u, v) \tag{5.13}$$

In addition, as the augmented system is *autonomous*, then $H(X, \lambda, \lambda_0, D, I)$ is constant along the optimal trajectories, *i.e.*, for almost all $t \in [0, T_f]$:

$$\frac{d}{dt}H(X(t), \lambda(t), \lambda_0, D(t), I(t)) = 0 \tag{5.14}$$

Using (5.7)-(5.10), we readily deduce (since Ψ and $\tilde{\varphi}$ do not depend on D, and φ and $\tilde{\varphi}$ do not depend on I) that the PMP maximization condition (5.13) leads to the following result.

Proposition 5.1

Let $T_f > 0$ be a fixed final time horizon. Then, for almost all $t \in [0, T_f]$, we get,
i) the optimal control $D(t)$ satisfies,

$$D(t) = \begin{cases} 0, & \text{if} \quad \lambda_x > 1, \\ D_{\max}, & \text{if} \quad \lambda_x < 1, \\ D_s(t), & \text{if} \quad \lambda_x(t) = 1, \end{cases} \tag{5.15}$$

ii) the optimal control $I(t)$ satisfies,

$$I(t) = \begin{cases} I_{\max} & \text{if } \lambda_c > \frac{-\lambda_x x K}{k_d \tau \sigma I_x^{\max}(2+\tau\sigma I_x^{\max})}, \\ I_s(t) & \text{otherwise,} \end{cases} \tag{5.16}$$

where we denote $I_x^{\max} = I_{\max} e^{-\xi x}$, D_s is the so-called singular arc control (when its associated switching function φ is zero), and I_s is given by,

$$I_s(t) = \frac{-1 + \sqrt{1 - \frac{\lambda_x(t) x(t) K}{\lambda_c(t) k_d}}}{\tau \sigma e^{-\xi x(t)}}. \tag{5.17}$$

Proof. As (5.7) holds, finding the optimal light I in (5.13) is equivalent to solve the problem for almost every $t \in [0, T_f]$,

$$I(t) \in \underset{0 \le I \le I_{\max}}{\operatorname{argmax}} \ \Psi(X, \lambda, I), \tag{5.18}$$

where Ψ is defined in (5.8). For fixed $t \in [0, T_f]$, we define the Lagrangian associated to the problem (5.18) as,

$$\mathcal{L}(I, \theta) = \Psi(X, \lambda, I) + \theta(I_{\max} - I). \tag{5.19}$$

where if (I^*, θ^*) is a saddle point of $\mathcal{L}$ with $\theta^* \ge 0$ then I^* is optimal for the problem (5.18). This condition is equivalent to the KKT conditions,

$$\frac{\partial \Psi(X, \lambda, I)}{\partial I} - \theta = 0, \tag{5.20}$$

$$\theta(I_{\max} - I) = 0, \tag{5.21}$$

$$\theta \ge 0. \tag{5.22}$$

Condition (5.20) gives,

$$\frac{\lambda_x x \mu}{1 + \tau\sigma I_x} + \frac{\lambda_c k_d \tau \sigma I_x \mu (2 + \tau \sigma I_x)}{K(1 + \tau \sigma I_x)} - \theta = 0.$$

As (5.22) holds, we deduce that,

$$\begin{aligned} \frac{\lambda_c k_d \tau \mu \sigma I_x (2 + \tau\sigma I_x)}{K(1 + \tau\sigma I_x)} &\ge -\frac{\lambda_x x \mu}{1 + \tau \sigma I_x}, \\ \lambda_c &\ge -\frac{\lambda_x x K}{k_d \tau \sigma I_x (2 + \tau \sigma I_x)}, \end{aligned} \tag{5.23}$$

where the equality holds if and only if $I < I_{\max}$, and the optimal light is given by,

$$(1 + \tau\sigma I_x)^2 - 1 = -\frac{\lambda_x x K}{\lambda_c k_d}.$$

As $(1 + \tau\sigma I_x)$ is always positive, it follows that,

$$\tau \sigma I_x = -1 + \sqrt{1 - \frac{\lambda_x x K}{\lambda_c k_d}}. \tag{5.24}$$

On the other hand, $I = I_{\max}$ if and only if the inequality in (5.23) is strict due to conditions (5.21) and (5.22). For the dilution-control, we use the same argument, since D maximizes the function,

$$\varphi(X, \lambda)D = (-\lambda_x + 1)D, \tag{5.25}$$

and since it is linear in D, we deduce that $D = 0$ if $-\lambda_x + 1 < 0$ and $D = D_{\max}$ if $-\lambda_x - 1 > 0$. Next, when $-\lambda_x + 1 = 0$ (over a specific time interval $[t_1, t_2]$, where $t_2 > t_1$), we write $D(t) = D_s(t)$, $t \in [t_1, t_2]$, D_s is the singular control arc that may appear in the structure of the optimal control D. □

From *Proposition 5.1*, we can assert that the optimal control over $[0, T_f]$ for the dilution rate D can be a concatenation of arcs *Bang*(0), *Bang*($D_{\max}$) and *Singular* (not necessarily in this order). On the other hand, the optimal control for light intensity I over $[0, T_f]$ can be a concatenation of arcs *Bang*($I_{\max}$) and I_s.

5.5 Properties of the adjoint variables and the optimal controls

Proposition 5.2

The adjoint variables λ_x and λ_c are non-negative and non-positive, respectively.

Proof. Inequality (5.23) can be rewritten as

$$\lambda_x \geq -\lambda_c \frac{k_d \tau \sigma I_x (2 + \tau \sigma I_x)}{xK}, \tag{5.26}$$

and replacing the above in the dynamics of λ_c given by (5.11) we get:

$$\begin{aligned}
\dot{\lambda}_c &\geq -\frac{\lambda_c k_d \tau (\sigma I_x)^2 (2 + \tau \sigma I_x)}{1 + \tau \sigma I_x} + \lambda_c \left[\frac{k_d \tau (\sigma I_x)^2}{1 + \tau I_x} + k_r \right], \\
\dot{\lambda}_c &\geq \lambda_c [k_r - k_d \tau (\sigma I_x)^2].
\end{aligned}$$

For simplicity, let us denote $\psi = k_r - k_d \tau (\sigma I_x)^2$ and let be $t_0, t, s \in [0, T_f]$ with $t_0 \leq s \leq t$, we have:

$$\begin{aligned}
\dot{\lambda}_c(s) &\geq \lambda_c(s)\psi(s), \\
\frac{d}{ds}\left(\lambda_c e^{-\int_{t_0}^{s} \psi(w)dw} \right) &\geq 0, \\
\lambda_c(t) e^{-\int_{t_0}^{t} \psi(w)dw} - \lambda_c(t_0) &\geq 0.
\end{aligned}$$

This is valid for every $t_0 \leq t \leq T_f$, replacing t by T_f and using the transversality condition (5.12) we get,

$$0 \geq \lambda_c(t_0) \ \forall t \in [0, T_f].$$

Then λ_c is non-positive, and by (5.26) we conclude that λ_x is non-negative. □

Proposition 5.3

There exists an interval $[T_f - \varepsilon, T_f]$ where $D(t) = D_{\max}$. If $\lambda_x(T_f - \varepsilon) = 1$, and let $\bar{\mu}$ be an upper bound of μ satisfying $\bar{\mu} < D_{\max} + R$, then,

$$\varepsilon \geq \frac{1}{D_{\max} + R - \bar{\mu}} \ln\left(\frac{D_{\max}}{\bar{\mu} - R}\right). \tag{5.27}$$

Proof. The existence of the time interval $[T_f - \varepsilon, T_f]$ is straightforward since λ_x is continuous, non-negative and satisfies (5.12). Now, to prove the inequality (5.27), we substitute (5.23) in the λ_x-dynamics (5.11), then we get,

$$\dot{\lambda}_x \geq \lambda_x \left[\mu\left(\frac{\xi x}{1 + \tau\sigma I_x} - 1\right) + (D + R)\right] - D - \frac{\lambda_x \xi x \mu}{1 + \tau\sigma I_x}.$$

Denoting $\phi = -\mu + D + R$, let be $t_0, t, s \in [0, T_f]$ with $t_0 \leq s \leq t$, multiplying (5.28) by $e^{-\int_{t_0}^{s} \phi(w)dw}$ and integrating,

$$\frac{d}{ds}\left(\lambda_x(s) e^{-\int_{t_0}^{s} \phi(w)dw}\right) \geq -D(s) e^{-\int_{t_0}^{s} \phi(w)dw},$$
$$\lambda_x(t) e^{-\int_{t_0}^{t} \phi(w)dw} - \lambda_x(t_0) \geq -\int_{t_0}^{t} D(s) e^{-\int_{t_0}^{s} \phi(w)dw} ds.$$

Then, we get (5.27) by evaluating t at T_f and t_0 at $T_f - \varepsilon$. □

5.5.1 An assumption over the growth rate

Function μ is continuous and non-negative in $[0, T_f]$, then it is bounded. We consider the following assumption.

Hypothesis 5.1

There exists a strictly positive lower bound $\underline{\mu}$ of the growth rate μ that satisfies

$$\underline{\mu} > R. \tag{5.28}$$

This condition is common in photobioreactor optimization [91, 18]. Under this assumption, we can get the value of the light I and the dilution D, in the singular arc. In the following, let us denote $[t_1, t_2]$ the interval of the singular arc.

Proposition 5.4

Under Hypothesis 5.1, $I = I_{\max}$ in the singular arc

Proof. As $\lambda_x = 1$ in $[t_1, t_2]$, $\dot{\lambda}_x = 0$ in $]t_1, t_2[$, then in this interval, from (5.11) we get,

$$0 = \mu \left(\frac{\xi x}{1 + \tau\sigma I_x} - 1 \right) + R + \lambda_c \frac{k_d \xi K}{\mu} \left[(1 + \tau\sigma I_x)^2 - 1 \right],$$

developing this equation leads to,

$$\lambda_c \left[(1 + \tau\sigma I_x)^2 - 1 \right] = -\frac{Kx}{k_d} + \frac{K(1 + \tau\sigma I_x)}{k_d a} \left[1 - \frac{R}{\mu} \right].$$

As $I \leq I_{\max}$, using (5.28) we deduce that,

$$\begin{aligned} \lambda_c \left[\left(1 + \tau\sigma I_{\max} e^{-\xi x}\right)^2 - 1 \right] &\geq \lambda_c \left[(1 + \tau\sigma I_x)^2 - 1 \right] \\ &> \frac{-Kx}{k_d}. \end{aligned}$$

Replacing $\lambda_x = 1$, condition (5.16) is fulfilled. □

Proposition 5.5

Under Hypothesis 5.1 the dilution in the singular arc satisfies,

$$D_s = \mu - R. \tag{5.29}$$

Proof. From Proposition 5.4 the light in $]t_1, t_2[$ remains constant and equal to $I_{\max}$. Then, over $]t_1, t_2[$, we get,

$$H = (\mu - R)x + [(-\gamma + k_r)c + \gamma]\lambda_c, \tag{5.30}$$

where,

$$\gamma = \frac{k_d \tau (\sigma I_x^{\max})^2}{1 + \tau\sigma I_x^{\max}}. \tag{5.31}$$

As H is constant in time, taking the derivative in (5.30) we get:

$$0 = \dot{\mu}x + (\mu - R)\dot{x} + \dot{\lambda}_c[-(\gamma + k_r)c + \gamma] + \lambda_c[-\dot{\gamma}c + (\gamma + k_r)\dot{c} + \dot{\gamma}]. \tag{5.32}$$

The derivative of μ in $]t_1, t_2[$ is,

$$\dot{\mu} = -\frac{\xi \mu \dot{x}}{1 + \tau\sigma I_x^{\max}} - \frac{\mu k_d \tau (\sigma I_x^{\max})^2}{1 + \tau\sigma I_x^{\max}} + \frac{K\sigma I_x^{\max} k_r c}{1 + \tau\sigma I_x^{\max}}, \tag{5.33}$$

and the derivative of γ is given by,

$$\dot{\gamma} = \frac{k_d \tau \xi \left(\sigma I_x^{\max}\right)^2 \left(2 + \tau\sigma I_x^{\max}\right)}{(1 + \tau\sigma I_x^{\max})^2} \dot{x}. \tag{5.34}$$

By replacing (5.33)-(5.34) in (5.32) we get,

$$(\mu - R)(\mu - R - D)x = 0,$$

then, as $\mu > R$, we have that $\mu - R \neq 0$. Also, unless the initial condition of x is zero, $x(t) \neq 0 \ \forall t \in [0, T_f]$. Then, we conclude that $D = \mu - R$. □

The next result is immediately deduced:

Corollary 5.1

Let us assume that a singular arc occurs in an interval $[t_1, t_2]$ with $t_1 < t_2$, under Hypothesis 5.1 the biomass concentration is constant in $[t_1, t_2]$.

5.6 Estimating biomass in the singular arc

We saw that biomass in the photobioreactor x and the light intensity are constant in the singular arc, but this value must be determined. We assume that the singular arc $[t_1, t_2]$ is long enough for the state c to reach its equilibrium, this is because the equation (5.2) becomes *autonomous* in $[t_1, t_2]$ and c converges to the unique asymptotically stable steady state given by:

$$c_s = \frac{k_d \tau (\sigma I_x^{\max})^2}{k_r(1 + \tau\sigma I_x^{\max}) + k_d \tau (\sigma I_x^{\max})^2}.$$

Then the growth rate μ is constant and equal to

$$\mu_s = \frac{K\sigma I_x^{\max}}{1 + \tau\sigma I_x^{\max} + \frac{k_d}{k_r}\tau(\sigma I_x^{\max})^2}. \tag{5.35}$$

This is the Haldane description corresponding to the growth rate of the Han model at steady state. This function reaches its maximum at the value

$$I_x^{\max} = I_{\text{opt}} \coloneqq \frac{1}{\sigma\sqrt{\frac{k_d}{k_r}\tau}}. \tag{5.36}$$

In this static condition, λ_c is constant, and we can find its value from (5.11),

$$\lambda_c = -\frac{\mu_s x}{k_r}.$$

Replacing this value in the first equation, we get,

$$\frac{R}{\mu_s} = 1 - \xi x \frac{k_r - k_d \tau (\sigma I_x^{\max})^2}{k_r(1 + \tau\sigma I_x^{\max}) + k_d \tau (\sigma I_x^{\max})^2}. \tag{5.37}$$

We denote x_s the biomass concentration satisfying (5.37). It is important to note that this value does not depend on either $D_{\max}$ or the initial conditions of X.

5.7 Direct optimization

We solve numerically the problem (OCP), with a direct method implemented in the software `BOCOP` [22]. The problem is discretized by a two stage Gauss-Legendre method with 15000 time steps, and the tolerance for the IPOPT NLP solver is set at 10^{-25}. We consider the parameters of

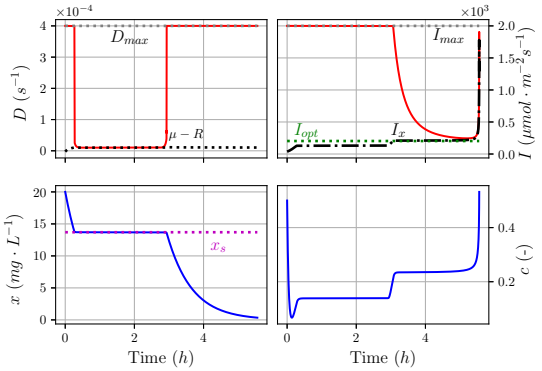

(a) **Example 1.** Initial biomass $x(0) > x_s$.

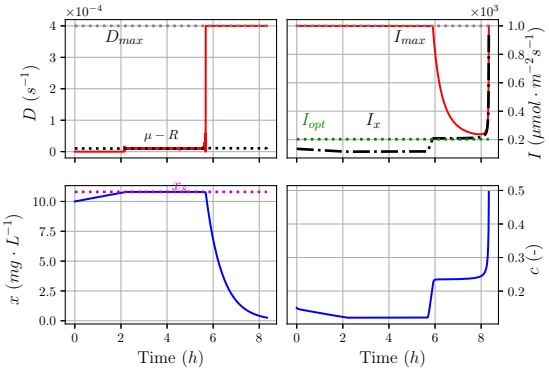

(b) **Example 2.** Initial biomass $x(0) < x_s$.

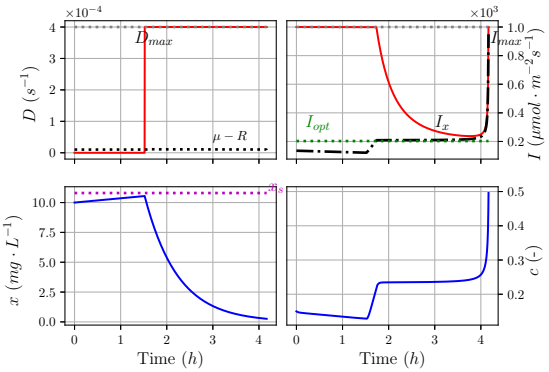

(c) **Example 3.** The parameters are the same as in the Example 2, with a shorter final time T_f.

Figure 5.1: The optimal controls (in red), and the states (in blue). In the dilution plot, we also represent $\mu - R$ (black dotted line) to illustrate the Proposition 5.5. In the light plot, we also represent I_{opt} defined in (5.36), and the value of the perceived light I_x (the black dotted line). The magenta dashed line in the biomass concentration plot corresponds to x_s defined in Section 5.6.

Table 5.1: Parameters values for the biological model.

Parameter	Value			Unit
	Ex. 1	Ex. 2	Ex. 3	
T_f	$2 \cdot 10^4$	$3 \cdot 10^4$	$1.5 \cdot 10^4$	s
$x(0)$	20	10		$m\text{g} \cdot \text{L}^{-1}$
$c(0)$	0.5	0.15		-
K	$8.70 \cdot 10^{-6}$			-
k_d	$2.99 \cdot 10^{-4}$			-
k_r	$6.80 \cdot 10^{-3}$			s^{-1}
τ	$0.25 \cdot 10^0$			s
σ	$4.70 \cdot 10^{-2}$			$m^2 \cdot \mu mol^{-1}$
$D_{\max}$	$4.00 \cdot 10^{-4}$			s^{-1}
$I_{\max}$	$1.00 \cdot 10^3$			$\mu\text{mol} \cdot \text{m}^{-2}\text{s}^{-1}$
R	$8.00 \cdot 10^{-6}$			s^{-1}
ξ	0.20			$m\text{g}^{-1} \cdot \text{L}$

the Han model from [61]. We consider three different examples with the listed parameter values in Example 1-3.

Figure 5.1a, 5.1b and 5.1c show the simulation results. In the first example, the control structure of the dilution rate is *Bang-Singular-Bang* and for the light it is *Bang-Singular*. The initial biomass is higher than the concentration x_s predicted in the section 5.6, then the dilution is settled at maximum until the biomass reaches x_s, subsequently, the singular arc of dilution is activated, and the biomass x_s is maintained during this period. Finally, the dilution is settled at maximum, as was demonstrated in Proposition 5.3. On the other hand, in Figure 5.1b, the behavior of the controls are similar, but, the initial biomass is lower than x_s, then the dilution rate is zero to allow the system to reach x_s.

The curve $\mu - R$ takes negative values in the first arc ($Bang(D_{\max})$) presented in Figure 5.1a), this is because the initial biomass is too high leading to a lack of light in the culture and leading to growth rate close to zero. The Hypothesis 5.1 is not fulfilled in the entire interval. But, it is in the singular arc of dilution $[t_1, t_2]$. Actually, the results proved in Section 5.5 are still valid if we relax the inequality (5.28) for the condition $\mu(t) \geq R \ \forall t$ in the singular arc of dilution.

In the three examples presented, the average light perceived by the algae culture I_x together with the light intensity I, it appears, coherently with Section 5.6. In example 1, I_x is lower than the optimal light intensity I_{opt}, and in the singular arc of light, the value of I_x is equal to the value of I_{opt}.

In Figure 5.1c we present the results for Example 3 which has the same parameters as in the Example 2, but considering a shorter final time $T_f = 1.5 \cdot 10^4$. In this case, the structure of the dilution rate is *Bang-Bang* and the structure of the light is the same as in the Example 2. Then existence of the singular arc for dilution is not always ensured. In this case, there is not enough time for the biomass to reach the value estimated in Section 5.6 and let a time window for harvesting the biomass at the end. In Proposition 5.3 we discuss the length of this time window.

5.8 Conclusion

The singular arc for the dilution rate is key in the optimal problem (OCP). We prove that in this arc the biomass remains constant, at a concentration independent of the value of the maximum dilution rate and the final time for harvesting depends on the maximal dilution rate. The solution of this equation cannot be given explicitly. It is also interesting to note that the associated light in the singular arc of dilution is lower than the optimal light for the Han model at steady state. On the other hand, numerical results show that, when $I = I_s$, the optimal irradiance corresponds to the optimum of the Han model at steady state.
Larger values of the maximum light $I_{\max}$ allow operating the photobioreactor at higher biomasses. This fact is in agreement with experimental observations, for high density cultures [57], where photoinhibition is negligible due to the self shading of the cells.

Chapter 6

Optimal control of photobioreactor accounting for photoinhibition and photoacclimation

This chapter reproduces [51] presented at the 12th IFAC Symposium on Advanced Control of Chemical Processes (ADCHEM 2024), and some unpublished results on the unperturbed optimal control problem associated to the one studied in the original paper.

Abstract

The industrial cultivation of microalgae has increased substantially over the past two decades. These microorganisms have the ability to adapt their photosynthetic pigments in response to the amount of light they experience. Herein, we investigate a dynamic model that describes pigment adaptation and its effect on microalgal productivity in a photobioreactor where light is shone onto the surface and attenuated as it traverses the culture medium. We consider two controls – the light irradiance and the dilution rate of the photobioreactor under continuous operation and constant volume – and analyze strategies for maximal production of microalgal biomass using Pontryagin's maximum principle. We also conduct a numerical investigation of turnpike properties in this context and discuss how self-shading within the culture could be exploited to increase productivity.

6.1 Introduction

The main focus in this chapter is on photoinhibition and photoacclimation, the combined effect of which has not been studied extensively thus far. Photoinhibition is triggered by an excess of light causing damage to key photosynthetic proteins, thereby affecting cell growth. Photoacclimation, on the other hand, is a protective mechanism to mitigate photoinhibition through adjusting the amount of cellular pigments in response to light intensity variations. These phenomena take place on different timescales [68, 20]. An optimal control problem for maximizing the amount of biomass

produced has already been studied in Chapter 5considering the rapid dynamics of photoinhibition in a turbid medium where the cells are advected through a light gradient. In this chapter, the objective is to extend this work by focusing on the slower timescales and include in the analysis the photoacclimation dynamics. An interesting problem when both light and dilution rate can be controlled is how to start the reactor to avoid loss of productivity due to high photoinhibition at low initial biomass density. This phenomenon is even more marked if the culture was pre-acclimated to low light, as it is the case for a high density inoculum in which light penetration is limited. It leads to a new control problem that we formulate and analyse. We then show how photoacclimation impacts the optimal strategy. This chapter is organized as follows: Section 6.2 introduces the dynamic model describing the growth of biomass in the photobioreactor, based on a model by [105] integrating both photoinhibition and photoacclimation. Section 6.3 formulates the optimal control problem before conducting a formal analysis based on Pontryagin's Maximum Principle in Section 6.4. A numerical investigation is conducted in Section 6.6 to validate and complement the theoretical results. Finally, Section 6.7 discusses the main insights, in particular the role played by both timescales and the benefits of self-shading on the process productivity.

6.2 Dynamic Model Formulation

We consider a planar photobioreactor operated in continuous mode and illuminated by an artificial light perpendicular to the plan. The biomass concentration, x [$\mathrm{g_C\,L^{-1}}$] follows the dynamics:

$$\dot{x} = \mu x - Rx - Dx, \tag{6.1}$$

where μ [$\mathrm{s^{-1}}$] is the specific gross growth rate, R [$\mathrm{s^{-1}}$] the specific maintenance rate [21], and D [$\mathrm{s^{-1}}$] the dilution rate of the reactor (ratio between the feed rate and the volume of the reactor).

The photobioreactor is illuminated with a light irradiance I [$\mu\mathrm{mol\,m^{-2}s^{-1}}$]. This irradiance is attenuated by the biomass concentration x and the amount of chlorophyll $x\theta$, where the chlorophyll quota θ [$\mathrm{g_{Chl}\,g_C^{-1}}$] is the amount of chlorophyll per unit of biomass. The chlorophyll content in microalgae, and more generally their pigment composition, changes in response to variations in the light irradiance. In the model developed by [105], the chlorophyll quota θ depends on the *growth irradiance* I_g [$\mu\mathrm{mol\,m^{-2}s^{-1}}$], which corresponds to the light at which the microalgae are acclimated:

$$\theta(I_\mathrm{g}) = \psi \frac{k_I}{I_\mathrm{g} + k_I}, \tag{6.2}$$

with parameters ψ [$\mathrm{g_{Chl}\,g_C^{-1}}$] and k_I [$\mu\mathrm{mol\,m^{-2}s^{-1}}$]. The dynamics of the growth irradiance I_g are given by:

$$\dot{I}_\mathrm{g} = \delta\mu(\bar{I} - I_\mathrm{g}), \tag{6.3}$$

where δ [–] is a scaling constant, and the specific growth rate μ depends on the average perceived light $\bar{I}$

The average light that the microalgae perceived along their advection in the reactor can be approximated using the Beer-Lambert law as:

$$\bar{I}(I, x, I_\mathrm{g}) = I \frac{1 - e^{-(E_\mathrm{C} + E_\mathrm{Chl}\theta)xL}}{(E_\mathrm{C} + E_\mathrm{Chl}\theta)xL}, \tag{6.4}$$

where L [m] is the depth of the photobioreactor (the distance between the illuminated side and the opposite side), E_{Chl} [$\mathrm{g}_{\mathrm{Chl}}^{-1}\mathrm{m}^{-1}\mathrm{L}$] and E_{C} [$\mathrm{g}_{\mathrm{C}}^{-1}\mathrm{m}^{-1}\mathrm{L}$] are constants that account for light absorption by the pigments and the biomass, respectively.

For simplicity, we denote

$$\varepsilon(x, I_{\mathrm{g}}) = \frac{1 - e^{-(E_{\mathrm{C}} + E_{\mathrm{Chl}}\theta)xL}}{(E_{\mathrm{C}} + E_{\mathrm{Chl}}\theta)xL}, \tag{6.5}$$

as the average attenuation factor. In particular, we have $\bar{I} = I\varepsilon$.

According to the reduced Han model [66, 68, 53]:

$$\mu(I, x, I_{\mathrm{g}}) = \frac{K\sigma\bar{I}}{1 + \tau\sigma\bar{I} + \frac{k_d}{k_r}\tau(\sigma\bar{I})^2}, \tag{6.6}$$

with K [$-$] the growth rate coefficient, σ [$\mathrm{m}^2\mu\mathrm{mol}^{-1}$] the effective cross-section, τ [s] the turnover time (time needed to harvest one photon), and k_d [$-$] and k_r [s^{-1}] the damage and repair rates, respectively. The maximal growth rate,

$$\mu_{\max} = \frac{K}{2\sqrt{\frac{k_d}{k_r}\tau} + \tau}, \tag{6.7}$$

is achieved under the following condition:

$$\sigma\bar{I} = \frac{1}{\sqrt{\frac{k_d}{k_r}\tau}}. \tag{6.8}$$

Finally, the dependence between the effective cross-section and the chlorophyll quota is assumed to follow a power law relationship [105]:

$$\sigma(I_g) = \beta\theta(I_g)^{\kappa}, \tag{6.9}$$

where β and κ are two constants.

6.3 Optimal Control Problem Statement

The goal is to speed up the initial reactor starting phase, or equivalently to maximize the total biomass production over the time horizon of the reactor start-up $[0, T_{\mathrm{f}}]$, defined as:

$$J_{T_{\mathrm{f}}}(D, I) = \int_0^{T_{\mathrm{f}}} x(t)D(t)dt\,. \tag{6.10}$$

The controls are the dilution rate D and the artificial irradiance I, within the following sets of admissible controls:

$$\begin{aligned} \mathcal{D} &\coloneqq \{D : [0, +\infty) \to [0, D_{\max}] \;\; ; \;\; D(\cdot) \in \mathcal{L}^{\infty}_{loc}(\mathbb{R}_+)\}, \\ \mathcal{I} &\coloneqq \{I : [0, +\infty) \to [0, I_{\max}] \;\; ; \;\; I(\cdot) \in \mathcal{L}^{\infty}_{loc}(\mathbb{R}_+)\}, \end{aligned} \tag{6.11}$$

where $\mathcal{L}^{\infty}_{loc}(\mathbb{R}_+)$ denotes the set of locally integrable functions on every compact set in $[0,\infty)$. In particular, the upper bounds $D_{\max}$ and $I_{\max}$ on the controls are assumed to be large enough to drive biomass washout, e.g., $D_{\max} > \mu_{\max}$ with $\mu_{\max}$ as defined in Equation (6.7).

The resulting optimal control problem is given by:

$$\begin{aligned} \max_{\substack{D\in\mathcal{D},\\ I\in\mathcal{I}.}} \quad & J_\delta = \int_0^{T_\mathrm{f}} x(t)D(t)dt, \\ \text{s.t.} \quad & \dot{x} = \mu(I,x,I_\mathrm{g})x - Dx - Rx, \\ & \dot{I}_\mathrm{g} = \delta\mu(I,x,I_\mathrm{g})\left[\bar{I}(I,x,I_\mathrm{g}) - I_\mathrm{g}\right], \\ & x(0), I_\mathrm{g}(0) \text{ given.} \end{aligned} \tag{P_δ}$$

6.4 Formal Analysis

To apply Pontryagin's maximum principle (PMP) [33, 71] to the optimal control problem (P_δ), we define the Hamiltonian function H as:

$$H(x, I_\mathrm{g}, D, I, \lambda_x, \lambda_\mathrm{g}) \coloneqq \lambda_x(\mu - R - D)x + \delta\lambda_\mathrm{g}\mu(\bar{I} - I_\mathrm{g}) + xD\,. \tag{6.12}$$

The dynamics of the co-states λ_x and λ_g are given by:

$$\begin{cases} \dot{\lambda}_\mathrm{g} = -\lambda_x \dfrac{\partial\mu}{\partial I_\mathrm{g}} x - \delta\lambda_\mathrm{g}\left(\dfrac{\partial\mu}{\partial I_\mathrm{g}}(\bar{I} - I_\mathrm{g}) - \mu\left(\dfrac{\partial\bar{I}}{\partial I_\mathrm{g}} - 1\right)\right), \\ \dot{\lambda}_x = -\lambda_x\left(\dfrac{\partial\mu}{\partial x}x + \mu - R - D\right) - \delta\lambda_\mathrm{g}\left(\dfrac{\partial\mu}{\partial x}(\bar{I} - I_\mathrm{g}) + \mu\dfrac{\partial\bar{I}}{\partial x}\right) - D. \end{cases} \tag{6.13}$$

Since the terminal state values are free, the terminal co-states are given by:

$$\lambda_x(T_\mathrm{f}) = \lambda_\mathrm{g}(T_\mathrm{f}) = 0. \tag{6.14}$$

The optimal control trajectories $D^*(t), I^*(t)$ are those maximizing the Hamiltonian function for almost all $t \in [0, T_\mathrm{f}]$:

$$(D^*(t), I^*(t)) \in \operatorname*{argmax}_{\substack{D\in[0,D_{\max}],\\ I\in[0,I_{\max}].}} H(x^*(t), I^*_\mathrm{g}(t), D, I, \lambda^*_x(t), \lambda^*_\mathrm{g}(t))\,. \tag{6.15}$$

Based on condition (6.15), the dilution rate can take three different values depending on the value of the co-state λ_x, as summarized in Proposition 6.1 below.

Proposition 6.1

For almost all $t \in [0, T_\mathrm{f}]$, the optimal control D^* satisfies

$$D^*(t) = \begin{cases} 0, & \text{if} \quad \lambda_x > 1, \\ D_{\max}, & \text{if} \quad \lambda_x < 1, \\ D_{\mathrm{sing}}(t), & \text{if} \quad \lambda_x(t) = 1, \end{cases} \tag{6.16}$$

where D_{sing} is a singular arc.

Likewise, the optimal irradiance I^* is a solution to the following problem almost everywhere:

$$I^*(t) \in \underset{I \in [0, I_{\max}]}{\operatorname{argmax}} \ \phi(I) \coloneqq \lambda_x \mu x + \delta \lambda_\mathrm{g} \mu (\bar{I} - I_\mathrm{g}). \tag{6.17}$$

The KKT conditions for this problem are given by:

$$\frac{\partial \phi(I)}{\partial I} - \nu = 0, \tag{6.18}$$

$$\nu(I_{\max} - I) = 0, \tag{6.19}$$

$$\nu \geq 0. \tag{6.20}$$

In particular, the stationarity condition (6.18) expands as:

$$\lambda_x x \frac{\partial \mu}{\partial \bar{I}} \frac{\partial \bar{I}}{\partial I} + \delta \lambda_\mathrm{g} \frac{\partial \mu}{\partial \bar{I}} \frac{\partial \bar{I}}{\partial I} (\bar{I} - I_\mathrm{g}) + \delta \lambda_\mathrm{g} \mu \frac{\partial \bar{I}}{\partial I} - \nu = 0, \tag{6.21}$$

and since $\frac{\partial \bar{I}}{\partial I} \geq 0$, it follows from the dual feasibility condition (6.20) that

$$\Psi \coloneqq \lambda_x x \frac{\partial \mu}{\partial \bar{I}} + \delta \lambda_\mathrm{g} \left(\frac{\partial \mu}{\partial \bar{I}} (\bar{I} - I_\mathrm{g}) + \mu \right) \geq 0. \tag{6.22}$$

The switching function Ψ is such that $I^*(t) = I_{\max}$ whenever $\Psi > 0$. Next, we seek an expression of $I^*(t)$ when $\Psi = 0$:

$$\lambda_x x \frac{\partial \mu}{\partial \bar{I}} + \delta \lambda_\mathrm{g} \left(\frac{\partial \mu}{\partial \bar{I}} (\bar{I} - I_\mathrm{g}) + \mu \right) = 0. \tag{6.23}$$

In the case that $\delta \lambda_\mathrm{g} = 0$, the previous condition simplifies to:

$$\lambda_x x \frac{\partial \mu}{\partial \bar{I}} = 0, \tag{6.24}$$

then dismissing the case $\lambda_x = 0$, the optimal solution corresponds to:

$$\sigma \bar{I}^* = \frac{1}{\sqrt{\frac{k_d}{k_r} \tau}}. \tag{6.25}$$

In the other case that $\delta \lambda_\mathrm{g} \neq 0$, the condition (6.23) can be rewritten as

$$\frac{\partial \mu}{\partial \bar{I}} \left[\lambda_x x + \delta \lambda_\mathrm{g} (\bar{I} - I_\mathrm{g}) \right] + \delta \lambda_\mathrm{g} \mu = 0, \tag{6.26}$$

then replacing the definition of μ, leads to the following quadratic equation:

$$\left(\frac{\lambda_x x}{\delta\lambda_{\mathrm{g}}} - I_{\mathrm{g}}\right)\left(1 - \frac{k_d}{k_r}\tau(\sigma\bar{I})^2\right) + 2\bar{I} + \tau\sigma\bar{I}^2 = 0\,. \tag{6.27}$$

Candidate solutions are of the form:

$$\bar{I}^* = \frac{-1 \pm \sqrt{1 - \tau\sigma\left(\frac{\lambda_x x}{\delta\lambda_{\mathrm{g}}} - I_{\mathrm{g}}\right) + \frac{k_d}{k_r}\tau\sigma^2\left(\frac{\lambda_x x}{\delta\lambda_{\mathrm{g}}} - I_{\mathrm{g}}\right)^2}}{\tau\sigma\left[1 - \frac{k_d}{k_r}\tau\sigma\left(\frac{\lambda_x x}{\delta\lambda_{\mathrm{g}}} - I_{\mathrm{g}}\right)\right]}, \tag{6.28}$$

of which only the positive values are admissible.

Proposition 6.2

For almost $t \in [0, T_{\mathrm{f}}]$, the optimal control I^* satisfies

$$I^*(t) = \begin{cases} I_{\max} & \text{if } \bar{I}^* > \epsilon I_{\max}, \\ \bar{I}^*/\epsilon & \text{otherwise.} \end{cases} \tag{6.29}$$

The function Ψ, combined with the transversality conditions, is also useful to estimate the final arc of the optimal control D^*. From the terminal condition (6.14) and by continuity of λ_x, there is a time interval on which $\lambda_x(t) < 1$; it follows from Proposition 6.1 that $D(t) = D_{\max}$ on this interval.

To estimate the corresponding switching time T_{harv}, we rewrite the dynamic of the co-state λ_x as

$$\dot{\lambda}_x = -\Psi\frac{\partial\bar{I}}{\partial x} - \lambda_x(\mu - R - D) - D, \tag{6.30}$$

with Ψ as defined in (6.22) and noting the chain rule $\frac{\partial\mu}{\partial x} = \frac{\partial\mu}{\partial\bar{I}}\frac{\partial\bar{I}}{\partial x}$. Since $\frac{\partial\bar{I}}{\partial x} = I\frac{\partial\varepsilon}{\partial x}$ is non-positive (as more biomass decreases the average light in the photobioreactor), the condition (6.22) can be rewritten as:

$$\begin{aligned} \dot{\lambda}_x &\geq -\lambda_x(\mu - R - D) - D, \\ &\geq -\lambda_x(\mu_{\max} - R - D_{\max}) - D_{\max}. \end{aligned} \tag{6.31}$$

Multiplying both side by $e^{(\mu_{\max}-R-D_{\max})(t-(T_{\mathrm{f}}-T_{\mathrm{harv}}))}$ and integrating over time gives:

$$\begin{aligned} &\lambda_x(T_{\mathrm{f}})e^{(\mu_{\max}-R-D_{\max})T_{\mathrm{harv}}} \\ -\lambda_x(T_{\mathrm{f}} - T_{\mathrm{harv}}) \geq &\frac{-D_{\max}(e^{(\mu_{\max}-R-D_{\max})T_{\mathrm{harv}}} - 1)}{\mu_{\max} - R - D_{\max}}, \end{aligned} \tag{6.32}$$

After replacing the transversality condition and $\lambda_x(T_{\mathrm{f}} - T_{\mathrm{harv}}) = 1$, we obtain:

$$\frac{\mu_{\max} - R}{D_{\max}} \geq e^{(\mu_{\max}-R-D_{\max})T_{\mathrm{harv}}}. \tag{6.33}$$

We summarize this insight in Proposition 6.3 below.

Proposition 6.3: Final harvest time

There exists $T_{\text{harv}} > 0$ such that $D^*(t) = D_{\max}$ for all $t \in [T_{\text{f}} - T_{\text{harv}}, T_{\text{f}}]$. If $\lambda_x(T - T_{\text{harv}}) = 1$, then

$$T_{\text{harv}} \leq \frac{1}{\mu_{\max} - R - D_{\max}} \ln\left(\frac{\mu_{\max} - R}{D_{\max}}\right).$$

6.5 The non-perturbed problem

The photoacclimation has a slow timescale with respect to the growth of the microalgae. The optimal control problem (P_δ) is regular perturbed optimal control problem [45], where the perturbation is $\delta > 0$. The non-perturbed problem (P_0) is defined as

$$\begin{aligned} \max_{\substack{D\in\mathcal{D},\\ I\in\mathcal{I}.}} \quad & J_0 = \int_0^{T_{\text{f}}} x(t)D(t)dt, \\ \text{s.t.} \quad & \dot{x} = (\mu(I, x, I_g(0)) - R - D)x, \\ & x(0), I_g(0) \text{ given.} \end{aligned} \tag{P_0}$$

The problem (P_δ) is well posed in the sense of performance convergence [45], meaning that

$$\lim_{\delta\to 0} \max_{\substack{D\in\mathcal{D},\\ I\in\mathcal{I}.}} J_\delta = \max_{\substack{D\in\mathcal{D},\\ I\in\mathcal{I}.}} J_0.$$

This due to the fact that the dynamics of problem (P_δ) varies continuously as a function of δ. Then, it is interesting to look the solution of problem (P_0).

The growth irradiance does not change, *i.e.*, microalgae are not acclimating to the light. In this case, the growth function only depends on the biomass and the light control I. Before studying the solution of the non-perturbed problem, note that the function

$$\bar{I} \mapsto \mu - R$$

has two non-negative zeros I_1, I_2 with $I_1 < I_2$. If $I_{\max} < I_2$, then it exists a unique $x_c > 0$ such that

$$\mu(I_{\max}, x_c, I_g(0)) - R = 0,$$

and also,

$$\mu(I_{\max}, x, I_g(0)) - R < 0 \ \forall x \in (0, x_c).$$

In this case, the biomass is so dense, that light can not compensate the specific maintenance rate R. Then, there is no interest to study the case where $x(0) \geq x_c$. Under the assumption $x(0) < x_c$, and $I_{\max} < I_c$ we can fully characterize the optimal controls of the reduced problem as follows: :

Theorem 6.1

Assume that $R < \mu_{\max}$, $I_{\max} < I_2$ and $x(0) < x_c$. Let us denote x_s the only positive solution

of

$$x_s \frac{\partial \mu(I_{\max}, x_s, I_g(0))}{\partial x} = \mu(I_{\max}, x_s, I_g(0)) - R,$$

and let D_s defined by:

$$D_s = \mu(I_{\max}, x_s, I_g(0)) - R.$$

Then the optimal light control I^* of the problem (P_0) can be written as a feedback control given by

$$I^*(x) = \min\{I_{\max}, I_{\text{opt}}\varepsilon^{-1}(x)\}, \tag{6.34}$$

where I_{opt} is defined as

$$I_{\text{opt}} = \frac{1}{\sigma(I_g(0))\sqrt{\frac{k_d}{k_r}\tau}}.$$

Finally, there are four possible forms of the optimal control D^*:

- *Constant* control at $D = D_{\max}$.
- *Bang-Bang* control with $D(0) = 0$ and a single switch to $D = D_{\max}$.
- *Bang-Singular-Bang* control with $D(0) = 0$ if $x(0) < x_s$ or $D(0) = D_{\max}$ if $x(0) > x_s$, taking place first a single switch to $D = D_s$ and a switch to $D = D_{\max}$.
- *Singular-Bang* control with $x(0) = x_s$, with $D = D_s$ and a single switch to $D = D_{\max}$.

Proof. We use the Pontryagin's maximum principle [114], where we define the Hamiltonian of the problem (P_0) as

$$H = \lambda_x(\mu - R - D)x + xD, \tag{6.35}$$

where the co-state λ_x follows the dynamics:

$$\dot{\lambda}_x = -\frac{\partial H}{\partial x} = \lambda_x \left(D - \frac{\partial \mu}{\partial x} x - \mu + R \right) - D. \tag{6.36}$$

Since the terminal state $x(T)$ is free, the transversality condition correspond to

$$\lambda_x(T) = 0. \tag{6.37}$$

The optimal controls D^* and I^* are those maximizing H for almost all $t \in [0, T]$, i.e.,

$$(D^*(t), I^*(t)) \in \underset{\substack{D\in[0,D_{\max}],\\ I\in[0,I_{\max}].}}{\operatorname{argmax}} H(x(t), D, I, \lambda_x(t)). \tag{6.38}$$

First, let us remark that that

$$\lambda_x \geq 0 \quad \forall t \in [0, T]. \tag{6.39}$$

From (6.36) we have for every $s \in (0, T)$:

$$\dot{\lambda_x}(s) - \lambda_x(s) \left(D(s) - \frac{\partial \mu(I(s), x(s), I_g(0))}{\partial x} x(s) - \mu(I(s), x(s), I_g(0)) + R \right) = -D,$$

denoting $h(s) = D - \frac{\partial \mu(I(s),x(s),I_g(0))}{\partial x} x(s) - \mu(I(s), x(s), I_g(0)) + R$, we have for every $s < t$

$$\frac{d}{dt}\left(\lambda_x e^{\int_s^t h(\tau)d\tau}\right) = -De^{\int_s^t h(\tau)d\tau}.$$

Then, integrating from s to T:

$$\lambda_x(T)e^{\int_s^T h(\tau)d\tau} - \lambda_x(s) = -\int_s^T De^{\int_s^t h(\tau)d\tau}dt,$$

and replacing the transversality condition (6.37) in the above:

$$\lambda_x(s) = \int_s^T De^{\int_s^t h(\tau)d\tau}dt.$$

Then, as the right hand of the equation is non-negative, $\lambda_x(s)$ is also non-negative. Now, we can determine the value of the optimal control I^* noting that condition (6.38) together with (6.39) drive to the equivalent condition:

$$I^*(t) \in \underset{0\leq I\leq I_{\max}}{\operatorname{argmax}}\ \mu(I, x, I_g(0)). \tag{6.40}$$

For a given x, μ has a unique maximum in $[0, +\infty)$ at I_{opt}, the solution of (6.40) fulfil the condition

$$I^*\varepsilon(x) = I_{\text{opt}},$$

if $I^* < I_{\max}$, otherwise $I^* = I_{\max}$, giving us the formulation (6.34). Now, For the dilution control D, from the definition of H (6.35), it is direct that

$$D^* = \begin{cases} 0 \text{ if } \lambda_x > 1 \\ D_s \text{ if } \lambda_x = 1 \\ D_{\max} \text{ if } \lambda_x < 1 \end{cases}$$

where D_s is the so-called singular arc which is unknown. As λ_x is a continuous function, D^* is the concatenation of bang and singular arcs. Also, as (6.37) holds, the final arc is always set at $D^* = D_{\max}$, then if no switch occurs, meaning that $\lambda_x(t) < 1 \forall t \in [0, T]$, the solution is the constant control $D = D_{\max}$.

Let us suppose the existence of a singular arc in $[t_1, t_2]$, meaning that $\lambda_x = 1\ \forall t \in [t_1, t_2]$, then, for every $t \in (t_1, t_2)$:

$$0 = \dot{\lambda}_x = -\frac{\partial \mu}{\partial x} x - \mu + R.$$

In this case, if $\mu - R = 0$, $\frac{\partial \mu}{\partial I \epsilon(x)} = 0$, then, $I\varepsilon(x) = I_{\text{opt}}$, then $\mu_{\max} - R = 0$, which contradicts the hypothesis $\mu_{\max} > R$. This proves that $I^* = I_{\max}$ in the singular arc. Then

$$0 = -\frac{\partial \mu(I_{\max}, x, I_g(0))}{\partial x} x - \mu(I_{\max}, x, I_g(0)) + R.$$

Note that x is then constant, as x is the only variable in the above. We will denote its value by x_s. As x is constant in (t_1, t_2), then $\dot{x} = 0$, then for every $t \in (t_1, t_2)$:

$$D_s = \mu(I_{\max}, x_s, I_g(0)) - R.$$

The switching between the different arcs occurs when $\lambda_x = 1$, in this switching time, we have that:

$$\dot{\lambda}_x = -x\frac{\partial \mu(I^*, x, I_g(0))}{\partial x} - \mu(I^*, x, I_g(0)) + R,$$
$$\dot{\lambda}_x = -\frac{\partial}{\partial x}(x(\mu(I^*, x, I_g(0)) - R)),$$

which is non-positive for $x \leq x_s$ and non-negative for $x \geq x_s$. Then, we can deduce the following:

- If $x \geq x_s$, no switch is possible from $D = 0$ to $D = D_{\max}$.
- If $x \leq x_s$, no switch is possible from $D = D_{\max}$ to $D = 0$.

We have two scenarios: one where a singular arc exists, and one where it does not.

First case: There is no singular arc. As the last arc is always set at $D = D_{\max}$, one possibility is that no switch happens, then the solution is the constant control $D^* = D_{\max}$. Now, let us suppose that at least one switch occurs, we want to prove that there is only one. Let us denote by t_s the last switching time, which is from $D = 0$ to $D = D_{\max}$, then $x(t_s) < x_s$. If another switching time occurs before, from $D = D_{\max}$ to $D = 0$ at time $t = t'_s$, then $x(t'_s) > x_s$, but $x(t_s) > x(t'_s)$ as $\dot{x} > 0$ in (t'_s, t_s), which contradicts the fact that $x(t_s) < x_s$.

Second case: There is a singular arc. We start proving that there is only possible singular arc. Let us assume that there are two singular arcs (t_1, t_2) and (t_3, t_4) with $t_2 < t_3$. Remark that $x(t) = x_s \forall t \in (t_1, t_2) \cup (t_3, t_4)$. There are two cases: a switch in t_2 to $D = 0$ or a switch in t_2 to $D = D_{\max}$. If there is a switch to $D = 0$, then $x > x_s$ in (t_2, t_3) which means that no switch to $D_{\max}$, and therefore x can not take the value x_s in (t_3, t_4), on the other side, if there is a switch to $D = D_{\max}$, then $x < x_s$ and no switch to $D = 0$ can occur, but in the same way, x can not take the value x_s in (t_3, t_4).

The last arc must be $D = D_{\max}$ and it is possible to repeat the argument presented in the first case, to prove that there is no another switch between the singular arc and the last one.

To finish the proof, let us understand what happens before the singular arc. If $x(0) > x_s$ and $D(0) = 0$, then no switch can take place to $D_{\max}$, then x is non-decreasing (as we assume $x(0) < x_c$), then is not possible to reach the value x_s of the singular arc. If $x(0) > x_s$, $D(0) = D_{\max}$, then a switch to $D = 0$ before the singular arc can only occur if $x > x_s$ and, for the same reason, x is non-decreasing and can not achieve the value of the singular arc (we use again that $x(0) < x_c$). Then if $x(0) > x_s$, $D(0) = D_{\max}$. Then, there is one possible arc with $D = D_{\max}$. The case $x(0) < x_s$ follows the same argument, and the only possible arc is $D = 0$. If no other arc is present before the singular one, it must fulfil the condition $x = x_s$. □

6.6 Numerical Investigations

We solve the optimal control problem (P_δ) using the direct sequential method, as implemented in the software BOCOP [22] with the NLP solver IPOPT [155]. Figure 6.1 displays the results of the states and the controls with $I_{\max} = 1000$ µmol m^{-2}s^{-1}, $D_{\max} = 0.001$ s^{-1}, and $T_f = 20.8$ d together with the corresponding model parameter values. The *Bang-Singular-Bang* structure is clearly visible, where in the first arc, the dilution is set to zero to allow the microalgae to growth, then the singular arc stabilizes the biomass to a certain value that does not depend on the initial

Figure 6.1: **Left:** Numerical solution with initial conditions $x(0) = 1$ and $I_g(0) = 200$. Red lines: optimal dilution rate and irradiance controls. Blue lines: optimal biomass concentration and growth irradiance states. Black dotted lines: value of $\mu - R$ (D plot) and approximate feedback control in Equation (6.45) (I plot). Vertical gray dotted lines: final harvest time T_{harv}. Blue dotted line: solution of Equation (6.46). **Right:** Model parameter values [105].

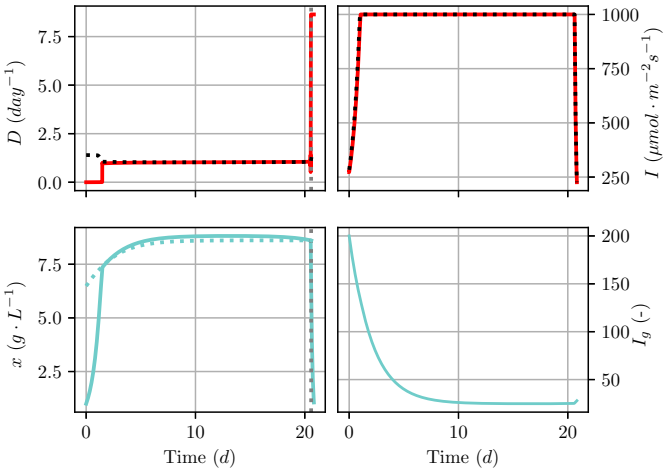

Parameter	Value
K	1.00×10^{-6} –
τ	5.50×10^{-3} s
k_d	5.00×10^{-6} –
k_r	1.50×10^{-4} s^{-1}
δ	2.30×10^{-1} –
ψ	3.10×10^{-1} $\text{g}_{\text{Chl}}\,\text{g}_{\text{C}}^{-1}$
k_I	4.40×10^{2} $\mu\text{mol}\,\text{m}^{-2}\text{s}^{-1}$
R	1.45×10^{-5} s^{-1}
E_c	8.00×10^{1} $\text{g}_{\text{C}}^{-1}\text{m}^{-1}\text{L}$
E_{chl}	4.00×10^{1} $\text{g}_{\text{Chl}}^{-1}\text{m}^{-1}\text{L}$
κ	1.00 –
β	5.48 (µmol, m, g)
L	5.00×10^{-2} m

condition of the growth irradiance (see Figure 6.2), and finally, as it was predicted in Proposition 6.3 the dilution is set to its maximum value.

The numerical solution confirms the presence of three main arcs in the optimal dilution rate control, as described in Proposition 6.1. First, the optimal dilution control is set to zero in order for the biomass to grow at maximal rate, while the optimal irradiance control is chosen to minimize the effect photoinhibition. Next, the singular arc of dilution is activated, soon after the irradiance control has reached its maximum value $I_{\max}$. The final arc is activated around $t = T_{\text{f}} - T_{\text{harv}}$, as shown in Proposition 6.3, where the optimal dilution control is set at its maximum value $D_{\max}$. We refine the insight derived form the numerical solution below, with a focus on characterizing the optimal solution structure and approximating the optimal dilution rate along the singular arc and the optimal irradiance during the initial growth phase.

6.6.1 Structure of the Optimal Dilution Rate

Since λ_x is a continuous function and according to Proposition 6.1, the optimal dilution rate profile is necessarily a concatenation of arcs, either $D^*(t) = 0$, $D^*(t) = D_{\max}$, or $D^*(t) = D_{\text{sing}}(t)$. Our computational investigations suggest that the structure of the optimal dilution rate follows a similar pattern presented in [64, Theorem 2], where structures are possible for the optimal dilution rate:

1. *Constant* control with $D^*(t) = D_{\max}$;
2. *Bang-Bang* with $D^*(t) = 0$, and single switch to $D^*(t) = D_{\max}$;

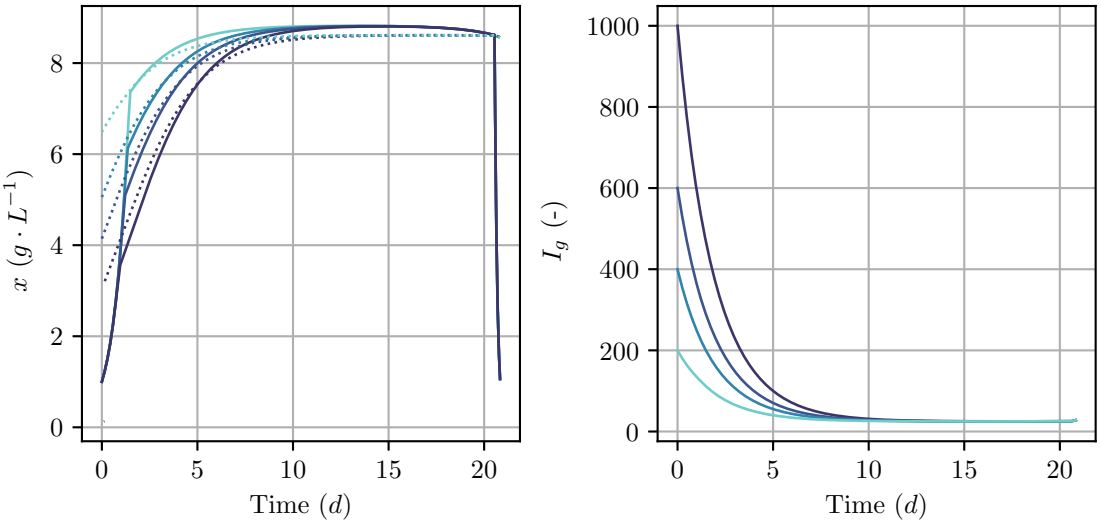

Figure 6.2: Optimal trajectories for the initial concentration $x(0) = 1\ \mathrm{g\,L^{-1}}$ and different initial growth irradiance $I_{\mathrm{g}}(0) = 1000, 600, 400, 200\ \mu\mathrm{mol\,m^{-2}s^{-1}}$. The dotted lines represent the solution of the Equation (6.46), which correspond to the approximation of the optimal biomass.

3. *Bang-Singular-Bang* with $D^*(t) = 0$ or $D^*(t) = D_{\max}$, a switch to $D(t) = D_{\mathrm{sing}}(t)$, followed by a single switch to $D^*(t) = D_{\max}$.

The presence of the singular arc depends on the final time T_{f}, where the turnpike property appears; while the case $D^*(t) = 0$ or $D^*(t) = D_{\max}$ in the initial bang of the bang-singular-bang structure depends on the initial biomass concentration [52]. The analysis of the non-perturbed problem in the previous section supports this argument. Next, we focus on the more interesting case where T_{f} is large enough to trigger the singular arc and the initial biomass concentration is small enough for $D^*(t) = 0$ along the first arc. If the singular arc takes place in the interval $[t_1, t_2]$, then $\dot{\lambda}_x = 0$ for every $t \in (t_1, t_2)$. Then, from (6.30) we have:

$$-\Psi \frac{\partial \bar{I}}{\partial x} = \mu - R. \tag{6.41}$$

Recalling that $\frac{\partial \bar{I}}{\partial x}$ is non-positive, and Ψ is also non-negative, we conclude that $\mu - R \geq 0$. Numerical simulations show that actually, $\mu - R > 0$, and by consequence $I^* = I_{\max}$ in the singular arc. We can always ensure that $I^* = I_{\max}$ in the singular arc if we assume the existence of a strictly positive lower bound $\underline{\mu}$ on the growth rate μ that satisfies

$$\underline{\mu} > R. \tag{6.42}$$

This condition is common in photobioreactor optimization [91, 18], where it is assumed that microalgae keep growing when continuously exposed to light. This condition is not easy to establish, since it depends on the model parameters and on the choice of $I_{\max}$. However, we can notice that I^*

is not equal to $I_{\max}$ only if $\mu = R$. This equation has two solutions when $R < \mu_{\max}$, one related to a photolimited condition and in a phoinhibited condition. If we rule out the case when this equality occurs in photoinhibition conditions (which imposes a condition over $I_{\max}$), then $I^* < I_{\max}$ does not fulfil the condition (6.15).

6.6.2 Approximate Feedback Control on Light Irradiance

The equation (6.26) can be rewritten as

$$\lambda_x x \frac{\partial \mu}{\partial \bar{I}} + \delta \lambda_{\mathrm{g}} \left(\frac{\partial \mu}{\partial \bar{I}} (\bar{I} - I_{\mathrm{g}}) + \mu \right) = 0. \tag{6.43}$$

Since δ is relatively small, the quantity $\delta\lambda_{\mathrm{g}}$ itself is small enough to approximate its value to zero. We could confirm this through numerical simulations. Consequently, the optimal average irradiance $\bar{I}^*$ can be approximated using Equation (6.25), instead of the complex expression in Equation (6.28):

$$\bar{I}^*(t) \approx \frac{1}{\sigma \sqrt{\frac{k_d}{k_r}\tau}}, \tag{6.44}$$

whenever $\bar{I}^*(t) \leq \epsilon(x^*(t), I_{\mathrm{g}}^*(t)) I_{\max}$. The optimal light irradiance control, therefore, can be approximated using the following closed-loop feedback control law:

$$I_{\mathrm{cl}}(x^*(t), I_{\mathrm{g}}^*(t)) \coloneqq \min \left\{ \frac{1}{\sigma(I_{\mathrm{g}}^*(t)) \epsilon(x^*(t), I_{\mathrm{g}}^*(t)) \sqrt{\frac{k_d}{k_r}\tau}}, I_{\max} \right\}, \tag{6.45}$$

Refer to Figure 6.1 for a comparison showing excellent agreement between the feedback control I_{cl} (black dotted line) and the numerically optimized I^* (red solid line). Also note that the optimal control in (6.29) converges pointwise to I_{cl} as δ approaches 0.

6.6.3 Approximate Optimal Biomass Concentration

Numerical simulations show that the biomass concentration x is constant along the singular arc, suggesting that the optimal dilution rate is adjusted to fulfil the condition $D_s = \mu - R$. Together with the approximation $\Psi \approx \lambda_x x \frac{\partial \mu}{\partial \bar{I}}$ for sufficiently small δ, the optimal biomass concentration along the singular arc can then be approximated using (6.41) with $\lambda_x = 1$:

$$-x \frac{\partial \mu}{\partial x} \approx \mu - R. \tag{6.46}$$

This approximation matches the first-order optimality condition of the unrestricted, static problem $\max_x x(\mu - R)$ for a fixed I_{g} and $I = I_{\max}$. Refer to Figure 6.1 for a comparison between the solution to Equation (6.46) (dotted blue line) and the numerically optimized response x^* (solid blue line). Moreover, Figure 6.3 shows a plot of the net biomass productivity, defined by $(\mu(x, I_{\mathrm{g}}) - R)x$ for different biomass concentrations x and growth irradiance I_{g}. This phase diagram illustrates the turnpike property, whereby a range of optimal trajectories from different initial growth irradiance (blue solid lines) approach the maximal biomass concentration (black solid line), and ultimately the maximal net productivity. The same trajectories are shown in Figure 6.2 where it is possible to see that, after the initial phase initial condition dependent, the dilution rate maintains a biomass density for which (at maximum irradiance) the average irradiance in the reactor leads to optimal photoacclimation and maximum growth rate.

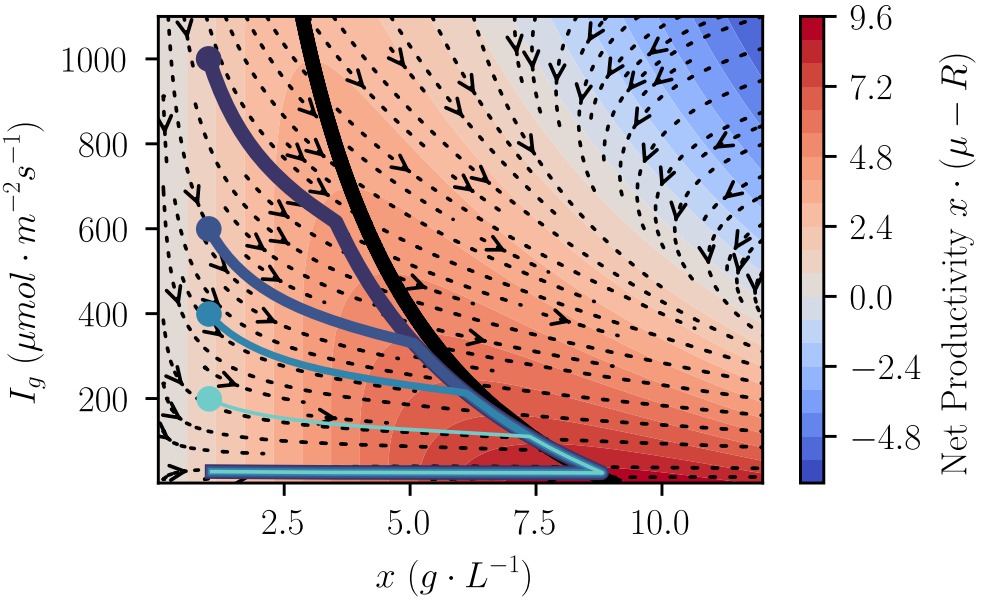

Figure 6.3: Phase diagram of the net biomass productivity $(\mu(x, I_g) - R)x$ and turnpike-like behavior. Dotted black lines: dynamic trajectories of biomass concentration x and growth irradiance I_g under the feedback control I_{cl}. Solid black line: maximal biomass concentration in terms of the growth irradiance I_g. Solid blue lines: selected trajectories from the initial biomass concentration $x(0) = 1\ \mathrm{g\,L^{-1}}$ and different initial growth irradiance $I_g(0) = 1000, 600, 400, 200\ \mu\mathrm{mol\,m^{-2}s^{-1}}$.

6.7 Discussion

6.7.1 The effect of Timescales

When considering the fast dynamics of photoinhibition [52] in the growth model, the solution of the optimal control D follows a turnpike strategy. Here, when accounting for the slower dynamics of photoacclimation, the turnpike property remains unchanged. Upon combining the rapid protein damage and recovery dynamics with the gradual adaptation of pigments (photoacclimation), we can thus anticipate consistent results. However, it is worth noting that in neither of these scenarios can we formally establish the turnpike property, e.g. using the results in [146], due to the singularity of the Hessian matrix $\frac{\partial^2 H}{\partial D^2}$.

6.7.2 Exploiting Self-Shading

One of the key features of the optimal strategy identified when accounting for both photoinhibition and photoacclimation relies on exploiting self-shading to enhance the biomass growth by adjusting the maximal light irradiance into the photobioreactor. Typically, a small inoculum of microalgae is initially introduced into the photobioreactor. During the initial growth phase, the irradiance can be carefully adjusted to ensure that the average light intensity does not trigger

significant photoinhibition. This initial phase of the optimal strategy cannot be applied in photobioreactors that use natural light, unless an external system decreases the irradiance. Throughout this initial phase, the dilution rate remains at zero. Then, once the optimal irradiance reach its maximum value and the optimal biomass level is attained, the dilution rate is set to keep this biomass concentration constant until the final harvesting time is reached.

6.8 Conclusions

We studied the optimal control problem of reactor startup considering photoinhibition, light gradient in the photobioreactor and photoacclimation dynamics, by combining a formal analysis with a numerical investigation. The rate of photoacclimation has a dynamics considerably slower than microalgal growth, dictated by the time-scaling constant $\delta \ll 1$. This timescale difference translates into a magnitude difference in the co-states, in turn making it possible to formulate an approximate close-loop optimal control law for the light irradiance. The optimal dilution rate presents a more challenging behavior for deriving a feedback control law, since it depends on the time horizon T_f. However, its value can be approximated along the singular arc, which takes the values necessary to uphold optimal biomass levels, as it was shown in Figure 6.3, to enhance net productivity. Once the biomass is dense enough, self-shading enables operating the photobioreactor using the maximal irradiance to maximize biomass growth and the net productivity. This effect was previously studied, but only in the scenario where photoinhibition is negligible due to strong self-shading [57]. Our analysis furthermore remains valid for average irradiance taking the form of $\bar{I} = \varepsilon I$, making the results transportable to other photobioreactor geometries, such as tubular photobioreactors [96, 62].

Part III

Neural differential equations for microalgae modelling and control

Chapter 7

NeuralODEs for microalgae growth modelling

7.1 Introduction

Microalgae are commonly cultivated in photobioreactors (PBRs) using solar or artificial light. These PBRs vary in geometry, size, hydrodynamics, light distribution, CO_2 source, and mode of operation; they can be open, like raceway ponds, or closed systems, like tubular PBRs. Various factors affect these microorganisms' growth; therefore, monitoring and predicting the biomass evolution of a microalgae culture in a PBR is a challenging problem, and the system dynamics result from the complex interplay between species, PBR design, and operational model. The evolution of microalgal biomass inside a PBR can be modelled using ordinary differential equations, relying either on kinetic.[19, 120] or data-driven models [54, 126].

The distribution of photons is not uniform inside the PBR due to the self-shading and scattering caused by the microalgae cells; second, the light distribution is highly dependent on the photobioreactor's geometry. Besides that, a mixing device is always present to ensure the nutrients are evenly distributed, and hydrodynamics is also a factor.

A perfect mixed bioreactor is one of the most common assumptions in modelling the biomass evolution of microorganisms such as bacteria or yeast. In the case of microalgae, the mixing affects the number of photons that each cell perceives. As a strong irradiance gradient is present, a cell can go from a very bright to a very dark area, affecting the growth rate. The problem is even more tricky since microalgae adapt to their environment and can modify physiological characteristics such as pigment quality and quantity, cell size, or other factors influencing growth and light distribution.

Kinetic models within kinetic approaches outline how microalgae respond to the growth-controlling factor, encompassing variables such as light, temperature, and nutrients [37], neglecting many other possible influences. Machine and Deep learning can have better prediction and fitting capabilities than kinetic models since they can indirectly account for many effects that need to be better understood. However, machine learning models depend heavily on the quality and the number of

data, which strongly restricts their use [157]. Hybrid modelling has been proposed to offset the advantages of data-driven-based and kinetic modelling approaches [107]. This method incorporates neural networks into differential equations to estimate parameters that can change in different situations. Hybrid models have better interpretability and extrapolation properties. Furthermore, they are data efficient and do not require large datasets for training [150].

Neural Ordinary Differential Equations (NeuralODEs) [30] were introduced as a continuous depth neural network, in which the input is continuously transformed in the vector field defined by the Neural ODE. They are widely employed to solve problems such as image classification, physical modelling, and continuous normalizing flows. They can learn the dynamics of a differential equation with its trajectories without estimating the derivative from the data.

This chapter studies two models based on neuralODEs fed by the irradiance perceived by a soft sensor and temperature, two external factors crucial in a microalgae culture. We implement a solver based on the Runge-Kutta neural network [151, 101].

7.2 Methods

7.2.1 The general neural ODE model

We consider two types of variables: the internal variables (or state variables) $\boldsymbol{x} \in \mathbb{R}^{n_x}$ that evolve in time following a specific ordinary differential equation and the external variables $\boldsymbol{y} \in \mathbb{R}^{n_y}$ that affect the dynamics of $\boldsymbol{x}$.

We are interested in the evolution of the variables $\boldsymbol{x}$, for example, the concentration of microalgal biomass or the concentration of nutrients inside the photobioreactor. The variables $\boldsymbol{y}$ affect the evolution of the internal variables; however, they act mainly as data, for example, the light intensity that illuminates the photobioreactor or the temperature, which is usually controlled.

Let us consider the system:

$$\frac{d\boldsymbol{x}(t)}{dt} = f_{\boldsymbol{\Omega}}(t, \boldsymbol{y}(t), \boldsymbol{x}(t)), \tag{7.1}$$

where $f_{\boldsymbol{\Omega}} : [0, +\infty) \times \mathbb{R}^{n_y} \times \mathbb{R}^{n_x}$ is the dynamics of the system, $\boldsymbol{\Omega} = (\boldsymbol{\theta}, \boldsymbol{\omega})$ are the parameters split into two types, $\boldsymbol{\theta}$ denotes the parameters of a neural network (weights and biases) and $\boldsymbol{\omega}$ denotes the other parameters, not included in the neural network. The parameters contained in $\boldsymbol{\omega}$ have a physical interpretation, but they are not necessarily known, meaning that they need to be tuned to fit the model to the data; these are the physic-informed parameters.

7.2.2 The integrator cell

Recurrent neural networks (RNNs) are a class of ANN suitable for dynamic systems; they have been used successfully to deal with dynamic systems problems [8]. In addition, RNN handles the sequence of inputs which can be of any length. As in [148], to solve the equation (7.1), we implement an RNN where the hidden state is the numerical solution given by a Runge-Kutta scheme [117] which is usually called Runge-Kutta RNNs [100, 151]. Any explicit Runge-Kutta method applied

to the equation (7.1) can be described as

$$
\begin{aligned}
\boldsymbol{x}_{n+1} &= \boldsymbol{x}_n + \Delta t_n \sum_{i=1}^{s} b_i \boldsymbol{k}_i, \\
\boldsymbol{k}_1 &= f_{\boldsymbol{\Omega}}(t_n, \boldsymbol{y}_n, \boldsymbol{x}_n), \\
\boldsymbol{k}_2 &= f_{\boldsymbol{\Omega}}(t_n + c_2 \Delta t_n, \boldsymbol{y}_n + c_2 \Delta \boldsymbol{y}_n, \boldsymbol{x}_n + (a_{21}\boldsymbol{k}_1)\Delta t_n), \\
\boldsymbol{k}_3 &= f_{\boldsymbol{\Omega}}(t_n + c_3 \Delta t_n, \boldsymbol{y}_n + c_3 \Delta \boldsymbol{y}_n, \boldsymbol{x}_n + (a_{31}\boldsymbol{k}_1 \\
&\qquad + a_{32}\boldsymbol{k}_2)\Delta t_n), \\
&\vdots \\
\boldsymbol{k}_s &= f_{\boldsymbol{\Omega}}(t_n + c_s \Delta t_n, \boldsymbol{y}_n + c_s \Delta \boldsymbol{y}_n, \boldsymbol{x}_n + (a_{s1}\boldsymbol{k}_1 \\
&\qquad + a_{s2}\boldsymbol{k}_2 + \cdots + a_{s,s-1}\boldsymbol{k}_{s-1})\Delta t_n).
\end{aligned}
\tag{7.2}
$$

where $(t_n)_n$ is a discretization of the time window $[0, T_f]$, $\Delta t_n = t_{n+1} - t_n$, $\Delta y_n = \boldsymbol{y}_{n+1} - \boldsymbol{y}_n$, s denotes the number of stages, and the coefficients $(a_{ij})_{1 \le j < i \le s}, (b_i)_{i=1}^{s}$ and $(c_i)_{i=2}^{s}$ are fixed and determine the method. The Runge-Kutta Neural Network is illustrated in figure 7.1.

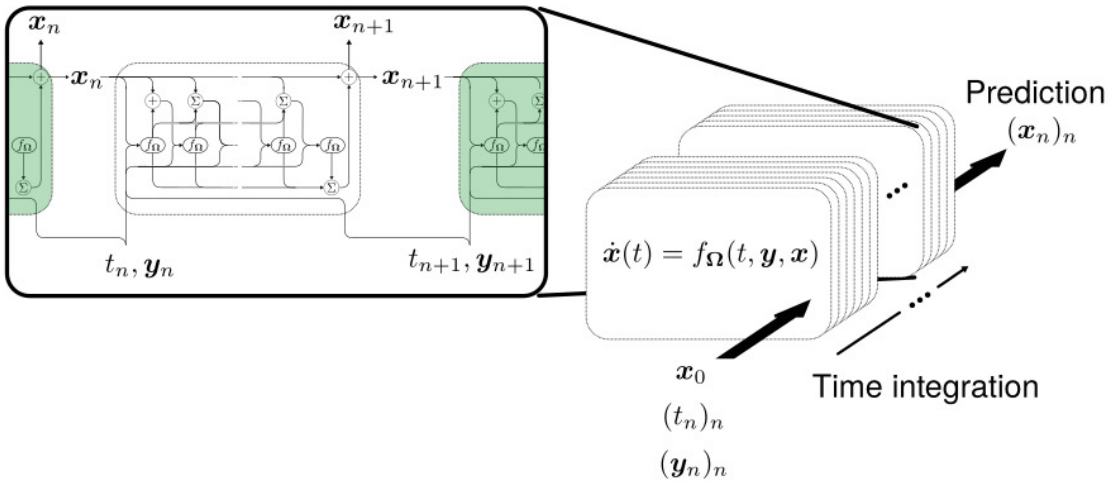

Figure 7.1: The integrator cell corresponds to an explicit Runge-Kutta method implemented as a recurrent neural network. The collection of all the hidden states corresponds to the numerical solution of the equation (7.2).

7.2.3 Training the model

Let us consider the loss function

$$
L(\boldsymbol{\Omega}) = \int_0^{T_f} g(\boldsymbol{x}(t), \hat{\boldsymbol{x}}(t)) dt,
$$

where T_f is the time horizon and g is a smooth function that takes into account the difference between the predictions of the model and the data, in our case we use $g = (\boldsymbol{x} - \hat{\boldsymbol{x}})^2$, with $\hat{\boldsymbol{x}}$ the training data.

To train the parameters $\boldsymbol{\Omega}$ of the model, we use a gradient-descent type algorithm with automatic differentiation and the backpropagation algorithm [153]. We present two methods: the direct one, where backpropagation is applied to the internal operations of the solver of the equation (7.1), and the adjoint method, which computes the gradient of the loss function based on the Lagrangian multipliers of the minimization problem.

7.2.4 Sensitivity equations

Given a loss function $L(\boldsymbol{\Omega})$ between the solution of equation (7.1). For the optimization (or learning) process, it is necessary to compute the gradient:

$$\frac{\partial L}{\partial \boldsymbol{\Omega}} = \frac{\partial L}{\partial \boldsymbol{x}} \frac{\partial \boldsymbol{x}}{\partial \boldsymbol{\Omega}},$$

where, assuming that the solution of (7.1) is $\mathcal{C}^2$, we have:

$$\frac{d}{dt}\left(\frac{\partial \boldsymbol{x}}{\partial \boldsymbol{\Omega}}\right) = \frac{\partial f_{\boldsymbol{\Omega}}}{\partial \boldsymbol{x}} \frac{\partial \boldsymbol{x}}{\partial \boldsymbol{\Omega}} + \frac{\partial f_{\boldsymbol{\Omega}}}{\partial \boldsymbol{\Omega}}, \tag{7.3}$$

which are the so-called sensitivity equations. As the initial condition $\boldsymbol{x}(t = 0)$ is independent of the parameters $\boldsymbol{\Omega}$, the initial condition of equation (7.3) is always zero. This equation was solved to train early hybrid models [119, 131, 58] applied to biotechnology. In practice, these equations are not solved directly because the number of equations is the number of parameters. As any forward Runge-Kutta method is composed of successive evaluations of a linear combination of the function $f_{\boldsymbol{\Omega}}$, we can prove that the sensitivity equations are solved through backpropagation. Considering the interpolation of the external variables $\boldsymbol{y}$, the proof is presented in Appendix 1.

7.2.5 Direct method

Employing backpropagation in the internal operations of the solver is called *Direct method*, and we resume the method in the Algorithm 1. The numerical scheme is attached to the directed acyclic graph (DAG) used to implement automatic differentiation (AD) when the backpropagation algorithm is called, which implies that memory usage increases. The most significant benefit of this model is that it is easy to implement. The number of gradients $\frac{\partial f_{\boldsymbol{\Omega}}}{\partial \boldsymbol{x}}$ computed is in the order of sN_T, where N_T is the number of time steps and s the order of the Runge-Kutta method. This is not suitable if deep architectures or higher-order solvers are considered.

7.2.6 Adjoint method

The adjoint method is another way to avoid the computation of the gradients $\frac{\partial \boldsymbol{x}}{\partial \boldsymbol{\Omega}}$ whose complexity scales with the number of parameters of the model, i.e., the weights and the biases of the neural network and the physical parameters. In this case, we solve a differential equation whose dimension is equal to n_x following the next result:

Algorithm 1 Direct Method

Require: n_epochs.
  for i in range(n_epochs) **do**
    Solve forward $\dot{\boldsymbol{x}}(t) = f_{\boldsymbol{\Omega}}(t, \boldsymbol{y}(t), \boldsymbol{x}(t))$.
    Compute loss $L(\boldsymbol{x}, \boldsymbol{\Omega})$.
    Compute $\frac{\partial L}{\partial \boldsymbol{\Omega}}$ using backpropagation.
    Make gradient descent step.
  end for

Proposition 7.1

Assuming that the solution $\boldsymbol{x}$ of the equation (7.1) is $\mathcal{C}^2$ (for example, if the dynamics $f_{\boldsymbol{\Omega}}$ is $\mathcal{C}^1$). The gradient of the loss function is given by

$$\frac{\partial L(\boldsymbol{\Omega})}{\partial \boldsymbol{\Omega}} = \int_0^{T_f} \boldsymbol{\lambda}^\intercal(t) \frac{\partial f_{\boldsymbol{\Omega}}(t, \boldsymbol{y}(t), \boldsymbol{x}(t))}{\partial \boldsymbol{\Omega}} dt, \tag{7.4}$$

where $\boldsymbol{\lambda}^\intercal$ is the solution of the equation:

$$\begin{cases} \dfrac{d\boldsymbol{\lambda}^\intercal}{dt} = -\boldsymbol{\lambda}^\intercal \dfrac{\partial f_{\boldsymbol{\Omega}}}{\partial \boldsymbol{x}} - \dfrac{\partial g}{\partial \boldsymbol{x}}, \\ \boldsymbol{\lambda}^\intercal(T_f) = 0. \end{cases} \tag{7.5}$$

Proposition 7.1 allows us to compute the gradient of the loss function without backpropagation on the integrator cell, which is expensive for higher-order methods or large time series. Based on this proposition, the training method is resumed in Algorithm 2. For the sake of completeness, we present this method using the Lagrangian theory [114] in B.2.

This method offers some advantages compared with direct backpropagation in the integral cell. First, the solution $\boldsymbol{x}$ must not be computed with the directed acyclic graph (DAG) employed for automatic differentiation (AD). Then, the gradients $\frac{\partial f_{\boldsymbol{\Omega}}}{\partial \boldsymbol{x}}$ and $\frac{\partial g}{\partial \boldsymbol{x}}$ can be computed using AD with the solution $\boldsymbol{x}$ detached from the DAG. This implies that the amount of gradient computed does not scale with the order of the numerical scheme used.

One disadvantage is the accumulation of numerical discretization errors. To solve numerically the backward equation (7.5), the starting point is the value of $\boldsymbol{x}(T_f)$, which already has a numerical error associated with it from solving the forward equation (7.1).

7.2.7 Description of the dataset

The microalgae *Phaeodactylum tricornutum* UTEX 640 was cultivated for about 60 days under natural light in five 180L flat-panel airlift (FPA) photobioreactor from the company Subitec® [138] in a greenhouse in Leuna, Germany, from July to September 2015 (see Figure 7.4). The temperature, pH level, and substrate feeding of the FPA-PBRs were controlled by Siemens programmable logic

Algorithm 2 Adjoint Method

Require: n_epochs.
  for i in range(n_epochs) **do**
    Solve forward $\dot{\boldsymbol{x}}(t) = f_{\boldsymbol{\Omega}}(t, \boldsymbol{y}(t), \boldsymbol{x}(t))$.
    Solve backward $\dot{\boldsymbol{\lambda}}^\intercal + \boldsymbol{\lambda}^\intercal \frac{\partial f_{\boldsymbol{\Omega}}}{\partial \boldsymbol{x}} + \frac{\partial g}{\partial \boldsymbol{x}} = 0$.
    Compute $\frac{\partial L(\boldsymbol{x}, \boldsymbol{\Omega})}{\partial \boldsymbol{\Omega}} = \int_0^{T_f} \boldsymbol{\lambda}^\intercal(t) \frac{\partial f_{\boldsymbol{\Omega}}}{\partial \boldsymbol{\Omega}} dt$.
    Make gradient descent step.
  end for

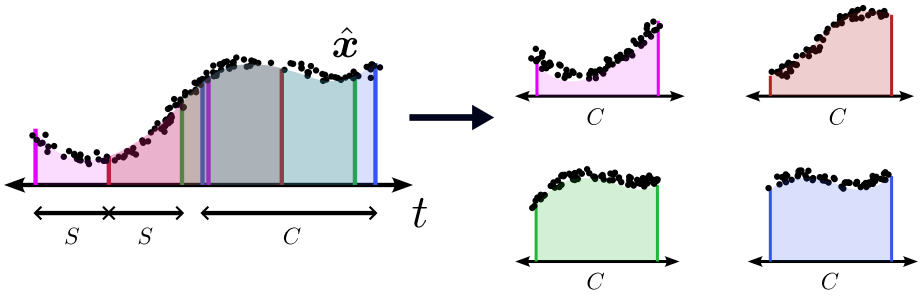

Figure 7.2: Illustration of the cropping process for data augmentation. The first batch is obtained from the first C data points; the second batch selects the C data points after a stride S starting from the initial point; the third one corresponds to the C data points after twice S from the initial point, and so on the following ones. The last C data points are also added. Then the sequence is split into batches of the same length C, covering all the original time vectors. Then the small batches are used to train the model solving equation (7.1) with the respective initial condition.

controller (PLC units). The culture was carried out in a repeated-batch manner using a modified Mann and Myers medium [88].

Temperature and pH were maintained controlled at 20 ± 1 °C and 7.3 ± 0.1 , respectively. Across all the cultivation, additional ammonium and phosphate solutions were introduced as nutritional sources, and nutrients are not considered as limiting factors (nutrients do not affect the evolution of the biomass). The online measurements were recorded every 10 minutes. A turbidity sensor was used to measure the biomass concentration. An LI-190R Quantum sensor measured the Photosynthetically Active Radiation (PAR), which is the light intensity. The data is illustrated in Figure 7.3.

In a batch PBR, the reactor is filled with the nutrient media and the microorganisms are introduced; after some time, the biomass is harvested; during this period, no nutrients are added. In this case, the biomass inside the PBR, denoted with x, follows the growth equation.:

$$\frac{dx}{dt} = \mu x, \tag{7.6}$$

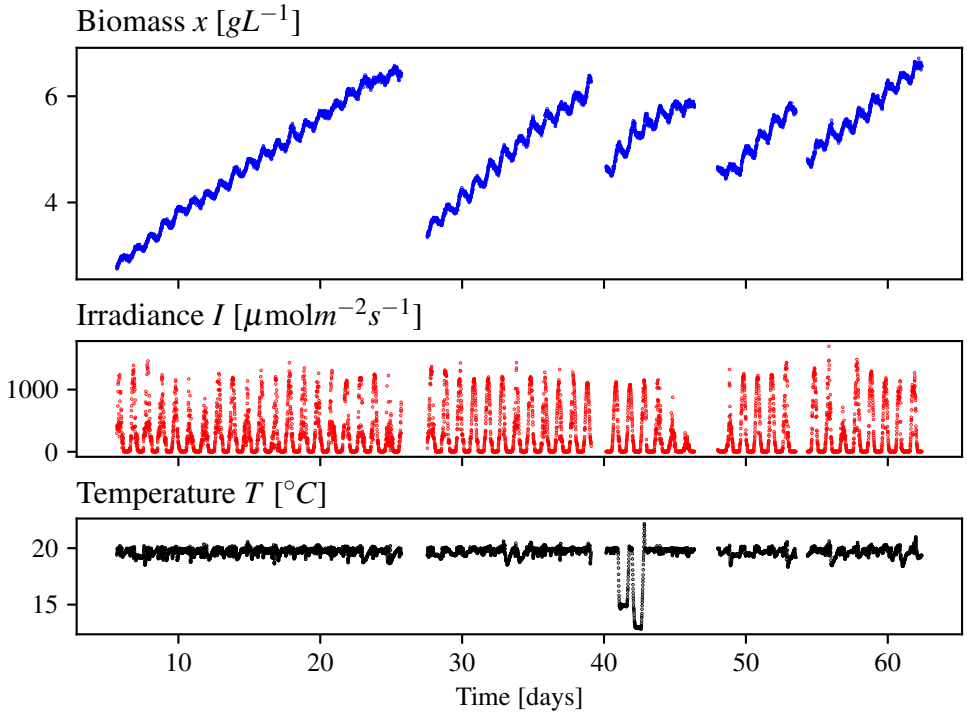

Figure 7.3: Measured biomass, irradiance, and temperature for batch cultivation of *Phaeodactylum tricornutum* in a flat-panel airlift photobioreactor.

7.2.8 Data augmentation and mini-batch training

Effectively training neural networks is commonly a challenging task that encounters several problems. Mini-batch training strongly influences the optimization performance [135]. Also, data augmentation can be a determinant for successfully training models for solving time series-related tasks [152]. Considering the theorem of existence and uniqueness of solutions of ordinary differential equations, the natural data augmentation technique consists of cropping the time window of the time series. The differential equation (7.1) is solved using the new initial condition (the starting point of the cropped sequence).

Let us consider one time-serie denoted by $(t_i, \hat{\boldsymbol{y}}_i, \hat{\boldsymbol{x}}_i)_{i=0}^{N}$. We choose two numbers, the crop size $C \leq N$ and the stride S. From the same time series we generate a sequence of smaller batches, all of them with the same size C as $(t_i, \hat{\boldsymbol{y}}_i, \hat{\boldsymbol{x}}_i)_{i=0}^{C-1}$, $(t_i, \hat{\boldsymbol{y}}_i, \hat{\boldsymbol{x}}_i)_{i=S}^{C+S-1}$, $(t_i, \hat{\boldsymbol{y}}_i, \dots)$, $(t_i, \hat{\boldsymbol{y}}_i, \hat{\boldsymbol{x}}_i)_{i=rS}^{C+rS-1}$, with the condition $C + (r+1)S - 1 > N$, where r is the number of strides of size S that we can make. Also, we add the end of the time series, including the sequence $(t_i, \hat{\boldsymbol{y}}_i, \hat{\boldsymbol{x}}_i)_{i=N-C-1}^{N}$. Eventually, it results in a total of $r+1$ mini-batches extracted from a one-time series. This process is repeated for every time series. We illustrate the process in Figure 7.2.

Name	t_0 [day]	t_f [day]	Data points
Batch 1	5.66	25.71	2889
Batch 2	27.54	39.08	1664
Batch 3	40.15	46.36	897
Batch 4	48.01	53.51	793
Batch 5	54.34	62.39	1161

Table 7.1: Details of the dataset.

Figure 7.4: Flat panel photobioreactor where the microalgae were cultivated.

7.2.9 First model: NN as growth function

We assume that the biomass x in the photobioreactor follows the growth equation:

$$\frac{dx}{dt} = \mu_{\boldsymbol{\theta}}(I, T, x)x, \tag{7.7}$$

where μ corresponds to the output of an artificial neural network. This is the simplest model for microorganisms. Using the change of variable $z = \ln(x)$, we have that equation (7.7) can be

rewritten as

$$\frac{dz}{dt} = \mu_{\boldsymbol{\theta}}(I, T, z).$$

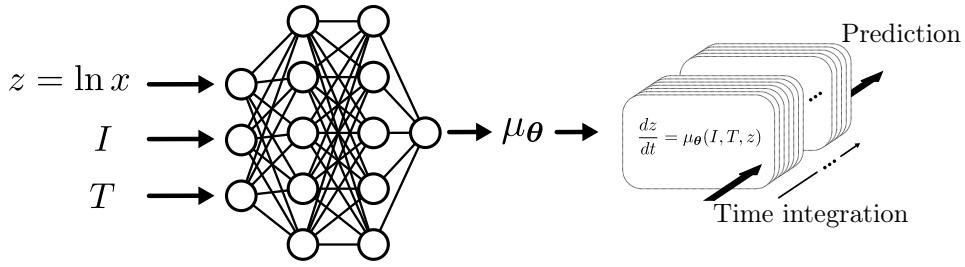

Figure 7.5: Schematic representation of the model (7.7) using a neural network composed of two hidden layers.

We use a NN with three hidden layers, five nodes each. The crop size $C = 700$, stride $S = 100$, and batch size equal to 5. Using the Adam optimizer [80] with 3000 epochs, and the `MultiStepLR` learning rate scheduler implemented in `PyTorch`, starting with a learning rate of 0.01, multiplied by the coefficient $\gamma = 0.3$ in the milestones $[600, 1200, 2500]$.

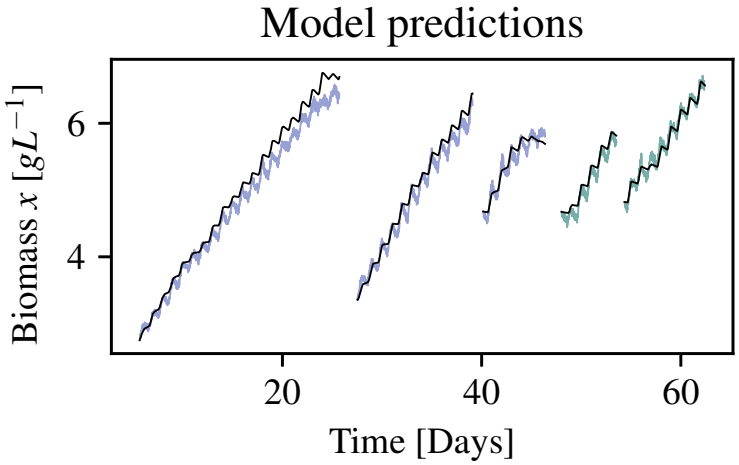

Figure 7.6: Predictions of the Model 7.7 in black. Training set in blue, test set in green.

7.2.10 Second model: Using NNs to correct bias of kinetic model

Some parameters during cultivation can be regulated, such as temperature, which does not vary significantly (see Figure 7.3). For the second model, we start from a kinetic one that describes the influences of the light using a Monod-like function and the averaged irradiance inside the photo-

bioreactor [14] assuming that the geometry is completely flat and the light penetrates perpendicular to the surface of the PBR. This model is given by the equation:

$$\frac{dx}{dt} = g_{\boldsymbol{\omega}}(I, x) = \frac{\mu_{\max}}{kx^b L} \ln\left(\frac{I + K_I}{Ie^{-kx^b L} + K_I}\right) x - Rx, \tag{7.8}$$

where R is the specific maintenance rate, $\mu_{\max}$ the maximal growth rate, K_I the half saturation rate of irradiance, L the depth of the PBR, k and b two constants for the light gradient. In this case, $\boldsymbol{\omega} = (\mu_{\max}, k, b, K_I, R)$ are the physical parameters of the model. These parameters are also trained using gradient descend methods. In this case, the kinetic model is only driven by light, which has a much greater influence than temperature on the growth rate. More details about this model can be found in B.3. This model is trained in a first step using also a gradient descend algorithm. Then a neural network denoted by $\varepsilon_{\boldsymbol{\theta}}$ is added to the dynamics as follows:

$$\frac{dx}{dt} = g_{\boldsymbol{\omega}}(I, x) + \varepsilon_{\boldsymbol{\theta}}(I, T, x), \tag{7.9}$$

where $\boldsymbol{\theta}$ represents the parameters (weights and biases) of the neural network. The objective of this NN is to bridge the gap between the pure mechanistic model (the same equation without the output of the NN) and the data. This process of two-step training is needed due to the difference of scales of the gradients $\frac{\partial L}{\partial \boldsymbol{\omega}}$ and $\frac{\partial L}{\partial \boldsymbol{\theta}}$ [79].

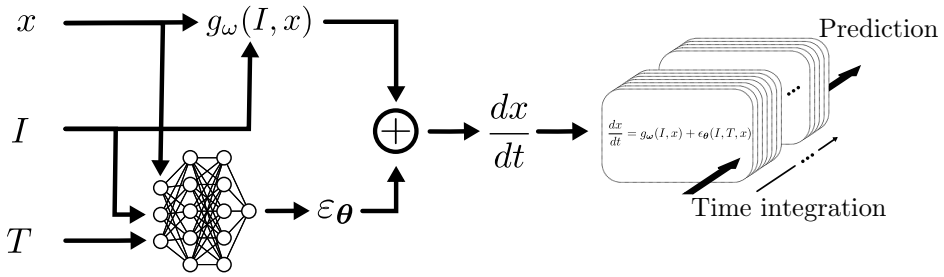

Figure 7.7: Schematic representation of the model (7.8), where the neural network is turned off, and the model (7.9), where the neural network is trained after fixing the physical parameters $\boldsymbol{\omega}$.

The NN $\varepsilon_{\boldsymbol{\theta}}$ contains 2 hidden layers, each containing 5 nodes. We use the same data loader with $C = 700$ and $S = 100$. For both training steps, we use the same learning scheduler as in the example one but with different $\gamma = 0.2$.

7.2.11 Implementation in other libraries

In this section, we discuss how to implement the model using a well-known package in the machine learning community. *Torchdyn* [113] is a library dedicated to neural differential equations, based on the model:

$$\frac{d\boldsymbol{x}(t)}{dt} = f_{\boldsymbol{\Omega}}(t, \boldsymbol{x}(t)).$$

In our case, the data presented in Figure 7.3 is composed by 5 different batches. Each of these batches presents different light and temperature regimes, then we have 5 different non-autonomous

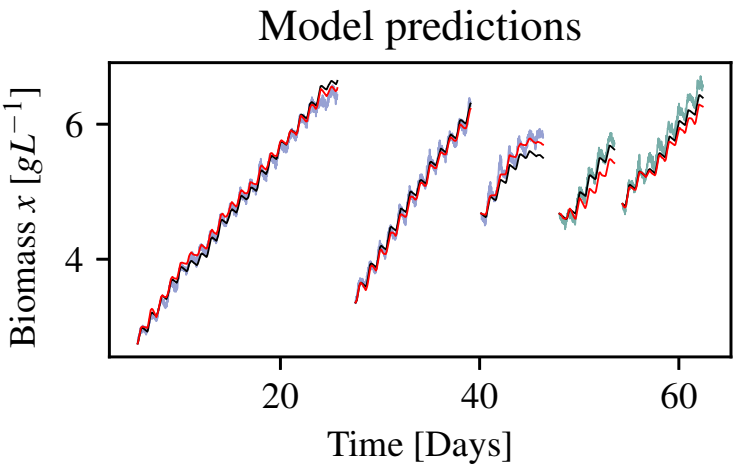

Figure 7.8: The continuous black line and the continuous red line correspond to the predictions of the model (7.8) and model (7.9) respectively. Train set is coloured in blue and the test set in green. The details of the error of each batch is shown in Table 7.3.

dynamics. To train the growth function $\mu_{\boldsymbol{\theta}}$ of the model (7.7), using the package *torchdyn* [113], we define for each $i = 1, .., 5$, a neuralODE as

$$\frac{dx}{dt} = \mu_{\boldsymbol{\theta}}(I^i(t), T^i(t), x(t))x(t) \quad \text{for } t \in (t_0^i, t_f^i), \tag{7.10}$$

where I^i, T^i are the functions defining the light and temperature from the instance t_0^i and t_f^i for the i batch. We call equation (7.10) a BatchNeuralODE.

The function I^i and T^i are computed interpolating the data of light and temperature over time. All BatchNeuralODE share the same growth function μ. Then, for each batch, mini-batch training is possible using sub-intervals of its time interval $[t_0^i, t_f^i]$.

7.2.12 Comparison with a Support Vector Regression approach

Support Vector Regression (SVR) is a classical machine learning algorithm that can be applied to linear and nonlinear regression problems [136]. In a previous work [156], using the same data set, an SVR approach was used with 12-h of light history data, which correspond to 72 data points (see Figure 7.3 and Table 7.1). The regression was carried out using a nonlinear Gaussian kernel and a kernel scale set at 2.2. The input data underwent standardization, where each feature was scaled using its mean and standard deviation. The training process involved one batch, while four batches were utilized for evaluation. The growth rate μ in equation (7.6) is replaced by the SVR model and then trained using the discrete difference of the biomass.

Our approach does not consider the previous 12 hours of light and aims to predict the growth rate based on the actual light intensity. Additionally, while [156] incorporated various filtering

techniques, such as Gaussian filtering. In the models presented here, there is no necessity to smooth the data, but it can be easily integrated. The comparative analysis between the SVR approach and the three models across different factors is presented in 7.2. Furthermore, 7.3 illustrates the varying performance of both models across different batches and model iterations.

Factor	**SVR**	**Models** (7.7),(7.8) & (7.9)
Input	Utilized past 12 hours of light intensity data	Instant light intensity
Preprocessing	Gaussian filtering technique	No preprocessing
Train test ratio	1 Batch for training	3 batches for training

Table 7.2: The comparison of SVR and the hybrid model in terms of various factors

7.3 Results and Discussions

The models are compared using the root mean squared error (RMSE) between their predictions and the real measurements from the turbidity sensor, and is calculated batch by batch as follows:

$$\text{RMSE} = \sqrt{\frac{1}{N}\sum_{i=1}^{N}(x_i - \hat{x}_i)^2}.$$

Also, we compared the error in percentage computed as

$$\text{Percentage error} = 100 \cdot \frac{1}{N}\sum_{i=1}^{N}\frac{|x_i - \hat{x}_i|}{\hat{x}_i}.$$

The results are resumed in Table 7.3, where the error is computed for each batch of the experiment. The predictions of the first model (7.7), represented in black in Figure 7.5, have an error of less than 1% in each batch. However, the model cannot predict negative values of the derivate at the beginning of the first batch. It has, on average, a good performance, but from the biological point of view, there is a phenomenon that is not that it fails to identify on its own, known as respiration or maintenance rate. During the night, microalgae lose biomass through respiration. This phenomenon is imposed in model (7.8) and (7.9).

The fully kinetic model (7.9) is trained successfully with the ADAM algorithm; no constraints were imposed for the optimization process. Nevertheless, the values of the parameters $\boldsymbol{\omega}$ obtained were in the range of the literature. The model (7.9) appears after adding and training the neural network $\varepsilon_{\boldsymbol{\theta}}$, whose predictions are represented with red lines. The error is reduced in the training set and increases in the testing set. This overfitting can be caused by the low influence of the temperature, which is controlled and almost constant, except for the third batch, which had a drop in temperature on two consecutive days.

As the kinetic model does not consider temperature and the neural network does, the latter forces the dynamics to accommodate this temperature change by improving the prediction on the

third batch. But at the same time, as is controlled, including temperature in the model also drives overfitting.

To compare the models presented here, a Support Vector Regression (SVR) based soft sensor was developed to compare the performance with the Hybrid model. The RMSE and the percentage error are reported in the Table 7.3

	Model	Training dataset			Test dataset	
		Batch 1	Batch 2	Batch 3	Batch 4	Batch 5
RMSE	(7.7)	0.012	0.015	0.020	0.015	0.019
	(7.8)	0.086	0.067	0.186	0.078	0.140
	(7.9)	0.077	0.078	0.089	0.215	0.209
	SVR	0.021	0.093	0.054	0.05	0.078
Percentage	(7.7)	0.700	0.827	0.978	0.745	0.986
	(7.8)	1.345	1.146	2.896	1.258	2.087
	(7.9)	1.408	1.296	1.316	3.412	3.028
	SVR	1.23	1.29	1.23	1	1.02

Table 7.3: RSME and the percentage error of the models in every batch of the dataset.

7.4 Conclusions

NeuralODEs are efficient in monitoring biomass evolution inside a photobioreactor. Two models, including neural networks, were tested; the first one (7.7) represents the growth rate of the microalgae by a neural network, and the second one (7.9) uses a neural network to correct the bias of a kinetic model (7.8) based on the literature.

The models were implemented in the integrator cell described in Section 7.2.2, which includes data interpolation while solving the differential equations in batch. For completeness, we present the theory of the gradient computations. In addition, we give the directions to implement the model using *Torchdyn*, the state-of-the-art library for solving neuralODEs problems.

Standard techniques for training neural networks were used as mini-batch training and implementing learning rate schedulers. The mini-batch training is enabled by cropping the data from the batches used. In the case of the model (7.9), a two-step training was used to ensure the kinetic model's interpretability. The accuracy is comparable with other machine learning models.

This type of models results to be suitable for the modelling of biomass evolution within a photobioreactor due to the large amount of factors that influence the growth rate. Different and complex photobioreactors geometries make it difficult to model microalgae growth. The method presented here can be very useful for bioprocesses that need rapid monitoring, which is carried out with sensors that often have to be constantly recalibrated (as for light sensors).

Chapter 8

Solving optimal control problems using neural differential equations

8.1 Introduction

After the development of neuralODEs [30] and PINNs [121], a new variety of models have been emerged. These types of models are gray boxes that mix the (physic, chemical, biologic) interpretation with the adaptive ability of artificial neural networks. While physical (chemical, or biological) laws can be written in the form of differential equations, some parts of these equations are not easy to identify, where artificial neural networks can act as functions that can recognize such components by offering more interpretation than the mere use of a pure machine learning method. This is an identification or modelling problem. But we can also use the artificial neural networks to study optimization problems. In this chapter, we focus on the connection between optimal control problems and neural networks. Recently, the use of neural networks to solve optimal control problems have attracted the attention of the control community [48, 12, 31, 112], but few papers discuss the solutions offered by neural networks when used as controls for dynamic systems.

Non-linear optimal control problems arise in various fields, including engineering, economics, biology, etc. There are many techniques to tackle this type of problem. For example, Pontryagin's maximum principle (PMP) is a tool that provides necessary conditions of optimality based in the co-states of the system. Regarding artificial neural networks in control problems, different strategies have been proposed in the literature to solve optimal control problems with them, and they depend on how the neural network is used. For example, an error function can contain PMP conditions [48, 47] and then be minimized, or we can approximate the solution of the Hamilton-Jacobi-Bellman (HJB) differential equation using a base of neural networks [32]. Another more recent approach involves approximating the solution of HJB equation with a PINNs approach, where the cost function contains the discretized scheme for solving the differential equations of the HJB equations [129, 130].

Solving optimal control problems with neural networks can be classified as *Parameterization methods*. Based on their popular ability of universal approximator, several results can be found

in the literature involving neural methods [93, 128, 147]. The comparison between the solution provided by a neural network and the actual optimal control identified with an analytic approach such as the PMP has rarely been studied, especially when the structure of the optimal solution is discontinuous, as in the case of singular controls.

In this chapter, we study the case where the control of the systems is replaced by an artificial neural network, also called *neural control*. In this case, it is possible to establish a relation between the PMP conditions and the training of the neural control [23]. This relationship is shown when the gradient of the parameters of the neural control is computed via variational methods [12].

8.2 Materials and methods

We consider the following optimal control problem with free final conditions and fixed time horizon:

$$\begin{aligned} \min_{\mathbf{u}\in\mathcal{U}} \quad & J_{[0,T]}(\mathbf{u}) = \int_0^T g(t,\mathbf{z}(t),\mathbf{u}(t))dt, \\ \text{subject to } & \dot{\mathbf{z}}(t) = f(t,\mathbf{z}(t),\mathbf{u}(t)), \\ & \mathbf{z}(0) = \mathbf{z}_0, \end{aligned} \tag{P}$$

where $T > 0$ is fixed, $\mathbf{z}(t) \in \mathbb{R}^n$ is the state vector with the initial condition $\mathbf{z}_0 \in \mathbb{R}^n$, $\mathbf{u} \in \mathbb{R}^m$ is the control vector, f and g are assumed to be $\mathcal{C}^1$ from $\mathbb{R}^{1+n+m}$ to $\mathbb{R}^n$. $\mathcal{U}$ corresponds to the set of admissible controls defined as

$$\mathcal{U} = \mathcal{L}^\infty_{\text{loc}}([0,+\infty), C),$$

i.e., the set of locally integrable functions on every compact set in $[0,\infty)$ that take values in the compact set $C \subset \mathbb{R}^m$ defined as

$$C = \prod_{j=1}^{m} [a_j, b_j],$$

where a_i, b_i are the lower and upper bounds of $\mathbf{u}_i$.

8.2.1 Bounded neural controls

A simple way to include the box constrains is using the squashing function α in the last layer of the architecture of the neural network [89, 142]. More precisely, let consider the feedforward neural network defined as follows. Denote $d_1, ..., d_L$ the dimensions of the layers, $\theta = (W_1, b_1, ..., W_l, b_l)$ the weights, and the biases, where $W_l \in \mathbb{R}^{d_l \times d_l}$ and $b_l \in \mathbb{R}^{d_l}$. To be compatible with the optimal control problem, the input dimension is $d_1 = 1$ and the output dimension is $d_L = m$. Also, σ_l $l = 1, ..., L$ are the activation functions (as sigmoid, linear or ReLU) acting componentwise. The input layer has dimension one (corresponding to the time), and the output layer has dimension m. The last activation function is replaced by $\sigma_L = \alpha$, where α is defined as:

$$\begin{aligned} & \alpha : \mathbb{R}^m \to \mathbb{R}^m \\ & \theta = \begin{pmatrix} \theta_1 \\ \vdots \\ v_m \end{pmatrix} \mapsto \alpha(\theta) = \begin{pmatrix} (b_1 - a_1)\sigma(\theta_1) + a_1 \\ \vdots \\ (b_m - a_m)\sigma(\theta_m) + a_m \end{pmatrix}. \end{aligned} \tag{8.1}$$

Finally, a neural control u_θ can be defined as:

$$\mathbf{u}_\theta(t) = \alpha(W_L\sigma_{L-1}(\dots W_2\sigma_1(W_1 t + b_1) + b_2 \dots) + b_L), \tag{8.2}$$

We represent this model in Figure 8.1. The box constraints are imposed in the last layer of the architecture of the neural network, the resulting constrained control will approximate the optimal solution of the problem:

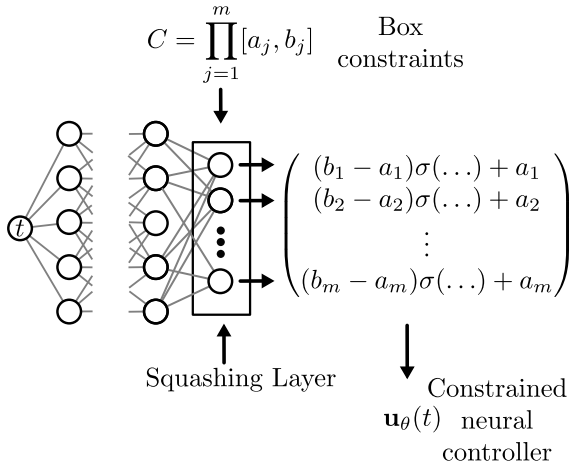

Figure 8.1: Scheme of the neural control with a squashing activation function. The output layer, that we call *Squashing Layer* is key to introduce the constraints of the optimal control problem.

When the control $\mathbf{u}$ is replaced by the parameterized control $\mathbf{u}_\theta$, we obtain the *Neural Optimal Control Problem* as

$$\begin{aligned} \inf_{\theta\in\mathbb{R}^p} J_{[0,T]}(\theta) &= \int_0^T g(t, \mathbf{z}_\theta(t), \mathbf{u}_\theta(t))dt, \\ \text{s.t.} \dot{\mathbf{z}}_\theta(t) &= f(t, \mathbf{z}_\theta(t), \mathbf{u}_\theta(t)), \\ \mathbf{z}_\theta(0) &= \mathbf{z}_0, \end{aligned} \tag{P_{NN}}$$

where $\mathbb{R}^p$ is the set of all possible parameters of the neural network. We cannot assure the existence of function minimizers, that's why we don't write the problem as $\min J(\theta)$. We will denote $v \in \mathbb{R}^m$ the input of the squashing activation function, *i.e.*, we write v as

$$v(t) = W_L\sigma_{L-1}(\dots W_2\sigma_1(W_1 t + b_1) + b_2 \dots) + b_L$$

Then, we have that

$$v_j(t) \to \infty \Leftrightarrow \mathbf{u}_{\theta,j}(t) \to b_j, \tag{8.3}$$

and

$$v_j(t) \to -\infty \Leftrightarrow \mathbf{u}_{\theta,j}(t) \to a_j. \tag{8.4}$$

Another way that can be used to bound a neural network is to *clip* the neural network into the box C. We can consider a neural network v_θ, with parameters θ and output dimension m, and define the neural control $\mathbf{u}^c_\theta$ as follows

$$[\mathbf{u}^c_\theta(t)]_j = \min(\max([v_\theta(t)]_j, a_j), b_j).$$

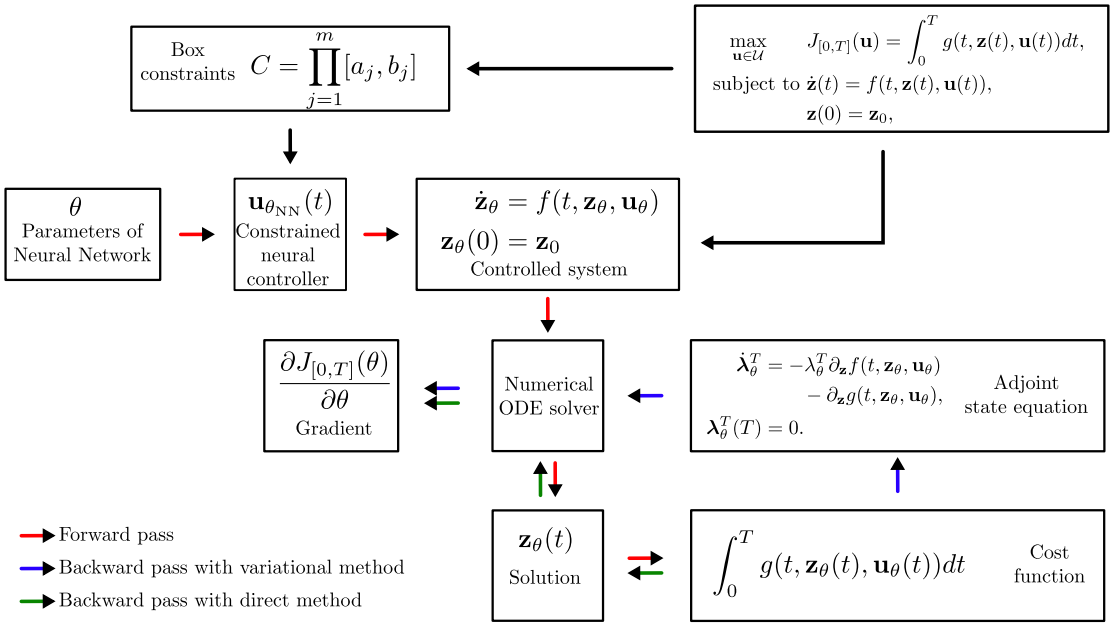

Figure 8.2: Scheme of the forward pass of the model and the two types of backward pass: the variational, solving the adjoint equation backward in time, and the direct one, where the backpropagation algorithm acts in the internal operations of the numerical solver.

However, the following problem exists: when the values of the neural network are larger or smaller than the bounds of the control, the gradients of the neural control $\mathbf{u}_\theta^c$ with respect to the parameters are zero. In practice, this lead to two problems:

- The initialization of the parameters. The weights and the bias of the neural network v_θ must be set in such a way that the initial guesses are inside the box C.
- At any point of the training, a large weight (or bias) update can push the output of the neural network v_θ outside the box C. This weight (or bias) will be *frozen* for the next steps of the optimization, affecting the ability to predict other values.

8.2.2 Gradient properties

Proposition 8.1

The gradient of the cost function $J_{[0,T]}(\mathbf{u}_\theta)$ with respect to the parameters θ is such that

$$\frac{\partial J_{[0,T]}(\theta)}{\partial \theta} = \int_0^T h_\theta(t) \frac{\partial \mathbf{u}_\theta(t)}{\partial \theta} dt, \tag{8.5}$$

where $h_\theta(t)$ is defined for every $t \in [0, T]$ as

$$h_\theta(t) = \boldsymbol{\lambda}_\theta^T \frac{\partial f(t, \mathbf{z}_\theta(t), \mathbf{u}_\theta(t))}{\partial \mathbf{u}} + \frac{\partial g(t, \mathbf{z}_\theta(t), \mathbf{u}_\theta(t))}{\partial \mathbf{u}},$$

with $\boldsymbol{\lambda}_\theta$ being the solution of the equation

$$\begin{cases} \dot{\boldsymbol{\lambda}}_\theta^T = -\boldsymbol{\lambda}_\theta^T \frac{\partial f(t, \mathbf{z}_\theta(t), \mathbf{u}_\theta(t))}{\partial \mathbf{z}} - \frac{\partial g(t, \mathbf{z}_\theta(t), \mathbf{u}_\theta(t))}{\partial \mathbf{z}}, \\ \boldsymbol{\lambda}_\theta(T) = 0. \end{cases} \tag{8.6}$$

The details of how to derive the equation (8.6) are presented in Appendix C. If we consider the neural control given by (8.2), the gradient $\frac{\mathbf{u}_\theta}{\partial \theta}$ is such that:

$$\frac{\mathbf{u}_{\theta,j}(t)}{\partial \theta} = \frac{(b_j - \alpha(v)_j)(\alpha(v)_j - a_b)}{(b_j - a_j)} \frac{\partial v_j(t)}{\partial \theta}.$$

Combining with (8.3) and (8.4), we have, for every $t \in (0, T)$:

$$\mathbf{u}_{\theta,j} \to b_j \Rightarrow \frac{\mathbf{u}_{\theta,j}}{\partial \theta} \to 0, \tag{8.7}$$

and

$$\mathbf{u}_{\theta,j} \to a_j \Rightarrow \frac{\mathbf{u}_{\theta,j}}{\partial \theta} \to 0. \tag{8.8}$$

Then we have that:

$$\mathbf{u}_{\theta,j} \to a_j \Rightarrow h_\theta(t) \frac{\partial \mathbf{u}_\theta(t)}{\partial \theta} \to 0,$$

and also

$$\mathbf{u}_{\theta,j} \to b_j \Rightarrow h_\theta(t) \frac{\partial \mathbf{u}_\theta(t)}{\partial \theta} \to 0.$$

If there exists a sequence of parameters θ^k such that $\mathbf{u}_{\theta^k} \to \mathbf{u}^*$, then

$$h_{\theta^k}(t) \to 0 \ \forall t \in [0, T],$$

which, by the dominated convergence theorem, it implies that

$$\frac{\partial J_{[0,T]}(\theta^k)}{\partial \theta} \to 0.$$

8.2.3 Numerical computation of the gradient

There are several ways to compute the gradient numerically. Here we make the difference between two methods:

Direct methods: The internal operations of the numerical method to solve the ODE are tracked in the directed graph of the automatic differentiation, then the gradient is computed using the backpropagation algorithm [153].

Variational methods: The gradient is computed using variational methods. An adjoint equation is solved, for example, Equation (8.6) is solved backward in time, *i.e.*, it is solved using the solution $\mathbf{z}_\theta(t)$ computed in the forward pass, and the final condition $\boldsymbol{\lambda}_\theta(T) = 0$. Then the gradient is computed using the identity (8.5).

8.3 Numerical Examples

8.3.1 A solver for Mayer problems

In order to write a solver for any optimal control problem, we convert the Lagrange problem (P_{NN}) into a Mayer problem (P_{Mayer}). This allows to write a simpler cost function.

$$\begin{aligned} \min_{\mathbf{u}\in\mathcal{U}} \quad & J_{[0,T]}(\mathbf{u}) = l(T), \\ \text{subject to } & \dot{\mathbf{z}}(t) = f(t, \mathbf{z}(t), \mathbf{u}(t)), \\ & \dot{l}(t) = g(t, \mathbf{z}(t), \mathbf{u}(t)), \\ & (\mathbf{z}(0), l(0)) = (\mathbf{z}_0, 0) \end{aligned} \tag{P_{Mayer}}$$

The package `TorchDyn` [113] is a neural differetial equations library that contains a variety of continuous-depth models. The computation of the gradient via direct method and adjoint methods are implemented, and they can be set using the `ODEProblem` class. The class *OCP*, described in Listing D.3, is an example of how to solve the optimal control problem using a gradient-based algorithm. This class needs the controlled dynamics $f(t, \mathbf{z}, \mathbf{u})$ written as a `nn.Module` from `Torch`, the initial conditions $\mathbf{z}_0$, the cost function $l(T)$ written as a function of the last value of the state $\mathbf{z}(T)$, the final time T_f, the control $\mathbf{u}_\theta$ which is previously set as a non-trained neural control.

8.3.2 A two hidden layers neural control

We write a neural control class consisting with two hidden layers and the squashing activation function in Listing D.1. The input of the neural control is one dimensional (corresponding to the time dimension). The object `TwoHidden` is constructed to receive as an input the box constraints. The squashing function described in Equation (8.1) corresponds to the function `alpha`.

8.3.3 Example 1: Simple Bang-Bang optimal control

We consider a single population x that grows exponentially at a growth rate μ, in a chemostat with dilution rate D (ratio of the renewable rate to the reactor volume). The population evolves following the equation

$$\dot{x} = \mu x - Dx,$$

where x denotes the concentration of microorganisms and, the harvesting rate is determined by the dilution rate D. The biomass harvesting rate is VDx (where V is the chemostat volume). The total harvested population during the operation period $[0, T]$ corresponds to

$$V \int_0^T D(t)x(t)dt. \tag{8.9}$$

As the volume V is considered as constant, the optimal problem, optimize (8.9) is equivalent to the problem

$$\begin{aligned} \max_{D\in\mathcal{L}^\infty_{\text{loc}}([0,T],[0,D_{\max}])} \quad & J_{[0,T]}(D) = \int_0^T xDdt \\ \text{s.t.} \quad & \dot{x} = (\mu - D)x, \\ & x(0) = x_0, \end{aligned} \tag{8.10}$$

where $D_{\max}$ is a positive constant. Considering a constant growth rate, the optimal control problem (8.10) has a solution given by Proposition 8.2

Proposition 8.2

The solution D^* of the problem (8.10) is given by

$$D^*(t) = \begin{cases} D_{\max} \text{ if } t > t_s, \\ 0 \text{ if } t \leq t_s, \end{cases} \tag{8.11}$$

where

$$t_h = \frac{\ln(D_{\max}/\mu)}{D_{\max} - \mu} \quad ; \quad t_s = T - t_h,$$

and, consequently, the optimal trajectory is given by:

$$x^*(t) = \begin{cases} x_0 e^{\mu t} \text{ if } t \geq t_s \\ x_0 e^{\mu t_s} e^{-(D_{\max}-\mu)t} \text{ if } t > t_s \end{cases} \tag{8.12}$$

and the value of the cost function is:

$$J_{[0,T]}(D^*) = \frac{x_0 D_{\max} e^{\mu t_s}(1 - e^{-(D_{\max}-\mu)t_h})}{D_{\max} - \mu}. \tag{8.13}$$

The proof of Proposition 8.2 is given in Appendix D.1.

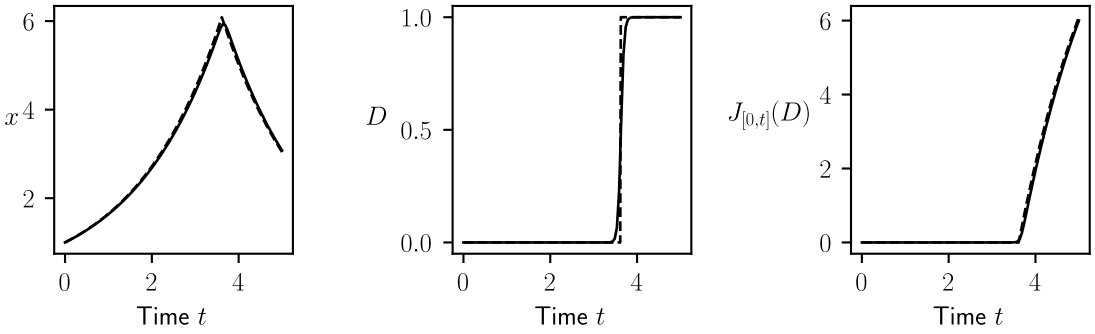

Figure 8.3: **Example 1**. Dashed line: theoretical solution. Continuous line: the solution given by $D_{w,b}$ after 10000 iterations.

The simplest single layer neural network with a sigmoid activation function is

$$D_{w,b}(t) = D_{\max}\sigma(wt + b), \tag{8.14}$$

where $w, b \in \mathbb{R}$ are the parameters. For any set of parameters w, b, it is possible to solve the equation with the neural control (8.14), this solution is given in the next proposition:

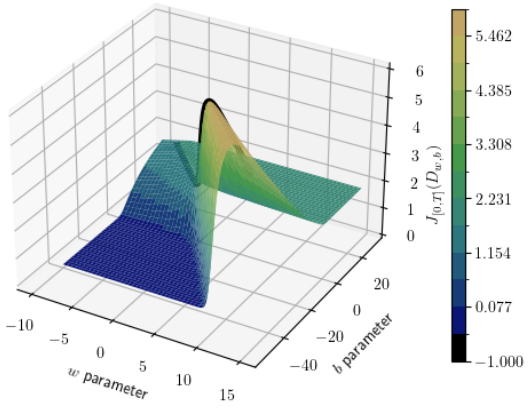

(a) The loss function $J_{[0,T]}(D_{w,b})$. The black line correspond to the line $b = -wt_s$.

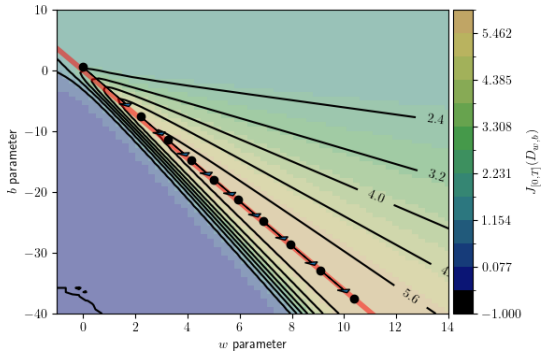

(b) Level set of the loss function $J_{[0,T]}(D_{w,b})$ computed with Equation (8.17). The red line correspond to the curve $\frac{-b}{w} = t_s$. The black dots represent the parameters every 1000 steps of the training.

Figure 8.4: **Example 1**. Loss function $J_{[0,T]}(D_{w,b})$ as a function of the parameters (w, b) together with the evolution of the parameters in the training process. The training process was carried out using the Adam optimization algorithm in 10000 epochs using a constant learning rate of 0.1

Proposition 8.3

The solution of the system

$$\begin{cases} \dot{x} = (\mu - D_{w,t})x, \\ x(0) = x_0, \end{cases} \tag{8.15}$$

can be written as

$$x_{w,b}(t) = x_0 e^{\mu t} \left(\frac{1 + e^{wt+b}}{1 + e^b} \right)^{-\frac{D_{\max}}{w}}, \tag{8.16}$$

and, consequently, the loss function is given by

$$J_{[0,T]}(D_{w,b}) = x_0 - x_0 e^{\mu T} \left(\frac{1 + e^{wT+b}}{1 + e^b} \right)^{-\frac{D_{\max}}{w}} + x_0 \mu \int_0^T e^{\mu t} \left(\frac{1 + e^{wt+b}}{1 + e^b} \right)^{-\frac{D_{\max}}{w}} dt. \tag{8.17}$$

Furthermore, setting $b = -wt_s$, the solution $x_{w,b}$ converges to x^* pointwise as $w \to \infty$.

The proof can be found in Appendix D.2. Proposition 8.3 shows that the solution offered by the neural control is able to approximate the solution of the optimal control (8.11). Figure 8.3 shows the results after 10000 iterations of the method. The same order of iterations was reported for controlling a two-dimensional system in [23, 24]. Table 8.1 shows the time needed to compute 1000

Time steps	Δt	Euler ODE solver	
		Direct method	Adjoint method
100	0.05	18.72 (s)	57.65 (s)
1000	0.005	3.22 (min)	9.14 (min)
10000	0.0005	50.42 (min)	1.71 (hrs)

Time steps	Δt	Runge-Kutta 4 ODE solver	
		Direct method	Adjoint method
100	0.05	1.10 (min)	2.29 (min)
1000	0.005	13.85 (min)	22.52 (min)
10000	0.0005	2.99 (hrs)	4.07 (hrs)

Time steps	Δt	Dormand-Prince ODE solver	
		Direct method	Adjoint method
100	0.05	2.37 (min)	7.93 (min)
1000	0.005	27.16 (min)	47.01 (min)
10000	0.0005	10.82 (hrs)	7.98 (hrs)

Table 8.1: **Example 1**. Computation times to solve problem (8.10). Time required to compute 1000 iterations of the Adam algorithm at constant learning rate of 0.1 for different ODE solvers with different number of time steps considering. To compute the total time (a solution with 10000 epochs), the time should multiply by 10. The numerical tests were run on a computer with an Intel Core i7-12700H using, 16GB RAM.

iterations of the training process with different ODE solvers, different time steps discretization (using constant steps), and using either a direct method (`autograd` option) or an adjoint method (`adjoint` option) to compute the gradient of the neuralODE implemented in `TorchDyn`. A *good* solution, as the one presented in Figure 8.3, needs in the order of 10000 iterations of Adam algorithm. In order to compare the computational time for different numerical scheme implemented in the `TorchDyn` package, we only run 1000 iterations of Adam algorithm. The solution presented in Figure 8.3 was computed using a simple Euler scheme with 100 time steps, whose computation time is around 0.018 s per iteration and a total time of 3.12 mins.

A higher order solver takes more time, as well as increasing the number of time-steps. The adjoint method of `TorchDyn` considerably increases computation time in all the cases presented in this example. The time computation of the adjoint method is highly influenced by the way the solution of the adjoint equation is computed within the package `TorchDyn`. A backward solver is not implemented in this library, instead, to solve the backward equation, a new forward solver object is created in every time step starting from the final value.

The chosen neural control (8.14) has two parameters, then it is possible to show the cost function as a two-dimensional function (see Figure 8.4). The values of the trained parameters moves along the curve $\Gamma = \{(w, b) \in \mathbb{R}^2 : -b/w = t_s\}$ without known explicitly the value of t_s. In theory, the gradient is never zero, but the cost function is very flat when following the curve Γ, then optimization gets slower and slower.

8.3.4 Example 2: the double integrator

We illustrate the use of the neural controls with the simple problem of controlling the double integrator with minimization of the energy [26]. This problem is in dimension 2.

$$\begin{aligned} \min \quad & x_3(T_f = 5) \\ & \dot{x}_1(t) = x_2(t), \\ & \dot{x}_2(t) = u(t), \\ & \dot{x}_3(t) = \frac{x_1^2 + x_2^2}{2}, \\ & u(t) \in [-1, 1], \\ & (x_1(0), x_2(0), x_3(0)) = (0, 1, 0). \end{aligned} \tag{8.18}$$

The Python code for the controlled system (8.18) together with the cost function, the initial conditions and the bounds of the control are written in Listing D.4.

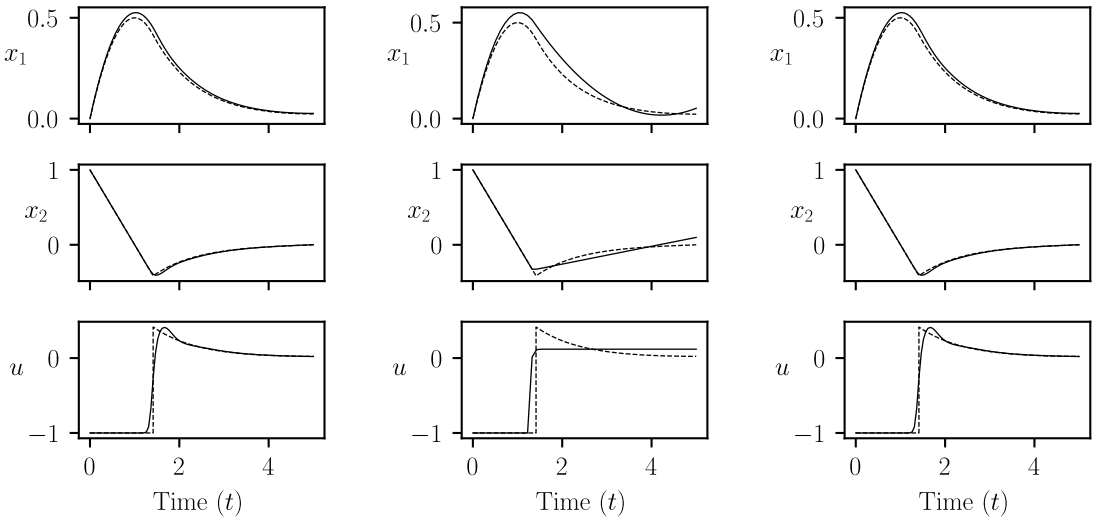

Figure 8.5: **Example 2**. Solutions of the neural controls compared with the solution proposed in [26] shown as a segmented line. The neural solutions are shown as solid lines. The same neural network is bounded in three different ways. **Left:** the neural network bounded with a squashing function (8.20). **Center:** the neural network clipped to the bounds of the control (8.21). **Right:** the neural network is bounded with a sin function (8.22).

We test three approaches to bound a neural network. Let v_θ the neural network

$$v_\theta(t) = W_3\sigma(W_2(\sigma(W_1 t + b_1)b_2)) + b_3, \tag{8.19}$$

where $W_1 \in \mathbb{R}^{h\times 1}$, $b_1 \in$, $W_2 \in \mathbb{R}^{d\times d}$, $b_2 \in \mathbb{R}^d$, $W_3 \in \mathbb{R}^{d\times m}$, $b_3 \in \mathbb{R}^m$. In this case, the dimension of the control is $m = 1$, and the bounds are $a = -1$, and $b = 1$. The neural network v_θ is composed

by two hidden layers with dimension d. For the numerical test, we choose $d = 100$. Based on this neural network, we analyze the solution given by three neural controls, the first one considering the squashing output function α described by (8.1), which is denoted by[1]

$$u_\theta = 2\sigma(v_\theta) - 1. \tag{8.20}$$

The second neural control clips the output of the neural network v_θ and it is denoted by

$$u_\theta^c = \min(\max(v_\theta, -1), 1). \tag{8.21}$$

The third neural control uses a sin function, and it is defined as

$$u_\theta^{\sin} = \sin(v_\theta). \tag{8.22}$$

The training results of the two controls are quite different. Both are presented in Figure 8.5. The neural control (8.20) (in continuous line), does not perfectly approximate the optimal control (in dashed line), but a similar one is founded. On the other side, the neural control (8.21) has a different behavior. The neural control (8.21) is far from approximating the optimal control. This is because it has many gradients that are exactly zero. Note that the results of the second neural control are very close to a *Bang-Bang* solution.

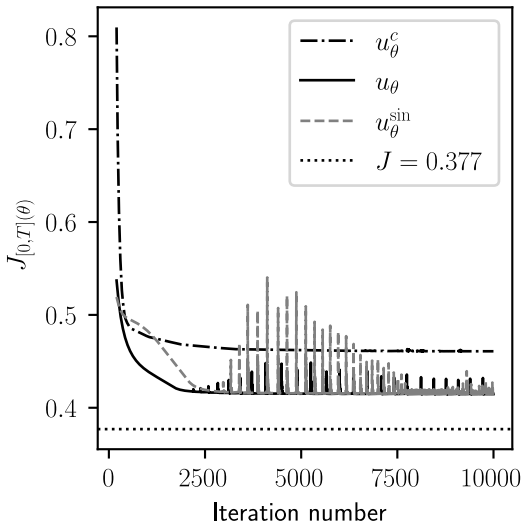

Figure 8.6: **Example 2**. Cost function over the iterations of the ADAM algorithm. Continuous line: the neural control (8.20). Dash-dotted line: the neural control (8.21) Gray dashed line: the neural control (8.22). Dotted line: the loss function reported in [26].

[1]Other squashing functions can be used, for example, an alternative to control (8.20) can be $u_\theta = \tanh(v_\theta)$. Some numerical test were made with this control. As the results do not differ from the one presented with control (8.20), they are not presented here.

Note that the neural control bounded with the squashing function (8.20) is, somehow, *guessing* the switching time, where the optimal control strategy goes from *Bang*(-1) to *Singular* control. The mechanism by which the neural network *guesses* the switching time is similar to the previous example, at least one of the parameters takes larger values.

8.3.5 Example 3: periodic harvesting of a photobioeactor

We analyze a problem of maximizing productivity in a microalgae photobioreactor, with periodic conditions from one day to another [64]:

$$\begin{aligned} \max_{0\leq u(t)\leq \bar{u}} J_{[0,T]} &= \int_0^T u(t)x(t)dt, \\ \text{s.t. } \dot{x} &= f(x,t) - rx - ux, \\ x(T) &= x(0), \end{aligned} \tag{8.23}$$

where x corresponds to the surfacic density of a microalgae population, the function $f(x,t)$ is the growth function. The function f depends on the light intensity impinging the surface of the photobioreactor, denoted by $I_0(t)$. The constant $r > 0$ corresponds to the respiration rate. The growth function is defined as

$$f(x,t) = \frac{\bar{\mu}}{a} \ln \frac{I_0(t) + K_I}{I_0(t)e^{-ax} + K_I}.$$

Here, a and K_I are constants of the model. This problem was solved in [64] when the light function $I_0(t)$ is given by

$$I_0(t) = \begin{cases} \bar{I}_0 \text{ if } 0 \leq t < \bar{T}, \\ 0 \text{ if } \bar{T} \leq t < T. \end{cases} \tag{8.24}$$

The constant $\bar{I}_0$ is the daylight intensity and $\bar{T} \leq T$ corresponds to the duration of the day. Under these conditions, then only three possible forms of the optimal control are allowed:

- *Bang-Bang*,
- *Bang-Singular-Bang*,
- *Constant*.

Notice that the neural problem (P_{NN}) does not allow periodic conditions. In order to tackle the problem (8.23), and to constrain periodicity, we consider a free initial condition $x(0)$ as a parameter x_0, and a penalization is added for the difference between the initial condition $x(0)$ and the final state $x(T)$ in the cost function. The problem (8.23) is then converted to problem (8.23)

$$\begin{aligned} \max_{0\leq u(t)\leq \bar{u}, x_0>0} G_{[0,T]} &= \int_0^T u(t)x(t)dt + \lambda(x(T) - x(0))^2, \\ \text{s.t.} \quad \dot{x} &= f(x,t) - rx - ux, \\ x(0) &= x_0, \end{aligned} \tag{8.25}$$

where $\lambda > 0$ is a positive hyperparameter chosen at the time of optimization. Setting $\lambda = 100$ we solve the neural problem obtaining, after 10000 iterations of the Adam algorithm, the neural control

shown in Figure (8.7), obtaining constant control. This control is almost constant. We compare this solution with the one obtained from the BOCOP [22], where the total harvest reported by BOCOP is 6.1876 and the one obtained by the neural method is about 6.4019. This does not mean that the neural control is better than the one obtained by a classic optimization algorithm, the problem solved by each one is, strictly speaking, different. While BOCOP's solution is able

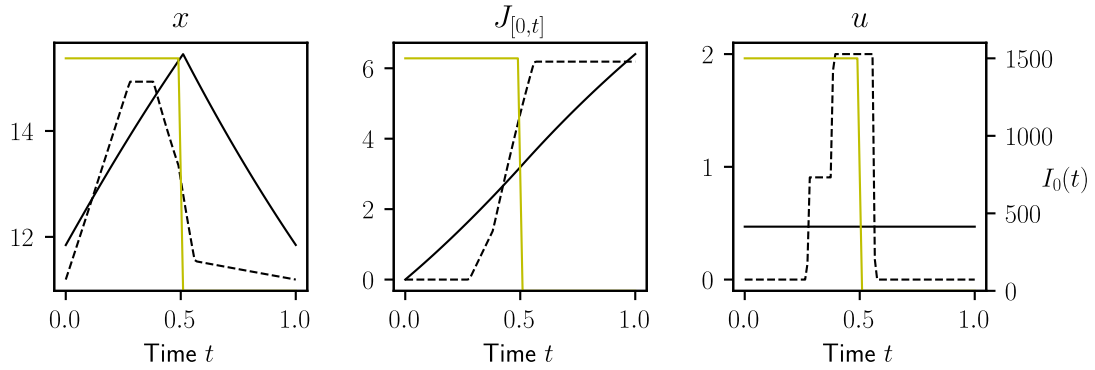

Figure 8.7: **Example 3**. $I_0(t)$ given by (8.24). The black continuous lines correspond to the solution given by a neural control composed of two hidden layers with 20 neurons for two different light regimes I_0. The dashed line correspond to the numerical solution given by BOCOP. The yellow continuous line correspond to the light regime.

to respect the periodicity condition perfectly, the solution given by the neural control has a small difference between the initial value $x(0) = 11.8454$ and the final value of the state $x(T) = 11.8473$. BOCOP's solution, on the other hand, returns $x(0) = x(T) = 11.1940$. This gives us an error of 0.01%.

Light Signal	P_h	
	Neural control	BOCOP's solutions
(8.24)	6.4038	6.1876
(8.26)	9.5677	9.4918

Table 8.2: **Example 3**. Comparison of the performance index P_h between the BOCOP's solution and the neural control.

This problem makes a simplification on the cycle and the amount of light that microalgae receive. One question arises, what happens when we modify the light function? For example, we now consider the light function:

$$I_0(t) = \max\left(0, \bar{I}_1 \sin(2\pi t)\right) + \bar{I}_2, \tag{8.26}$$

where $\bar{I}_1$ and $\bar{I}_2$ are two constants. The neural control and the optimal control computed with BOCOP are shown in Figure 8.8. In this case, the neural control is taking a constant value. On the other hand, BOCOP's solution give a more complex structure, in particular, we can observe a

control *Bang-Singular-Bang-Singular-Bang*. The harvest biomass of the neural solution is about 9.6129 and the one from BOCOP is 9.4918. The initial value of x obtained with the neural method is $x(0) = 12.4892$ and the final value $x(T) = 12.4440$, while the initial and the final value obtained with BOCOP are $x(0) = z(T) = 12.1771$. The error of the periodic condition is around 0.3%.

To make a fairer comparison between the neural control and the optimal control, we define the metric P_h as follows

$$P_h(D) = \int_0^T D(t)x(t) - (x(0) - x(T))dt,$$

which corresponds to the harvest biomass and a penalization if the amount of final biomass $x(T)$ is very low with respect to initial biomass.

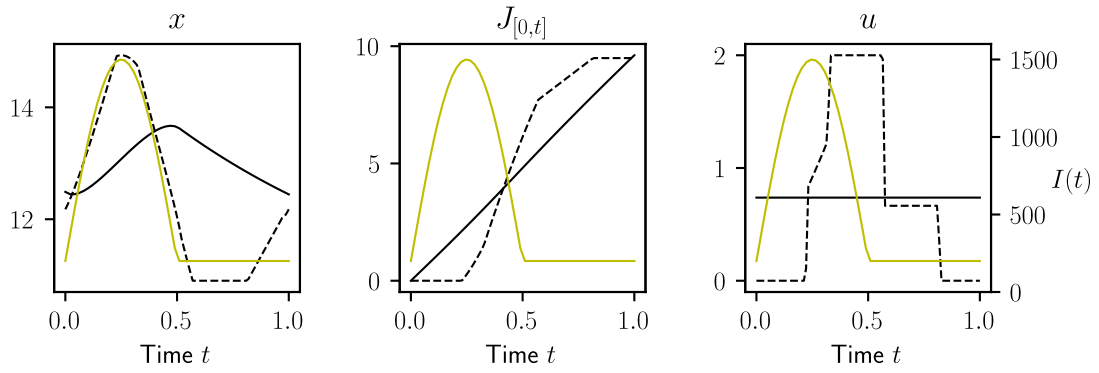

Figure 8.8: **Example 3**. $I_0(t)$ given by (8.26). The black continuous lines correspond to the solution given by a neural control composed of two hidden layers with 20 neurons for two different light regimes I_0. The dashed line correspond to the numerical solution given by BOCOP. The yellow continuous line correspond to the light regime.

This example serves, first, to extend the method to problems with periodic conditions and second, to illustrate a case where the neural control does not approximate the optimal control, but it gets a very close value of the value of the problem. The fact that the neural control has not been able to approximate the optimal control is not surprising for two reasons:

- The optimal control reported in [64] was only 1.11% better than the optimal constant control predicted by the neural control.
- Vanishing gradients. A similar behavior was already reported in the previous example, where the neural control can approximate the optimal control, but this approximation is stalled by vanishing gradients.

8.4 Conclusions

This chapter illustrates how neural networks can help in solving optimal control problems. The key capacity to approximate different types of functions makes neural networks perfect candidates

for solving optimal control problems. Furthermore, neural networks with sigmoid activation functions are able to model a bounded control if the output layer considers a squashing function.

However, the discontinuities in the optimal controls analyzed in this chapter are a difficulty for neural networks and their training, which need many iterations to approximate these discontinuities. The number of iterations using the Adam algorithm is in the order of 10000 iterations that can be computed from 3 (min) using a simple Euler scheme to 20 (min) using a more complex ODE solver as Dormand-Prince considering 100 time steps. The high number of iterations can be compensated with the fast computations of the gradients using automatic differentiation.

The capacity of the parametrized control to approximate the optimal solution also determines the solver's ability to find the solution of the optimal control problem. The simplest neural network analyzed in the *Bang-Bang* example will not predict a more complex solution. But, on the other hand, more complex architectures could drive to local optimal solutions, as the one presented in the second example. Even when the neural control is approaching the optimal control, the learning process may be stuck.

There are no major constraints on the neural network architecture, but the network must be bounded to take values within the control constraints. How the neural network is defined to be bounded is important. We have seen with an example how this affects optimal control learning.

Solving optimal control problems with neural networks is a relatively simple process that could be of great interest in bioprocessing or other areas of engineering. The neural control may or may not approximate the actual optimal control, but at least in the cases analyzed in this chapter, they show great performance to optimize the objective function reaching values very close to the one achieved by the actual optimal control.

Chapter 9

A method to solve non-linear optimal problems via squashing parameterization

This chapter described unpublished work. This work is not in line with microalgae, but it arises from the previous chapter, where we use a squashing function to bound neural networks. The use of this kind of functions inspires this chapter, where we analyze a way to solve numerically optimal control problems.

9.1 Introduction

Optimal control problems can be partially or completely solved using the Pontryagin's maximum principle (PMP), the Hamilton-Jacobi-Bellman equation, or using numerical solvers based on direct or indirect methods. When the PMP first order condition fails to unveil the value of the optimal control, we are in the presence of a singular control. When an optimizer faces a problem with a singular control, numerical problems arise.

In Chapter 8 we give details on how to solve optimal control problems using neural networks. One key of the method is that the neural control must fulfil the restrictions of the problem. To do so, we use a sigmoid function to keep the control within the box constrains, the so-called squashing function. In this chapter, we propose a numerical method based on the squashing function to better understand the issues of the training.

9.2 Problem formulation and methods

Let us consider the optimal control problem without restrictions over the trajectory, with free final conditions and fixed final time:

$$\begin{aligned} \min_{\mathbf{u}\in\mathcal{U}} \quad & J_{[0,T]}(\mathbf{u}) = \int_0^T g(t,\mathbf{z}(t),\mathbf{u}(t))dt, \\ \text{subject to } & \dot{\mathbf{z}}(t) = f(t,\mathbf{z}(t),\mathbf{u}(t)), \\ & \mathbf{z}(0) = \mathbf{z}_0, \end{aligned} \tag{P}$$

where $T > 0$ is fixed, $\mathbf{z}(t) \in \mathbb{R}^n$ is the state vector with the initial condition $\mathbf{z}_0 \in \mathbb{R}^n$, $\mathbf{u} \in \mathbb{R}^m$ is the control vector, f and g are assumed to be $\mathcal{C}^1$ from $\mathbb{R}^{1+n+m}$ to $\mathbb{R}^n$. $\mathcal{U}$ corresponds to the set of admissible controls, in this chapter we will consider

$$\mathcal{U} = \mathcal{L}^\infty_{\text{loc}}([0,+\infty), C),$$

i.e., the set of locally integrable functions on every compact set in $[0,\infty)$ that takes values in the compact set $C \subset \mathbb{R}^m$ defined as

$$C = \prod_{j=1}^m [a_j, b_j], \tag{9.1}$$

where a_i, b_i are the lower and upper bound of $\mathbf{u}_i$.

9.2.1 Approximated solution via squashing functions

We consider the family of functions $\mathbf{u}_\theta$ given by

$$\begin{cases} \mathbf{u}_\theta(t) = \displaystyle\sum_{i=1}^N \alpha(\theta_i)\chi_{I_i^N}(t) \\ \quad \theta_i \in \mathbb{R}^m \ \forall i = 1, ..., N \end{cases} \tag{9.2}$$

where $I_i^N = [t_i^N, t_{i+1}^N)$ for $i = 0, .., N-1$, and $I_N^N = [t_N, t_{N+1}]$, with the convention $t_1 = 0$ and $t_{N+1} = T$. χ_A correspond to the indicator function of the set A defined by

$$\chi_A(t) = \begin{cases} 0 \text{ if } t \notin A, \\ 1 \text{ if } t \in A. \end{cases}$$

The function $\alpha : \mathbb{R}^m \to \mathbb{R}^m$ is defined as follows:

$$\begin{aligned} & \alpha : \mathbb{R}^m \to \mathbb{R}^m \\ v = \begin{pmatrix} v_1 \\ \vdots \\ v_m \end{pmatrix} & \mapsto \alpha(\theta) = \begin{pmatrix} (b_1 - a_1)\sigma(v_1) + a_1 \\ \vdots \\ (b_m - a_m)\sigma(v_m) + a_m \end{pmatrix} \end{aligned} \tag{9.3}$$

where a_j, b_j are the bounds of the control for each $j = 1, ..., m$, and $\sigma(v) = 1/(1+e^{-v})$ is the sigmoid function. Note that by the construction, $\alpha(R^m) \subset \mathcal{U}$.

The function α is known as a squashing function. The use of squashing functions have different application in the literature, in particular, it was reported that their use with differential dynamic programming techniques can effectively solve a variety of optimal control problems, even when other solvers failed [89, 142].

The parameters $\theta = \{\theta_i \in R^m : i = 1, ..., N\}$ of the control $\mathbf{u}_\theta$ can be seen as elements of $\theta \in \mathbb{R}^{n\times m}$, and $\theta_{i,j}$ will denote the j-th component of the i-th parameter θ_i. Also, as $\alpha(\theta_i)_j = (b_j - a_j)\sigma(\theta_{i,j}) + a_j$ we will denote also $\alpha(\theta_{i,j}) = \alpha(\theta_i)_j$ to facilitate the notation. These parameters are *learnable*, in the sense that for every $i = 1, ..., N$, $j = 1, ..., m$ and every $t \in [0, T]$ the gradient

$$\left[\frac{\partial \mathbf{u}_\theta(t)}{\partial \theta_i}\right]_j = (b_j - a_j)\sigma(\theta_{i,j})(1 - \sigma(\theta_{i,j}))\chi_{I_i^N}(t),$$

is not always zero.

The cost function, is then written as a function of the parameters θ:

$$J_{[0,T]}(\theta) = \int_0^T g(t, \mathbf{z}_\theta, \mathbf{u}_\theta)dt.$$

where $\mathbf{z}_\theta$ is the solution of the controlled system

$$\begin{cases} \dot{\mathbf{z}}_\theta = f(t, \mathbf{z}_\theta(t), \mathbf{u}_\theta(t)), \\ \mathbf{z}_\theta(0) = \mathbf{z}_0. \end{cases} \tag{9.4}$$

The gradient of the cost function respect to the parameters, using the method detailed in Appendix C, is such that

$$\left[\frac{\partial J_{[0,T]}(\theta)}{\partial \theta_i}\right]_j = \frac{(\alpha(\theta_i)_j - a_j)(b_j - \alpha(\theta_i)_j)}{(b_j - a_j)} \cdot \int_{t_i}^{t_{i+1}} \left(\boldsymbol{\lambda}_\theta^T \frac{\partial f}{\partial \mathbf{u}} + \frac{\partial g}{\partial \mathbf{u}}\right)_j dt, \tag{9.5}$$

where $\boldsymbol{\lambda}$ is the solution of the adjoint equation:

$$\begin{cases} \dot{\lambda}_\theta^T = -\boldsymbol{\lambda}_\theta^T \dfrac{\partial f}{\partial \mathbf{z}} - \dfrac{\partial g}{\partial \mathbf{z}}, \\ \lambda_\theta(T) = 0. \end{cases}$$

The sigmoid function plays the role of an activation function, but as an activation of the restriction over the control $\mathbf{u}$, meaning that

$$\lim_{\theta_{i,j}\to\infty} \left[\frac{\partial J_{[0,T]}(\theta)}{\partial \theta_i}\right]_j = 0,$$

and

$$\lim_{\theta_{i,j}\to-\infty} \left[\frac{\partial J_{[0,T]}(\theta)}{\partial \theta_i}\right]_j = 0.$$

Furthermore, the following are equivalent:

i.

$$\left[\frac{\partial J_{[0,T]}(\theta)}{\partial \theta_i}\right]_j = 0$$

ii.

$$\int_{t_i}^{t_{i+1}} \left(\lambda_\theta^T \frac{\partial f(t, \mathbf{z}_\theta, \mathbf{u}_\theta)}{\partial \mathbf{u}} + \frac{\partial g(t, \mathbf{z}_\theta, \mathbf{u}_\theta)}{\partial \mathbf{u}}\right)_j dt = 0. \tag{9.6}$$

Let $\{I_i\}_{i=1}^N$ a partition of $[0, T]$, we introduce the reduced problem associated to (P) with the parameterized control u_θ defined in (9.2):

$$\begin{aligned} \inf_{\theta_1,\dots,\theta_N \in \mathbb{R}^m} & \int_0^T g(t, \mathbf{z}_\theta(t), \mathbf{u}_\theta(t))dt \\ \text{s.t. } & \dot{\mathbf{z}_\theta} = f(t, \mathbf{z}_\theta, \mathbf{u}_\theta) \\ & \mathbf{z}(0) = \mathbf{z}_0. \\ & \mathbf{u}_\theta(t) = \sum_{i=1}^N \alpha(\theta_i)\chi_{I_i}(t). \end{aligned} \tag{P_θ^N}$$

We define $\mathrm{Val}\left(\mathrm{P}_\theta^\mathrm{N}\right)$ the value of the problem (P_θ^N) as

$$\mathrm{Val}\left(P_\theta^N\right) = \inf_{\theta=\{\theta_1,\dots,\theta_N\}} \left\{J_{[0,T]}(\theta) : \mathbf{z}_\theta \text{ solution of (9.4)}\right\}$$

In the same way we denote the value of the problem (P) as $\mathrm{Val}(P)$.

9.2.2 Convergence analysis

The resulting Problem (P_θ^N) can only provide a suboptimal solution, meaning that we can not assure the existence of a set of parameters $\theta^* = \{\theta_i^* \in \mathbb{R}^m : i = 1, ..., N\}$ such that

$$\int_0^T g(t, \mathbf{z}_{\theta^*}(t), \mathbf{u}_{\theta^*}(t)) = \mathrm{Val}\left(\mathrm{P}_\theta^\mathrm{N}\right).$$

Instead, it offers an approximation of the solution of Problem (P), when the original problem admits a solution.

Proposition 9.1

Let us suppose that the partition $\{I_i^N : i = 0, ..., N\}$ is such that

$$\lim_{N\to\infty} \max_{i=0,\dots,N} |I_i^N| = 0$$

where $|I_i^N| = t_{i+1}^N - t_i^N$ is the length of the interval I_i^N. Then

$$\lim_{N\to\infty} \mathrm{Val}\left(\mathrm{P}_\theta^\mathrm{N}\right) = \mathrm{Val}\left(\mathrm{P}\right).$$

Proof. For the sake of simplicity, we present the proof in the case where $m = 1$, $a_1 = 0$ and $b_1 = 1$. the proof can be adapted to a multidimensional control with any box constraints. Let $\bar{\mathbf{u}}$ a solution of the Problem (P). For every $i = 1, ..., N$ we define

$$\bar{\beta}_i = \frac{1}{|I_i^N|} \int_{t_i}^{t_{i+1}} \bar{\mathbf{u}}(t)dt.$$

If we set

$$\mathbf{u}_\beta^N = \sum_{i=1}^{N} \beta_i \chi_{I_i^N},$$

then,

$$\lim_{N\to\infty} \int_0^T |\mathbf{u}_\beta^N(t) - u^*(t)| = 0.$$

For every $\varepsilon > 0$, we define

$$\bar{\theta}_i = \begin{cases} -1/\varepsilon \text{ if } \beta_i = a_1, \\ \alpha^{-1}(\beta_i) \text{ if } \beta_i \in (0,1), \\ 1/\varepsilon \text{ if } \beta_i = b_1, \end{cases}$$

where α^{-1} is the inverse function of the function α. Note that

$$|\mathbf{u}_{\bar{\theta}}^\epsilon(t) - \mathbf{u}_\beta^N(t)| = \left| \sum_{\{i:\alpha_i=0\}} -\sigma(-1/\varepsilon)\chi_{I_i}(t) + \sum_{\{i:\alpha_i=1\}} (1 - \sigma(1/\varepsilon))\chi_{I_i}(t) \right|,$$

as $\sigma(-1/\varepsilon) = 1 - \sigma(1/\varepsilon)$:

$$|\mathbf{u}_{\bar{\theta}}^\epsilon(t) - \mathbf{u}_\beta^N(t)| \leq K(N)\sigma(1/\varepsilon),$$

where $K(N)$ is the cardinality of the set $\{i : \beta_i = 0 \text{ or } \beta_i = 1\}$. This proves that for each N, $\mathbf{u}_{\bar{\theta}}^\epsilon$ converges in $L^\infty([0,T], \mathbb{R}^m)$ to $\mathbf{u}_\beta^N$ as $\epsilon \to 0$. From [59, Thorem 4.1]

$$\lim_{N\to\infty} J_{[0,T]}(\mathbf{u}_\beta^N) = \mathrm{Val}\,(\mathrm{P})\,.$$

Then by the Lebesgue dominated convergence theorem

$$\lim_{N\to\infty} \lim_{\varepsilon\to 0} J_{[0,T]}(\mathbf{u}_{\bar{\theta}}^\epsilon) = \mathrm{Val}\,(\mathrm{P})\,.$$

□

9.2.3 How Gradient descent activate restrictions

We are interested in the evolution of the parameters and the value of the cost function when we use a gradient descent like algorithm. The Gradient Descent Algorithm (GDA), for every $i = 1, ..., N$, updates the value of θ_i^k recursively following:

$$\theta_i^{k+1} = \theta_i^k - l_k \frac{\partial J_{[0,T]}(\theta^k)}{\partial \theta_i}, \tag{9.7}$$

where l_k is the so-called learning rate and θ^0 is the initial guess of the parameters. We will assume that l_k is bounded from above by a positive constant. In recent years, many variations and improvements to this algorithm have been developed to improve the performance of the optimized models, resulting in a wide range of algorithms like Nesterov accelerated gradient, Adam, among others [125].

Proposition 9.2

Let us consider the sequence of parameters $\{\theta_i^k \in \mathbb{R}^m : i = 1, ..., N\}_{k\in\mathbb{N}}$ generated by (9.7), and for each $i = 1, ..., N$, $j = 1, ..., m$ let us denote

$$h_{i,j}(\theta^k) = \int_{t_i}^{t_{i+1}} \left(\boldsymbol{\lambda}_{\theta^k}^T \frac{\partial f(t, \mathbf{z}_{\theta^k}, \mathbf{u}_{\theta^k})}{\partial \mathbf{u}} + \frac{\partial g(t, \mathbf{z}_{\theta^k}, \mathbf{u}_{\theta^k})}{\partial \mathbf{u}} \right)_j dt.$$

If $\theta_{i,j}^k$ converge to some $\theta_{i,j}^*$, then

$$\lim_{k\to\infty} h_{i,j}(\theta^k) = 0.$$

On the other hand, if $h_{i,j}(\theta^k)$ do not converge to 0, we have that:

- If $h_{i,j}(\theta^k) > 0 \ \forall k \in \mathbb{N}$, then $\lim_{k\to\infty} \theta_{i,j}^k = -\infty$, and consequently, $\lim_{k\to\infty} \alpha(\theta_i^k)_j = a_j$.
- If $h_{i,j}(\theta^k) < 0 \ \forall k \in \mathbb{N}$, then $\lim_{k\to\infty} \theta_{i,j}^k = \infty$, and consequently, $\lim_{k\to\infty} \alpha(\theta_i^k)_j = b_j$.

Proof. Replacing (9.5) in (9.7), we have for each $i = 1, ..., N$, $j = 1, ..., m$ the following relation:

$$\theta_{i,j}^{k+1} = \theta_{i,j}^k - l_k \frac{(\alpha(\theta_i^k)_j - a_j)(b_j - \alpha(\theta_i^k)_j)}{(b_j - a_j)} h_{i,j}(\theta^k).$$

If $\theta_{i,j}^k$ converge to some $\theta_{i,j}^*$, then

$$\lim_{k\to\infty} l_k \frac{(\alpha(\theta_i^k)_j - a_j)(b_j - \alpha(\theta_i^k)_j)}{(b_j - a_j)} h_{i,j}(\theta^k) = 0.$$

As l_k do not converge to 0, it follows that

$$\lim_{k\to\infty} h_{i,j}(\theta^k) = 0.$$

Then if $h_{i,j}(\theta^k)$ do not converge to 0, we analyze the two cases. **First case:** The sequence $h_{i,j}^k$ is non-negative and does not converge to zero. Then sequence (9.2) is bounded below by a positive constant, *i.e.*, there exists a $\epsilon > 0$

$$h_{i,j}^k > \epsilon \ \forall k \in \mathbb{N}.$$

Then, as $a_j < \alpha(\theta_i)_j < b_j$, we have that

$$\theta_{i,j}^{k+1} < \theta_{i,j}^{k_n} - l_k \frac{(\alpha(\theta_i^k)_j - a_j)(b_j - \alpha(\theta_i^k)_j)}{(b_j - a_j)} \epsilon$$

then $\theta_{i,j}^k$ is a strictly decreasing sequence, and

$$\lim_{k\to\infty} \theta_{i,j}^k = -\infty,$$

which implies that

$$\lim_{k\to\infty} \alpha(\theta_i^k)_j = a_j,$$

i.e.,, in the limit, the lower bound of the control $\mathbf{u}_j = a_j$ is activated. **Second Case:** The sequence $h_{i,j}^k$ is non-positive and do not converge to zero. The argument is the same: there exists a $\epsilon > 0$ such that

$$h_{i,j}^k < -\epsilon \ \forall k \in \mathbb{N},$$

and we can conclude as above that

$$\lim_{k\to\infty} \alpha(\theta_i^k)_j = b_j.$$

□

This illustrates that if the sequence $h_{i,j}$ does not converge to zero, and if it does not change sign, then it will activate one of the restrictions via the squashing function α. Of course, a change of sign of $h_{i,j}(\theta^k)$ is possible. In the case where $h_{i,j}(\theta^k)$ change the sign, by continuity of the function $h_{i,j}$, there exists a θ^* such that $h_{i,j}(\theta^*) = 0$, and the gradient descent algorithm would converge to this value θ^* with a proper election of the learning rate.

In the next proposition, we present the relationship between the value of $\alpha(\theta^k)$, the sequence θ^k and the iterations of the gradient descent in the one dimensional case.

Proposition 9.3

Suppose that the function $F : \mathbb{R} \to \mathbb{R}$ is $\mathcal{C}^1$, let $\alpha : \mathbb{R} \to (a, b)$ the one dimensional squashing function $\alpha(\theta) = (b - a)\theta + a$, then the sequence θ^k generated by the recurrence

$$\theta^{k+1} = \theta^k - l_k \frac{dF(\alpha(\theta^k))}{d\theta}, \tag{9.8}$$

with $\theta_0 \in \mathbb{R}$ and $l_k > 0 \ \forall k \in \mathbb{N}$. Then

$$\alpha(\theta^{k+1}) = \alpha(\theta^k) - l_k \left[\alpha'(\theta^k)\right]^2 F'(\alpha(\theta^k)) + r_k(\theta^{k+1}),$$

where for every $k \in \mathbb{N}$, $r_k : \mathbb{R} \to \mathbb{R}$ is a function such that $r_k(v) \to 0$ as $v \to \theta_k$.

Proof. By the chain rule (9.8) can be written as

$$\theta^{k+1} = \theta^k - l\alpha'(\theta^k)F'(\alpha(\theta^k)). \tag{9.9}$$

By the Taylor's theorem,

$$\alpha(\theta^{k+1}) = \alpha(\theta^k) + \alpha'(\theta^k)(\theta^{k+1} - \theta^k) + r_k(\theta^{k+1}), \tag{9.10}$$

where $h_k(v) \to 0$ if $v \to \theta^k$. replacing (9.10) in (9.9), we get (9.3). □

Using Proposition 9.3, we have that for every $k \in \mathbb{N}$:

$$\alpha(\theta_i^{k+1})_j = r_k^{i,j}(\theta_{i,j}^{k+1}) + \alpha(\theta_i^k)_j - l_k \left[\frac{(\alpha(\theta_i^k)_j - a_j)(b_j - \alpha(\theta_i^k)_j)}{(b_j - a_j)}\right]^2 h_{i,j}(\theta^k),$$

and we can make the approximation

$$\alpha(\theta_i^k)_j \approx \alpha(\theta_i^k)_j - \tilde{l}_k h_{i,j}(\theta^k), \tag{9.11}$$

where

$$\tilde{l}_k = l_k \left[\frac{(\alpha(\theta_i^k)_j - a_j)(b_j - \alpha(\theta_i^k)_j)}{(b_j - a_j)}\right]^2,$$

which correspond to make a gradient descent over the values of the control.

Algorithm 3 Direct shooting method via squashing functions

Require: Discretized interval time $\{t_i\}_{i=0}^N$ of $[0, T]$.
Require: Number of iterations n_e.
Require: $\theta = \{\theta_i \in \mathbb{R}^m : i = 1, ..., N\} \in \mathbb{R}^N$ Initial guess of the parameters.
Require: Gradient descent like algorithm GDA.
  for i in n_e **do**
    Define $\mathbf{u}_\theta = \sum_{i=1}^N \sigma(\theta_i)\chi_{(t_{i-1},t_i)}$.
    Solve forward $\dot{\mathbf{z}}_\theta = f(t, \mathbf{z}_\theta, \mathbf{u}_\theta)$.
    Solve backward $\dot{\boldsymbol{\lambda}}^\intercal + \boldsymbol{\lambda}^\intercal \frac{\partial f}{\partial \mathbf{z}} + \frac{\partial g}{\partial \mathbf{z}} = 0$.
    Compute gradient $\frac{\partial J_{[0,T]}(\theta)}{\partial \theta}$.
    Update parameters θ with GDA.
  end for

9.3 Numerical example: The double integrator problem

We use the Algorithm 3 to solve the double integrator problem presented in (8.18). The comparison between the solution given by the method is presented in Figure 9.1 together with the cost function through the optimization process. The optimization is made with 10000 optimization steps, using Adam's algorithm with a constant learning rate to 0.1. The solution is notably better than the one presented with the neural control, showed in Figure 8.5.

Now we try a more powerful optimal solver in order to compare the solution that the parameterized control $\mathbf{u}_\theta$, described in Equation (9.2), can offer versus a classic parameterization. We compare the parameterization (9.2) with the parameterization given by

$$\begin{cases} \mathbf{u}_\beta(t) = \displaystyle\sum_{i=1}^N \beta_i \chi_{I_i^N}(t), \\ \quad \alpha_i \in C \ \forall i = 1, ..., N. \end{cases} \tag{9.12}$$

The study of the convergence of this method was reported in [59].

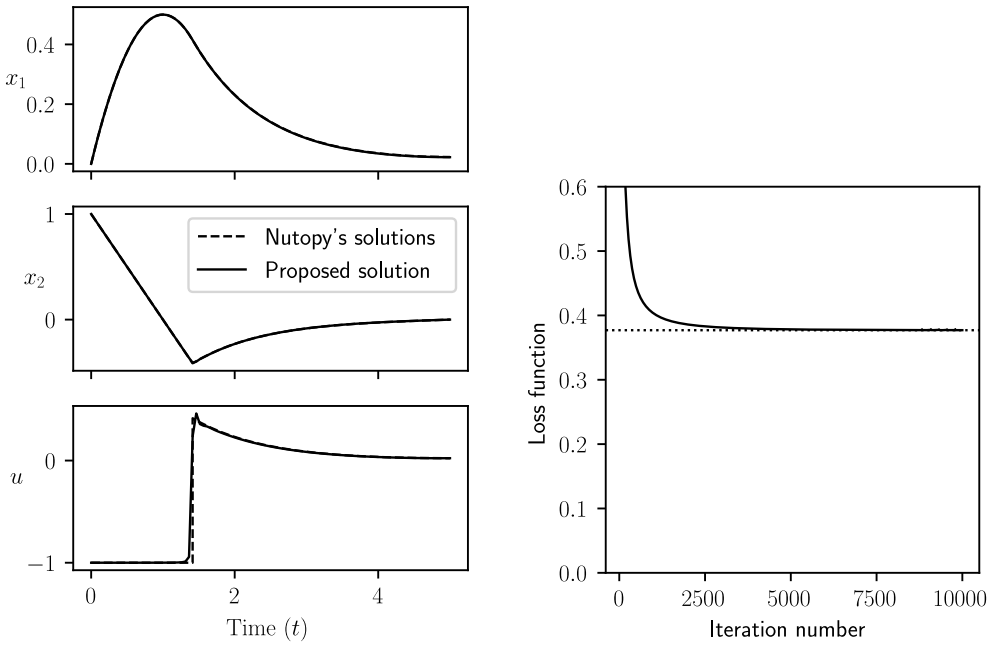

Figure 9.1: **Left:** Comparison between the solution of the method proposed, and the solution presented in [26]. **Right:** The cost function for each step as a continuous line and the optimal value founded in [26] plotted with a dotted line.

The number of software that implement automatic differentiation, and gradient-based optimizers, has increased in the last years, for example, Pytorch [110], Jax [25], Tapenade [70] and CasADi [6]. The speed of computation is one of the major importance of these software programs. We choose CasADi to compare the convergence speed of the algorithm using the same non-linear optimizer. CasADi [6] is a tool to solve constrained nonlinear optimization problems that implements different optimization solvers combined with a fast automatic differentiation algorithm.

The two parameterizations are implemented in CasADi [6] to present the following test: the two parameterization methods, the proposed here (9.2) and the classical one given by (9.12), are used to discretize the problem (8.18) using a Runge-Kutta 4 as an integrator. The discretized problem associated to the parameterization (9.2), compared to the problem associated to parameterization (9.12), is a non-constrained one. Then both problems are solved using four different solvers, with the same stop criteria. The computational times to solve the problem for different solvers are presented in Table 9.1, where the time to solve the discretized problem associated to the parameterization (9.2) is higher in every case. Then, removing the constraints from the problem and put them in the control via squashing functions does not improve the convergence time of the algorithm nor the quality of the solution.

Another point to note about this test is that the solutions given by the algorithm FATROP and FSQP have an erroneous value at the beginning. Instead of giving the value zero, the solver

gives the value 1. This is explained by the fact that the gradient, when the parameterized control $\mathbf{u}_\theta$ approximates the value of the upper (or lower) bound, the gradient of the cost function (9.5) vanishes.

Figure 9.2 shows the solutions given by the different NLP solvers. The FATROP and the FSQP algorithm fail to predict the initial value of the optimal control, and the IPOPT's solution oscillate considerably more than the other solvers. From this experience, we choose the BONMIN's algorithm to compare the solutions using the parameterizations (9.12) and (9.2). In Figure 9.4 we show this comparison with $N = 1000$ time steps. Both solutions have problems in approximating the values of the control in the switching time. This is to be expected when the time discretization does not coincide exactly with the switching time, but more numerical errors can be seen when using parameterization (9.2) at the end of the control, this could be due to the change of convexity of the function at point zero.

	Solver			
	BONMIN	FATROP	IPOPT	FSQP
Squashing Method (9.2)	3.14 (s)	3.13 (s)	5.60 (s)	2.22 (s)
Restricted Method (9.12)	0.67 (s)	0.49 (s)	0.80 (s)	0.13 (s)

Table 9.1: Computation time for solving problem (8.18) using different NLP solvers implemented in CasADi considering $N = 100$ time steps.

9.4 Discussion: neural controls

There is a close relationship between the method studied here, and the method studied in the previous chapter. In Chapter 8 we study the solutions offered by neural networks using them as controls in dynamic systems, the so-called neural controls. In both cases, the sigmoid function acts over the parameters that must be optimized, converting the original (possible convex) optimization problem to a non-convex one. There are two important remarks:

- The solution can oscillate when the values of the control are close to the inflection point of the squashing problem due to the change of convexity o the sigmoid function.
- The bounds of the controls are local minima of the problem. This means that, depending on the initialization of the initial guess of the control, the iterative algorithm may be stuck at these minimum values.

The neural controls, then, are limited to solve optimal control problems due to the points mentioned above.

9.5 Conclusions

In this chapter, we analyze a numerical method to approximate the solutions of optimal control problems with box constraints. This method consists of implementing the constraints in the control parameterization using a squashing function. We give some insight of how the activation of the box constraints are carried out in the evolution of the parameters in a gradient descent scheme.

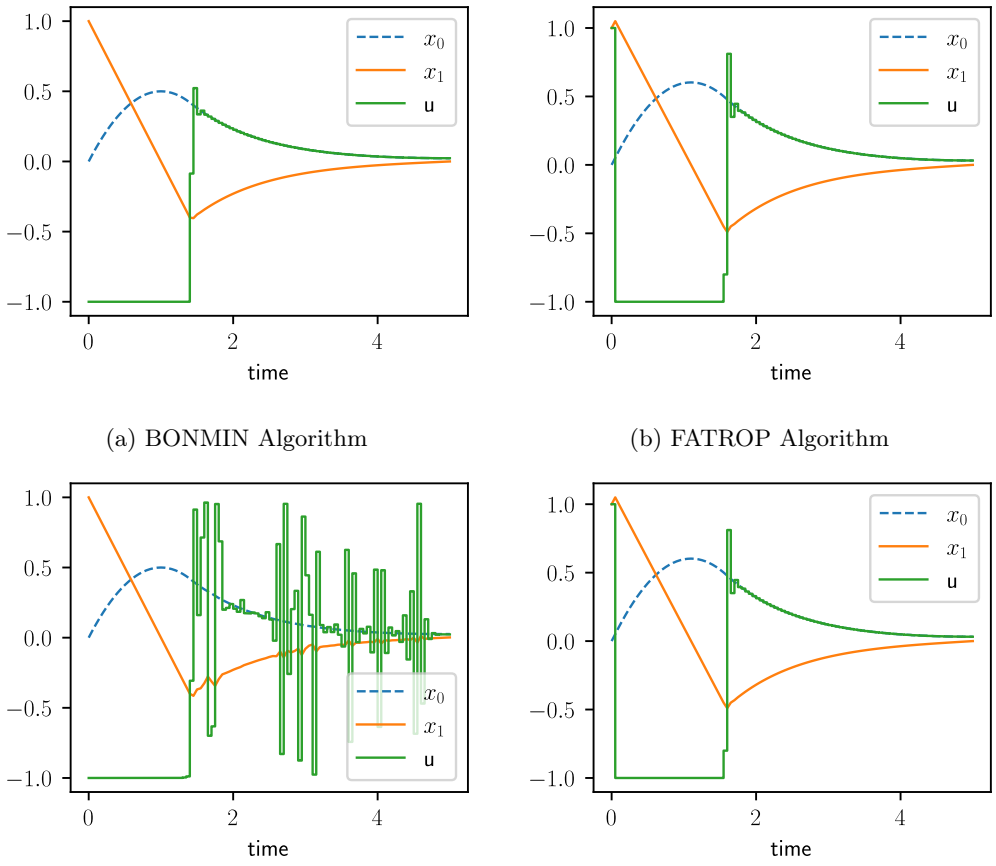

(a) BONMIN Algorithm

(b) FATROP Algorithm

(c) IPOPT Algorithm

(d) FSQP Algorithm

Figure 9.2: Solutions of four NLP solvers using the parameterization (9.2) using a direct shooting method.

When constraints are imposed on the parameterized control, the resulting problem is non-convex as a function of the parameters (due to the sigmoid function). But, the problem is still convex as a function of the value of the control, this fact allows us to establish a relation between the gradient descent over the parameters of the control and the values that the control takes. Also, including the box constraints allows us to use unconstrained optimization methods.

The inclusion of the restrictions in the parameterized control does not improve the speed of convergence of the optimization algorithm, nor does it improve the quality of the solution. This includes the method studied in the previous chapter, where we studied how to solve optimal control problems with neural networks. In the case of neural networks, the solutions they provide are limited to the neural network's ability to approximate functions. For discontinuous controls such as those studied in this thesis, the neural network solutions have a slow convergence to the optimal

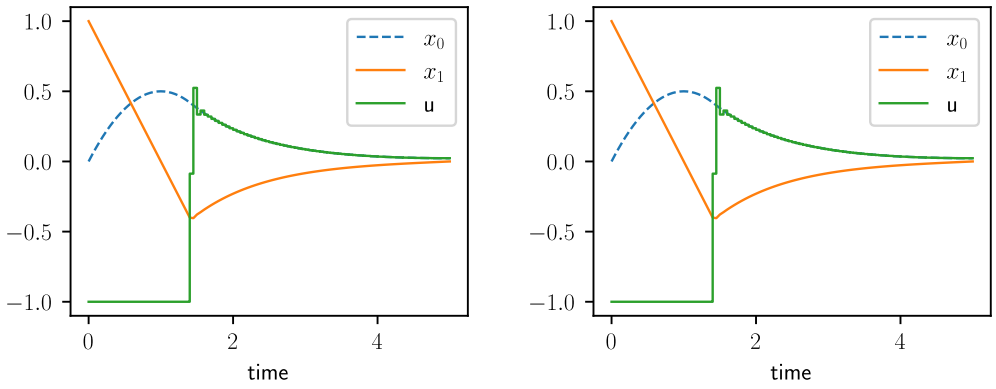

(a) BONMIN Algorithm

(b) FATROP Algorithm

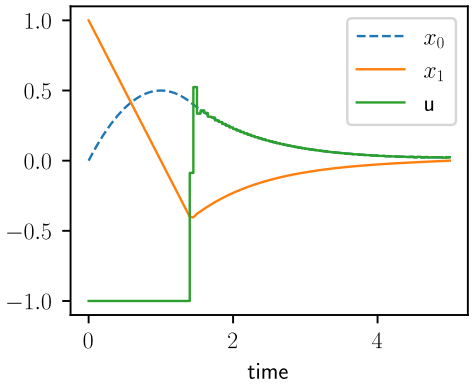

(c) IPOPT Algorithm

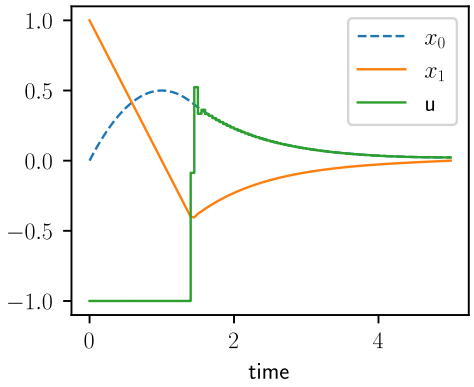

(d) FSQP Algorithm

Figure 9.3: Solutions of four NLP solvers using the parameterization (9.12) using a direct shooting method.

control precisely because they slowly approximate continuous functions where some parameters converge to infinity.

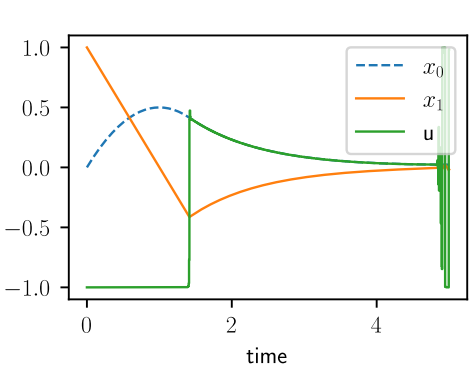

(a) Parameterization (9.2). The solution was computed in 8.41 (min).

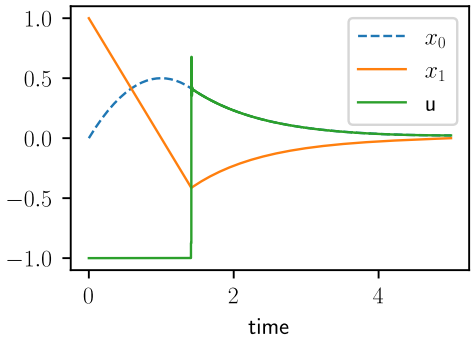

(b) Parameterization (9.12). The solution was computed in 53.33 (s) using the BONMIN algorithm from CasADi.

Figure 9.4: Solutions considering $N = 1000$ time steps using the BONMIN algorithm from CasADi.

Chapter 10

Conclusion

Main contributions

In this manuscript, we explore different problems associated with the mathematical modelling and optimization of microalgae-based processes, with a special focus on the influence of the dynamical light pattern received by the cells. Different mathematical tools are used to support our developments, mainly the theory of ordinary differential equations, optimal control, and the use of machine learning models. We have tackled three types of problems using approaches from nonlinear control science, later hybridizing them with Artificial Intelligence methods:

- The study of average microalgae growth rate under fluctuating light.
- The solution of optimal control problems considering a photobioreactor working in continuous mode and at constant volume.
- The inclusion of neural networks in dynamic models of photobioreactors and the use of neural networks to solve optimal control problems.

Average growth rate under fluctuating light

The starting point of this work is a broadly used model of photosynthesis in microalgae under dynamic light regime [67]. The three population model of Han was analysed in large and short periods of variable light. In Chapter (3) we study the average growth rate when the microalgae culture is subjected to a light that changes periodically between two positive values (*i.e.,* a square wave function). Two cases are possible: when the period of the square wave function is small with respect to the model parameters and when the period is larger than the model parameters. In both cases, we give an approximation of the average growth rate as a function of the parameters of the model. Then in Chapter 4 we extend the computations for the class of continuous functions.

In Chapter 4, we analyse the average growth rate for any continuous light, and we illustrate how mixing influences the average growth rate for simply periodic functions. Then, we discuss the challenge of computing the growth rate in photobioreactors simulated via computational fluid dynamics, considering a single-phase and incompressible fluid, and we end up our analysis presenting

the case of the raceway pond. Estimating microalgae growth tracking cells within the photobioreactor is difficult and computationally expensive, in particular, it is difficult to obtain an accurate representation of all the microalgae given the size of the system. To tackle this problem, we use a correction of the position distribution on the axis perpendicular to the base of the raceway pond. A higher paddle wheel velocity increases growth rate in the raceway pond case. In this case, we also present an upper bound relating the average growth rate and the average velocity on the z-axis.

Optimal control problems in photobioreactors

In a photobioreactor, due to the gradient of light, microalgae are successively exposed to conditions of low and high (inhibiting) light. This fact is illustrated in Chapter 4, where we simulated several cells moving within a raceway pond exposed to natural light. But many photobioreactors operate in a more controlled manner, using an artificial source of light. In this case, the light function can be a control of the system. However, we have still to deal with the fact that cells evolve in a light gradient where they are successively photo-inhibited or photo-limited.

Based on Han's description, in Chapter 5 we introduce a dynamic system of microalgae growth involving two control variables: the light intensity and the dilution rate of the reactor. Then, we formulate and study an optimal control problem in order to characterize the optimal light supply and dilution strategies that maximize the harvested biomass. Our study, mainly based on Pontryagin's maximum principle, shows that singular arcs and *turnpike*-like behaviours appear in the optimal solution. In particular, we prove that the optimal strategy maintains the biomass at a constant level along singular arcs, and we determine its static value. The theoretical results are illustrated throughout this chapter using a direct optimization method implemented in BOCOP. The focus here is the behaviour of the dilution control. The numerical solutions presented are *Bang-Singular-Bang* type or *Bang-Bang* type for the dilution control. The last arc of the dilution control is always settled at its maximum value, we give a lower bound for the duration of this arc. We conjecture that the existence of the singular arc depends on whether the system has enough time to reach the value of the singular arc (biomass concentration) and to respect the lower bound of the final arc.

In Chapter 6 we study a similar optimal control problem where light intensity and dilution rate are again used as controls. A small modification was made in the light model to consider the geometry of the photobioreactor. The average light is considered as an input of the growth function that is now affected by the light at which the microalgae is acclimated, the so-called growth irradiance. There are several similarities with the problem analysed in Chapter 5, for example, the last arc of the optimal dilution control is equal to the upper bound of the control and the duration of this arc is also estimated. Taking advantage of the difference between the timescale of microalgae growth and the timescale of photoacclimation, an approximated optimal feedback control is given for the light control. Numerical simulations show that the biomass is close to a stationary regime in the presence of a singular arc of dilution. Using this approximation, an estimation of the biomass in the singular arc is presented and illustrated with different initial conditions.

Neural differential equations for microalgae modelling and control

Motivated by the complexity of photobioreactor related problems, we tackle the modelling and control of microalgae processes with machine learning approaches. In this part, we investigate how artificial neural networks can contribute to improve the modelling and the optimization of

microalgae.

In Chapter 7 we replace the growth rate in the microalgae dynamics by a neural network. This neural network takes exogenous variables such as light and temperature. We establish the theoretical framework for training the neural network using direct and adjoint methods. We develop an integrator that solves ordinary differential equations and delivers the interpolation of the exogenous variables to the model. Also, we discuss how to use classical neural network training techniques, such as mini-batch training. To demonstrate how flexible this approach can be, two different approaches were tested. First, a neural network is developed to learn the microalgal growth rate as a function of light and temperature. Second, a neural network is used to correct the biases from a pre-existing kinetic model implementing a Monod function combined with the Beer-Lambert law of light extinction. Both neural networks have light intensity and temperature as inputs. These factors are interpolated in our solver for ordinary differential equation problems. This solver also allows us to solve a set of equations simultaneously, enabling batch training. These methods are compared with a regression carried out with support vector machine.

While in Chapter 7 neural networks were used to represent *a missing part* of the model, in Chapter 8 they are implemented to identify the optimal control strategy of a dynamical system. We focus on the type of problems solved in the second part of this manuscript: optimal control problems with fixed initial conditions, fixed final time and free final condition with box constraints on the control. First, we discuss how to define bounded neural controls, then we establish the relation between the Pontryagin's Maximum Principle conditions and the computation of the gradient of the cost function with respect to the parameters of the neural network. We implement a solver in `Pytorch` using a package dedicated to solve ODE problems (`Torchdyn`). Then we illustrate the efficiency of our solver with three examples. The first is a simple problem where the simplest possible neural network can approximate not only the value of the cost function but also find the optimal control, which corresponds to a *Bang-Bang* control. The second example is a more challenging one. We test a more complex structure of the neural network and fixing the neural network, we use three different methods to bound it. In this case, using a squashing function or a sinusoidal function show a better convergence than simply clipping the output of the neural network. However, both neural controllers struggle for approximating the values of the optimal control near the switching time. This is due to the limitations of neural networks to approximate discontinuous functions. The last problem, for the production of microalgae biomass under periodic light, is a case where the neural control does not offer a control close to the optimal control, but proposes sub-optimal strategies leading to very close values for the harvested biomass. This demonstrates that neural controls can be used to give sub-optimal solutions of periodic problems using a penalization method.

Finally, in Chapter 9 we use the squashing trick to bound a neural network and end up with a method to solve any non-linear optimal control problem with box constraints on the control, free final states and fixed final time. The control is parametrized using sigmoid functions, which allow us to include the problem restrictions in the control. We implement the method using `Pytorch` and CasADi, a fast solver for non-linear optimization problems. We show a strong connection between the approach efficiency and the chosen squashing method to bound the neural network for control purposes. The convergence time of our approach compared to classical parameterization are slower. This method helps to understand why the training of the neural control in Chapter 8 requires a large number of iterations.

Discussion and perspectives

Modelling and controlling microalgae systems are quite difficult problems to tackle. Many factors affecting microalgae growth must be considered. In this manuscript, we analysed in depth the influence of light on microalgae and yet this work is not sufficient to analyse the complex relationship between light and an industrial culture of microalgae, for example, non-photochemical quenching [60] was not taken into account in the models presented here. Other limiting factors must be considered when modelling or controlling microalgae-based processes. Coupling light models with nutrients models, for example, can change drastically the optimal operation of a photobioreactor, especially, for dilution, which highly affects the concentration of nutrients within the photobioreactor. Furthermore, coupling light, nutrients, and hydrodynamics models makes even more challenging the study of the system. Where hydrodynamics affect the light perceived by each individual cell, it can also lead to nutrient concentration gradients, especially for large-scale systems. To effectively model or control microalgae-based processes, these additional factors must be considered.

The first part of this manuscript is a lesson in how complicated it can be to model the influence of light on microalgae growth; for example, the simulations of the hydrodynamics of the raceway pond can take several days, which is quite computationally expensive. Furthermore, microalgae growth can be affected by seasonal factors. Therefore, the development of adaptive techniques to control such complex systems is a contribution to future intelligent digital twins. One of the main contributions of this work is the use of neural networks to model the growth of microalgae. These *Neural models* can be adapted to different situations and data types. Furthermore, these models can be coupled to online sensors, creating a versatile and easy to calibrate framework. The introduction of neural networks for modelling and control could reduce the expert manpower required, the computational costs and finally improve the scalability of these systems, making them more powerful for large-scale production. This applied perspective makes the research highly transferable for the biotechnological industry, for which modelling and control is a complex and non-standard task for engineers. Future research could explore the generalisation and scalability of the methods developed here in different types of bioreactors and for other organisms, beyond the configurations studied in this manuscript.

When we attempt to solve optimal control problems with neural networks, many questions still remain unanswered, since we approach an area of research in machine learning that is relatively new. The study of bounded neural networks and discontinuous learning is poorly documented to date. For example, the architectures proposed in [39] were tested in Chapter 8 to solve optimal control problems, but no significantly better results than those presented here were observed. This could be due to the additional requirement of control bounding. More research needs to be done to define better architectures capable of adapting to the two requirements of control problems: boundedness and discontinuity. Finally, in this work, we focus on modelling and control with neural networks independently; Chapter 7 is an example of a microalgae-based process modelled with neural networks and Chapter 8 present several examples of controlling dynamical systems with these models. Future research may reveal the properties of systems that are both modelled and controlled by neural networks.

Appendix

Appendix A

Complement of Chapter 3

A.1 Analytical Computations

A.1.1 Case I: Large period T

For large period case, the evolution system (3.7) can be approximated by (3.10) which can be solved explicitly for a constant irradiance I as

$$C(y,t) = \frac{\alpha(I(y))}{\alpha(I(y)) + k_r}(1 - e^{-(\alpha(I(y))+k_r)t}) + e^{-(\alpha(I(y))+k_r)t}C(y,0), \quad t \in (0,T).$$

Moreover, the system is assumed to be periodic (*i.e.* $C(y,0) = C(y,T)$). For the constant light regime $I_M(y)$, one has $C(y,t) = \frac{\alpha(I_M(y))}{\alpha(I_M(y))+k_r}$, $\forall t \in [0,T]$. Using (3.18), the T-average growth rate is given by $(1-C)\gamma(I_M(y)) = \frac{K\sigma I_M(y)}{1+\tau\sigma I_M(y)+\frac{k_d}{k_r}\tau(\sigma I_M(y))^2} = \mu_S(I_M(y))$. For the high/low light regime, one has

$$C(y,t) = \begin{cases} \frac{\alpha_H(y)}{\alpha_H(y)+k_r}(1 - e^{-(\alpha_H(y)+k_r)t}) + e^{-(\alpha_H(y)+k_r)t}C(y,0), & t \in (0,\eta T) \\ \frac{\alpha_L(y)}{\alpha_L(y)+k_r}(1 - e^{-(\alpha_L(y)+k_r)(t-\eta T)}) + e^{-(\alpha_L(y)+k_r)(t-\eta T)}C(y,\eta T), & t \in (\eta T, T) \end{cases}$$

Using the periodic border condition of C, one has

$$C(y,0) = \frac{\frac{\alpha_L(y)}{\alpha_L(y)+k_r}\left(1-e^{-(\alpha_L(y)+k_r)T(1-\eta)}\right)+e^{-(\alpha_L(y)+k_r)T(1-\eta)}\frac{\alpha_H(y)}{\alpha_H(y)+k_r}\left(1-e^{-(\alpha_H(y)+k_r)T\eta}\right)}{1-e^{-(\alpha_L(y)+k_r)T(1-\eta)-(\alpha_H(y)+k_r)T\eta}}.$$

For a given local optical depth y, the T-average growth rate is given by

$$\begin{aligned}
\bar{\mu}^{\mathrm{T}}(y) =& \frac{1}{T}\int_0^T \mu(y,t)\mathrm{d}t \\
=& \frac{1}{T}\Big(\int_0^{\eta T} \mu(y,t)\mathrm{d}t + \int_{\eta T}^T \mu(y,t)\mathrm{d}t\Big) \\
=& \eta\frac{\gamma_H(y)k_r}{\alpha_H(y)+k_r} + (1-\eta)\frac{\gamma_L(y)k_r}{\alpha_L(y)+k_r} \\
&+ \frac{\gamma_H(y)}{T(\alpha_H(y)+k_r)}\left(\frac{\alpha_H(y)}{\alpha_H(y)+k_r} - C(y,0)\right)\left(1-e^{-(\alpha_H(y)+k_r)T\eta}\right) \\
&+ \frac{\gamma_L(y)}{T(\alpha_L(y)+k_r)}\left(\frac{\alpha_L(y)}{\alpha_L(y)+k_r} - C(y,T\eta)\right)\left(1-e^{-(\alpha_L(y)+k_r)T(1-\eta)}\right) \\
=& \eta\mu_S(I_H(y)) + (1-\eta)\mu_S(I_L(y)) + \frac{\zeta_1(y,\eta,T)\zeta_2(y)}{Tk_r},
\end{aligned}$$

where $\gamma_H(y) := \gamma(I_H(y))$ and $\gamma_L(y) := \gamma(I_L(y))$.

A.1.2 Case II: Small period T

For small period case, the dynamics of C is negligible (*i.e.* C is a constant). Integrating (3.7) from 0 to T gives

$$0 = \int_0^T \dot{C}\mathrm{d}t = -k_rTC - k_d\sigma C\int_0^T I\mathrm{d}t + k_d\sigma\int_0^T I\mathrm{d}t - k_d\sigma\int_0^T IA\mathrm{d}t.$$

Let us denote by $\bar{I} := \frac{1}{T}\int_0^T I\mathrm{d}t$ and by $\overline{IA} := \frac{1}{T}\int_0^T IA\mathrm{d}t$, then one finds the constant value for C as

$$C = \frac{k_d\sigma(\bar{I}-\overline{IA})}{k_d\sigma\bar{I}+k_r}. \tag{A.1}$$

For high/low light regime, one has

$$A(y,t) = \begin{cases} e^{-\beta_H(y)t}A(0) + \frac{1-C}{\tau\beta_H(y)}(1-e^{-\beta_H(y)t}), & t\in[0,\eta T], \\ e^{-\beta_L(y)(t-\eta T)}A(\eta T) + \frac{1-C}{\tau\beta_L(y)}(1-e^{-\beta_L(y)(t-\eta T)}), & t\in[\eta T, T]. \end{cases}$$

The periodicity on A gives

$$A(y,0) = \frac{e^{-\beta_L(y)(1-\eta)T}\frac{1-C}{\tau\beta_H(y)}(1-e^{-\beta_H(y)\eta T}) + \frac{1-C}{\tau\beta_L(y)}(1-e^{-\beta_L(y)(1-\eta)T})}{1-e^{-\beta_L(y)(1-\eta)T-\beta_H(y)\eta T}}.$$

On the other hand, the average of IA can be computed by

$$
\begin{aligned}
T\overline{IA} =& \int_0^{\eta T} I_H(y)A(y,t)\mathrm{d}t + \int_{\eta T}^{T} I_L(y)A(y,t)\mathrm{d}t \\
=& A(y,0)I_H(y)\frac{1-e^{-\beta_H(y)\eta T}}{\beta_H(y)} + I_H(y)\frac{1-C}{\tau\beta_H(y)}(\eta T - \frac{1-e^{-\beta_H(y)\eta T}}{\beta_H(y)}) \\
&+ A(y,\eta T)I_L(y)\frac{1-e^{-\beta_L(y)(1-\eta)T}}{\beta_L(y)} + I_L(y)\frac{1-C}{\tau\beta_L(y)}\big((1-\eta)T \\
&- \frac{1-e^{-\beta_L(y)(1-\eta)T}}{\beta_L(y)}\big) \\
=& A(y,0)I_H(y)\frac{1-e^{-\beta_H(y)\eta T}}{\beta_H(y)} + I_H(y)\frac{1-C}{\tau\beta_H(y)}(\eta T - \frac{1-e^{-\beta_H(y)\eta T}}{\beta_H(y)}) \\
&+ \big(e^{-\beta_H(y)\eta T}A(0) + \frac{1-C}{\tau\beta_H(y)}(1-e^{-\beta_H(y)\eta T})\big)I_L(y)\frac{1-e^{-\beta_L(y)(1-\eta)T}}{\beta_L(y)} \\
&+ I_L(y)\frac{1-C}{\tau\beta_L(y)}\big((1-\eta)T - \frac{1-e^{-\beta_L(y)(1-\eta)T}}{\beta_L(y)}\big) \\
=& \frac{A(y,0)}{\beta_H(y)\beta_L(y)}\big(I_H(y)\beta_L(y)(1-e^{-\beta_H(y)\eta T}) + I_L(y)\beta_H(y)e^{-\beta_H(y)\eta T}(1 \\
&- e^{-\beta_L(y)(1-\eta)T})\big) + \frac{1-C}{\tau\beta_H(y)\beta_L(y)}(I_H(y)\beta_L(y)\eta T \\
&+ I_L(y)\beta_H(y)(1-\eta)T) + \frac{1-C}{\tau\beta_L(y)^2\beta_H(y)^2}\big(I_L(y)\beta_H(y)\beta_L(y)(1 \\
&- e^{-\beta_H(y)\eta T})(1-e^{-\beta_L(y)(1-\eta)T}) - I_H(y)\beta_L(y)^2(1-e^{-\beta_H(y)\eta T}) \\
&- I_L(y)\beta_H(y)^2(1-e^{-\beta_L(y)(1-\eta)T})\big) \\
=& \frac{1-C}{\tau\beta_L(y)^2\beta_H(y)^2}\frac{1}{1-e^{-\beta_L(y)(1-\eta)T-\beta_H(y)\eta T}}\big(I_H(y)\beta_L(y)^2(1 \\
&- e^{-\beta_H(y)\eta T})^2e^{-\beta_L(y)(1-\eta)T} + I_L(y)\beta_L(y)\beta_H(y)e^{-\beta_L(y)(1-\eta)T-\beta_H(y)\eta T}(1 \\
&- e^{-\beta_H(y)\eta T})(1-e^{-\beta_L(y)(1-\eta)T}) + I_H(y)\beta_L(y)\beta_H(y)(1 \\
&- e^{-\beta_H(y)\eta T})(1-e^{-\beta_L(y)(1-\eta)T}) + I_L(y)\beta_H(y)^2e^{-\beta_H(y)\eta T}(1 \\
&- e^{-\beta_L(y)(1-\eta)T})^2 + I_L(y)\beta_H(y)\beta_L(y)(1-e^{-\beta_H(y)\eta T})(1 \\
&- e^{-\beta_L(y)(1-\eta)T})(1-e^{-\beta_L(y)(1-\eta)T-\beta_H(y)\eta T}) - I_H(y)\beta_L(y)^2(1 \\
&- e^{-\beta_H(y)\eta T})(1-e^{-\beta_L(y)(1-\eta)T-\beta_H(y)\eta T}) - I_L(y)\beta_H(y)^2(1 \\
&- e^{-\beta_L(y)(1-\eta)T})(1-e^{-\beta_L(y)(1-\eta)T-\beta_H(y)\eta T})\big) \\
&+ \frac{1-C}{\tau\beta_H(y)\beta_L(y)}(I_H(y)\beta_L(y)\eta T + I_L(y)\beta_H(y)(1-\eta)T).
\end{aligned}
$$

To simplify the notations, let us denote by $a := -(\sigma I_{\max} + \frac{1}{\tau})\eta T$ and by $i := -(\sigma I_{\min} + \frac{1}{\tau})(1-\eta)T$, then $A(0) = \frac{1-C}{\tau\beta_L\beta_H(y)}\frac{1}{1-e^{a+i}}(\beta_L e^i(1-e^a) + \beta_L(1-e^i))$ and the previous computation can be written

as (we omitted the dependence on y)

$$
\begin{aligned}
T\overline{IA} =& A(0)I_H\frac{1-e^a}{\beta_H} + I_H\frac{1-C}{\tau\beta_H}(\eta T - \frac{1-e^a}{\beta_H}) + e^a A(0)I_L\frac{1-e^i}{\beta_L} \\
&+ \frac{1-C}{\tau\beta_H}(1-e^a)I_L\frac{1-e^i}{\beta_L} + I_L\frac{1-C}{\tau\beta_L}((1-\eta)T - \frac{1-e^i}{\beta_L}) \\
=& \frac{A(0)}{\beta_H\beta_L}(I_H\beta_H(1-e^a) + I_L\beta_L e^a(1-e^i)) + \frac{1-C}{\tau\beta_H\beta_L}(I_H\beta_L\eta T + I_L\beta_H(1-\eta)T) \\
&+ \frac{1-C}{\tau\beta_H^2\beta_L^2}\big(I_L\beta_H\beta_L(1-e^a)(1-e^i) - I_H\beta_L^2(1-e^a) - I_L\beta_H^2(1-e^i)\big) \\
=& \frac{1-C}{\tau\beta_H^2\beta_L^2}\frac{1}{1-e^{a+i}}\big(I_H\beta_L^2(1-e^a)^2e^i + I_L\beta_H\beta_L e^{a+i}(1-e^a)(1-e^i) \\
&+ I_H\beta_H\beta_L(1-e^a)(1-e^i) + I_L\beta_H^2 e^a(1-e^i)^2 + I_L\beta_H\beta_L(1-e^a)(1-e^i)(1-e^{a+i}) \\
&- I_H\beta_L^2(1-e^a)(1-e^{a+i}) - I_L\beta_H^2(1-e^i)(1-e^{a+i})\big) + \frac{1-C}{\tau\beta_H\beta_L}(I_H\beta_L\eta T + I_L\beta_H(1-\eta)T) \\
=& \frac{1-C}{\tau\beta_H^2\beta_L^2}\frac{1}{1-e^{a+i}}\big(I_H\beta_L^2(1-e^a)(e^i-1) + I_H\beta_L^2(e^a-1)(1-e^i) + I_H\beta_L\beta_L(1-e^a)(1-e^i) \\
&+ I_H\beta_L\beta_L(1-e^a)(1-e^i)\big) + \frac{1-C}{\tau\beta_L\beta_L}(I_H\beta_L\eta T + I_H\beta_L(1-\eta)T) \\
=& \frac{1-C}{\tau\beta_L^2\beta_L^2}\frac{(1-e^a)(1-e^i)}{1-e^{a+i}}\big(I_H\beta_L\beta_L + I_H\beta_L\beta_L - I_H\beta_L^2 - I_H\beta_L^2\big) \\
&+ \frac{1-C}{\tau\beta_L\beta_L}(I_H\beta_L\eta T + I_H\beta_L(1-\eta)T) \\
=& \frac{1-C}{\tau\beta_L^2\beta_L^2}\frac{(1-e^a)(1-e^i)}{1-e^{a+i}}(I_H\beta_L - I_H\beta_L)(\beta_L - \beta_L) + \frac{1-C}{\tau\beta_L\beta_L}(I_H\beta_L\eta T + I_H\beta_L(1-\eta)T).
\end{aligned}
$$

By using the definition of $I_H, I_H, \beta_L, \beta_L$, one has $(I_H\beta_L - I_H\beta_L)(\beta_L - \beta_L) = \frac{\sigma}{\tau}(I_{\max} - I_{\min})^2$ and $I_H\beta_L\eta T + I_H\beta_L(1-\eta)T = (\frac{I_M}{\tau} + \sigma I_{\max}I_{\min})T$. Replacing C by (A.1) in the previous equation gives

$$
T\overline{IA} = \frac{k_d\sigma\overline{IA} + k_r}{\tau\beta_L^2\beta_L^2(k_d\sigma I_\eta + k_r)}\Big(\Delta(y,T)\frac{\sigma}{\tau}(I_{\max} - I_{\min})^2 + (\frac{I_\eta}{\tau} + \sigma I_{\max}I_{\min})\beta_L\beta_L T\Big),
$$

where $\delta(y,T) = \frac{(1-e^a)(1-e^i)}{1-e^{a+i}}$. In other words

$$
\overline{IA} = \frac{k_r\left(\frac{\Delta(y,T)}{T\beta_L\beta_L}\frac{\sigma}{\tau}(I_{\max} - I_{\min})^2 + \frac{I_\eta}{\tau} + \sigma I_{\max}I_{\min}\right)}{\tau\beta_L\beta_L(k_d\sigma I_\eta + k_r) - k_d\sigma\left(\frac{\Delta(y,T)}{T\beta_L\beta_L}\frac{\sigma}{\tau}(I_{\max} - I_{\min})^2 + \frac{I_\eta}{\tau} + \sigma I_{\max}I_{\min}\right)}.
$$

We have that

$$
\Theta \coloneqq \frac{\Delta(y,T)(1+\tau\sigma I_\eta(y))}{(1+\tau\sigma I_H(y))(1+\tau\sigma I_L(y))\eta(1-\eta)} \to 1 \text{ as } T \to 0,
$$

and we can manipulate the value $\overline{IA}$ to get

$$\overline{IA} = \frac{\frac{k_r I_\eta}{(1+\tau\sigma I_\eta)\beta_L\beta_L\tau^2}\left(\tau^2\beta_L\beta_L\right) + (\Theta-1)\tau\sigma(I_L-I_H)^2\eta(1-\eta)}{k_r + k_d\sigma I_\eta - k_d\sigma\frac{I_\eta}{(1+\tau\sigma)\tau^2\beta_L\beta_L}\left(\tau^2\beta_L\beta_L\right) + (\Theta-1)\tau\sigma(I_L-I_H)^2\eta(1-\eta)},$$

and rearranging this last equality, we get

$$\bar{\mu}^{\mathrm{T}}(y) = \frac{K\sigma k_r I_M(y)\big(1+\xi_1(y)\xi_2(y,T)\big)}{k_r + k_r\tau\sigma I_M(y) + k_d\tau\big(\sigma I_M(y)\big)^2 + k_d\sigma I_M(y)\xi_1(y)\xi_2(y,T)}, \tag{A.2}$$

where

$$\begin{aligned}
\xi_1(y) &= \frac{\sigma\big(I_H(y)-I_L(y)\big)^2\eta(1-\eta)}{\tau\beta_H(y)\beta_L(y)},\\
\xi_2(y,T) &= \frac{(1-e^{-\beta_H(y)\eta T})(1-e^{-\beta_L(y)(1-\eta)T})}{T(1-e^{-\beta_H(y)\eta T-\beta_L(y)(1-\eta)T})}\frac{\eta\beta_H(y)+(1-\eta)\beta_L(y)}{\eta(1-\eta)\beta_H(y)\beta_L(y)} - 1.
\end{aligned}$$

A.1.3 Proof of Lemma 3.1

We split equation (3.7) into the high/low-flashing light configuration

$$\begin{cases}
\frac{\mathrm{d}}{dt}\begin{pmatrix}A(y,t)\\C(y,t)\end{pmatrix} = -M_H(y)\begin{pmatrix}A(y,t)\\C(y,t)\end{pmatrix} + N_H(y), & \text{if } t<\eta T,\\
\frac{\mathrm{d}}{\mathrm{d}t}\begin{pmatrix}A(y,t)\\C(y,t)\end{pmatrix} = -M_L(y)\begin{pmatrix}A(y,t)\\C(y,t)\end{pmatrix} + N_L(y), & \text{if } t>\eta T.
\end{cases}$$

One can solve this system by using the variation of parameters method and get

$$\begin{aligned}
\begin{pmatrix}A(y,t)\\C(y,t)\end{pmatrix} &= \left(\mathrm{Id}-e^{-tM_H(y)}\right)M_H^{-1}(y)N_H(y) + e^{-tM_H(y)}\begin{pmatrix}A(y,0)\\C(y,0)\end{pmatrix}, && \text{if } t<\eta T,\\
\begin{pmatrix}A(y,t)\\C(y,t)\end{pmatrix} &= \left(\mathrm{Id}-e^{-(t-\eta T)M_L(y)}\right)M_L^{-1}(y)N_L(y) + e^{-(t-\eta T)M_L(y)}\begin{pmatrix}A(y,\eta T)\\C(y,\eta T)\end{pmatrix}, && \text{if } t>\eta T,
\end{aligned}$$

where Id denotes the identity matrix in $\mathbb{R}^{2\times 2}$. Imposing then periodic conditions, i.e, $(A(y,0),C(y,0)) = (A(y,T),C(y,T))$, one can evaluate the values of $(A(y,0),C(y,0))$ and $(A(y,\eta T),C(y,\eta T))$:

$$\begin{pmatrix}A(y,\eta T)\\C(y,\eta T)\end{pmatrix} = \left(\mathrm{Id}-e^{-\eta T M_H(y)}\right)M_H^{-1}(y)N_H(y) + e^{-\eta T M_H(y)}\begin{pmatrix}A(y,0)\\C(y,0)\end{pmatrix}, \tag{A.3}$$

$$\begin{pmatrix}A(y,0)\\C(y,0)\end{pmatrix} = \left(\mathrm{Id}-e^{-(1-\eta)T M_L(y)}\right)M_L^{-1}(y)N_L(y) + e^{-(1-\eta)T M_L(y)}\begin{pmatrix}A(y,\eta T)\\C(y,\eta T)\end{pmatrix}. \tag{A.4}$$

Replacing finally (A.4) in (A.3) and vice versa, we obtain

$$\begin{aligned}\begin{pmatrix}A(y,\eta T)\\ C(y,\eta T)\end{pmatrix} &= \left(\mathrm{Id} - e^{-\eta T M_H(y)} e^{-(1-\eta)TM_L(y)}\right)^{-1} \\ &\cdot \left[\left(\mathrm{Id} - e^{-\eta T M_H(y)}\right) M_H^{-1}(y) N_H(y)\right. \\ &\left. + e^{-\eta T M_H(y)} \left(\mathrm{Id} - e^{-(1-\eta)TM_L(y)}\right) M_L^{-1}(y) N_L(y)\right],\end{aligned} \tag{A.5}$$

$$\begin{aligned}\begin{pmatrix}A(y,0)\\ C(y,0)\end{pmatrix} &= \left(\mathrm{Id} - e^{-(1-\eta)T M_L(y)} e^{-\eta TM_H(y)}\right)^{-1} \\ &\cdot \left[\left(\mathrm{Id} - e^{-(1-\eta)T M_L(y)}\right) M_L^{-1}(y) N_L(y)\right. \\ &\left. + e^{-(1-\eta)T M_L(y)} \left(\mathrm{Id} - e^{-\eta TM_H(y)}\right) M_H^{-1}(y) N_H(y)\right].\end{aligned} \tag{A.6}$$

The inverse matrix $(Id - e^{-\eta T M_H} e^{-(1-\eta)TM_L})$ exists because the matrix $e^{-\eta T M_H} e^{-(1-\eta)TM_L}$ has no eigenvalue equal to 1. The solution founded it is then unique.

A.1.4 Exact growth rate

To calculate the T-average of the growth rate, we calculate the integral $\int_0^T I(y,t)(A(y,t),C(y,t))dt$:

$$\begin{aligned}\int_0^T I(y,t)\begin{pmatrix}A(y,t)\\ C(y,t)\end{pmatrix} dt &= I_H(y)\int_0^{\eta T}\begin{pmatrix}A(y,t)\\ C(y,t)\end{pmatrix} dt + I_L(y)\int_{\eta T}^{T}\begin{pmatrix}A(y,t)\\ C(y,t)\end{pmatrix} dt \\ &= \eta T I_H(y) M_H^{-1}(y) N_H(y) \\ &\quad - I_H(y) M_H^{-1}(y)\left(\mathrm{Id} - e^{-\eta T M_H(y)}\right)\left[M_H^{-1}(y)N_H(y) - \begin{pmatrix}A(y,0)\\ C(y,0)\end{pmatrix}\right] \\ &\quad + I_L(y)(1-\eta)TM_L^{-1}(y)N_L(y) \\ &\quad - I_L(y) M_L^{-1}(y)\left(\mathrm{Id} - e^{-(1-\eta)T M_L(y)}\right)\left[M_L^{-1}(y)N_L(y) - \begin{pmatrix}A(y,\eta T)\\ C(y,\eta T)\end{pmatrix}\right].\end{aligned} \tag{A.7}$$

Using (A.5) we can compute

$$
\begin{aligned}
&M_L^{-1}(y)N_L(y) - \begin{pmatrix} A(y,\eta T) \\ C(y,\eta T) \end{pmatrix} \\
&= M_L^{-1}(y)N_L(y) - \left(\mathrm{Id} - e^{-\eta T M_H(y)} e^{-(1-\eta)TM_L(y)}\right)^{-1} \\
&\quad \cdot \Big[\left(\mathrm{Id} - e^{-\eta T M_H(y)}\right) M_H^{-1}(y)N_H(y) \\
&\qquad + e^{-\eta T M_H(y)} \left(\mathrm{Id} - e^{-(1-\eta)TM_L(y)}\right) M_L^{-1}(y)N_L(y)\Big] \\
&= \left(\mathrm{Id} - e^{-\eta T M_H(y)} e^{-(1-\eta)TM_L(y)}\right)^{-1} \\
&\quad \cdot \Big[(\mathrm{Id} - e^{-\eta T M_H(y)}) M_L^{-1}(y)N_L(y) - (\mathrm{Id} - e^{-\eta T M_H(y)}) M_H^{-1}(y)N_H(y) \\
&\quad - e^{-\eta T M_H(y)} (\mathrm{Id} - e^{-(1-\eta)TM_H(y)}) M_L^{-1}(y)N_L(y)\Big] \\
&= \left(\mathrm{Id} - e^{-\eta T M_H(y)} e^{-(1-\eta)TM_L(y)}\right)^{-1} \big[M_L^{-1}(y)N_L(y) \\
&\quad - e^{-\eta T M_H(y)} e^{-(1-\eta)TM_L(y)} M_L^{-1}(y)N_L(y) - M_H^{-1}(y)N_H(y) \\
&\quad + e^{-\eta T M_H(y)} M_H^{-1}(y)N_H(y) - e^{-\eta T M_H(y)} M_L^{-1}(y)N_L(y) \\
&\quad + e^{-e\eta T M_H(y)} e^{-(1-\eta)TM_L(y)} M_L^{-1} N_L(y)\Big] \\
&= \left(\mathrm{Id} - e^{-\eta T M_H(y)} e^{-(1-\eta)TM_L(y)}\right)^{-1} \Big[(\mathrm{Id} - e^{-\eta T M_H(y)}) M_L^{-1}(y)N_L(y) \\
&\quad - (\mathrm{Id} - e^{-\eta T M_H(y)}) M_H^{-1}(y)N_H(y)\Big] \\
&= \left(\mathrm{Id} - e^{-\eta T M_H(y)} e^{-(1-\eta)TM_L(y)}\right)^{-1} \cdot \\
&(\mathrm{Id} - e^{-\eta T M_H(y)})(M_L^{-1}(y)N_L(y) - M_H^{-1}(y)N_H(y)).
\end{aligned}
$$

In the same way, using (A.6) we can get

$$
\begin{aligned}
M_H^{-1}(y)N_H(y) - \begin{pmatrix} A(y,0) \\ C(y,0) \end{pmatrix} = \left(\mathrm{Id} - e^{-(1-\eta)TM_L(y)} e^{-\eta T M_H(y)}\right)^{-1} (\mathrm{Id} - e^{-(1-\eta)TM_L(y)}) \\
\cdot (M_H^{-1} N_H(y) - M_L^{-1} N_L(y)).
\end{aligned}
$$

Replacing the above calculations on (A.7), we have

$$
\int_0^T I(y,t) \begin{pmatrix} A(y,t) \\ C(y,t) \end{pmatrix} = \eta T I_H(y) M_H^{-1}(y) N_H(y) + (1-\eta) T I_L(y) M_L^{-1}(y) N_L(y) + \Delta, \qquad \text{(A.8)}
$$

where

$$
\begin{aligned}
\Delta = \Big[& I_H(y) M_H^{-1}(y) \left(\mathrm{Id} - e^{-\eta T M_H(y)}\right) \left(\mathrm{Id} - e^{-(1-\eta)TM_L(y)} e^{-\eta T M_H(y)}\right)^{-1} \left(\mathrm{Id} - e^{-(1-\eta)TM_L(y}\right) \\
& - I_L(y) M_L^{-1}(y) \left(\mathrm{Id} - e^{-(1-\eta)TM_L(y}\right) \left(\mathrm{Id} - e^{-\eta T M_H(y)} e^{-(1-\eta)TM_L(y)}\right)^{-1} \left(\mathrm{Id} - e^{-\eta T M_H(y)}\right)\Big] \\
& \cdot \left(M_H^{-1}(y)N_H(y) - M_L^{-1}(y)N_L(y)\right).
\end{aligned}
$$

Finally, the average growth rate $\frac{1}{T}\int_0^T K\sigma I A dt$ is proportional to the first coordinate of (A.8) multiplied by $\frac{K\sigma}{T}$. Denote δ the first coordinate of Δ and note that

$$M_H^{-1}(y)N_H(y) = \begin{pmatrix} \dfrac{k_r}{\tau k_d(\sigma I_H(y))^2 + \tau k_r \sigma I_H(y) + k_r} \\ \dfrac{\tau k_d(\sigma I_H(y))^2}{\tau k_d(\sigma I_H(y))^2 + \tau k_r \sigma I_H(y) + k_r} \end{pmatrix}, \tag{A.9}$$

$$M_L^{-1}(y)N_L(y) = \begin{pmatrix} \dfrac{k_r}{\tau k_d(\sigma I_L(y))^2 + \tau k_r \sigma I_L(y) + k_r} \\ \dfrac{\tau k_d(\sigma I_L(y))^2}{\tau k_d(\sigma I_L(y))^2 + \tau k_r \sigma I_L(y) + k_r} \end{pmatrix}, \tag{A.10}$$

where the first coordinate in (A.9) and (A.10) multiplied by $K\sigma$ is exactly $\mu_S(I_H(y))$ and $\mu_S(I_L(y))$ respectively. So, the T-average of the growth rate is

$$\bar{\mu}^{\mathrm{T}}(y) = \eta\mu_s(I_H(y)) + (1-\eta)\mu_S(I_L(y)) - \frac{K\sigma}{T}\delta(y,T). \tag{A.11}$$

A.1.5 Eigenvalues of matrix M

We will condense the analysis of the eigenvalues of M_H and M_L in the matrix

$$M(I) = \begin{pmatrix} \sigma I + \frac{1}{\tau} & \frac{1}{\tau} \\ k_d\sigma I & k_d\sigma I + k_r \end{pmatrix}.$$

Denoting λ_1 and λ_2 the eigenvalues, then we have

$$\mathrm{Tr}(M(I)) = \lambda_1 + \lambda_2 = \sigma I + \frac{1}{\tau} + k_d\sigma I + k_r, \tag{A.12}$$

$$\mathrm{Det}(M(I)) = \lambda_1\lambda_2 = k_d(\sigma I)^2 + k_r\sigma I + \frac{k_r}{\tau}. \tag{A.13}$$

From (A.13), λ_1 and λ_2 has the same sign, and since (A.12) holds, the two eigenvalues are positive.

A.2 Proof of Lemma 3.3

The second derivative of the function μ_S can be computed as

$$\frac{\mathrm{d}^2}{\mathrm{d}I^2}\mu_S(I) = -\frac{2K\sigma\left[\tau\sigma + \frac{k_d}{k_r}\tau\sigma^2 I\left(3 - \frac{k_d}{k_r}\tau\sigma^2 I^2\right)\right]}{\left(1 + \tau\sigma I + \frac{k_d}{k_r}\tau(\sigma I)^2\right)^3},$$

and it is zero in the point I_c which satisfies

$$\left(\frac{k_d}{k_r}\tau\sigma^2\right)^2 I_c^3 - 3\frac{k_d}{k_r}\tau\sigma^2 I_c - \tau\sigma = 0.$$

This is a depressed cubic equation, where the determinant correspond to

$$\Delta = \left(\frac{1}{\frac{k_d}{k_r}\tau\sigma^2}\right)^4 (\tau\sigma)^2 - 4\left(\frac{1}{\frac{k_d}{k_r}\tau\sigma^2}\right)^3$$

where if $\Delta \leq 0$ all the roots are real. Note that

$$\Delta \leq 0 \iff \tau \leq 4\frac{k_d}{k_r}.$$

In this case, the solutions are given by [158]:

$$l\cos\frac{\theta}{3}, \quad l\cos\frac{\theta+2\pi}{3}, \quad \text{and} \quad l\cos\frac{\theta+4\pi}{3}$$

where

$$l = \frac{2}{\sigma\sqrt{\frac{k_d}{k_r}\tau}}, \quad \text{and} \quad \theta = \arccos\left(\frac{\sqrt{\tau}}{2\sqrt{\frac{k_d}{k_r}}}\right).$$

From the three possible solutions, only $l\cos\frac{\theta}{3}$ is positive due to $\theta/3 \in (0, \pi/6)$. In the case that $\Delta > 0$ then the real solution can be written as [72]

$$l\cosh\left(\frac{1}{3}\operatorname{arccosh}\left(\frac{\sqrt{\tau}}{2\sqrt{\frac{k_d}{k_r}}}\right)\right).$$

Appendix B

Complement of Chapter 7

B.1 Sensitivity equations and the Runge-Kutta methods

Proposition 1. *The sensitivity equations* (7.3) *are solved through backpropagation in time.*

Proof. To simplify the notation, we write $\boldsymbol{v} = \frac{\partial \boldsymbol{x}}{\partial \boldsymbol{\Omega}}$ and we rewrite the sensitivity equation (7.3) as

$$\frac{d\boldsymbol{v}}{dt} = F(t, \boldsymbol{v}),$$

where

$$F(t, \boldsymbol{v}) = \frac{\partial f_{\boldsymbol{\Omega}}(t, \boldsymbol{y}, \boldsymbol{x})}{\partial \boldsymbol{x}} \boldsymbol{v} + \frac{\partial f_{\boldsymbol{\Omega}}(t, \boldsymbol{y}, \boldsymbol{x})}{\partial \boldsymbol{\Omega}}.$$

Setting $c_1 = 0$ we rewrite (7.2) as

$$\begin{aligned} \boldsymbol{x}_{n+1} &= \boldsymbol{x}_n + \Delta t_n \sum_{i=1}^{s} b_i \boldsymbol{k}_i, \\ \boldsymbol{k}_i &= f_{\boldsymbol{\Omega}} \left(t_n + c_i \Delta t_n, \boldsymbol{y}_n + c_i \Delta \boldsymbol{y}_n, \boldsymbol{x}_n + \Delta t_n \sum_{j=1}^{i-1} a_{ij} \boldsymbol{k}_j \right) \\ &\quad \text{for } i = 1, .., s. \end{aligned}$$

Applying $\frac{\partial}{\partial \boldsymbol{\Omega}}$ to the above we have that:

$$\boldsymbol{v}_{n+1} = \Delta t_n \sum_{i=1}^{s} b_i \frac{\partial \boldsymbol{k}_i}{\partial \boldsymbol{\Omega}},$$

and for $i = 1, .., s$:

$$\begin{aligned}\frac{\partial \boldsymbol{k}_i}{\partial \boldsymbol{\Omega}} &= \frac{\partial f_{\boldsymbol{\Omega}}}{\partial \boldsymbol{\Omega}} \left(t_n + c_i \Delta t_n, \boldsymbol{y}_n + c_i \Delta \boldsymbol{y}_n, \boldsymbol{x}_n + \Delta t_n \sum_{j=1}^{i-1} a_{ij} \boldsymbol{k}_j \right), \\ &= \frac{f_{\boldsymbol{\Omega}}}{\partial \boldsymbol{x}} \cdot \left(\boldsymbol{v}_n + \Delta t_n \sum_{j=1}^{i-1} a_{ij} \frac{\partial \boldsymbol{k}_j}{\partial \boldsymbol{\Omega}} \right) + \frac{\partial f_{\boldsymbol{\Omega}}}{\partial \boldsymbol{\Omega}}, \\ &= F \left(t_n + c_i \Delta t_n, \boldsymbol{v}_n + \Delta t_n \sum_{j=1}^{i-1} a_{ij} \frac{\partial \boldsymbol{k}_j}{\partial \boldsymbol{\Omega}} \right).\end{aligned}$$

Which corresponds to the same numerical scheme for the sensitivity equations. □

B.2 Proof of Propostion 7.1

Proof. Let us consider the problem:

$$\begin{cases} \min\limits_{\boldsymbol{\Omega}} & L(\boldsymbol{x}) = \int_0^{T_f} g(\boldsymbol{x}(t)) dt, \\ \text{s.t.} & \dfrac{d\boldsymbol{x}(t)}{dt} = f_{\boldsymbol{\Omega}}(t, \boldsymbol{y}(t), \boldsymbol{x}(t)). \end{cases} \tag{B.1}$$

We define the Lagrangian of the problem as

$$\mathcal{L}(\boldsymbol{x}, \boldsymbol{\Omega}, \boldsymbol{\lambda}) = \int_0^{T_f} g(\boldsymbol{x}(t)) dt + \int_0^{T_f} \boldsymbol{\lambda}^\intercal(t) \left(f_{\boldsymbol{\Omega}}(t, \boldsymbol{y}(t), \boldsymbol{x}(t)) - \frac{d\boldsymbol{x}(t)}{dt} \right) dt.$$

The gradient is computed as:

$$\frac{\partial \mathcal{L}}{\partial \boldsymbol{\Omega}} = \int_0^{T_f} \frac{\partial g}{\partial \boldsymbol{x}} \frac{\partial \boldsymbol{x}}{\partial \boldsymbol{\Omega}} + \boldsymbol{\lambda}^\intercal \left[\frac{\partial f_{\boldsymbol{\Omega}}}{\partial \Omega} - \frac{d}{dt} \left(\frac{\partial \boldsymbol{x}}{\partial \boldsymbol{\Omega}} \right) \right] dt.$$

Integrating by parts:

$$\int_0^{T_f} \boldsymbol{\lambda}^\intercal \frac{d}{dt} \left(\frac{\partial \boldsymbol{x}}{\partial \boldsymbol{\Omega}} \right) dt = \left[\boldsymbol{\lambda}^\intercal(T_f) \frac{\partial \boldsymbol{x}(T_f)}{\partial \boldsymbol{\Omega}} - \boldsymbol{\lambda}^\intercal(0) \frac{\partial \boldsymbol{x}(0)}{\partial \boldsymbol{\Omega}} \right] - \int_0^{T_f} \frac{d\boldsymbol{\lambda}^\intercal}{dt} \frac{\partial \boldsymbol{x}}{\partial \Omega} dt.$$

We have that $\frac{\partial \boldsymbol{x}(0)}{\partial \boldsymbol{\Omega}} = 0$, then replacing in the above:

$$\frac{\partial \mathcal{L}}{\partial \boldsymbol{\Omega}} = \int_0^{T_f} \boldsymbol{\lambda}^\intercal \frac{\partial f_{\boldsymbol{\Omega}}}{\partial \boldsymbol{\Omega}} dt - \boldsymbol{\lambda}^\intercal(T_f) \frac{\partial \boldsymbol{x}(T_f)}{\partial \boldsymbol{\Omega}} + \int_0^{T_f} \left[\frac{d\boldsymbol{\lambda}^\intercal}{dt} + \boldsymbol{\lambda}^\intercal \frac{\partial f_{\boldsymbol{\Omega}}}{\partial \boldsymbol{x}} + \frac{\partial g}{\partial \boldsymbol{x}} \right] \frac{\partial \boldsymbol{x}}{\partial \boldsymbol{\Omega}} dt.$$

Then as x is a solution of equation (7.1) and $\boldsymbol{\lambda}$ a solution of equation (7.5) we get the equality (7.4). □

B.3 Monod Model

The description of the growth rate with the Monod model is formulated in equation (B.2) as a function of the light intensity I. Beer-lambert law was used to calculate the average light intensity as shown in the below equation (B.3). The resulting equation (B.4) was used for the kinetic model for the biomass evolution.

$$\mu(I) = \mu_{max} \frac{I}{I + K_I}. \tag{B.2}$$

The light distribution profile of the photobioreactor will be simplified. We assume that it is equally illuminated from one side, and we ignore the complex shape of the FPA assuming that the geometry of the PBR is a rectangular cuboid. Under these assumptions and following [76] we compute the average growth rate in the PBR as

$$\mu_{avg} = \frac{\mu_{\max}}{L} \int_0^L \left(\frac{I e^{-k x^b z}}{I e^{-k x^b z} + K_I} \right) dz. \tag{B.3}$$

A respiration term R is also considered

$$\frac{dx}{dt} = \mu_{avg} x - R x. \tag{B.4}$$

After solving the integral (B.3), we deduce the dynamic in (7.8).

Appendix C

Optimal control problem with box constraints

Let us consider the optimal control problem without restrictions over the trajectory, with free final conditions and fixed final time:

$$\begin{aligned} \min_{\mathbf{u}\in\mathcal{U}} \quad & J_{[0,T]}(\mathbf{u}) = \int_0^T g(t,\mathbf{z}(t),\mathbf{u}(t))dt, \\ \text{subject to } & \dot{\mathbf{z}}(t) = f(t,\mathbf{z}(t),\mathbf{u}(t)), \\ & \mathbf{z}(0) = \mathbf{z}_0, \end{aligned} \tag{P}$$

where $T > 0$ is fixed, $\mathbf{z}(t) \in \mathbb{R}^n$ is the state vector with the initial condition $\mathbf{z}_0 \in \mathbb{R}^n$, $\mathbf{u} \in \mathbb{R}^m$ is the control vector, f and g are assumed to be $\mathcal{C}^1$ from $\mathbb{R}^{1+n+m}$ to $\mathbb{R}^n$. $\mathcal{U}$ correspond to the set of admissible controls. We will consider

$$\mathcal{U} = \mathcal{L}^\infty_{\text{loc}}([0,+\infty), C),$$

i.e., the set of locally integrable functions on every compact set in $[0,\infty)$ that takes values in the compact set $C \subset \mathbb{R}^m$ defined as

$$C = \prod_{j=1}^m [a_j, b_j],$$

where a_i, b_i are the lower and upper bound of $\mathbf{u}_i$. We will assume the following

1. there exists $K \in \mathbb{R}$ such that for all $u \in \mathcal{U}$

   $$\|\mathbf{z}(t)\| \leq K$$

   where $\mathbf{z}$ is the solution of the controlled system

   $$\begin{aligned} \dot{\mathbf{z}}(t) &= f(t,\mathbf{z}(t),\mathbf{u}(t)) \\ \mathbf{z}(0) &= \mathbf{z}_0 \end{aligned}$$

2. For every $(t, \mathbf{z}) \in \mathbb{R} \times \mathbb{R}^n$, the set

$$V(t, \mathbf{z}) = \{(-g(t, \mathbf{z}, \mathbf{u}), f(t, \mathbf{z}, \mathbf{u}) : u \in \mathcal{U}\},$$

is convex.

Under these two hypotheses, Problem (P) has a solution (see, for example, [145, Theorem 6.15].

According to the Maximum Pontryagin's Principle, if the control $\mathbf{u}^* \in \mathcal{U}$ is optimal in $[0, T]$, then there exists an absolutely continuous vector function $\boldsymbol{\lambda} : [0, T] \to \mathbb{R}^n$ called co-state or adjoint vector and a real $\lambda_0 \leq 0$ such that

$$\dot{\boldsymbol{\lambda}}^T(t) = -\frac{\partial H}{\partial \mathbf{z}}, \tag{C.1}$$

where H is the so-called Hamiltonian defined as

$$H(t, \mathbf{z}(t), \boldsymbol{\lambda}(t), \lambda_0, \mathbf{u}(t)) = \boldsymbol{\lambda}^T f(t, \mathbf{z}(t), \mathbf{u}(t)) + \lambda_0 g(t, \mathbf{z}(t), \mathbf{u}(t)).$$

As the problem is formulated with free final conditions, the transversality conditions are

$$\boldsymbol{\lambda}^T(T) = 0. \tag{C.2}$$

The optimal control $\mathbf{u}^*$, its trajectory $\mathbf{z}^*$ and its respective co-state $\boldsymbol{\lambda}^*$ fulfill the maximum condition:

$$\mathbf{u}^*(t) \in \underset{\mathbf{v} \in C}{\operatorname{argmax}}\, H(t, \mathbf{z}^*(t), \boldsymbol{\lambda}^*(t), \mathbf{v}), \tag{C.3}$$

for almost every $t \in [0, T]$. We will assume that the solution of (P) admits a solution where $\lambda_0 \neq 0$. In this case, we can normalize by λ_0, and reduce H to simply

$$H(t, \mathbf{z}(t), \boldsymbol{\lambda}(t), \mathbf{u}(t)) = \boldsymbol{\lambda}^T f(t, \mathbf{z}(t), \mathbf{u}(t)) + g(t, \mathbf{z}(t), \mathbf{u}(t)).$$

Then condition (C.3) is then replaced by

$$\mathbf{u}^*(t) \in \underset{\mathbf{v} \in C}{\operatorname{argmin}}\, H(t, \mathbf{z}^*(t), \boldsymbol{\lambda}^*(t), \mathbf{v}). \tag{C.4}$$

Then Equation (C.1), together with the transversality condition can be rewritten as

$$\begin{cases} \dot{\boldsymbol{\lambda}}^T = -\lambda^T \dfrac{\partial f(t, \mathbf{z}(t), \mathbf{u}(t))}{\partial \mathbf{z}} - \dfrac{\partial g(t, \mathbf{z}(t), \mathbf{u}(t))}{\partial \mathbf{z}}, \\ \boldsymbol{\lambda}^T(T) = 0. \end{cases} \tag{C.5}$$

The first order condition of (C.4) can be written for every $j = 1, ..., N$ as follows

$$\mathbf{u}^*(t) = a_j \Longleftrightarrow (\lambda^*)^T \frac{\partial f(t, \mathbf{z}^*, \mathbf{u}^*)}{\partial \mathbf{u}} + \frac{\partial g(t, \mathbf{z}^*, \mathbf{u}^*)}{\partial u^*} > 0,$$
$$\mathbf{u}^*(t) = b_j \Longleftrightarrow (\lambda^*)^T \frac{\partial f(t, \mathbf{z}^*, \mathbf{u}^*)}{\partial \mathbf{u}} + \frac{\partial g(t, \mathbf{z}^*, \mathbf{u}^*)}{\partial u^*} < 0$$

otherwise,

$$(\lambda^*)^T \frac{\partial f(t, \mathbf{z}^*, \mathbf{u}^*)}{\partial \mathbf{u}} + \frac{\partial g(t, \mathbf{z}^*, \mathbf{u}^*)}{\partial \mathbf{u}^*} = 0$$

C.1 Control parameterization methods

Within the optimization methods in optimal control, we can find direct and indirect methods. In a direct method, the state $\mathbf{z}$ and/or the control $\mathbf{u}$ are approximated with a base of functions. We will consider only an approximation of the control $\mathbf{u}$, which is also called a control parameterization method. Control $\mathbf{u}$ is parametrized using a specified functional form with parameters $\theta \in \mathbb{R}^p$, i.e., the control is a function of the parameters $\mathbf{u}_\theta(t) = \mathbf{u}(\theta, t)$. We assume that the gradients $\frac{\partial \mathbf{u}}{\partial \theta}$ exists. More precisely, we assume that the function

$$\begin{aligned} E : \mathbb{R}^p &\to \mathcal{U} \\ \theta &\mapsto \mathbf{u}_\theta \end{aligned}$$

is a $\mathcal{C}^1$ function. The associated parametrized controlled system is denoted as follows:

$$\begin{cases} \dot{\mathbf{z}}_\theta(t) = f(t, \mathbf{z}_\theta(t), \mathbf{u}_\theta(t)), \\ \mathbf{z}_\theta(0) = \mathbf{z}_0. \end{cases} \tag{C.6}$$

The cost function can be computed as a function of the parameters:

$$J_{[0,T]}(\theta) = \int_0^T g(t, \mathbf{z}_\theta, \mathbf{u}_\theta) dt.$$

The gradient of the cost function $J_{[0,T]}(\theta)$ with respect to the parameters θ can be computed with the so-called adjoint method described in the next Proposition:

Proposition 2. *The gradient of the cost function $J_{[0,T]}(\boldsymbol{u}_\theta)$ with respect to the parameters θ is given by*

$$\frac{\partial J_{[0,T]}(\theta)}{\partial \theta} = \int_0^T \boldsymbol{\lambda}_\theta^T(t) \frac{\partial f(t, \boldsymbol{z}_\theta(t), \boldsymbol{u}_\theta(t))}{\partial \boldsymbol{u}} \frac{\partial \boldsymbol{u}_\theta}{\partial \theta} dt + \int_0^T \frac{\partial g(t, \boldsymbol{z}_\theta, \boldsymbol{u}_\theta)}{\partial \boldsymbol{u}} \frac{\partial \boldsymbol{u}_\theta}{\partial \theta} dt$$

where $\boldsymbol{\lambda}_\theta$ is the solution of the equation

$$\begin{cases} \dot{\boldsymbol{\lambda}}_\theta^T = -\boldsymbol{\lambda}_\theta^T \dfrac{\partial f(t, \boldsymbol{z}_\theta(t), \boldsymbol{u}_\theta(t))}{\partial \boldsymbol{z}} - \dfrac{\partial g(t, \boldsymbol{z}_\theta(t), \boldsymbol{u}_\theta(t))}{\partial \boldsymbol{z}}, \\ \boldsymbol{\lambda}_\theta(T) = 0. \end{cases} \tag{C.7}$$

Proof. Let us denote $\mathcal{D}^1([0,T], \mathbb{R}^n)$ the set of continuous functions in $[0,T]$ and differentiable in $(0,T)$ that take values in $\mathbb{R}^n$. We define the Lagrangian $\mathcal{L} : \mathcal{D}^1([0,T], \mathbb{R}^n) \times \mathcal{D}^1([0,T], \mathbb{R}^n) \times \mathcal{U} \to \mathbb{R}$ as

$$\mathcal{L}(\boldsymbol{\lambda}, \mathbf{z}, \mathbf{u}) = \int_0^T g(t, \mathbf{z}(t), \mathbf{u}(t)) + \boldsymbol{\lambda}^T(t) \left(f(t, \mathbf{z}(t), \mathbf{u}(t)) - \dot{\mathbf{z}}(t) \right) dt.$$

Note that if $\dot{\mathbf{z}}(t) = f(t, \mathbf{z}(t), \mathbf{u}(t)) \ \forall t \in (0,T)$, then

$$\mathcal{L} = J_{[0,T]}(\mathbf{u}) \ \forall \boldsymbol{\lambda} \in \mathcal{D}^1([0,T], \mathbb{R}^n).$$

In particular, considering the $\mathbf{z} = \mathbf{z}_\theta$ the only solution of the system (C.6), the derivative of $\mathcal{L}$ as a function of θ satisfies $\forall \boldsymbol{\lambda} \in \mathcal{D}^1([0,T], \mathbb{R}^n)$:

$$\frac{\partial \mathcal{L}}{\partial \theta} = \int_0^T \frac{\partial g}{\partial \mathbf{z}} \frac{\partial \mathbf{z}_\theta}{\partial \theta} + \frac{\partial g}{\partial \mathbf{u}} \frac{\partial \mathbf{u}_\theta}{\partial \theta} + \boldsymbol{\lambda}^T(t) \left(\frac{\partial f}{\partial \mathbf{z}} \frac{\partial \mathbf{z}_\theta}{\partial \theta} + \frac{\partial f}{\partial \mathbf{u}} \frac{\partial \mathbf{u}_\theta}{\partial \theta} - \frac{d}{dt} \frac{\partial \mathbf{z}_\theta}{\partial \theta} \right) dt.$$

Integrating by parts:

$$\begin{aligned}\frac{\partial \mathcal{L}}{\partial \theta} &= \int_0^T \boldsymbol{\lambda}^T(t)\frac{\partial f}{\partial \mathbf{u}}\frac{\partial \mathbf{u}_\theta}{\partial \theta} + \frac{\partial g}{\partial \mathbf{u}}\frac{\partial \mathbf{u}_\theta}{\partial \theta}dt + \int_0^T \frac{d}{dt}\boldsymbol{\lambda}^T(t)\frac{\partial \mathbf{z}_\theta}{\partial \theta} + \frac{\partial f}{\partial \mathbf{z}}\frac{\partial \mathbf{z}_\theta}{\partial \theta} + \frac{\partial g}{\partial \mathbf{z}}\frac{\partial \mathbf{z}_\theta}{\partial \theta}dt. \\ &\quad - \boldsymbol{\lambda}^T(T)\frac{\partial \mathbf{z}(T)}{\partial \theta} + \boldsymbol{\lambda}^T(0)\frac{\partial \mathbf{z}(0)}{\partial \theta}, \\ &= \int_0^T \boldsymbol{\lambda}^T(t)\frac{\partial f}{\partial \mathbf{u}}\frac{\partial \mathbf{u}_\theta}{\partial \theta} + \frac{\partial g}{\partial \mathbf{u}}\frac{\partial \mathbf{u}_\theta}{\partial \theta}dt + \int_0^T \left(\frac{d}{dt}\boldsymbol{\lambda}^T(t) + \frac{\partial f}{\partial \mathbf{z}} + \frac{\partial g}{\partial \mathbf{z}}\right)\frac{\partial \mathbf{z}_\theta}{\partial \theta}dt \\ &\quad - \boldsymbol{\lambda}^T(T)\frac{\partial \mathbf{z}(T)}{\partial \theta} + \boldsymbol{\lambda}^T(0)\frac{\partial \mathbf{z}(0)}{\partial \theta}.\end{aligned}$$

As the initial condition is fixed it doesn't depend on the parameters θ, then $\frac{\partial \mathbf{z}_\theta(0)}{\partial \theta} = 0$. Finally, choosing $\boldsymbol{\lambda} = \boldsymbol{\lambda}_\theta$ fulfilling (C.7), then

$$\frac{\partial \mathcal{L}}{\partial \theta} = \int_0^T \boldsymbol{\lambda}_\theta^T \frac{\partial f}{\partial \mathbf{u}}\frac{\partial \mathbf{u}_\theta}{\partial \theta} + \frac{\partial g}{\partial \mathbf{u}}\frac{\partial \mathbf{u}_\theta}{\partial \theta}dt.$$

□

Typically, piecewise functions [59] are used to solve an approximate problem associated to (P) that inherits the properties of the original problem. This approximate problem is a constrained finite dimensional optimization problem that can be with different methods. In this work, we focus on the case where the parametrized control $\mathbf{u}_\theta$ is a neural network.

Appendix D

Complement of Chapter 8

D.1 Proof of Proposition 8.2

Proof. Let

$$H(x, \lambda_x, \lambda_0, D) = Dx(1 - \lambda_x) + \lambda_x \mu$$

be the Hamiltonian of the system (8.10), the Pontryagin's maximum principle establishes that

$$D(t) \in \underset{v \in [0, D_{\max}]}{\operatorname{argmax}} \; H(x(t), \lambda_x(t), v), \text{ a.e. } t \in [0, T].$$

λ_x satisfies the adjoint equation $\dot{\lambda}_x = -\frac{\partial H}{\partial x}$ with the final condition $\lambda_x(T) = 0$, that is:

$$\begin{aligned} \dot{\lambda}_x &= -\lambda_x(\mu - D) - D, \\ \lambda_x(T) &= 0. \end{aligned} \tag{D.1}$$

Let us suppose that there is an open interval (t_1, t_2) where $\lambda_x = 1$ for every $t \in (t_1, t_2)$. Then $\dot{\lambda}_x = 0, \ \forall t \in (t_1, t_2)$. Replacing this values in (D.1) we have that $0 = -(\mu - D) - D$, and consequently $\mu = 0$, which is not possible. Then λ_x can not take the value 1 in an open interval of $[0, T]$. Then, for almost all $t \in [0, T]$, the optimal control D^* is such that

$$D^* = \begin{cases} 0 \text{ if } \lambda_x > 1 \\ D_{\max} \text{ if } \lambda_x < 1 \end{cases}$$

As the final condition $\lambda_x(T) = 0 < 1$ the last arc is always with $D^* = D_{\max}$. The length of this arc can be computed in the switching point, if it exists, $\lambda_x(t_s) = 1$, where t_s is, for now, unknown. Then for all $t \in (t_s, T)$

$$\begin{aligned} \dot{\lambda}_x &= -\lambda_x(\mu - D_{\max}) - D_{\max}, \\ \dot{\lambda}_x + \lambda_x(\mu - D_{\max}) &= -D_{\max}, \\ \frac{d}{dt}\left(\lambda_x e^{(\mu - D_{\max})t}\right) &= -e^{(\mu - D_{\max})t} D_{\max}, \\ \lambda_x(T) e^{(\mu - D_{\max})T} - \lambda_x(t) &= -\int_t^T e^{(\mu - D_{\max})s} D_{\max} ds, \end{aligned}$$

then,

$$\lambda_x(t) = \frac{D_{\max}}{D_{\max} - \mu}\left(1 - e^{-(D_{\max}-\mu)(T-t)}\right).$$

Then replacing $t = t_s$ we have that

$$t_s = T - \frac{\ln(D_{\max}/\mu)}{D_{\max} - \mu}.$$

□

D.2 Proof of Proposition 8.3

Proof. Using the definition of $D_{w,b}$:

$$\begin{aligned}
\dot{x} &= (\mu - D_{w,b})x, \\
\frac{d}{dt}\left(xe^{-\int_0^T(\mu - D_{w,b}(s))ds}\right) &= 0, \\
x(t) &= x_0 e^{\int_0^t(\mu - D_{w,b}(s))ds}, \\
x(t) &= x_0 e^{\mu t} e^{-\frac{D_{\max}}{w}\ln\left(\frac{1+e^{wt+b}}{1+e^b}\right)}.
\end{aligned}$$

Then, the cost function $J_{[0,T]}(D_{w,b})$, can be computed as

$$\begin{aligned}
\dot{x} &= (\mu - D_{w,b})x, \\
\int_0^T \dot{x}(t)dt &= \mu\int_0^T x(t)dt - \int_0^T D_{w,b}(t)x(t)dt, \\
x(T) - x_0 &= \mu\int_0^T x(t)dt - \int_0^T D_{w,b}(t)x(t)dt,
\end{aligned}$$

then, using (8.16) and the definition of $J_{[0,T]}(D_{w,b})$, we can conclude (8.17).

Replacing $b = -wt_s$ in (8.16) we get

$$\begin{aligned}
x_{w,-wt_s}(t) &= x_0 e^{\mu t}\left(\frac{1+e^{w(t-t_s)}}{1+e^{-wt_s}}\right)^{-\frac{D_{\max}}{w}}, \\
&= x_0 e^{\mu t} e^{-\frac{D_{\max}}{w}\ln\left(\frac{1+e^{w(t-t_s)}}{1+e^{-wt_s}}\right)}.
\end{aligned}$$

Then, we need to study the limit

$$L = \lim_{w\to+\infty} -\frac{D_{\max}}{w}\ln\left(\frac{1+e^{w(t-t_s)}}{1+e^{-wt_s}}\right),$$

which can be calculated using the l'Hôpital's rule:

$$\begin{aligned}
L &\overset{\text{l'H}}{=} \lim_{w\to+\infty} -D_{\max}\frac{(1+e^{-wt_s})((t-t_s)e^{w(t-t_s)} + t_s e^{-wt_s})}{(1+e^{w(t-t_s)})(1+e^{-wt_s})^2}, \\
&= \lim_{w\to+\infty} -D_{\max}\frac{(t-t_s)e^{w(t-t_s)} + t_s e^{-wt_s}}{(1+e^{w(t-t_s)})(1+e^{-wt_s})}.
\end{aligned}$$

Here we have two cases: if $t - t_s \leq 0$, then,

$$L = 0,$$

and if $t - t_s > 0$, then

$$\begin{aligned} L &= \lim_{w \to +\infty} -D_{\max} \frac{(t - t_s) + t_s e^{-wt_s - w(t-t_s)}}{e^{-w(t-t_s)} + e^{-wt_s - w(t-t_s)} + 1 + e^{-wt_s}} \\ &= -D_{\max}(t - t_s). \end{aligned}$$

□

D.3 Implementation of a neural solver in Python

```
class TwoHidden(nn.Module):
    def __init__(self, output_dim, bounds, dim_hidden, *args, **kwargs) -> None:
        super().__init__(*args, **kwargs)
        self.output_dim   = output_dim
        self.input_layer  = nn.Linear(1,dim_hidden)
        self.hidden_layer = nn.Linear(dim_hidden,dim_hidden)
        self.output_layer = nn.Linear(dim_hidden,output_dim)
        self.ac           = nn.Sigmoid()
        self.lowerBounds  = torch.tensor( [bounds[i][0] for i in range(self.
    output_dim) ])
        self.upperBounds  = torch.tensor( [bounds[i][1] for i in range(self.
    output_dim) ])
    def forward(self,t):
        out = self.input_layer(t.view(-1))
        out = self.ac(out)
        out = self.hidden_layer(out)
        out = self.ac(out)
        out = self.output_layer(out)
        out = self.alpha(out)
        return out
    def alpha(self,v):
        out = self.ac(v)
        out = (self.upperBounds - self.lowerBounds)*out + self.lowerBounds
        return out
```

Listing D.1: Neural controller with two hidden layers.

```
from torchdyn.core import ODEProblem
import torch
import torch.nn as nn
import matplotlib.pyplot as plt
import numpy as np
from tqdm import tqdm
from optimizers import str_to_optimizer
```

Listing D.2: Packages imported

```
class OCP():

    def __init__(self,
```

```
                dynamics,
                z_0,
                Tf,
                cost,
                dim_u,
                bounds,
                control,
                solver_ode,
                sensitivity,
                N,
                optimizer,
                lr):
        self.z_0 = z_0
        self.dim_u = dim_u
        self.cost = cost
        self.time = torch.linspace(0,Tf,N)
        self.control = control
        self.controlled_dynamics = dynamics
        self.dynamics  = ControlledSystemToNonAutonomous(dynamics,self.control)
        self.optimizer = str_to_optimizer(optimizer, self.control, bounds, lr = lr)
        self.ode = ODEProblem(self.dynamics,
                              sensitivity = sensitivity,
                              solver = solver_ode)

    def get_sol(self):
        t_sol, z_sol = self.ode.odeint(self.z_0, self.time)
        return t_sol, z_sol

    def solve(self,epochs):
        for i in tqdm(range(epochs)):
           t_sol, z_sol = self.ode.odeint(self.z_0, self.time)
           z_sol_f = z_sol[-1,:]
           cost = self.cost(z_sol_f)
           cost.backward()
           self.optimizer.step()
           self.optimizer.zero_grad()
```

Listing D.3: OCP, a class for solving optimal control problems via neural networks

```
class Regulator(nn.Module):
    def __init__(self):
        super().__init__()
    def forward(self,t,z,u):
        x = z[0]
        v = z[1]
        l = z[2]
        dx = v
        dv = u
        dl = (x**2+v**2)/2
        return torch.cat([dx.view(1),dv.view(1),dl.view(1)])
cost_funtion = lambda z : z[-1]
initial_conditions = torch.tensor([0.,1.,0.0])
bounds = [(-1.0, 1.0)]
```

Listing D.4: Controlled dynamics of the regulator problem

Bibliography

[1] S. Abu-Ghosh, D. Fixler, Z. Dubinsky, and D. Iluz. Continuous background light significantly increases flashing-light enhancement of photosynthesis and growth of microalgae. *Bioresource technology*, 187:144–148, 2015.

[2] S. Abu-Ghosh, D. Fixler, Z. Dubinsky, and D. Iluz. Flashing light in microalgae biotechnology. *Bioresource Technology*, 203:357–363, 2016.

[3] S. Abu-Ghosh, D. Fixler, Z. Dubinsky, A. Solovchenko, M. Zigman, Y. Yehoshua, and D. Iluz. Flashing light enhancement of photosynthesis and growth occurs when photochemistry and photoprotection are balanced in *Dunaliella salina*. *European Journal of Phycology*, 50(4):469–480, 2015.

[4] H. Ali, T. A. Cheema, H.-S. Yoon, Y. Do, and C. W. Park. Numerical prediction of algae cell mixing feature in raceway ponds using particle tracing methods. *Biotechnology and bioengineering*, 112(2):297–307, 2015.

[5] S. Allgeyer, M.-O. Bristeau, D. Froger, R. Hamouda, V. Jauzein, A. Mangeney, J. Sainte-Marie, F. Souillé, and M. Vallée. Numerical approximation of the 3D hydrostatic Navier–Stokes system with free surface. *ESAIM: Mathematical Modelling and Numerical Analysis*, 53(6):1981–2024, 2019.

[6] J. A. E. Andersson, J. Gillis, G. Horn, J. B. Rawlings, and M. Diehl. CasADi – A software framework for nonlinear optimization and optimal control. *Mathematical Programming Computation*, 11(1):1–36, 2019.

[7] J. F. Andrews. A mathematical model for the continuous culture of microorganisms utilizing inhibitory substrates. *Biotechnology and bioengineering*, 10(6):707–723, 1968.

[8] A. Aussem. Dynamical recurrent neural networks towards prediction and modeling of dynamical systems. *Neurocomputing*, 28(1):207–232, 1999.

[9] M. Baklouti, V. Faure, L. Pawlowski, and A. Sciandra. Investigation and sensitivity analysis of a mechanistic phytoplankton model implemented in a new modular numerical tool (Eco3M) dedicated to biogeochemical modelling. *Progress in Oceanography*, 71(1):34–58, 2006.

[10] M. Barceló-Villalobos, J. G. Sánchez, I. M. Cara, J. S. Molina, and F. A. Fernández. Analysis of mass transfer capacity in raceway reactors. *Algal research*, 35:91–97, 2018.

[11] T. Bayen and F. Mairet. Optimisation of strain selection in evolutionary continuous culture. *International Journal of Control*, 90(12):2748–2759, 2017.

[12] Y. Becerikli, A. F. Konar, and T. Samad. Intelligent optimal control with dynamic neural networks. *Neural networks*, 16(2):251–259, 2003.

[13] Q. Béchet, A. Shilton, and B. Guieysse. Modeling the effects of light and temperature on algae growth: state of the art and critical assessment for productivity prediction during outdoor cultivation. *Biotechnology advances*, 31(8):1648–1663, 2013.

[14] O. Bernard. Hurdles and challenges for modelling and control of microalgae for CO_2 mitigation and biofuel production. *Journal of Process Control*, 21(10):1378–1389, 2011.

[15] O. Bernard, A.-C. Boulanger, M.-O. Bristeau, and J. Sainte-Marie. A 2d model for hydrodynamics and biology coupling applied to algae growth simulations. *ESAIM: Mathematical Modelling and Numerical Analysis*, 47(5):1387–1412, 2013.

[16] O. Bernard, J. Gouzé, and A. Benhammou. Hybrid neural modelling of an anaerobic digester with respect to biological constraints. *Water science and technology*, 43(7):1–8, 2001.

[17] O. Bernard and L.-D. Lu. Optimal optical conditions for Microalgal production in photobioreactors. Submitted paper, Aug. 2021.

[18] O. Bernard and L.-D. Lu. Optimal optical conditions for microalgal production in photobioreactors. *Journal of Process Control*, 112:69–77, 2022.

[19] O. Bernard, F. Mairet, and B. Chachuat. Modelling of microalgae culture systems with applications to control and optimization. *Microalgae Biotechnology*, pages 59–87, 2016.

[20] A. Bernardi, A. Nikolaou, A. Meneghesso, B. Chachuat, T. Morosinotto, and F. Bezzo. Semi-empirical modeling of microalgae photosynthesis in different acclimation states – Application to N. gaditana. *Journal of Biotechnology*, 259:63–72, 2017.

[21] W. Blanken, P. R. Postma, L. de Winter, R. H. Wijffels, and M. Janssen. Predicting microalgae growth. *Algal Research*, 14:28–38, 2016.

[22] J. Bonnans, Frederic, D. Giorgi, V. Grelard, B. Heymann, S. Maindrault, P. Martinon, O. Tissot, and J. Liu. Bocop – A collection of examples. Technical report, INRIA, 2017.

[23] L. Böttcher, N. Antulov-Fantulin, and T. Asikis. AI pontryagin or how artificial neural networks learn to control dynamical systems. *Nature communications*, 13(1):333, 2022.

[24] L. Böttcher and T. Asikis. Near-optimal control of dynamical systems with neural ordinary differential equations. *Machine Learning: Science and Technology*, 3(4):045004, 2022.

[25] J. Bradbury, R. Frostig, P. Hawkins, M. J. Johnson, C. Leary, D. Maclaurin, G. Necula, A. Paszke, J. VanderPlas, S. Wanderman-Milne, and Q. Zhang. JAX: composable transformations of Python+NumPy programs, 2018.

[26] J.-B. Caillau, O. Cots, and P. Martinon. ct: control toolbox–numerical tools and examples in optimal control. *IFAC-PapersOnLine*, 55(16):13–18, 2022.

[27] J.-B. Caillau, W. Djema, J.-L. Gouzé, S. Maslovskaya, and J.-B. Pomet. Turnpike property in optimal microbial metabolite production. *Journal of Optimization Theory and Applications*, pages 1–33, 2022.

[28] L. Chen, O. Bernard, G. Bastin, and P. Angelov. Hybrid modelling of biotechnological processes using neural networks. *Control Engineering Practice*, 8(7):821–827, 2000.

[29] L. Chen, Y. Hontoir, D. Huang, J. Zhang, and A. J. Morris. Combining first principles with black-box techniques for reaction systems. *Control Engineering Practice*, 12(7):819–826, 2004.

[30] R. T. Chen, Y. Rubanova, J. Bettencourt, and D. K. Duvenaud. Neural ordinary differential equations. *Advances in neural information processing systems*, 31, 2018.

[31] Y. Chen, Y. Shi, and B. Zhang. Optimal control via neural networks: A convex approach. *arXiv preprint arXiv:1805.11835*, 2018.

[32] T. Cheng, F. L. Lewis, and M. Abu-Khalaf. A neural network solution for fixed-final time optimal control of nonlinear systems. *Automatica*, 43(3):482–490, 2007.

[33] F. Clarke. *Functional analysis, calculus of variations and optimal control*, volume 264. Springer, 2013.

[34] C. Combe, P. Hartmann, S. Rabouille, A. Talec, O. Bernard, and A. Sciandra. Long-term adaptive response to high-frequency light signals in the unicellular photosynthetic eukaryote *Dunaliella salina*. *Biotechnology and Bioengineering*, 112(6):1111–1121, 2015.

[35] J.-F. Cornet and C.-G. Dussap. A simple and reliable formula for assessment of maximum volumetric productivities in photobioreactors. *Biotechnology progress*, 25(2):424–435, 2009.

[36] J. A. V. Costa, B. C. B. Freitas, G. M. Rosa, L. Moraes, M. G. Morais, and B. G. Mitchell. Operational and economic aspects of spirulina-based biorefinery. *Bioresource technology*, 292:121946, 2019.

[37] P. Darvehei, P. A. Bahri, and N. R. Moheimani. Model development for the growth of microalgae: A review. *Renewable and Sustainable Energy Reviews*, 97:233–258, 2018.

[38] E. A. del Rio-Chanona, J. L. Wagner, H. Ali, F. Fiorelli, D. Zhang, and K. Hellgardt. Deep learning-based surrogate modeling and optimization for microalgal biofuel production and photobioreactor design. *AIChE Journal*, 65(3):915–923, 2019.

[39] F. Della Santa and S. Pieraccini. Discontinuous neural networks and discontinuity learning. *Journal of Computational and Applied Mathematics*, 419:114678, 2023.

[40] D. Demory, C. Combe, P. Hartmann, A. Talec, E. Pruvost, R. Hamouda, F. Souillé, P.-O. Lamare, M.-O. Bristeau, J. Sainte-Marie, et al. How do microalgae perceive light in a high-rate pond? towards more realistic lagrangian experiments. *Royal Society open science*, 5(5):180523, 2018.

[41] W. Djema, T. Bayen, and O. Bernard. Optimal darwinian selection of microorganisms with internal storage. *Processes*, 10(3):461, 2022.

[42] W. Djema, O. Bernard, and L. Giraldi. Separating two species of microalgae in photobioreactors in minimal time. *Journal of Process Control*, 87:120–129, 2020.

[43] W. Djema, L. Giraldi, and O. Bernard. An optimal control strategy separating two species of microalgae in photobioreactors. *IFAC-PapersOnLine*, 52(1):910–915, 2019.

[44] W. Djema, L. Giraldi, S. Maslovskaya, and O. Bernard. Turnpike features in optimal selection of species represented by quota models. *Automatica*, 132:109804, 2021.

[45] A. L. Dontchev. *Perturbations, approximations and sensitivity analysis of optimal control systems*. Springer, 1983.

[46] M. R. Droop. Vitamin B12 and marine ecology. IV. the kinetics of uptake, growth and inhibition in monochrysis lutheri. *Journal of the Marine Biological Association of the United Kingdom*, 48(3):689–733, 1968.

[47] A. D'ambrosio, E. Schiassi, F. Curti, and R. Furfaro. Pontryagin neural networks with functional interpolation for optimal intercept problems. *Mathematics*, 9(9):996, 2021.

[48] S. Effati and M. Pakdaman. Optimal control problem via neural networks. *Neural Computing and Applications*, 23:2093–2100, 2013.

[49] P. Falkowski and C. Wirick. A simulation model of the effects of vertical mixing on primary productivity. *Marine Biology*, 65:69–75, 1981.

[50] J. M. Fernández-Sevilla, C. Brindley, N. Jiménez-Ruíz, and F. G. Acién. A simple equation to quantify the effect of frequency of light/dark cycles on the photosynthetic response of microalgae under intermittent light. *Algal Research*, 35:479–487, 2018.

[51] I. Fierro, B. Chachuat, and O. Bernard. Optimal control of photobioreactor accounting for photoinhibition and photoacclimation. In *ADCHEM 2024*, 2024.

[52] J. I. Fierro U., W. Djema, and O. Bernard. Optimal control of microalgae culture accounting for photoinhibition and light attenuation. *IFAC-PapersOnLine*, 56(2):7222–7227, 2023.

[53] J. I. Fierro Ulloa, L.-D. Lu, and O. Bernard. Theoretical growth rate of microalgae under high/low-flashing light. *Journal of Mathematical Biology*, 86(4):48, 2023.

[54] F. García-Camacho, L. López-Rosales, A. Sánchez-Mirón, E. Belarbi, Y. Chisti, and E. Molina-Grima. Artificial neural network modeling for predicting the growth of the microalga *Karlodinium veneficum*. *Algal research*, 14:58–64, 2016.

[55] F. García-Camacho, A. Sánchez-Mirón, E. Molina-Grima, F. Camacho-Rubio, and J. Merchuck. A mechanistic model of photosynthesis in microalgae including photoacclimation dynamics. *Journal of theoretical biology*, 304:1–15, 2012.

[56] P. Georgieva and S. F. De Azevedo. Neural network-based control strategies applied to a fed-batch crystallization process. *International Journal of Chemical and Molecular Engineering*, 1(12):145–154, 2007.

[57] D. J. Gerla, W. M. Mooij, and J. Huisman. Photoinhibition and the assembly of light-limited phytoplankton communities. *Oikos*, 120(3):359–368, 2011.

[58] J. Glassey and M. Von Stosch. *Hybrid modeling in process industries*. CRC Press, 2018.

[59] C. Goh and K. L. Teo. Control parametrization: a unified approach to optimal control problems with general constraints. *Automatica*, 24(1):3–18, 1988.

[60] M. Y. Gorbunov, F. I. Kuzminov, V. V. Fadeev, J. D. Kim, and P. G. Falkowski. A kinetic model of non-photochemical quenching in cyanobacteria. *Biochimica et Biophysica Acta (BBA)-Bioenergetics*, 1807(12):1591–1599, 2011.

[61] J. Grenier, F. Lopes, H. Bonnefond, and O. Bernard. Worldwide perspectives of rotating algal biofilm up-scaling. Submitted paper, 2020.

[62] E. M. Grima, J. F. Sevilla, J. S. Pérez, and F. G. Camacho. A study on simultaneous photolimitation and photoinhibition in dense microalgal cultures taking into account incident and averaged irradiances. *Journal of Biotechnology*, 45(1):59–69, 1996.

[63] F. Grognard, A. Akhmetzhanov, P. Masci, and O. Bernard. Optimization of a photobioreactor biomass production using natural light. In *49th IEEE Conference on Decision and Control (CDC)*, pages 4691–4696. IEEE, 2010.

[64] F. Grognard, A. R. Akhmetzhanov, and O. Bernard. Optimal strategies for biomass productivity maximization in a photobioreactor using natural light. *Automatica*, 50(2):359–368, 2014.

[65] P. L. Gupta, S.-M. Lee, and H.-J. Choi. A mini review: photobioreactors for large scale algal cultivation. *World Journal of Microbiology and Biotechnology*, 31:1409–1417, 2015.

[66] B.-P. Han. A mechanistic model of algal photoinhibition induced by photodamage to photosystem-II. *Journal of theoretical biology*, 214(4):519–527, 2002.

[67] B.-P. Han, M. Virtanen, J. Koponen, and M. Straškraba. Effect of photoinhibition on algal photosynthesis: a dynamic model. *Journal of plankton research*, 22(5):865–885, 2000.

[68] P. Hartmann, Q. Béchet, and O. Bernard. The effect of photosynthesis time scales on microalgae productivity. *Bioprocess and biosystems engineering*, 37(1):17–25, 2014.

[69] P. Hartmann, D. Demory, C. Combe, R. Hamouda, A.-C. Boulanger, M.-O. Bristeau, J. Sainte-Marie, B. Sialve, J.-P. Steyer, S. Rabouille, et al. Growth rate estimation of algae in raceway ponds: A novel approach. *IFAC Proceedings Volumes*, 47(3):6216–6221, 2014.

[70] L. Hascoet and V. Pascual. The Tapenade Automatic Differentiation tool: principles, model, and specification. *ACM Transactions on Mathematical Software*, 39(3), 2013.

[71] L. M. Hocking. *Optimal control: an introduction to the theory with applications*. Oxford University Press, 1991.

[72] G. Holmes. The use of hyperbolic cosines in solving cubic polynomials. *The Mathematical Gazette*, 86(507):473–477, 2002.

[73] R. Hreiz, B. Sialve, J. Morchain, R. Escudié, J.-P. Steyer, and P. Guiraud. Experimental and numerical investigation of hydrodynamics in raceway reactors used for algaculture. *Chemical Engineering Journal*, 250:230–239, 2014.

[74] G. Hu, Z. Mao, D. He, and F. Yang. Hybrid modeling for the prediction of leaching rate in leaching process based on negative correlation learning bagging ensemble algorithm. *Computers & chemical engineering*, 35(12):2611–2617, 2011.

[75] J. Huisman, H. C. Matthijs, P. M. Visser, H. Balke, C. A. Sigon, J. Passarge, F. J. Weissing, and L. R. Mur. Principles of the light-limited chemostat: theory and ecological applications. *Antonie van Leeuwenhoek*, 81(1):117–133, 2002.

[76] J. Huisman and F. J. Weissing. Light-limited growth and competition for light in well-mixed aquatic environments: an elementary model. *Ecology*, 75(2):507–520, 1994.

[77] R. Kandilian, B. Jesus, J. Legrand, L. Pilon, and J. Pruvost. Light transfer in agar immobilized microalgae cell cultures. *Journal of Quantitative Spectroscopy and Radiative Transfer*, 198:81–92, 2017.

[78] H. Khalil. *Nonlinear Systems*. Pearson Education. Prentice Hall, 2002.

[79] P. Kidger. On neural differential equations. *arXiv preprint arXiv:2202.02435*, 2022.

[80] D. P. Kingma and J. Ba. Adam: A method for stochastic optimization, 2017.

[81] T. Lafarga, J. M. Fernández-Sevilla, C. González-López, and F. G. Acién-Fernández. *Spirulina* for the food and functional food industries. *Food Research International*, 137:109356, 2020.

[82] P. Lamare, N. Aguillon, J. Sainte-Marie, J. Grenier, H. Bonnefond, and O. Bernard. Gradient-based optimization of a rotating algal biofilm process. *Automatica*, 105:80–88, 2019.

[83] E. Lee, M. Jalalizadeh, and Q. Zhang. Growth kinetic models for microalgae cultivation: A review. *Algal research*, 12:497–512, 2015.

[84] J. Legrand, A. Artu, and J. Pruvost. A review on photobioreactor design and modelling for microalgae production. *Reaction Chemistry & Engineering*, 6(7):1134–1151, 2021.

[85] L.-D. Lu. *Lagrangian approach for modelling and optimization of coupled hydrodynamics-photosynthesis*. Theses, Sorbonne Université, Sept. 2021.

[86] H. L. MacIntyre, T. M. Kana, T. Anning, and R. J. Geider. Photoacclimation of photosynthesis irradiance response curves and photosynthetic pigments in microalgae and cyanobacteria 1. *Journal of phycology*, 38(1):17–38, 2002.

[87] F. Mairet and T. Bayen. The promise of dawn: microalgae photoacclimation as an optimal control problem of resource allocation. *Journal of Theoretical Biology*, 515:110597, 2021.

[88] J. E. Mann and J. Myers. On pigments, growth, and photosynthesis of phaeodactylum tricornutum 1 2. *Journal of Phycology*, 4(4):349–355, 1968.

[89] J. Marti-Saumell, J. Solà, C. Mastalli, and A. Santamaria-Navarro. Squash-box feasibility driven differential dynamic programming. In *2020 IEEE/RSJ International Conference on Intelligent Robots and Systems (IROS)*, pages 7637–7644. IEEE, 2020.

[90] C. Martínez, F. Mairet, and O. Bernard. Theory of turbid microalgae cultures. *Journal of theoretical biology*, 456:190–200, 2018.

[91] P. Masci, F. Grognard, and O. Bernard. Microalgal biomass surface productivity optimization based on a photobioreactor model. *IFAC Proceedings Volumes*, 43(6):180–185, 2010. 11th IFAC Symposium on Computer Applications in Biotechnology.

[92] J. Masojídek, R. Lhotskỳ, K. Štěrbová, G. C. Zittelli, and G. Torzillo. Solar bioreactors used for the industrial production of microalgae. *Applied Microbiology and Biotechnology*, 107(21):6439–6458, 2023.

[93] S. Massaroli, M. Poli, F. Califano, J. Park, A. Yamashita, and H. Asama. Optimal energy shaping via neural approximators. *SIAM Journal on Applied Dynamical Systems*, 21(3):2126–2147, 2022.

[94] D. Mauzerall and N. L. Greenbaum. The absolute size of a photosynthetic unit. *Biochimica et Biophysica Acta (BBA) - Bioenergetics*, 974(2):119–140, 1989.

[95] E. Molina, J. Fernández, F. Acién, and Y. Chisti. Tubular photobioreactor design for algal cultures. *Journal of biotechnology*, 92(2):113–131, 2001.

[96] E. Molina Grima, F. García Camacho, J. Sánchez Pérez, F. Acién Fernández, and J. Fernández Sevilla. Evaluation of photosynthetic efficiency in microalgal cultures using averaged irradiance. *Enzyme and Microbial Technology*, 21(5):375–381, 1997.

[97] J. Monod. The growth of bacterial cultures. *Annual review of microbiology*, 3(1):371–394, 1949.

[98] A. Morel. Optical modeling of the upper ocean in relation to its biogenous matter content (case i waters). *Journal of geophysical research: oceans*, 93(C9):10749–10768, 1988.

[99] M. Mowbray, T. Savage, C. Wu, Z. Song, B. A. Cho, E. A. Del Rio-Chanona, and D. Zhang. Machine learning for biochemical engineering: A review. *Biochemical Engineering Journal*, 172:108054, 2021.

[100] K. Narendra and K. Parthasarathy. Identification and control of dynamical systems using neural networks. *IEEE Transactions on Neural Networks*, 1(1):4–27, 1990.

[101] R. G. Nascimento, K. Fricke, and F. A. Viana. A tutorial on solving ordinary differential equations using python and hybrid physics-informed neural network. *Engineering Applications of Artificial Intelligence*, 96:103996, 2020.

[102] M. A. Nielsen. *Neural networks and deep learning*, volume 25. Determination press San Francisco, CA, USA, 2015.

[103] A. Nikolaou, A. Bernardi, A. Meneghesso, F. Bezzo, T. Morosinotto, and B. Chachuat. A model of chlorophyll fluorescence in microalgae integrating photoproduction, photoinhibition and photoregulation. *Journal of Biotechnology*, 194:91–99, 2015.

[104] A. Nikolaou, P. Booth, F. Gordon, J. Yang, O. Matar, and B. Chachuat. Multi-physics modeling of light-limited microalgae growth in raceway ponds. *IFAC-PapersOnLine*, 49(26):324–329, 2016.

[105] A. Nikolaou, P. Hartmann, A. Sciandra, B. Chachuat, and O. Bernard. Dynamic coupling of photoacclimation and photoinhibition in a model of microalgae growth. *Journal of theoretical biology*, 390:61–72, 2016.

[106] R. Noguchi, T. Ahamed, D. S. Rani, K. Sakurai, M. A. Nasution, D. S. Wibawa, M. Demura, M. M. Watanabe, et al. Artificial neural networks model for estimating growth of polyculture microalgae in an open raceway pond. *Biosystems Engineering*, 177:122–129, 2019.

[107] R. Oliveira. Combining first principles modelling and artificial neural networks: a general framework. *Computers & Chemical Engineering*, 28(5):755–766, 2004.

[108] P. Otálora, J. Guzmán, F. Acién, M. Berenguel, and A. Reul. Microalgae classification based on machine learning techniques. *Algal Research*, 55:102256, 2021.

[109] R. Pandey and M. Premalatha. Design and analysis of flow velocity distribution inside a raceway pond using computational fluid dynamics. *Bioprocess and Biosystems engineering*, 40(3):439–450, 2017.

[110] A. Paszke, S. Gross, S. Chintala, G. Chanan, E. Yang, Z. DeVito, Z. Lin, A. Desmaison, L. Antiga, and A. Lerer. Automatic differentiation in pytorch, 2017.

[111] W. B. Penta, J. Fox, and K. H. Halsey. Rapid photoacclimation during episodic deep mixing augments the biological carbon pump. *Limnology and Oceanography*, 66(5):1850–1866, 2021.

[112] A. Perrusquía and W. Yu. Identification and optimal control of nonlinear systems using recurrent neural networks and reinforcement learning: An overview. *Neurocomputing*, 438:145–154, 2021.

[113] M. Poli, S. Massaroli, A. Yamashita, H. Asama, and J. Park. Torchdyn: A neural differential equations library. *arXiv preprint arXiv:2009.09346*, 2020.

[114] L. S. Pontryagin. *Mathematical theory of optimal processes*. CRC press, 1987.

[115] A. Porretta and E. Zuazua. Long time versus steady state optimal control. *SIAM Journal on Control and Optimization*, 51(6):4242–4273, 2013.

[116] V. Pozzobon and P. Perre. Han's model parameters for microalgae grown under intermittent illumination: Determined using particle swarm optimization. *Journal of Theoretical Biology*, 437:29–35, 2018.

[117] W. H. Press, S. A. Teukolsky, W. T. Vetterling, and B. P. Flannery. *Numerical recipes 3rd edition: The art of scientific computing*. Cambridge university press, 2007.

[118] M. Prussi, M. Buffi, D. Casini, D. Chiaramonti, F. Martelli, M. Carnevale, M. R. Tredici, and L. Rodolfi. Experimental and numerical investigations of mixing in raceway ponds for algae cultivation. *Biomass and bioenergy*, 67:390–400, 2014.

[119] D. C. Psichogios and L. H. Ungar. A hybrid neural network-first principles approach to process modeling. *AIChE Journal*, 38(10):1499–1511, 1992.

[120] J. Quinn, L. De Winter, and T. Bradley. Microalgae bulk growth model with application to industrial scale systems. *Bioresource technology*, 102(8):5083–5092, 2011.

[121] M. Raissi, P. Perdikaris, and G. Karniadakis. Physics-informed neural networks: A deep learning framework for solving forward and inverse problems involving nonlinear partial differential equations. *Journal of Computational Physics*, 378:686–707, 2019.

[122] F. Rayen, T. Behnam, and P. Dominique. Optimization of a raceway pond system for wastewater treatment: a review. *Critical reviews in biotechnology*, 39(3):422–435, 2019.

[123] R. Reimann, B. Zeng, M. Jakopec, M. Burdukiewicz, I. Petrick, P. Schierack, and S. Rödiger. Classification of dead and living microalgae *Chlorella vulgaris* by bioimage informatics and machine learning. *Algal research*, 48:101908, 2020.

[124] A. W. Rogers, I. O. S. Cardenas, E. A. Del Rio-Chanona, and D. Zhang. Investigating physics-informed neural networks for bioprocess hybrid model construction. In *Computer Aided Chemical Engineering*, volume 52, pages 83–88. Elsevier, 2023.

[125] S. Ruder. An overview of gradient descent optimization algorithms. *arXiv preprint arXiv:1609.04747*, 2016.

[126] R. Salazar-Peña, V. Alcaraz-Gonzalez, V. González-Álvarez, R. Snell-Castro, and H. Méndez-Acosta. Neural network modeling of the light profile in a novel photobioreactor. *Bioprocess and biosystems engineering*, 37:1031–1042, 2014.

[127] J. A. Sanders, F. Verhulst, and J. Murdock. *Averaging Methods in Nonlinear Dynamical Systems*. Applied Mathematical Sciences. Springer-Verlag New York, 2 edition, 2007.

[128] I. O. Sandoval, P. Petsagkourakis, and E. A. del Rio-Chanona. Neural ODEs as feedback policies for nonlinear optimal control. *IFAC-PapersOnLine*, 56(2):4816–4821, 2023.

[129] E. Schiassi, A. D'Ambrosio, and R. Furfaro. Bellman neural networks for the class of optimal control problems with integral quadratic cost. *IEEE Transactions on Artificial Intelligence*, 5(3):1016–1025, 2022.

[130] E. Schiassi, R. Furfaro, C. Leake, M. De Florio, H. Johnston, and D. Mortari. Extreme theory of functional connections: A fast physics-informed neural network method for solving ordinary and partial differential equations. *Neurocomputing*, 457:334–356, 2021.

[131] J. Schubert, R. Simutis, M. Dors, I. Havlik, and A. Lübbert. Bioprocess optimization and control: Application of hybrid modelling. *Journal of Biotechnology*, 35(1):51–68, 1994.

[132] P. S. Schulze, C. Brindley, J. M. Fernández, R. Rautenberger, H. Pereira, R. H. Wijffels, and V. Kiron. Flashing light does not improve photosynthetic performance and growth of green microalgae. *Bioresource Technology Reports*, 9:100367, 2020.

[133] R. Sirohi, A. K. Pandey, P. Ranganathan, S. Singh, A. Udayan, M. K. Awasthi, A. T. Hoang, C. R. Chilakamarry, S. H. Kim, and S. J. Sim. Design and applications of photobioreactors-a review. *Bioresource technology*, 349:126858, 2022.

[134] P. Spolaore, C. Joannis-Cassan, E. Duran, and A. Isambert. Commercial applications of microalgae. *Journal of bioscience and bioengineering*, 101(2):87–96, 2006.

[135] P. Stapor, L. Schmiester, C. Wierling, S. Merkt, D. Pathirana, B. M. Lange, D. Weindl, and J. Hasenauer. Mini-batch optimization enables training of ode models on large-scale datasets. *Nature Communications*, 13(1):34, 2022.

[136] I. Steinwart and A. Christmann. *Support vector machines*. Springer Science & Business Media, 2008.

[137] D. Stramski, A. Sciandra, and H. Claustre. Effects of temperature, nitrogen, and light limitation on the optical properties of the marine diatom *Thalassiosira pseudonana*. *Limnology and Oceanography*, 47(2):392–403, 2002.

[138] Subitec. Flat panel airlift photobioreactor. `https://www.subitec.com/en/`. accessed: November 8, 2024.

[139] T. Syed, F. Krujatz, Y. Ihadjadene, G. Mühlstädt, H. Hamedi, J. Mädler, and L. Urbas. A review on machine learning approaches for microalgae cultivation systems. *Computers in Biology and Medicine*, page 108248, 2024.

[140] H. Takache, G. Christophe, J.-F. Cornet, and J. Pruvost. Experimental and theoretical assessment of maximum productivities for the microalgae *Chlamydomonas reinhardtii* in two different geometries of photobioreactors. *Biotechnology progress*, 26(2):431–440, 2010.

[141] H. Tamiya, E. Hase, K. Shibata, A. Mituya, T. Iwamura, T. Nihei, and T. Sasa. Kinetics of growth of *Chlorella*, with special reference to its dependence on quantity of available light and on temperature. *Algal culture from laboratory to pilot plant*, pages 204–32, 1953.

[142] Y. Tassa, N. Mansard, and E. Todorov. Control-limited differential dynamic programming. In *2014 IEEE International Conference on Robotics and Automation (ICRA)*, pages 1168–1175. IEEE, 2014.

[143] S. Y. Teng, G. Y. Yew, K. Sukačová, P. L. Show, V. Máša, and J.-S. Chang. Microalgae with artificial intelligence: A digitalized perspective on genetics, systems and products. *Biotechnology advances*, 44:107631, 2020.

[144] Z.-X. Tong, M.-J. Li, J.-J. Yan, and Z.-L. Gu. A theoretical analysis of the hydrodynamic influence on the growth of microalgae in the photobioreactors with simple growth kinetics. *International Journal of Heat and Mass Transfer*, 158:119986, 2020.

[145] E. Trélat. *Contrôle optimal: théorie & applications*, volume 36. Vuibert Paris, 2005.

[146] E. Trélat and E. Zuazua. The turnpike property in finite-dimensional nonlinear optimal control. *Journal of Differential Equations*, 258(1):81–114, 2015.

[147] E. M. Turan and J. Jäschke. Closed-loop optimisation of neural networks for the design of feedback policies under uncertainty. *Journal of Process Control*, 133:103144, 2024.

[148] F. A. Viana, R. G. Nascimento, A. Dourado, and Y. A. Yucesan. Estimating model inadequacy in ordinary differential equations with physics-informed neural networks. *Computers & Structures*, 245:106458, 2021.

[149] R. B. Vinter and R. Vinter. *Optimal control*. Springer, 2010.

[150] M. Von Stosch, R. Oliveira, J. Peres, and S. F. de Azevedo. Hybrid semi-parametric modeling in process systems engineering: Past, present and future. *Computers & Chemical Engineering*, 60:86–101, 2014.

[151] Y.-J. Wang and C.-T. Lin. Runge-Kutta neural network for identification of dynamical systems in high accuracy. *IEEE Transactions on Neural Networks*, 9(2):294–307, 1998.

[152] Q. Wen, L. Sun, F. Yang, X. Song, J. Gao, X. Wang, and H. Xu. Time series data augmentation for deep learning: A survey. *arXiv preprint arXiv:2002.12478*, 2020.

[153] P. J. Werbos. Backpropagation through time: what it does and how to do it. *Proceedings of the IEEE*, 78(10):1550–1560, 1990.

[154] X. Wu and J. C. Merchuk. A model integrating fluid dynamics in photosynthesis and photoinhibition processes. *Chemical Engineering Science*, 56(11):3527–3538, 2001.

[155] A. Wächter and L. T. Biegler. On the implementation of an interior-point filter line-search algorithm for large-scale nonlinear programming. *Mathematical Programming*, 106(1):25–57, 2006.

[156] Y.-C. Yeh, T. Syed, G. Brinitzer, K. Frick, U. Schmid-Staiger, B. Haasdonk, G. E. Tovar, F. Krujatz, J. Mädler, and L. Urbas. Improving microalgae growth modeling of outdoor cultivation with light history data using machine learning models: A comparative study. *Bioresource Technology*, 390:129882, 2023.

[157] D. Zhang, E. A. Del Rio-Chanona, P. Petsagkourakis, and J. Wagner. Hybrid physics-based and data-driven modeling for bioprocess online simulation and optimization. *Biotechnology and bioengineering*, 116(11):2919–2930, 2019.

[158] D. Zwillinger. *CRC standard mathematical tables and formulas*. chapman and hall/CRC, 2018.